# Experimental Investigation of Liquid Fragmentation in Hypersonic Cross Flow

Cem Ozan Asma

Promotoren: prof. Olivier Chazot, prof. dr. ir. J. Vierendeels
Proefschrift ingediend tot het behalen van de graad van
Doctor in de Ingenieurswetenschappen: Werktuigkunde-Elektrotechniek

Vakgroep Mechanica van Stroming, Warmte en Verbranding
Voorzitter: prof. dr. ir. R. Sierens
Faculteit Ingenieurswetenschappen
Academiejaar 2008 - 2009

UNIVERSITEIT
GENT

ISBN 978-90-8578-299-5
NUR 120
Wettelijk depot: D/2009/10.500/57

EXPERIMENTAL INVESTIGATION OF LIQUID FRAGMENTATION
IN HYPERSONIC CROSS FLOW

Dit proefschrift is goedgekeurd door de promotoren:

Assoc. Prof. Olivier Chazot
von Karman Institute for Fluid Dynamics
Aeronautics and Aerospace Department

Prof. Jan Vierendeels
Universiteit Gent
Department of Flow, Heat and Combustion mechanics

Vakgroep Mechanica van Stroming, Warmte en Verbranding
Sint-Pietersnieuwstraat 41
B-9000 Gent
Belgium

*This research was carried out at the von Karman Institute for Fluid Dynamics, Waterloose Steenweg 72, B-1640, Belgium.*

# Acknowledgments

Although my name appears on the title page, this thesis would not have been possible without the very valuable contributions of many others who have assisted, guided, supervised, encouraged and supported me during the last four and a half years.

This thesis came out of a research contract that was sponsored by the French MoD and DGA, under the supervision of Professors Olivier Chazot and Patrick Rambaud at the von Karman Institute for Fluid Dynamics. Olivier Chazot is also one of the supervisors of this PhD and he was the one who has shaped all the research, guiding me at any moment. I have learned a lot from his technical supervision, and even more from his philosophical approach to engineering problems, without forgetting the human aspects. Professor Jan Vierendeels has always been a very professional supervisor, able to answer any technical or non-technical question I had in a very short time and making it incredibly smooth for me to pass through the bureaucratic obstacles. I am also grateful to Professor Patrick Rambaud, Professor Jean-Marie Buchlin, Dr. Raf Theunissen and Dr. M. Rosaria Vetrano for their technical suggestions. The past and the present directors of the von Karman Institute, Mario Carbonaro and Jean Muylaert have been extremely kind and encouraging to allow me to carry out this research while I am full time employed at the Aeronautics and Aerospace Department of the von Karman Institute. I appreciate very much the fact that they do care for my personal development.

There has been many researchers who have contributed to this research as students. I am proud to have carried out a research project with them and to have contributed to their education while they were contributing to the research. In my opinion, the biggest outcome of this thesis is the total success of all the students who have worked with me in this research. Alp Marangoz, Eduardo Zornoza-Garcia-Andrade, Alfonso Blanco Mateo, Darshan Karwat, Sonja Bernhardt and Deniz Ayse Ozuncer all contributed to this research. Among them, the biggest contribution came from two brilliant - I am proud to say - friends and colleagues, Josu Beloki Perurena and Davide Masutti.

The von Karman Institute, where this research is carried out, has always provided a very friendly environment, particularly in the Aeronautics and Aerospace department. Sebastien Paris was always there to share the workload whenever I was in need. Pascal Collin, Alain Petit and Patrick Daneels were the very experienced and skilled force behind the experiments. Vincent van der Haegen has contributed to most of the experimental setups, other than being a patient office mate and a

good friend to share my frustrations. His son, Matisse was the official balloon sponsor of this thesis, being considerate for science and letting out his balloons burst in a hypersonic wind tunnel. I am thankful to all of them.

It is a very difficult and tiring effort to try to get a PhD degree while working full time, especially during the times of literature survey and writing down the dissertation. My greater family's support was irreplaceable, as I shared all of my depressions and frustrations with them. My parents had full confidence on me. They knew that the very good education they supplied would help me in solving every problem. My sister, being far away and trying to get her own PhD, was always the first one in giving me courage or congratulating me for every single achievement I had. The biggest support always came from my love, Evrim, who did not complain even once (although she had the opportunity so many times), and showed a great act of patience and support at all times. Evrim, this thesis, just like my life, has been very meaningful to me, thanks to your support, presence and love. Your name deserves to be next to mine on this thesis. You are the Doctor of my life and this thesis is dedicated to you.

# Nomenclature

| | |
|---|---|
| $\alpha(s)$ | Weight function |
| $\delta$ | Penetration height, mm |
| $\mu$ | Viscosity, Pa.s |
| $\rho_\infty$ | Cross flow freestream density, $kg/m^3$ |
| $\rho_j$ | Liquid jet density, $kg/m^3$ |
| $\sigma$ | Surface tension, N/m |
| $\Theta$ | Jet temperature to freestream temperature ratio |
| $\theta$ | Angular component of cylindrical coordinate system |
| $a$ | Width or diameter of the roughness element, mm |
| $AR$ | Aspect Ratio |
| $C_p$ | Pressure coefficient |
| $CFD$ | Computational Fluid Dynamics |
| $CVP$ | Counter Rotating Vortex Pair |
| $d$ | Droplet diameter, $\mu$m |
| $d_j$ | Jet exit diameter, mm |
| $DCT$ | Discrete Cosine Transform |
| $DFT$ | Discrete Fourier Transform |
| $E$ | Energy function (snake) |
| $f$ | Frequency, Hz |
| $fps$ | frames per second |
| $GVF$ | Gradient Vector Field |
| $h$ | Penetration height, m |
| $I$ | Pixel intensity |
| $IDCT$ | Inverse Discrete Cosine Transform |
| $JICF$ | Jet In Cross Flow |
| $K$ | Experimental to theoretical heat flux ratio, % |
| $k$ | Height of the roughness element, mm |
| $M$ | Mach number |
| $PDF$ | Probability density function |
| $PDI$ | Phase Doppler Interferometry |
| $PDPA$ | Phase Doppler Particle Anemometry |
| $PIV$ | Particle Image Velocimetry |
| $PR$ | Ratio of total injection gas pressure to freestream static presssure |
| $Q$ | Heat flux, $W/m^2$ |
| $q$ | Momentum Flux Ratio |

| | |
|---|---|
| $Re$ | Reynolds number |
| $Re_u$ | Unit Reynolds number, $m^{-1}$ |
| $RMS$ | Root Mean Square |
| $s$ | Spatial coordinate |
| $SMD$ | Sauter Mean Diameter, $\mu$m |
| $SN$ | Signal to Noise Ratio |
| $St$ | Strouhal number |
| $STD$ | standard deviation |
| $TPM$ | Thermal Protection Material |
| $TPS$ | Thermal Protection System |
| $U_j$ | Liquid jet exit velocity, m/s |
| $U_\infty$ | Cross flow freestream velocity, m/s |
| $V/STOL$ | Very Short Take-Off and Landing |
| $VKI$ | von Karman Institute for Fluid Dynamics |
| $VTOL$ | Vertical Take-Off and Landing |
| $w$ | Lateral extension, m |
| $We$ | Weber number |
| $x$ | Coordinate |
| $y$ | Coordinate |
| $z$ | Coordinate |

# Contents

# Summary

This thesis presents an experimental investigation carried out to study penetration and fragmentation of liquid injected into Mach 6 hypersonic cross flow. Flow topology, shock and vortex systems, fragmentation and atomization mechanisms are investigated using high-speed photography, Schlieren photography, flow visualization and Phase Doppler Interferometry techniques. All experiments are conducted at the H-3 Mach 6 wind tunnel facility of the von Karman Institute. Water is used for all tests. Freestream conditions of air flow are kept constant. The variation of the injector geometry and the effect of momentum flux ratio are studied throughout the experimental campaign. Three different injector geometries are utilised, varying the aspect ratio from 1/3 (streamwise rectangular) to 1 (circular) and 3 (spanwise rectangular). All injector geometries have the same cross-sectional area so that they have the same jet exit bulk velocity for a given mass flow rate of water. In a second experimental campaign, water-filled balloons exposed to Mach 6 flow are investigated to understand the fragmentation mechanism in a transient flow field.

The injection of a liquid jet into a crossing Mach 6 air flow is investigated by using a sharp leading edge flat plate with flush mounted liquid injectors. Water jets are introduced through different nozzle shapes with different aspect ratios at relevant jet-to-air momentum flux ratios. Sufficient temporal resolution to capture small scale effects is obtained by high-speed recording, using a Phantom high speed camera, at frame rates as high as sixty thousand images per second. Shock pattern is visualized by Schlieren photography, whereas oil flow visualization and laser cross-section visualization techniques are utilized to study the vortex system and the flow topology. Correlations are proposed, relating water jet penetration height and lateral extension with the injection ratio and orifice diameter for circular injector jets. Penetration height and lateral extension are compared for different injector shapes at relevant jet-to-air momentum flux ratios showing that penetration height and lateral extension decrease and increase, respectively, with injector's aspect ratio. As a result, it is seen that low aspect ratio injectors (such as streamwise rectangular) are favorable when higher penetration is required, in the case of fuel injection into a scramjet engine. On the other hand, high aspect ratio injectors (such as spanwise rectangular) are favorable when lower penetration height and wider lateral extension are required, as in the case of film cooling for the thermal protection systems of space vehicles during an atmospheric entry. Penetration height measurements via image processing technique agree very well with probability density function

analysis. Probability density function analysis has also shown that the mixing of the jet with the cross flow is completed before a distance of 40 injection diameters downstream of the injection point, independent of the momentum flux ratio. The core of the liquid phase, where the liquid population has a maximum, is found to be between 40% and 60% of the penetration height, according to probability density function analysis. Mean velocity profiles related with the liquid jet are extracted by means of an ensemble correlation Particle Image Velocimetry algorithm. The velocity maps of the liquid phase help in identifying the general flow topology, by indicating the main direction of liquid phase velocity. It is observed that the exit velocity of the water jet measured using ensemble Particle Image Velocimetry agrees well with the water mass flow measurements by a rotameter, which is an indication that the technique is applicable to high speed images. The mean and Sauter mean diameter of the liquid droplets are measured at different locations along the median plane on the jet using Phase Doppler Interferometry technique. The droplet size measurements are analyzed and treated to characterize the atomization process of the liquid jet. The Sauter Mean Diameter and the standard deviation of the droplet size distribution are calculated and presented as a function of location and momentum flux ratio. The obtained Sauter Mean Diameter distribution is compared with the theory available in the literature for lower cross flow speed cases. Finally, frequency analyses of the jet breakup and fluctuating shock pattern are performed and characteristic Strouhal numbers of St = 0.18 for the liquid jet breakup and of St = 0.011 for the separation shock fluctuation are obtained. The whipping phenomenon observed for the low momentum flux ratio liquid injections is explained by frequency maps, which allow one to see the flow domains with similar frequency content. This analysis proposes that the penetration of liquid jet determines the shape of the bow shock, which determines the location and angle of the separation shock. The separation shock is observed to penetrate into liquid phase, playing an important role in fragmentation of liquid, thus changing the penetration height and the shape of the bow shock. A continuous interaction between the liquid penetration, bow shock, separation shock and liquid fragmentation is believed to be the mechanism responsible of the whipping phenomenon.

The fragmentation of liquid exposed to Mach 6 air flow is also investigated. Experiments are conducted using water-filled balloons mounted on sharp and blunt leading edge supports. The water-filled balloons are exposed to Mach 6 air flow and high speed camera measurements are taken during the bursting of the balloon, to study the fragmentation of water. Shock patterns and flow topology are visualized by Schlieren photography. The fluctuation of the main oblique shock and its interaction with the liquid phase is studied, using standard deviation analysis of recorded images. Techniques such as "snake movement algorithm" or "time interpolation by discrete cosine transformation" are used to follow the motion of water chunks or droplets during fragmentation. The motions of liquid chunks are displayed and the mechanism leading to fragmentation and atomization is discussed. It is observed that the main shock system plays a major role on the fragmentation of liquid. An

unstable and fluctuating shock system (as in the case of sharp leading edge support) causes a more chaotic and faster fragmentation; whereas a stable shock system (as in the case of blunt leading edge support) causes a slower and less chaotic fragmentation. The balloon tests have shown that the atomization process is basically a fight between the local aerodynamic shear force and the surface tension of the liquid. Both the balloon tests and the Phase Doppler Interferometry tests have shown that the local conditions (such as local velocity of the air stream) should be taken into account rather than freestream conditions while calculating non-dimensional numbers, such as Weber, Reynolds or Ohnesorge numbers.

# Samenvatting

Deze thesis beschrijft het experimentele onderzoek naar penetratie en fragmentatie van een vloeistof geïnjecteerd in een hypersone kruisstroming bij Mach 6. De topologie van de stroming, de schok- en vortexsystemen, fragmentatie en atomisatie mechanismes werden onderzocht met behulp van hoge snelheidsfotografie, Schlieren fotografie, stromingsvisualisatie en fase-Doppler interferometrie technieken. Alle experimenten werden uitgevoerd in de H3, Mach 6 windtunnel aan het von Karman Instituut. Bij alle testen werd water gebruikt, en de condities van de vrije stroming werden constant gehouden. Tijdens de testcampagne werden de variaties van de geometrie van de injector en het effect van de verhouding van impuls fluxen bestudeerd. Hierbij werden drie verschillende injectorgeometrieën gebruikt, waarbij de vormfactor varieert tussen 1/3 (rechthoekig, parallel met de stroming), 1 (rond), en 3 (rechthoekig, dwars op de stroming). Alle injectoren hebben doorstroom dezelfde oppervlakte, zodat voor een gegeven massadebiet van het water de gemiddelde snelheid van de waterstraal dezelfde is. Tijdens een tweede testcampagne werden ballonnen, gevuld met water, blootgesteld aan een stroming bij Mach 6. Dit onderzoek werd uitgevoerd om een beter begrip te krijgen van de fragmentatiemechanismen in een transiënte stroming.

Voor het onderzoek van een waterstraal in een kruisstroming bij Mach 6 werd een vlakkeplaat met een scherpe invalsboord gebruikt, waarbij de injectoren verzonken gemonteerd werden. Er werd gebruik gemaakt van drie injectoren met verschillende vormfactoren, waarbij de verhouding van impuls fluxen van water en supersone stroming in acht werd genomen. Een adequate tijdsresolutie om kleinschalige effecten te onderzoeken werd bekomen met behulp van een Phantom hoge-snelheidscamera. Hierbij werden tot zestigduizend beelden per seconde opgenomen. Schokpatronen werden gevisualiseerd met behulp van Schlierenfotografie. Vortexsystemen en de algemene stromingstopologie werden onderzocht met behulp van olie visualisatie en het beschijnen van de stroming met behulp van een laserwaaier. Een aantal correlaties worden voorgesteld in verband met de hoogte en de breedte van de waterstraal in functie van de verhouding van de impuls fluxen en injectordiameter (voor de ronde injector). De hoogte en breedte van de waterstraal worden vergeleken bij het gebruik van verschillende vormen van injectoren bij relevante verhoudingen van de waterstraal/luchtstroom massafluxen. Dit toonde aan dat de hoogte en debreedte van de waterstraal vermindert, respectievelijk vermeerdert met de vormfactor van de injector. Bijgevolg werd aangetoond dat injectoren met een kleine vormfactor

(rechthoekige injectors, parallel met de stroming) de voorkeur genieten wanneer een krachtige, diepe injectie vereist is, zoals in het geval van brandstofinjectie in de motor van een scramjet. Anderzijds worden injectoren met een hoge vormfactor (bijvoorbeeld rechthoekige injectoren haaks op de stroming) verkozen wanneer een lagere penetratiediepte en bredere stroming is vereist, bijvoorbeeld bij filmkoeling van hitteschilden van ruimteschepen tijdens de terugkeer in de atmosfeer.

Metingen van de penetratiediepte van de waterstraal met behulp van het beeldverwerkingstechnieken komen goed overeen met de resultaten van een probabiliteitsdichtheidsfunctie analyse. Deze laatste toont ook aan dat de waterstraal volledig vermengd is met de haakse luchtstroming ten hoogste 40 injectie diameters stroomafwaarts van de plaats van de injectie. Dit is onafhankelijk van de verhouding van impuls fluxen. De probabiliteitsdichtheidsfunctie analyse toonde ook aan dat het hart van de vloeistoffase, waar de concentratie van vloeistof het hoogst is, zich blijkt zich te bevinden tussen 40% en 60% van de injectiediepte. Profielen van gemiddelde snelheid van de vloeistof stroming werden bepaald door gebruik te maken van een algoritme voor ensemble correlation Particle Image Velocimetry. Het snelheidsveld van de vloeibare fase verschaft een beter inzicht in de algemene stromingstopologie, doordat dit een idee geveft van de richting van de snelheidsvectoren van deze fase. Er is vastgesteld dat de snelheid van de waterstraal, gemeten door middel van ensemble Particle Image Velocimetry goed overeenkomt met de metingen van het massadebiet met behulp van een rotameter. Dit is een goede indicatie dat deze techniek toepasbaar is op hoge-snelheidsopnames. De gemiddelde en Sauter diameter van de vloeistofdruppels werden gemeten op verschillende locaties langsheen het symetrievlak van de jet met behulp van phase Doppler interferometrie. Metingen van de grootte van de druppels werden geanalyseerd om het atomisatieproces van de vloeistofstroom te karakteriseren. De Sauter diameter en de standaarddeviatie van de distributie van de druppelgrootte werden berekend en voorgesteld in functie van de positie en de verhouding van impuls fluxen. De Sauter diameter distributie werd vergeleken met de theorie zoals beschreven in de relevante literatuur. Tenslotte werd een frequentieanalyse uitgevoerd op de desintegratie van de jet stroming en het fluctuerend schok patroon. Daarbij werden karakteristieke Strouhalgetallen van St=0.18 voor de desintegratie van de vloibare jetstroming en St=0.011 voor de fluctuatie van de separatieschok gevonden. Het "wapperen"dat werd geobserveerd bij lage verhoudingen van impuls fluxen wordt verklaard aan de hand van frequentiegrafieken, waarbij stromingsregimes met gelijkaardige oscillaties worden geïdentificeerd. Uit deze analyse wordt geconcludeerd dat de penetratiediepte van de vloeistofstraal de vorm van de boeggolf bepaalt. Deze bepaalt op zijn beurt de positie en hoek van de separatie schok. Er wordt verder vastgesteld dat de separatie schok in de vloeistoffase binnendringt, hetgeen een belangrijke rol speelt in de fragmentatie van de vloeistof. Daardoor worden de penetratiediepte en de vorm van de boegschok beïnvloed. Een gedurige interactie tussen de penetratie van de vloeistof, boegschok, separatie schok en vloeistoffragmentatie wordt verondersteld de oorzaak te zijn van het fenomeen van het "wapperen".

Tevens werd de fragmentatie van een vloeistof die blootgesteld wordt aan een supersone stroming bij Mach 6 bestudeerd. Voor deze testen werden waterballonnen bevestigd op een vlakkeplaat met een scherpe of stompe aanvalsboord. Deze opstelling werd onderworpen aan een supersone stroming en een hoge-snelheidscamera registreet het ontploffen van de waterballon en de fragmentatie van het watervolume. Schokpatronen en de stromingstopologie worden bestudeerd met behulp van Schlierenfotografie. De fluctuatie van de belangrijkste schuine schok en zijn interactie met de vloeistof werden bestudeerd, gebruikmakend van een analyse van de standaarddeviatie van de opgenomen beelden. Technieken zoals het "snake-movement-algoritme en "tijdsinterpolatie door discrete cosinus transformatie"werden gebruikt om de beweging van watervolumes of -druppels tijdens de fragmentatie te volgen. Het gedrag van vloeistofvolumes werd geobserveerd en het mechanisme achter fragmentatie en atomisatie werd besproken. Er wordt aangetoond dat de positie van de schokken een belangrijke rol speelt bij fragmentatie en atomisatie. Inderdaad, een onstabiel, fluctuerend schoksysteem (zoals bij het gebruik van een scherpe aanvalsboord) veroorzaakt een chaotischer en snellere fragmentatie, terwijl een stabiel schok systeem (zoals bij het gebruik van een afgeronde aanvalsboord) een tragere en minder chaotische fragmentatie oplevert. De ballontesten hebben aangetoond dat het proces van atomisatie in se een balans is tussen de lokale aërodynamische wrijvingskrachten en de oppervlaktespanning van de vloeistof. Zowel de ballontesten en de Phase Doppler Interferometry testen toonden aan dat lokale eigenschappen van de stroming (waaronder de lokale snelheid van de luchtstroom) van belang zijn, in tegenstelling tot de vrije stromingscondities, bij het berekenen van dimensioloze getallen zoals het Weber, Reynolds of Ohnesorge getal.

# 1 Introduction

Liquid injection into a crossing flow is a three dimensional and unsteady problem that has been widely investigated for the last sixty years. Its main application is the fuel injection in supersonic combustion ramjet (SCRAMJET) engines, with other applications such as thrust vectoring of high speed vehicles or film cooling of re-entry vehicles. Jets in cross flow are canonical flowfields used in a variety of technological applications for its ability to mix rapidly with cross flow and to introduce a controlled jet force into the flowfield. A schematic diagram of a jet in cross flow (JICF) is shown in Fig. 1.1, and a photo of the typical "instantaneous" structure of the JICF, obtained via smoke visualization is shown in Fig. 1.2 [62]. This photo is taken at an exposure time of 1/2000sec, with a jet of $3.1m/s$ speed injected into a cross flow of $1.2m/s$ [97]. While the jet may seem to issue at a steady rate into the cross flow, the flow structure has in fact a very complicated and unsteady nature of evolution [62].

This thesis presents the details and outcomes of a long-term experimental campaign for the investigation of liquid injection into a Mach 6 hypersonic cross flow. The present chapter is devoted to the explanation of the problem, scope, applications, historical elements and finally the bibliography published for the purpose of the study; whereas Chapter 2 is devoted to the explanation of the problem in general, with a referral to theory of fragmentation and atomization. The experimental set-up and experimental techniques are explained in Chapter 3. Chapters 4 to 6 present the details on experimental work carried out to investigate the general flowfield characteristics, details on atomization, the flow topology of liquid injection compared with gas injection and rigid obstacles in cross flow and finally the details on fragmentation, respectively. Finally, the conclusions and possible enhancements

for future work are presented in Chapter 8, together with a summary of the complete work.

## 1.1 SCOPE AND OBJECTIVE

A conventional rule defines the hypersonic regime as a flow where the Mach number is higher than 5. However, a hypersonic flow is best defined as a regime where certain characteristic physical flow phenomena become progressively more and more important as the Mach number is increasing. The main characteristic of hypersonic flow is that high kinetic energy is dissipated by friction occurring in the boundary layer resulting in a high aerodynamic shear force. This energy is converted to high temperature, causing dissociation of gas molecules and even ionization at extreme conditions. The thermal aspect of hypersonic regime plays a major role in the design of space vehicles (or other very high speed aerial vehicles) and their Thermal Protection Systems (TPS), to reduce local heat flux and to protect the vehicle from extreme aerodynamic heating. In some cases, the vehicle surface is ablated and complex chemical reactions take place, resulting in a chemically reacting boundary layer. The density increase across the shock wave becomes progressively larger as the Mach number increases, making hypersonic vehicles surrounded by a

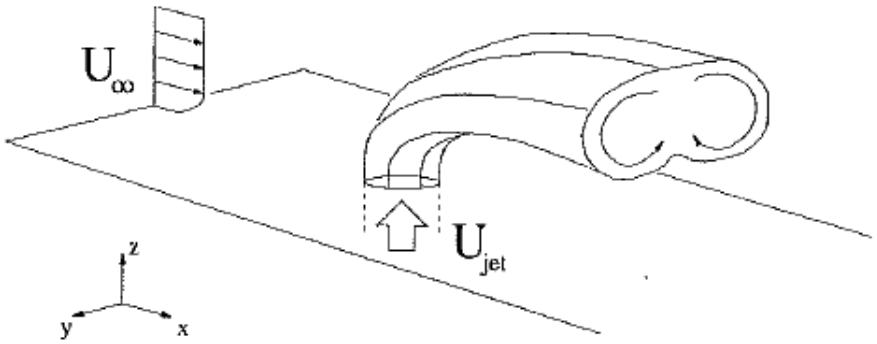


**Figure 1.1:** Global flowfield associated with a jet in cross flow

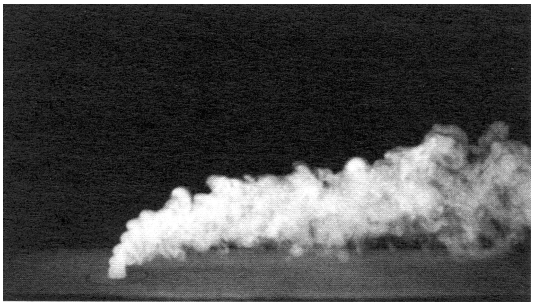

**Figure 1.2:** Smoke visualization of a jet in cross flow

thin shock layer. High temperature and chemical reactions contribute to the thinning of the shock layer. The consequence of a thin shock layer meeting a shock wave with strong curvature is the presence of strong entropy gradients, called entropy layer. The boundary layer grows inside the entropy layer with a strong vorticity and it is affected by the presence of the entropy layer. This interaction is called vorticity interaction [6, 143].

The flow field gets even more complex when secondary flows are introduced, as in the case of jets in hypersonic cross flow. Liquid injection into a compressible cross flow makes the investigation more complicated because of the multi-phase nature of the flow field, with 3-D vortical flows, mixing of gas and liquid phases, fragmentation and atomization of the liquid. The thermodynamic aspects of such a flowfield would bring additional complexity such as chemical reactions occurring during combustion processes, or flashing of the liquid jet.

The scope of the experimental work presented in this thesis covers a non-reactive liquid injection into cold Mach 6 cross flow, where perfect gas assumption is still valid. Although similar problems have been investigated for subsonic or supersonic cross flow cases, no comprehensive experimental investigation is found in the open literature regarding fragmentation of liquid injected into hypersonic flow. The purpose of this study is to carry out such a study for the first time in literature and to start collecting scientific evidence explaining the phenomenon in hypersonic conditions. The data presented in this thesis can also be used for the validation of numerical results obtained by state-of-the-art simulations. Well known measurement techniques are applied for these purposes and the results are discussed in the forthcoming chapters.

Keeping in mind the main goal of this thesis being collecting experimental data for liquid fragmentation in hypersonic flow conditions, seeking answers to the following questions is the reason of most of the activity performed in this study:

- What is the typical flow topology of liquid injection into hypersonic cross flow?
- How do the shock and vortex systems influence the flow field?
- What is the effect of momentum flux ratio and injector geometry on penetration height and lateral extension of liquid jets injected into hypersonic cross flow?
- What are the main parameters influencing the fragmentation mechanism?
- Up to which point are the previous studies and conclusions valid for the hypersonic flow case?
- How are the typical droplet mean and Sauter mean diameter distributions, following the atomization of the water by hypersonic cross flow?

## 1.2 FIELDS OF APPLICATION

The jet in cross flow (JICF) is a basic flowfield which is relevant to a wide variety of applications. The JICF consists of a jet exhausting at a large angle into a freestream flow. Jets are used in widespread engineering systems and as such constitute a canonical set of flowfields. The most common goal of jet flows is to promote mixing of the injectant fluid with the fluid into which the jet is introduced. The impulse created by a jet additionally allows introduction of a localized force into the flowfield, hence thrust or force vector control may also be achieved through the introduction of jets. Variations of the JICF include the jet in a cross flow in ground-effect and cases where there is no freestream velocity; hover out of ground-effect and hover in ground-effect. Specific applications where the JICF represents the primary flowfield feature include plume dispersion, gas turbine combustor cooling, turbofan thrust reversers, turbine cooling, turbojet thrust vectoring, reaction control for missiles and aircraft, and many variants associated with vertical and/or short take off/landing aircraft in transition flight both in and out of ground-effect [91].

Initially, there were some JICF studies related to plume dispersal from smoke stacks, and more recently, volcanos. Mount Pinatubo in the Philippines has spread sufficient ash to put a red hue in the sky at sunset in the northern hemisphere. The 'smoke' exits with an upward momentum due to buoyancy into either a stagnation air mass or sometimes into a cross wind causing dispersal. Smoke distribution at both the ground level and downwind are important. This is a pollution problem where smoke concentration is of primary interest. It is customary to evaluate the upward momentum until buoyancy becomes negligible and then to apply a suitable diffusion formulation.

A second application has been effluent dispersal for liquid disposal in streams. This relates to some manufacturing and the current interest in reducing environmental pollution. Typically the 'jet' represents a pipe or stream flowing into a large lake or river. The research emphasis is diffusion of the 'jet'. The goal is identification of the polluted region and the pollutant concentrations. Another application of this group deals with jets of oil and gas entering the flow in oil wells.

In jet engine combustors, turbines, and others applications, a hot stream of gas can be cooled by injecting jets of cool gas. Injection of fuel is another interest. Jets in cross flow are also found within high speed air breathing engines, such as ramjets and scramjets, as a means of fuel injection into high speed air entering the combustion chamber [63]. Rapid fuel penetration, mixing with cross flow, and ignition and sustainment of combustion processes are highly desirable, since high air speeds entering the combustion chamber (supersonic or even hypersonic in the case of a scramjet) require very rapid completion of the reaction process [31]. The reacting jet in cross flow, such as fuel injection into an air breathing engine, has been a popular study field in the context of both gaseous (fuel-air) reactions and liquid (acid-base) reactions. Both types of applications allow examinations of jet/flame trajectories as well as the dependence of flame length on flow conditions. Fundamental studies of

gas phase reactive jets in cross flow [24] suggest that the jet/flame trajectory follows that of the non-reactive, "cold" jet rather closely.

Reaction control jets have been used on rockets and missiles where the jet pressure ratio tends to be very large. There is usually an underexpanded plume which increases the jet induced effect when compared with a sonic, fully expanded jet. Additional applications include control jets on either underwater vehicles or aircraft to produce control moments. In all of those control applications, the jet induced aeropropulsion interactions and their effect on the net control moment are of primary interest.

Perhaps the largest application over a period of forty years is related to V/STOL aircraft and the recent variant, short takeoff/vertical landing (STOVL) aircraft. Many configurations of these vehicles use jets for take-off and landing with varying forward velocities. During the transition between hover and wing borne flight, the jets usually induce a loss in lift force and a nose-up pitching moment. The design challenge is to locate the jets to minimize these effects and still balance the aircraft for trimmed flight. In ground-effect there are additional complications: a) damaging the ground; b) generating ground wall jets and upwash fountains which modify the aerodynamic forces and moments; and c) ingesting recirculated hot, exhaust gas in engine inlets.

All the fields mentioned above are the most commonly studied applications of jets in cross flows; however, they are not applications related to liquid injections into hypersonic cross flows. The complexity of liquid injection into hypersonic flow regime is increased further due to complex shock–shock, shock–liquid and shock–boundary layer interactions in a multi-phase environment. For example, ablative materials used on thermal protection systems (TPS) of space vehicles experience release of pyrolysis gases, which might alter the flowfield and even the flight characteristics of the vehicles [147, 152, 87]. Gas injection into hypersonic crossing flow can also be done on purpose, for example to promote turbulence to avoid choking of scramjet inlets due to complex shock-shock interactions [126, 22, 19]. On the other hand, the injection of liquid (fuel) into crossing hypersonic flow inside a scramjet engine is another important field of application. The combustion efficiency of such engines depends strongly on the liquid jet penetration depth, atomization and the consequent mixing between the atomized fuel and the free stream air. Thrust vector controlling of missiles and transpiration cooling of the thermal protection system of space vehicles are other typical applications of liquid injection into hypersonic crossflow [91, 16, 30].

## 1.3 Historical Elements

The background of the studies in the field of jet in cross flow (JICF) stands on the scientific work performed on free jets, hence reviewing the flow characteristics of a jet exhausting in an ambient region or co-flowing stream. An example of the earliest works is the work of Tollmien [144] in 1926, applying Prandtl's mix-

ing length theory to a homogeneous air jet with adjacent still air. This theoretical work is followed by the experimental work of Keuthe in 1935 [71] accounting for two parallel streams of different velocities and presenting the initial mixing adjacent to the potential core region. Liepmann and Laufer [82] criticized this work in 1947 by demonstrating a discrepancy between the assumed mixing characteristics and their detailed measurements of the turbulence within the jet. Albertson et al [3] (in 1950) and Taylor [139] (in 1958) advanced the investigation.

The historical development of the investigation performed on JICF are presented in three different periods in the following sections: a) the early work up to 1970, b) experimental mean flowfield investigations and refinement of empiricism in potential flow based methods of calculation until about 1980, and c) recent experimental investigations which begin to provide more detailed data needed to validate contemporary computational fluid dynamic computations [91].

### 1.3.1 EARLY RESEARCH 1923-1970

Systematic investigations started in the 1930's with studies of chimney plumes in cross wind conditions [43, 133]. In a textbook, Kuchemann and Weber [75] described mid-1940's research in Germany for jet induced effects on a jet powered aircraft at high angles-of-attack or with deflected thrust. In 1944 Germany built the first vertical take-off/landing (VTOL) aircraft, the Bachem BA 349 Natter. After an unsuccessful first attempt, a second 1940's VTOL concept considered ramjets on rotating wing tips but was not built. Starting in the late 1940's in the USA at the NACA (now NASA) Lewis Research Center, Callaghan et al. [26, 120] conducted a series of experimental investigations oriented toward injection in a jet engine combustor, with the primary focus being on the penetration of the jet into the freestream and the downstream mixing including temperature effects and effect of the jet orifice shape [25]. Initial interest in V/STOL aircraft provided the impetus for much of the very extensive jet in cross flow (JICF) investigations conducted in the USA and Europe during the fifties and sixties. Wooler developed the most efficient computational model of this period, using doublets and sinks to model the jets in cross flow [157]. In 1969, a JICF symposium [7] was held. At this point, a detailed quantitative description of the flowfield was not available either experimentally or analytically. However there was a broad agreement about the jet cross section shape, appropriate correlation parameter and jet path [91].

Analysis of the jet cross-section shape was started by studying the formation of a vortex pair from a surface of discontinuity in a separation region [118]. These ideas were used in a 1942 analytical study by Chang [28], who was concerned with a circular jet of fluid injected normal to a stream and the subsequent jet deflection and shape change of the separation boundary between the jet fluid and the freestream fluid. Chang also computed the deformation of the boundary.

The discussion on an appropriate correlation parameter started by using the ratio of jet velocity to freestream velocity $U_j/U_\infty$, which was soon recognized to be

not appropriate as it does not include temperature effects. In addition, V/STOL aircraft investigations were concerned with transition flight between hover and wing borne flight. Thus, it was desirable to have a parameter that covers a velocity range from zero (hover condition) to maximum flight speed values. Williams and Wood [156] observed that the jet induced forces and moments were primarily but not solely a function of velocity ratio. The effects of either Reynolds number based on jet exit conditions or freestream velocity were of secondary importance. They showed that a better parameter to account for the effects of temperature and compressibility was the *effective speed ratio*, or the dynamic pressure ratio, finally resulting in the acceptance of the momentum flux ratio $q = \rho_j U_j^2 / \rho_\infty U_\infty^2$ as the main correlation parameter.

Another property of JICF which received early attention was determination of the jet trajectory. The path of the jet is associated with the locus of the maximum velocity. Smy and Ransom [133] summarized all the efforts to predict the trajectory of a jet in 1976. Most of the empirical correlations used the form shown in Eq 1.1, where h is the penetration height, x is the distance from the injection point, $V_e$ is the velocity ratio, $\delta_j$ is the penetration angle and F, G, n and m are constants. Comparison of the coefficients (F and G) and exponents (n and m) used in the equation by various researchers was presented in [90]. The most robust empirical expression seems to be the one by Ivanov [58].

$$\frac{h}{d_j} = F V_e^n \left( \frac{x}{d_j} \right)^m + \frac{x}{d_j} G cot(\delta_j) \tag{1.1}$$

### 1.3.2 Research During 1970's

In the 1969 JICF symposium [7], the need for detailed flowfield surveys was identified as the highest priority research area. As a result, Fearn et al. [34, 36] conducted a series of investigations during the 1970's to measure the flowfield and the pressures induced in the plane adjacent to the jet exit for a range of jet deflection angles and several ratios of jet velocity to freestream velocity. Other effects measured by various investigators in this era were: rectangular, elliptic and more complex jet exit geometries; varying jet deflection angle; jet temperature; and velocity/vorticity profiles. In the 1970's, an extensive database was obtained which has provided a basis for understanding the mean velocity flowfield and pressure distributions. An attempt was also made to simulate the JICF using computational methods.

One well documented aspect of the JICF is the pressure distribution on an adjacent flat surface, by many investigators [98, 149, 35]. In most of the reports the jet-off pressures are subtracted from the jet-on pressures to give the increment due to the existence of the jet as the pressure coefficient $C_p$. While contour plots are probably the most convenient form for data comparisons, there are some errors which affect the interpretation of these plots. Generally, the $C_p$ contour locations become less definite as the $C_p$ gradient approaches zero which is where $C_p$ tends to zero away from the jet [91].

One factor that affects the typical pressure distribution is the shape and orientation of the jet exit. The effect of injector geometry has been investigated by McMahon and Mosher [104] and also by Weston and Thames [154], for different aspect ratios of the injector. The blunt jet (spanwise injector, AR $>$ 1) is characterized by a large low pressure region which spreads laterally and downstream; as well as a region of positive pressure which extends relatively far upstream. The pressures induced by the streamwise jet (AR $<$ 1) were quite different. The primary effect was a low pressure region which spread laterally with almost no wake region and a small positive pressure region. The circular jet (AR = 1) induced pressure distributions are seen to be bracketed by those from the blunt and streamwise jets. The paths of the jet centerline and the vortex curve show the greatest penetration into the freestream for the streamwise jet and the least for the blunt jet. The circular jet paths are between those for the two rectangular jets. For a given jet deflection angle and effective velocity ratio, the vorticity strength is greater for the streamwise jet than for the spanwise jet.

The effect of the jet deflection angle $\delta_j$ on the surface pressure distribution was investigated by Taylor [141], where the angle was varied from 15° to 90°. The decay of the total pressure $C_{pt}$ on the jet centerline increased with increased deflection angle. Aoyagi and Snyder [8] obtained surface pressure data for jet deflection angles which ranged from 90° to 45°. The results were consistent with Taylor's data [141]; the pressure field shifted downstream and the entrainment effect decreased with decreasing jet deflection angle.

The effect of multiple, specifically dual jets has been investigated by Wooler et al. [163] and by Schetz et al. [125] to evaluate their effects on jet interference. Both sets of investigations included in-line jet configurations and side-by-side jet configurations. The results obtained for in-line configuration are similar to those generated by a streamwise jet. The combined result is a decreased lift loss when compared with a single jet which has the same total thrust as the pair of jets. Side-by-side jet configuration results [125, 103] show that the gross interaction features are characterized by two interrelated effects: 1) significantly enhanced flow velocity (reduced surface pressures) between the jets because of the *channeling* of flow between the jets, and 2) increased (when compared with single jet) blocking of the cross flow and spillover to the sides which result in increased flow velocities (lower pressure) on the free sides of the jet. The combined result is an increased lift loss when compared with a single jet which has the same total thrust as the pair of jets.

The decay characteristics of a jet exhausting into ambient conditions are well-documented. The velocity decay for several temperature ratios $\Theta$ (jet temperature to freestream temperature ratio) are studied by Harms [49]. Flowfield velocity surveys indicate little effect of temperature for a given effective velocity ratio. It was found that when the jet temperature is increased, the strength and size of the vortex motion is increased. As a result, more heat is transferred to the vortex region and the maximum temperature path appears to correspond to the vortex path. It should be noted that there is no JICF data from this era for jet temperatures as hot as

modern high pressure ratio turbojet engines.

Considering the velocity/vorticity profiles, the vortex pair generated by the JICF (See also Sections 2.1 and 5.4) appears to be the major flowfield feature. Fearn and Weston [38] measured and computed the path of the vortex curve relative to the jet centerline curve, for different velocity ratio and jet injection angle cases. Initially the vortex paths were obtained by integrating extensive velocity measurements made at selected planes perpendicular to jet path. Fearn and Weston [38] uniquely described the counter-rotating vortex pair strength, location, and a measure of their diffuseness. The vortex pair is formed at the jet exit within the jet flow as relatively concentrated vortices, whose initial strength is inversely proportional to the effective velocity ratio. The vortices are deflected by the cross flow and they diffuse at a rate which is a function of the effective velocity ratio. The vortices gradually weaken each other by the diffusion of vorticity across the symmetry plane.

On the numerical part, several potential-flow, vortex-lattice or panel method based schemes have been developed which account for jet induced interactions. A comparison [92] of five surface panel methods and one vortex-lattice method [93] demonstrated that good agreement for conventional aircraft aerodynamics can be achieved between any of these methods and experimental data. Several investigators have extended potential flow based methods to develop approximate predictive JICF methods. One of the earliest and most complete calculation methods for jet induced effects was developed by Wooler [158]. This model used a double lifting line to represent a simple wing and a sink-doublet model to represent the jet. The Wooler method later incorporated the vortex lattice with the sink-doublet jet model to provide a more comprehensive, modular procedure [158]. For the first module, the incompressible jet model neglected viscous effects other than the entrainment caused by potential flow sinks or doublets. A second module [93] evaluated the jet induced forces and moments using the vortex-lattice method to represent lifting planforms. The method gives good agreements with experimental data for wing-body combinations by including the planform of the body in addition to the wing. Experimental data [102] were used to evaluate these methods. Adler and Baron [2] improved the Wooler-type method to predict the inner structure of the deflected jet more accurately. Two features of the jet were changed. First, the Chang [28] method for determining jet cross section was incorporated. Second, a method was developed to more accurately represent the non-similar velocity profile within the jet cross-section.

### 1.3.3 Research Since 1980's

In the early 1980's, the Harrier dramatically demonstrated the value of the V/STOL capability in the Falkland Islands conflict. However, there has been a slackening of interest in military V/STOL applications, also because of the dissolution of the USSR. There has been continuous interest in turbojet engine applications (such as combustor fuel injection, combustor wall cooling, and injection cooled turbine

blades) and increased interest in deflected thrust for combat aircraft maneuverability. There was an increased interest in the ground effect interaction. There were applications of potential flow panel methods which represented major extensions of the Wooler [158] and Adler-Baron [2] computational methods. However, these efforts provided only modest improvements in numerical solutions. The research emphasis has rather shifted to the application of modern computational fluid dynamics (CFD) methods to JICF and to experimental investigations to obtain specific data for use in CFD verification. Several experiments were conducted which used laser velocimetry to measure the JICF flowfield velocities in finer detail [91].

The first experimental investigations by laser velocimeters [37, 134] demonstrated the feasibility of this device for measuring the flowfield. Later investigations produced some useful data. For example, several reports present different parts of the data obtained during a series of NASA Ames Research Center tests in the 7 by 10 Foot Tunnel [135, 110]. The data included a quantitative measurement of the weak vortex pair near the flat plate immediately downstream of the jet exit. This result demonstrates the ability of laser velocimetry to resolve the fine flow features in this complex flowfield. In addition, a procedure was developed to follow mean streamlines in the flow while measuring the three velocity components. The raw data also included turbulence information [91].

The biggest advantage since 1980 has come from the many CFD investigations undertaken to obtain finite difference numerical solutions to the Navier-Stokes equations for the JICF. Several examples of recent results are examined with an emphasis on their comparisons with experimental data. It was shown by several investigators [119, 68, 29] that Navier-Stokes solutions can adequately represent most of the flowfield. To date, these computational investigations have shown that the flow near the jet exit and on the surface downstream of the jet exit has not been resolved. This is an area of current activity where both improved experimental understanding of the flowfield and recent advances in computer hardware and algorithms have enabled more elaborate numerical solutions. Comparisons with experimental data demonstrate that there is a need for improved numerical solutions.

The most recent works include testing of different fluids (Newtonian or viscoelastic) exposed to higher speeds [59, 60] and also the development of several measurement techniques to serve in such tests. Optical techniques are the most popular and useful techniques that are developed to characterize the droplets and/or particles even if they are not spherical [32]. Among all optical techniques, the Phase Doppler Interferometry (PDI) technique is a non-intrusive technique employed by many researchers to measure the velocity and size of atomized droplets [4]. Reference [77] summarizes the most recent modern experimental techniques to study liquid fragmentation. Mie scattering [101, 52] is a popular technique where a certain plane of the mixing layer is illuminated with a laser sheet. The probability density functions of the illuminated cross-section yields detailed information about the percentage of mixing. Raman spectroscopy is the measurement of the wavelength and intensity of inelastically scattered light from molecules. The Raman scattered light occurs

at wavelengths that are shifted from the incident light by the energies of molecular vibrations. This shift of the lines is specific to the scattering molecule and hence, in multi-component systems, Raman scattering allows the detection of each individual component. This feature of Raman spectroscopy is, therefore, particularly advantageous in the analysis of mixing processes in near-critical jets [77]. Planar laser induced fluorescence (PLIF) is a non-invasive measurement technique that can provide qualitative as well as quantitative flow field information. A laser beam is used to excite a specific species to a higher energy state, thereby causing these molecules to fluoresce. The fluorescence intensity is proportional to the concentration of the excited species (the tracer), which can be interpreted, for example, as a measure of the mixing in the flow field. The tracer can be either added in small concentration to the fluid of interest or the fluid can be completely substituted with the tracer. An example of seeding approach is Planar Laser Induced Exciplex Fluorescence (PLIEF) technique [77]. Planar Laser Induced Fluorescence and Phosphorescence (PLIFP) is a novel spectroscopic technique, first proposed and validated by [145, 146] for an acetone transcritical jet. The technique is capable of characterising quantitatively the mixing behaviour of fluids in a transcritical/supercritical environment as well as identifying the location of the subcritical/supercritical interface. More specifically, the fluorescence signal from the liquid, vapour and/or supercritical phase is used to measure acetone concentration and mixture fraction within the flow field. The phosphorescence emission from liquid acetone is employed to determine the location of the transition to supercritical fluid or the interface between the liquid and vapour region [77].

In the field of theory and modeling, the work of Villermaux [148] for the investigation of fragmentation and the process of atomization is one of the most important ones. Villermaux has performed various observations, to give a unified picture of the overall transition between a compact macroscopic liquid volume and its subsequent dispersion into stable drops. Heister et al. [161, 53, 54] have made important contributions to the numerical modeling of atomization, with a series of codes based on Boundary Element Methods and homogeneous flow modeling. The boundary element methodology permits solution of incompressible, inviscid free-surface problems by placing a series of nodes only on the boundary of the domain. Finally, the work of Frolov et al. [41, 42] that provides experimental and computational data in initiation, propagation, and stability of gaseous fuel–air detonations, is worth noting.

All of the existing experimental studies in supersonic cross flow [61, 83, 107, 73, 27] focus on penetration height of liquid injected into a cross flow with a Mach number varying between 2 and 4. Among these studies, [27] proposes a more complex correlation for penetration height that is supposed to include a cross flow Mach number range up to 8.6. However, compared with experimental data, the proposed correlation of [27] results in a deviation of more than $\pm 20\%$, especially close to the injection point. A summary of research on experimentation and modelisation of liquid injected normally into compressible cross flow is presented in [65]. An exten-

sive study on the breakup of a droplet exposed to Mach 2 or Mach 3 cross flow is carried out by [59], comparing fragmentation mechanism of different liquids. A very recent publication [136] has made the work of G. Smeets and G. Patz publicly available, exposing the experimental work performed to investigate the fragmentation of droplets in shock tubes with freestream velocities as high as Mach 5.

There is a sufficient database in the open literature to achieve an in-depth analysis of the flow topology involving liquid injected into supersonic cross flow or liquid exposed to supersonic flow. Although there is a significant discrepancy between the results obtained by different researchers, it is still possible to agree on the main elements and mechanisms of the flow topology for supersonic conditions. The discrepancies occur mainly because of the differences in the facilities and the measurement techniques that are utilized. For such a complex two-phase flow field, it is regarded as acceptable to have differences in the experimental results owing to the variations in the boundary conditions of the experimental conditions, such as Mach number, total pressure, total temperature, test duration, liquid properties, injector geometries, injection angle, etc... However, the adequate number of independent research performed at supersonic conditions helps the scientists to agree on the main elements of the flow field, such as modeling of the penetration height of the liquid jet, the effect of the major non-dimensional numbers on fragmentation and atomization, the effects of shock waves and shock – shock or shock – boundary layer interactions, and the presence of major vortices. These elements are presented in detail in Chapter 2. On the other hand, the lack of such a database for hypersonic flow conditions is the main source of motivation behind this work. The work performed for supersonic conditions gives important information on the complexity of the flow field and the necessity of collecting individual experimental data to comprehend the flow physics. The challenges faced in the supersonic experiments would certainly remain also for hypersonic conditions, if not significantly increased. The increase in Mach number would bring additional challenges and difficulties as the shock wave system is altered and all phenomena become faster. On the other hand, the measurement techniques applied to supersonic conditions and the results obtained by them would be the guiding force to carry out similar research in hypersonic conditions and to publish in the open literature.

## 1.4 PUBLICATIONS RELATED TO THE THESIS

The experimental findings and the results presented in this dissertation have led to several high-level scientific publications. One journal paper [16] and three AIAA[1] conference proceedings have been published [10, 12, 95]. The journal article [16] summarizes the work presented in Chapter 4; whereas the three conference articles summarize the works presented in Chapters 5 [12], 6 [95] and 7 [10] respectively. A comparison of the works presented in Chapters 4 and 7 is also published [9] as a contribution to a book, the Lecture Notes of the Lecture Series organized by the von

[1] American Institute of Aeronautics and Astronautics. *http : //www.aiaa.org*

Karman Institute[2] entitled "Liquid Fragmentation in High Speed Flows" [11]. The list of published articles is as follows:

- J. Beloki Perurena, C. O. Asma, R. Theunissen, and O. Chazot, *Experimental investigation of liquid jet injection into mach 6 hypersonic crossflow*, Experiments in Fluids, DOI 10.1007/s00348-008-0566-5, vol. 46, no 3, March 2009.

- C. Asma, D. Masutti, and O. Chazot, *Experimental investigation of liquid fragmentation in hypersonic crossflow*, in 27th AIAA Applied Aerodynamics Conference, AIAA 2009-3506, June 2009.

- C. O. Asma, S. Tirtey, and F. Schloegel, *Flow topology of gas, liquid and 3d obstacles in hypersonic flow*, in 27th AIAA Applied Aerodynamics Conference, AIAA 2009-3944, June 2009.

- D. Masutti, S. Bernhardt, C. O. Asma, and R. Vetrano, *Experimental Characterization of Liquid Jet Atomization in Mach 6 Crossflow*, in 39th AIAA Fluid Dynamics Conference, AIAA 2009-4220, June 2009.

- C. O. Asma, D. Masutti, J. Beloki Perurena, *Fragmentation of Liquid in Hypersonic Cross Flow*, Contribution to VKI Lecture Series 2009-04, to be published with ISBN 978-2-930389-92-3.

The research that is presented in this dissertation is a result of a long-duration team work, where many researchers have contributed. This has resulted in several internal publications at von Karman Institute for Fluid Dynamics. All of the work presented in these internal publications have been supervised by the author of this thesis, and they all serve for the purposes mentioned in Section 1.1. Reference [89] focuses on the development of the post-processing tools, while references [15] and [94] are works on liquid injection and fragmentation. A literature survey is presented by [164]. Reference [112] covers the experiments performed for oil flow visualization. The droplet diameter measurements are studied by the researchers [66, 94, 18, 111]. These documents are listed below in chronological order and they are available to public by contacting the Library Services of the von Karman Institute.

- A. Marangoz, *Investigation of liquid jet injection into a hypersonic cross flow*, Project Report 2006-21, von Karman Institute for Fluid Dynamics, Rhode Saint Genèse, Belgium, June 2006.

- J. Beloki Perurena, *Experimental investigation of a liquid jet injection into a crossing hypersonic crossflow*, Project Report 2007-04, von Karman Institute for Fluid Dynamics, Rhode Saint Genèse, Belgium, June 2007.

[2] von Karman Institute for Fluid Dynamics, Brussels, Belgium. *http : //www.vki.ac.be*

- E. Zornoza-Garcia-Andrade and A. Blanco Mateo, *Penetration and atomization of a liquid jet injected in a crossing hypersonic stream*, Stagiaire Report 2007-15, von Karman Institute for Fluid Dynamics, Rhode Saint Genèse, Belgium, September 2007.

- D. Karwat, *Phase doppler particle anemometry analyses of liquid jets injected in hypersonic crossflow*, Stagiaire Report 2008-08, von Karman Institute for Fluid Dynamics, Rhode Saint Genèse, Belgium, 2008.

- D. Masutti, *Experimental investigation of liquid fragmentation in hypersonic crossflow*, Project Report 2008-14, von Karman Institute for Fluid Dynamics, Rhode Saint Genèse, Belgium, June 2008.

- S. Bernhardt, *Measurement of droplet size of liquid injected into a hypersonic cross-flow*, Stagiaire Report 2008-23, von Karman Institute for Fluid Dynamics, Rhode Saint Genèse, Belgium, August 2008.

- A. D. Ozuncer, *Oil flow visualization of liquid injection into Mach 6 crossflow*, Stagiaire Report 2008-43, von Karman Institute for Fluid Dynamics, Rhode Saint Genèse, Belgium, September 2008.

- A. D. Ozuncer, *Phase Doppler Interferometry Measurements of Liquid Injected in Mach 6 Cross Flow*, Stagiaire Report 2009-XX, von Karman Institute for Fluid Dynamics, Rhode Saint Genèse, Belgium, May 2009, to be published.

- C. O. Asma and P. Rambaud (editors), *Liquid Fragmentation in High Speed Flow*, Lecture Series 2009-04, von Karman Institute for Fluid Dynamics, Rhode Saint Genèse, Belgium, March 2009, to be published with ISBN 978-2-930389-92-3.

# 2 Theory

The present chapter is devoted to the explanation of the problem, with a referral to theory of fragmentation and atomization. The typical flow topology of liquid injection into (compressible) cross flow is presented in Section 2.1, where the shock and vortex system are also explained. Section 2.2 summarizes all important non-dimensional numbers that are believed to have a dominant role in fragmentation and atomization of liquids. After the non-dimensional numbers are introduced, the theory of fragmentation and atomization is presented in Section 2.3.

## 2.1 Flow Topology

The flow topology related with liquid jet injection into supersonic and hypersonic cross flow is currently of large interest. Applications related with this topic cover a wide range from thrust vectoring of high speed vehicles to fuel injection in supersonic combustion ramjet engines and transpiration cooling of re-entry vehicles. The break up process of a liquid jet injected into a crossing hypersonic flow is however considerably complex. A simplified schematic of the involved flow topology is presented in Fig. 2.1. Upstream of the bow shock, which is located in front of the injected liquid jet, the accompanying adverse pressure gradient causes the boundary layer to detach, yielding a separation shock. Separation and bow shocks interact, giving rise to alterations in pressure distribution, which in turn modify the bow shock angle. The latter induces a shift in separation point and inclination of separation shock, creating a further change in bow shock angle and jet flow. The resolving chain in events is perceived macroscopically as a continuous vibration of the shock system, which is also called whipping phenomena. The appearance of a separation shock further forces the liquid jet to mix with the air upstream of the injection under subsonic

conditions. Exactly this zone is of importance in cases involving combustion due to its flame-holding capability [45, 17] . After injection, the jet is deflected in a manner dependent on the momentum flux ratio [124]. Downstream of the liquid injection point, the surface of the deflected jet is subject to wavelike disturbances [121]. According to [124] these are most likely attributed to Kelvin-Helmholtz instabilities as a result of the acceleration of a greater density fluid by a high-speed fluid flow of lower density. KelvinŰHelmholtz instability occurs when a shear force is present within a continuous fluid or, when there is sufficient velocity difference across the interface between two fluids. As reported by [80], these waves grow in amplitude, wavelength and speed on the surface of the jet, yielding the primary break up in the form of clump-detachment along the outer portion of the jet (Fig. 2.1). This abrupt clump detachment can be promoted by the bow shock - separation shock interaction and the increasing pressure and heat flux associated with it [33]. In the secondary break up zone, the formed spray decomposes into ever smaller droplets under action of aerodynamic forces of the cross flow until a critical droplet radius is reached. The latter is attained when surface tension force in the droplet surpasses the aerodynamic forces.

In this interaction between the cross flow and the jet, well-known characteristic vortical structures appear:

- Transverse vortices on the boundaries of the jet, named jet-shear-layer vortices, stemming from Kelvin-Helmholtz instabilities.
- Counter rotating vortex pair or kidney vortices, produced by folding of the vortex ring, which is a downstream manifestation of the vorticity arising from the injector's sidewall boundary layers. This vortex system has been extensively reported in many studies [51, 30]. Reference [51] demonstrates that the kidney vortices are generated from the boundary layer of the injector's sidewalls and the injector geometry has a strong influence on the near field character of the kidney vortices.
- Horseshoe vortices, due to the reverse flow upstream of the jet resulting from the blockage of the main flow by the jet [74].

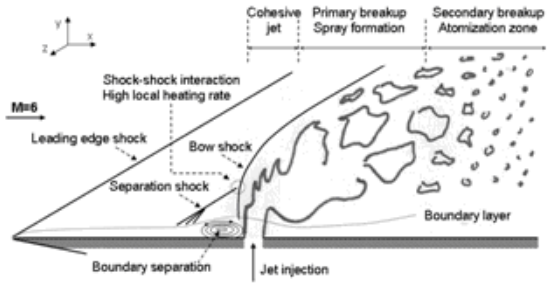


**Figure 2.1:** Schematic of liquid jet injection into hypersonic cross flow, [16]

- Wake vortices downstream of the jet injection. It is discovered that [39] these vortices are generated from the vorticity of the boundary layer of the bottom wall and propagate vertically up to the jet.

A schematic representation of the above phenomena is depicted in Fig. 2.2, according to [39]. The interaction of the crossflow with the liquid jet causes waves to occur on the surface of the jet and it is believed that folding of these waves causes the occurrence of a counter rotating vortex pair [20]. The counter rotating vortex pair is not the only vortex system in the flow field. For example, there is also an "anti-kidney" vortex pair accompanying the kidney shaped vortex pair just above the concave part of the kidney shaped vortex system. The horseshoe vortex system emanating from the boundary layer can also be seen in Fig. 2.2. It has also been observed that wake vortices exist, emanating from the boundary layer on the flat plate towards the jet body. However, these vortices are observed only for specific jet to cross flow dynamic pressure ratios. All of these vortex systems make the flow field highly complex and unsteady. Yet another phenomenon occurs, especially in supersonic or hypersonic cross flows, which makes the situation even worse: the disintegration of the liquid is not from larger particles to smaller ones. It also happens that the smaller particles fold together to form "clumps" [10].

Many studies have been devoted to the liquid jet's penetration height into supersonic crossflow in view of its important relation between mixing performance and combustion efficiency. Reference [73] proposed a simple correlation between the penetration height and the momentum-flux ratio based on experimental data. Reference [61] arrived to similar conclusions assessing the injector geometry dependence on penetration height and also showed that lateral dimension of the jet depends more on the lateral extension of the injector than the momentum-flux ratio. Reference

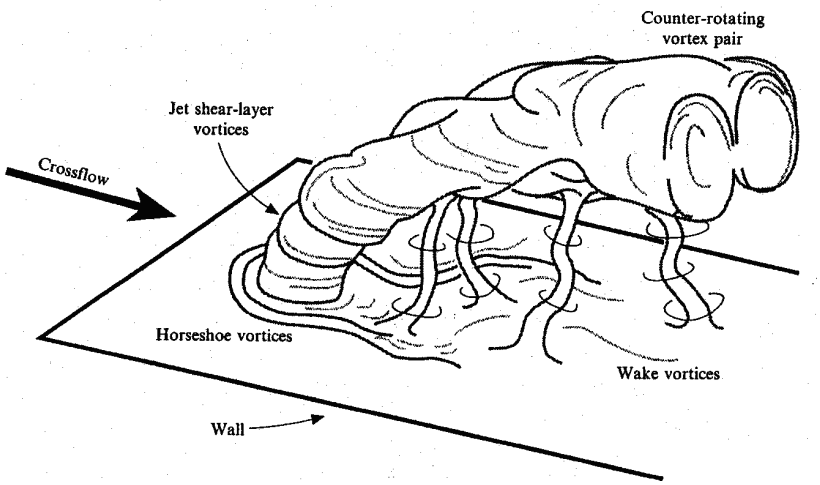


**Figure 2.2:** Characteristic vortical structures in jet injection into cross flow topology [39]

[83] has proposed one of the newest correlations based on shadowgraph measurements, in which, alike the previous studies, the penetration height relates to the momentum-flux ratio and downstream distance. Reference [85] obtained a similar correlation based on Phase Doppler Particle Anemometry (PDPA) measurements, differing the constants and powers of the correlation. Reference [84] demonstrated liquid jet aeration, presenting a two-phase flow comprising air and liquid, to increase the jet penetration height due to an increase of momentum flux ratio between the jet and cross-flow. In a similar manner, [106] showed, for a supersonic gas injection study, that forced injection provides higher penetration of the jet into the free stream in comparison to baseline jets due to the periodic appearance of large-scale eddies on the jet/free stream interface. Further research has been devoted to other important parameters such as the break-up and structure of these jets. Regarding the break-up, [80] discovered that the jet column fractures shortly after the sonic point behind the curved bow shock, which was verified by [81]. On the topic of the structure of the jet, [85] discovered that centerline distribution profiles of droplet plume properties in the freestream direction can be normalized by the penetration height of each spray to obtain universal curves in the regions where the liquid atomization process is complete.

The effects of liquid properties such as viscosity and surface tension have been studied by [115] concluding that these properties do not affect the penetration height for very high cross flow velocities. On the other hand, [107] discovered that by decreasing the surface tension both the wavelength and wave amplitude increase, intensifying the process of break up whereas wavelength and amplitude decrease and increase respectively with viscosity. According to [124], the momentum flux ratio is also an important parameter of the flow topology revealing the characterization of high injection rate jets (momentum flux ratio greater than 6) to be well defined by a jet body while low injection rate jets (momentum flux ratio less than or equal to 1) break up immediately upon injection and vibrate continuously. The definition of momentum flux ratio can be seen in Section 2.2.

Most of the mentioned research is confined to supersonic conditions whereas scramjet engines could also operate in the hypersonic regime. Bibliography regarding hypersonic flow is not plenty and not much data is available. Reference [27] arrived to similar conclusions for hypersonic flows as [73] for supersonic flows and showed that the penetration height is a function of the momentum-flux ratio, the angle of injection and the orifice geometry. Reference [55] attested that variation in inclination of the water injection from a perpendicular angle to a lower angle reduces the penetration height and the lateral extension. As no profuse data is available regarding hypersonic cross flow, the present study aims at presenting results that give a better insight of the flow topology of liquid jet injection into hypersonic cross flow.

## 2.2 Non-Dimensional Numbers

### 2.2.1 Momentum Flux Ratio

The momentum exchange between the jet and the cross flow is defined by the momentum flux ratio or the dynamic pressure ratio defined as:

$$q = \frac{\rho_j U_j^2}{\rho_\infty U_\infty^2} \tag{2.1}$$

where the subscript j corresponds to liquid jet and the subscript $\infty$ corresponds to cross flow conditions. The term $d_j$ is the diameter of the injector for liquid injection cases. The momentum flux ratio is a very important parameter in jet injection into a cross flow as the penetration of the jet and thus the trajectory scales with this parameter. Moreover, in jet injection into supersonic cross flow, the behavior of the jet will differ depending on this parameter [124]. High injection rate jets ($q \geq 6$) are characterized by a relatively well defined jet body with a substantial movement of the outer region of the jet, which "snaps" or fractures violently detaching liquid clumps from the surface. Low injection rate jets ($q \leq 2$ ) show a continuous vibration and whipping motion of the entire jet. Jets with intermediate values of q, $1 < q < 6$ , show a combined behavior of both characteristics.

### 2.2.2 Weber Number

Apart from the momentum flux ratio, which is related with the momentum transfer between the jet and the cross flow, there is another important non-dimensional number related with the break up of the jet due the viscous shear forces in the interface between the jet liquid and the gaseous cross flow. This number is called the Weber number and it is the ratio between the aerodynamic forces that try to disintegrate the liquid jet body and the restoring surface tension force of the liquid that tries to avoid this disintegration. It is defined as:

$$We = \frac{d_j \rho_\infty (U_\infty - U_j)^2}{\sigma} \tag{2.2}$$

where the subscript j corresponds to liquid jet and the subscript $\infty$ corresponds to cross flow conditions. The Weber number determines the type of primary break up of the liquid jet. Injections with low Weber numbers, where the surface tension can be of the order of magnitude of the cross flow aerodynamic forces, show a different type of primary break up than injections with higher Weber numbers, where the aerodynamic forces are considerably higher than the surface tension [121]. In the case of this study, the Weber number is always high, between $10^3$ and $10^4$, and the type of primary break up mechanism is always the same. As explained, this type of

break up is explained because of the growing of wavelike disturbances that end in clump detachment over the surface of the jet. The formed spray decomposes into smaller droplets until a critical droplet radius is reached, in this moment the critical Weber number is obtained and the surface tension forces in the droplets surpass the surrounding aerodynamic forces.

### 2.2.3 OHNESORGE NUMBER

The change of break up type occurs at certain critical Weber numbers, but these critical Weber numbers depend on the type of the fluid and the jet diameter. Another non-dimensional number, Ohnesorge number, can be introduced to define these critical Weber number, relating the viscous and surface tension properties of the liquid:

$$Oh = \frac{\mu_j}{\sqrt{\rho_j d_j \sigma_j}} \tag{2.3}$$

where the subscript j corresponds to liquid jet properties. The variation of Ohnesorge number is not studied during this study and it is kept constant at 0.014 for water injected into Mach 6 cross flow through a 1mm diameter injector.

## 2.3 FRAGMENTATION AND ATOMIZATION

The break-up of a liquid droplet induced by a high-speed gas stream is a well known multiphase flow problem. This problem has many engineering and scientific applications such as damage caused by rain droplets impinging on aircraft in a high-speed flight, combustion and detonation in multiphase mixtures, ablation of space vehicles during an atmosphere re-entry, fuel-coolant interaction in light water reactors, and sodium-water reaction in steam generators of fast breeder reactors, etc. As a result, the break-up of a liquid droplet has been extensively studied by many researchers. The comprehensive reviews of droplet break-up were proposed by [155] and by [59]. However, the mechanism of the three-dimensional droplet break-up at higher Mach numbers is still unclear and there are not many studies performed at hypersonic conditions.

In principle, the types of liquid droplet break-up according to the Weber number can be classified into different modes. The most complete classification of the different modes of fragmentation based on experimental data is explained by [130]. In this investigation, the transition from each mode to the next one is imposed mainly by the increase in aerodynamic forces acting on droplets, compared to the surface tension of the liquid droplet.

Figure 2.3 shows the different modes, which can be summarized as follows:

i. *The vibrational mode* of fragmentation usually occurs at small intensities of action due to aerodynamic forces. The drop affected by the gas stream starts oscillating at the frequency of its natural oscillation, whose amplitude increases.

The drop becomes dumbbell-like and then is decomposed into several big fragments (most often two or four, sometimes up to eight). The overall time of fragmentation is considerably greater in this mode than in the others.

ii. *Bag fragmentation* (the drop shape is sometimes called parachute) is somewhat similar to the break-up of soap bubbles attached to a ring. Initially, the drop is shrunk in the direction of the flow and takes the shape of an oblate spheroid with a hollow on its windward surface. Then the middle part of the drop is blown off into a thin film attached to a massive toroidal rim. Break-up begins from the bottom of the bag, out of which many small fragments are formed. Fragmentation of the rim into several big drops takes place at the last stage. This mode is most typical for liquids with low viscosities (water like).

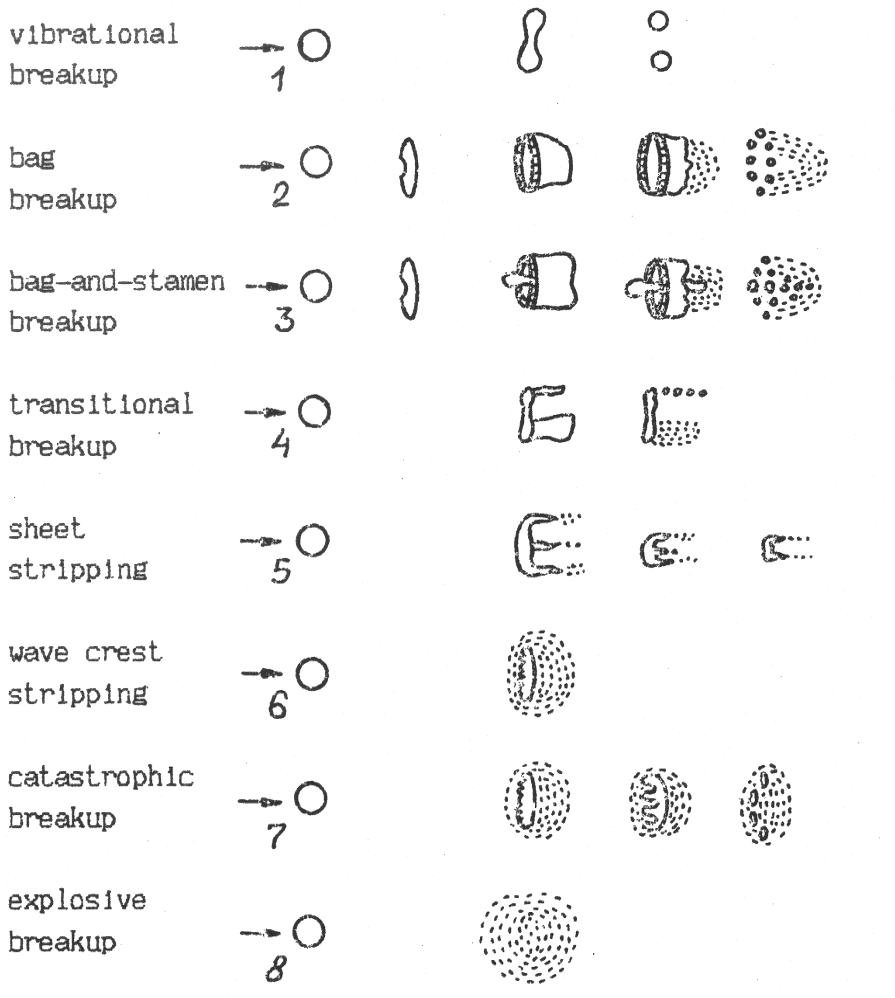


**Figure 2.3:** Modes of drop fragmentation, after [130]

iii. The mode of *bag-and-stamen break-up* (umbrella drop shape) is observed for more intense action for a broad range of viscosity values. This mode has several features in common with the preceding mode. Simultaneously with formation of a bag, a central spray directed against the flow is formed along the axis of the drop. As a rule, the spray is fragmented a bit later than the rim; secondary drops forming during spray break-up may have the same sizes as the rim fragments, or they may become somewhat bigger.

iv. *Transitional mode* (multimode, irregular, or chaotic break-up) is characterized both by blowing off the bag and by the formation of shrouds and threads, and also by very strong deformations.

v. Fragmentation in the mode of *sheet stripping* is essentially different from the pictures described for modes 1-3. The drop shrinks in the direction of the flow, and shrouds or threads (braids) are formed on its surface (mainly on the periphery). Small fragments split off from these sheets and threads. It is worth noting that during the entire process of fragmentation, the initial drop exists as a whole; it breaks up into several fragments at a certain stage.

vi. Under very strong action of the aerodynamic forces, short waves with sufficiently large amplitudes are formed on the windward surface of the drop. Crests of these waves are continuously stripped away by the gas stream. This phenomenon is called *wave crest stripping.*

vii. *Catastrophic fragmentation* is connected with the formation of long waves on the surface of the drop, from which several big fragments are slit off. Later, they are fragmented in their turn, and this process can proceed in several stages until sufficiently small 'daughters' drops are formed. Along with this, the process of wave crest stripping can also be observed.

viii. The mode of *explosive destruction* (to avoid confusion, it should be noted that in some cases this mode is called "catastrophic") usually occurs in strong shock waves. In this case, stripping is practically absent and the drop instantly decomposes into the smallest fragments.

An excellent theoretical analysis of fragmentation is presented in [148]. According to [148], the droplet to be fragmented is probably all contained in Fig.2.4 showing how a liquid drop, falling in a counter ascending air current first deforms, then destabilizes, and finally breaks into disjointed fragments which will remain afterwards stable. The process, usually called "bag breakup" exemplifies the three stages shared by all atomization processes:

- A change of topology of the initial object: the big drop flattens in a pancake shape as it decelerates downwards.
- The formation of ligaments: the toroidal bag rim collects most of the initial drop volume.

- A broad distribution of fragment sizes: the rim is highly corrugated and breaks in many but small, and less frequent but larger drops.

If $\Delta u$ is the velocity difference between the drop and the air stream in a Galilean frame, the drop will break as soon as the stagnation pressure of order $\rho_j \Delta u^2$ overcomes the capillary restoring pressure $\sigma/d_j$ where $\rho_j$, $d_j$ and $\sigma$ represent the liquid density, initial drop size and liquid surface tension, respectively. This condition indicates that the Weber number (see Eqn. 2.2) should be larger than some number with some corrections accounting for possible viscous effects. In such an atomization process, there is no typical size of fragment. There is an average size, and an obvious upper bound, $d_0$, namely the size of the initial drop. It is even unclear if there should be a lower bound. However, the hierarchy of fragment sizes d follows a regular distribution p(d), giving the probability to find a drop size between $d$ and $d + \Delta d$, essentially uniformly decreasing in an exponential-like form with d

$$p(d) \sim e^{-d/d_0} \tag{2.4}$$

up to some cutoff parametrized by the drop's initial size $d_0$ and freestream conditions [148].

Drops come from the rupture of objects in the form of threads or ligaments; the smooth, uniform, long liquid cylinder has become the paradigm of droplet formation. Following the observations of Mariotte (1686) and Savart (1833) that a liquid jet eventually ends in a train of droplets, subsequent studies have explained why the basic smooth state is unstable, how quickly the instability develops [113], and how the thread finally disrupts into unconnected parcels down to nanometric scales [148].

The disintegration of a liquid volume by a gas stream is a phenomenon that is involved in many natural and industrial operations. The spray droplets torn off by the wind at the wave crests in the ocean are an obvious example. As Fig. 2.5 suggests, a shear between the light, fast stream and the slow, dense liquid is at the root of the disintegration process. The change of liquid topology proceeds from a two-stage instability mechanism: First, a shear instability of a Kelvin-Helmholtz

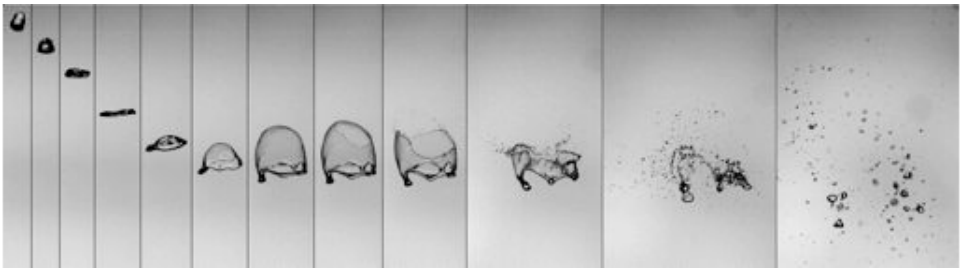

**Figure 2.4:** Fragmentation of a 5 mm water drop falling relatively to an ascending stream of air; after [148]

type forms axisymmetric waves. It is controlled by adapting Rayleigh's analysis [114]; the boundary layer of the gas at the interface produces interfacial undulations whose selected wavelength is proportional to the boundary layer thickness and square root of the ratio of liquid density to gas density. For a large enough amplitude, these undulations undergo a transverse destabilization, of a Rayleigh - Taylor type, caused by the accelerations imposed on the liquid-gas interface by the passage of the primary undulations [148]. The Rayleigh - Taylor instability is an instability of an interface between two fluids of different densities, which occurs when the lighter fluid is pushing the heavier fluid.

Rayleigh-Taylor instabilities [140] always play a role in drop breakup. Rayleigh showed that a heavy fluid over a light fluid is unstable, as common experience dictates. He treated the stability of heavy fluid over light fluid without viscosity, and he found that a disturbance of the flat free surface grows exponentially like $e^{nt}$, where

$$n = \left( \frac{kg(\rho_j - \rho_\infty)}{\rho_j + \rho_\infty} \right)^{1/2} \tag{2.5}$$

where $\rho_j$ is the density of the heavy fluid, $\rho_\infty$ is the density of the light fluid, $g$ is the acceleration of gravity and $k = 2\pi/\lambda$ is the wave number and $\lambda$ is the wave length. The instability described by Eqn. 2.5 is catastrophic since the growth rate n tends to infinity, at any fixed time, no matter how small, as the wave length tends to zero (see also the catastrophic breakup mode in Fig. 2.3). The solutions are unstable to short waves even at the earliest times. Such kinds of disastrous instabilities are called "Hadamard unstable" and the initial value problems associated with these instabilities are said to be "ill posed". Nature will not allow such a singular instability; for example, neglected effects like viscosity and surface tension will enter the physics strongly at the shortest wave lengths. Surface tension eliminates the instability of the short waves; there is a finite wave length depending strongly on viscosity as well as surface tension for which the growth rate n is maximum. This is

**Figure 2.5:** Snapshots of an 8-mm-diameter, slow (0.6 m/s) water jet destabilized by a coaxial fast air stream.; after [148]

the wave length that should occur in a real physical problem and would determine the wave length on the corrugated fronts of breaking drops in a high speed air flow.[59].

The work of [59] at Mach 2 and Mach 3 freestream conditions aims to show that breakup at high accelerations, corresponding to high Weber numbers, is controlled at early times by Rayleigh-Taylor instabilities. They back up this claim by comparing theory with experiment. From the high-speed movies of a droplet exposed to Mach 2 flow in a shock tube, they get accurate displacement-time graphs, one point every $5\mu s$, from which the huge accelerations which drive Rayleigh-Taylor instabilities can be measured. The movie frames can be processed for images of unstable waves from which the length of the most dangerous wave can be measured and compared with theory. An example image showing how the length of Rayleigh-Taylor Waves can be measured is shown in Fig. 2.6, where a water droplet is exposed to Mach 2 air flow. The tick marks on the photographs locate wave troughs.

As translated and made publicly available by [136], the work of G. Smeets and G. Patz at Institute Saint-Louis claims three main mechanisms for the fragmentation of a droplet. The first mechanism addresses the question whether or not the liquid, released in the atmosphere with a velocity of 2 to 3 km/s, evaporates significantly due to associated high stagnation point temperature. The kinetic energy amounts to a multiple of the heat energy required for complete evaporation. A more precise consideration of the flowfield around the droplet with ablation however, shows that

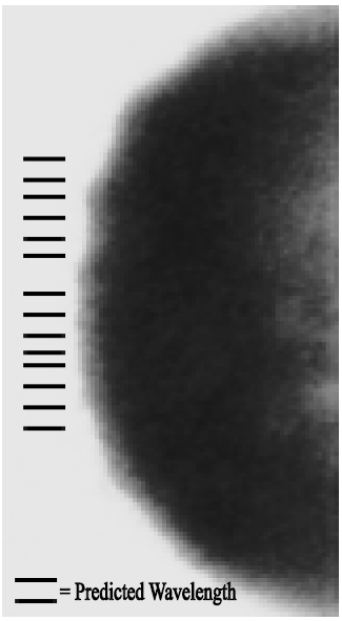


**Figure 2.6:** Rayleigh-Taylor waves on a drop of water exposed to Mach 2 air flow, after [59]

it builds up a kind of vapour barrier between the liquid and the hot gas in the stagnation region limiting a strong heat flux to the drop surface (see sketch in Fig. 2.7). This is comparable to the Leidenfrost effect in which a liquid, in near contact with a mass significantly hotter than its boiling point, produces an insulating vapour layer which keeps that liquid from boiling rapidly. This mechanism is found to cause negligible mass loss for hypersonic cross flow cases.

The fragmentation mechanisms that result in non-negligible mass loss for a droplet in hypersonic freestream are introduced as "tearing up by pressure forces" and "peeling through friction forces" by [136]. The first process is effective when the stagnation pressure strongly predominates compared to the internal pressure existing due to the surface tension in the droplet i.e., if the Weber number is much greater than 1. Figure 2.8 shows how an initially spherical-shaped droplet is being deformed by the flowing air stream. Since the pressure in the stagnation point possesses a maximum, the spherical drop is first flattened to a disk. In the case of very high Weber numbers, the disk can be deformed to a bag, which later bursts

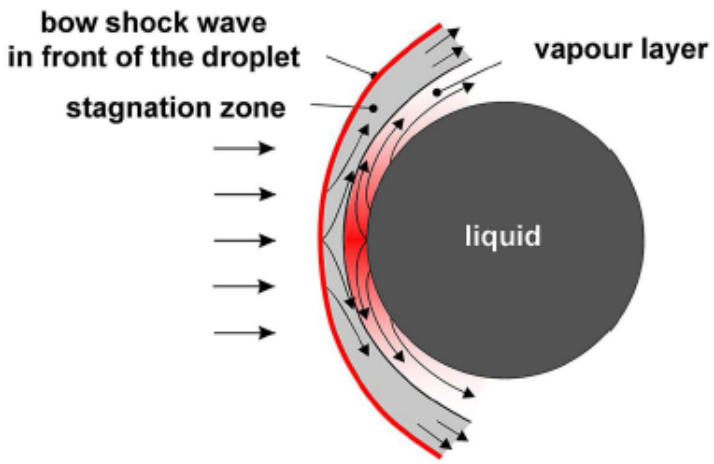


**Figure 2.7:** Droplet with a vapour layer around it, in a flow at high stagnation temperature; after [136]

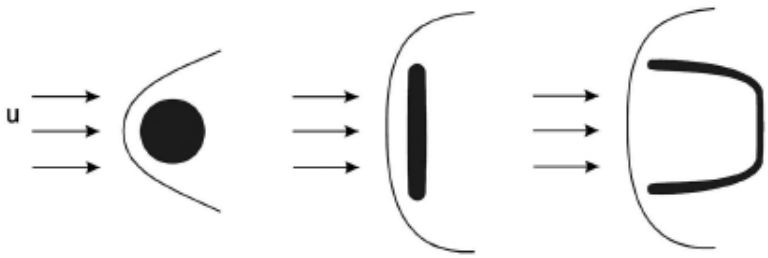


**Figure 2.8:** Mass loss due to pressure forces; after [136]

into fragments bag break-up. The last disintegration process is shown in Fig. 2.9. Every body in motion through a fluid develops a velocity boundary layer region on its surface. This is also valid at the surface of a liquid droplet where a shear stress is produced on the body's surface. While in the case of a solid body the impulse transmitted by the shear stress delays it as a whole and results in a drag resistance, the impulse transferred to a liquid is only transmitted to a thin layer close to the surface. This layer moves to the rear end of the droplet and detaches there. As a result, the drop cannot recover the lost impulse. Finally, it disintegrates into individual droplets, whose dimensions are about those of the boundary layer thickness. This mechanism is similar to the "sheet stripping" mechanism shown in Fig. 2.3. The sheet stripping mechanism is supposed to act on the droplet until the droplet reaches a final diameter of twice the liquid boundary layer thickness, according to [136].

The fight between the aerodynamic shear force and the surface tension of the liquid droplets ends when the droplets become small enough (hence with a higher surface tension force) to resist the aerodynamic shear force. The distribution of droplet dimensions can be identified by an average droplet diameter ($D_{10}$), as well as the Sauter mean diameter ($D_{32}$). The Sauter mean diameter (SMD), also referred as $D_{32}$, is defined as the diameter of a drop having the same volume/surface area ratio as the entire spray. Originally developed by German scientist J. Sauter in the late 1920s, the SMD is a common measure in fluid dynamics as a way of estimating the average particle size. The formulation to compute the mean diameter and the SMD for a generic spray are

$$D_{10} = \frac{\sum_{i=1}^{N} D_i}{N} \tag{2.6}$$

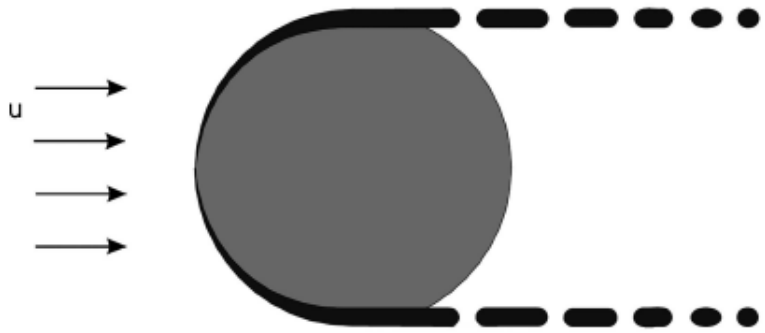


**Figure 2.9:** Mass loss by a detaching liquid boundary layer; after [136]

$$SMD = D_{32} = \frac{\sum_{i=1}^{N} n_i D_i^3}{\sum_{i=1}^{N} n_i D_i^2} \tag{2.7}$$

Knowing only the SMD could be helpful to characterize the drop size distribution of a spray. Measuring the complete distribution of droplet dimensions is a very expensive way to compute the SMD. Several methods have been devised to obtain a good estimate of the SMD, starting from the initial flow conditions. A first empirical estimation is referred by [57], who used a high speed photographing of microscopic droplets travelling at high velocities in combination with a sampling probe technique. By such a combination, they were able to observe and characterize the drop size distribution data obtained for liquid jets atomized by cross-stream injection from simple orifices into high-velocity air stream. The empirical expressions they derived from a dimensional analysis of the data is shown as:

$$D_{32} = D_0 (WeRe_j)^{-n} \tag{2.8}$$

where n is a constant ($n = 0.25$ according to [57]), $We$ is the Weber number and $Re_j$ is the Reynolds number of the injected liquid jet, based on the liquid jet velocity.

$$WeRe_j = \left( \frac{\rho_\infty d_j (U_\infty - U_j)^2}{\sigma_j} \right) \left( \frac{\rho_j d_j U_j}{\mu_j} \right) \tag{2.9}$$

Another expression to empirically predict the Sauter mean diameter is given by [80], who uses an instrumentation based of the Fraunhofer diffraction technique to analyze the atomization zone of a liquid jet in a crossflow. They compared the results with the estimation given by [57], proposing their own formulation

$$D_{32}(\mu m) = 3500 \left( \frac{\mu_j \sigma}{U_\infty U_j} \right)^{0.2} \left( \frac{1}{\rho_j} \right)^{0.25} \tag{2.10}$$

A prediction expression of the Sauter mean diameter is also presented by [56], where they observe the droplet size distribution after the secondary breakup domain:

$$D_{32} = 6.2 D_0 \left( Oh^{1/2} \right) \left( We^{1/4} \right) \tag{2.11}$$

# 3

# Experimental Set-Up and Tools

The present chapter is devoted to the explanation of the experimental set-up, as well as the tools and measurement techniques used to acquire and process data. Two different experimental set-ups are utilized for studying fragmentation and atomization of liquid injected into hypersonic cross flow. The first set-up involves continuous liquid injection through an injector which is flush mounted to a flat plate subject to Mach 6 cross flow. The second set-up involves the bursting of a balloon filled with water and subject to Mach 6 cross flow. The VKI H-3 wind tunnel facility (see Section 3.1) is used for all tests, in combination with different experimental techniques that are described in Section 3.3. The wind tunnel models are described in Section 3.2.

## 3.1 Facility

The VKI H-3 hypersonic wind tunnel is an open loop blow-down facility operating with an axisymmetric nozzle providing a 12cm diameter uniform Mach 6 free air jet, which is swallowed by a movable supersonic diffuser. Dry air is supplied from a 60 $m^3$, 40 bar air storage reservoir of VKI. A pebble-bed heater, as illustrated in Fig. 3.1, heats the gas to a maximum stagnation temperature of 550 K to avoid condensation inside the flow field. The stagnation pressure can vary from 7 to 35 bar. Unit Reynolds number may be varied from $3\times10^6$ to $30\times10^6$ per meter. The test section contains a three-degree-of freedom traversing mechanism for model or probe support that also allows the angle of incidence to vary between -5 and +5 degrees.

In order to achieve the high pressure ratio between the tunnel settling chamber and the exit of the diffuser, required for starting and running the tunnel at Mach 6,

a supersonic ejector is employed to provide the necessary suction at the downstream end of the diffuser, as shown in Fig. 3.1. The design of this diffuser incorporates a second throat. The ejector exhausts into atmosphere. It was chosen as a cost-efficient and more robust solution over that of a vacuum chamber used as exhaust, due to the availability of high pressure air in the 40 bar reservoir of VKI [131].

A fast acting valve serves to rapidly open and close the high pressure pipeline to prevent problems when starting or stopping the flow field. For avoiding wind-tunnel blockage, the facility is started without any model in the test-section. A mechanism for rapid injection is used for injecting the models or probes in 0.1 second, once the hypersonic flow is established and stable. Within the axisymmetric nozzle the flow is considered to be uniform. At a distance of 100mm from the nozzle, the Mach number is found to vary between 5.92 and 6.07 in the furthest region from the center of the jet. More details about the calibration of the hypersonic jet are given by [21]. The tunnel is equipped with optical shadow and Schlieren systems and various other classical measurements techniques are commonly used.

In order to define the test conditions in every run, the total pressure and temperature in the settling chamber are measured using an absolute Statham Strain Gauge pressure transducer and a type K thermocouple. These two values, in conjunction with the nominal test section Mach number (6.0), are adequate to calculate the flow properties such as velocity, Reynolds number etc, by isentropic flow relations. The minimum stagnation temperature necessary to avoid condensation in the test section is recommended to be 470K by [131]. Throughout the whole test campaign, the total temperature is set at 500±20K, and the total presure is set at 20±0.3 bar, resulting in a unit Reynolds number of $18\times10^6\mathrm{m}^{-1}$ ± 3%.

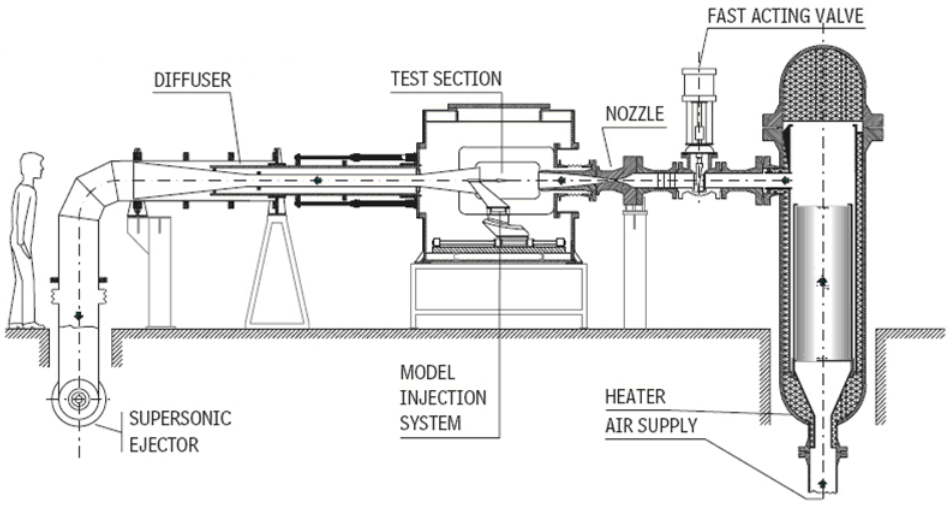


**Figure 3.1:** Schematic of the VKI H-3 hypersonic wind-tunnel

A recent study [47] has been conducted at VKI using double hot-wire probes for measuring the disturbance level in the free-stream of the H-3 wind tunnel. The main results of this investigation are summarized in Fig. 3.2. The measured disturbance spectrum has been restricted to the [10Hz-10KHz] frequency band due to the limitations of the experimental setup. Both mass-flow and total temperature disturbance spectrum have been measured and compared to other equivalent facilities' (Langley 20 feet Mach 6 facility and the Ames 3.5 feet Mach 6 tunnel before and after modifications) performances [128, 96, 137]. Figure 3.2 shows a mass-flow disturbance level of about 2.5% for low Reynolds conditions and 1.5% for high Reynolds conditions of H-3 wind tunnel. The mass-flow has been found to be a good parameter in the literature for the characterization of the disturbance level.

These investigations show that the disturbance level is comparable to other equivalent facilities' performances but is one order of magnitude higher than those measured in so-called *quiet* wind-tunnels and encountered in real flight conditions. Despite its noise level, the H-3 wind tunnel is considered to be comparable to other well established hypersonic wind tunnels and therefore is seen as a suitable facility for hypersonic testing [143]. This facility is chosen for the experimental investigation of liquid fragmentation in high speed cross flow conditions because of its well defined and long duration Mach 6 flow envelope. The facility is easy to operate and up to 10 tests can be performed per day in ideal conditions. Because of these reasons, the H-3 facility is preferred over higher Mach number Longshot facility that is much more costly and that can be operated maximum once a day in ideal conditions.

## 3.2 Wind Tunnel Models

Two different experimental set-ups are utilized throughout the test campaign. The first one is a flat plate with a liquid injector flush mounted to it, as explained in Section 3.2.1. The flat plate model is used for continuous liquid injection into hypersonic cross flow to study penetration height, mixing, liquid - shock interaction,

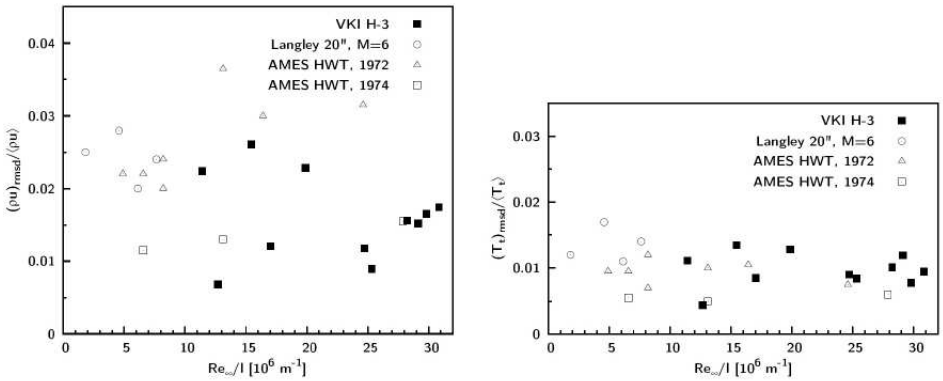


**Figure 3.2:** Comparison of H3 free-stream mass-flow (left) and total temperature (right) disturbance level to other equivalent facilities

shock - shock interaction, and atomization phenomena. The second test model, a balloon full of water and subject to hypersonic flow, is presented in Section 3.2.2. This model is utilized to study the transient fragmentation phenomena.

### 3.2.1 FLAT PLATE MODEL

A flat plate having dimensions 230mm×80mm and a sharp leading edge is utilized for continuous liquid injection into hypersonic cross flow. The model is mounted to the fast injection arm of the H-3 wind tunnel facility and it is injected into the flow field after the Mach 6 flow has been established and maintained for some time in the test section. This is necessary to avoid the possible blockage of the wind tunnel. A sketch of the flat plate model and a photograph showing the flat plate installed in the H-3 wind tunnel are shown in Figure 3.3 [15].

The water injectors are interchangeable inserts that fit into the round chamber in the flat plate. The chamber is flush with the flat surface and its location is 70mm downstream of the leading edge. Three different geometries of injectors have been used, where all have the same cross-sectional area although they have different aspect ratios (AR).

- 1mm diameter circular injector (AR = 1)
- streamwise rectangular (0.5mm x 1.6mm) injector (AR = 1/3)
- transverse rectangular (1.6mm x 0.5mm) injector (AR = 3)

The edges of the rectangular injectors are rounded in order to obtain a more uniform flow over the length of the rectangle. The range of jet Reynolds numbers based on the jet exit diameter d and the exit velocity, varied from Re = 11000 for low injection rates up to Re = 28000 for the highest injection rate. Figure 3.4 depicts a detailed view of the three injectors used during the investigation [16].

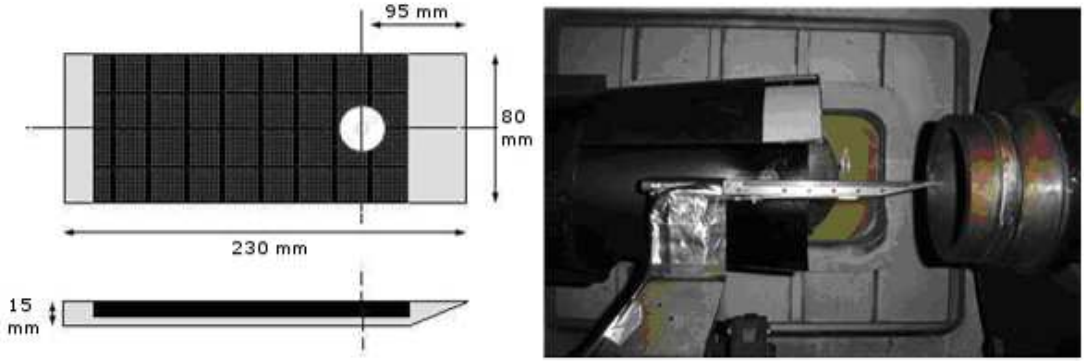


**Figure 3.3:** Dimensions of flat plate (left) and flat plate installed in the test section of H-3

Throughout the experimental campaign, tap water at room temperature is used as liquid injectant. The water temperature is measured with a K type thermocouple and monitored by a data acquisition system unit. Frequencies of fluctuations of the injected water pressure are observed by a pressure transducer. A L63/2400-16862 model rotameter downstream of the first valve fixes the mass flow rate of the water and of the desired dynamic pressure ratio [1]. The rotameter is calibrated before every test campaign. A schematic of the setup is shown in Fig. 3.5 [16].

### 3.2.2 Balloon Model

Liquid fragmentation tests are simply performed by exposing a water-filled balloon to Mach 6 flow and taking measurements while the balloon bursts and the water is fragmented by the hypersonic cross flow. Two different supports are used for balloon experiments in the H3 wind tunnel. The first one is a sharp leading

[1] See Section 2.2 for the definition of dynamic pressure ratio

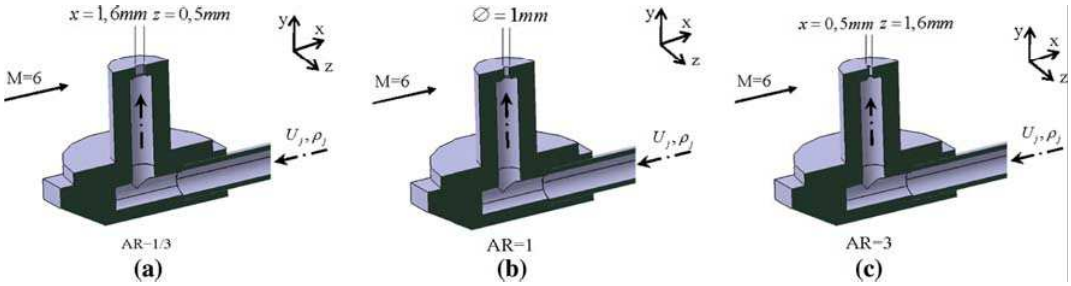


**Figure 3.4:** a) Streamwise rectangular injector, AR = 1/3; b) circular injector, AR = 1 and c) spanwise rectangular injector, AR = 3

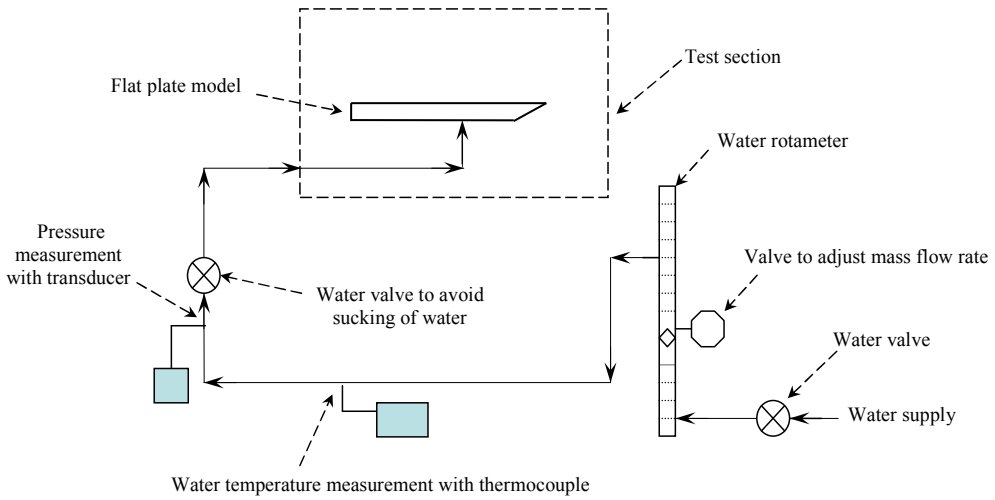


**Figure 3.5:** Schematic of the experimental set-up

edge support (Fig. 3.6) with a thickness of 12mm and an angle of 25degrees at the leading edge. The second one is a blunt support with a highly rounded leading edge (Fig. 3.7), at a thickness of 12mm and a radius of curvature of 9mm at the leading edge. The balloon can be tightened between the sections shown in green and yellow in Fig. 3.7. Both supports are used for testing of water balloons in H-3, in combination with the high speed camera to study the fragmentation of water in Mach 6 cross flow. An oblique shock wave occurs with the sharp leading edge support, whereas a detached normal shock wave occurs with the blunt support. A balloon filled with 2.8±0.2g of water is fixed to the support and the support is mounted inside the test section. The balloons are twisted before mounting them on the support to assure that the skin of each balloon is tight. The typical diameter of a water balloon is 1cm. The support with the balloon is kept outside the flow at the beginning of the test to avoid bursting while the wind tunnel is starting. Once the Mach 6 flow is established, the balloon is injected. It is observed that the bursting of the balloon happens only after the balloon is moved to the center-line of the Mach 6 stream and the bursting of the skin of the balloon is completed in less than 2 milliseconds [94, 10].

## 3.3 MEASUREMENT TECHNIQUES

Photographic techniques , such as schlieren technique or high-speed imaging are the main techniques that are utilized. A high-speed camera is used in conjunction with all visualization tests, including schlieren photography, oil flow visualization and laser cross-section visualization. Phase Doppler Interferometry (PDI) is the other technique which does not involve any viusalization but is used for droplet size estimation. The visualization techniques are described through Sections 3.3.2 to 3.3.6, whereas the PDI technique is explained in 3.3.7.

### 3.3.1 HIGH-SPEED CAMERA

A Phantom v7.1 high speed camera from Vision Research [2] is used for all high-speed photography during the experimental campaign. The Phantom v7.1 camera

[2] http://www.visionresearch.com/

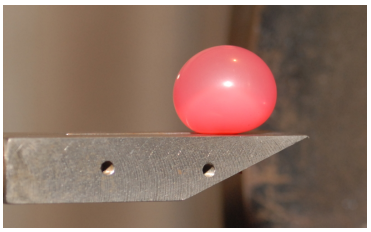

**Figure 3.6:** Sharp leading edge support with balloon inside the test section

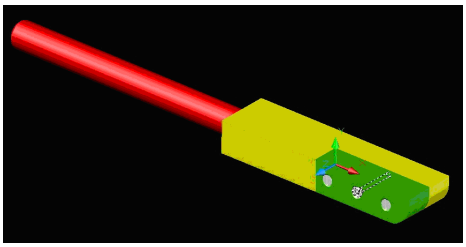

**Figure 3.7:** Blunt leading edge support

is equipped with an 8bit resolution SR-CMOS 800x600 pixels sensor. It permits acquiring images at sampling rates as high as 4800fps for full resolution, or up to a maximum of 150000fps for a reduced 32x32 pixels resolution. The acquired images are in gray scale with a color depth of 8 bits and at an exposure time as low as 2 $\mu$s. Light sources as powerful as 1600W are used to get the minimum shutter time and high frame frequency. The high speed camera is used to obtain both schlieren movies and also back-light illuminated movies, around 10000fps sampling rate for both cases. The acquisition speed of the high speed camera has been increased up to 60000fps for the back-light illuminated movies of continuous liquid injection tests. The camera can be used with any F-mount lens. The typical lenses used are Nikkor 50mm (maximum aperture f1:1.4), 110mm (maximum aperture f1:2.8) and 200mm (maximum aperture f1:4.0) lenses.

The Phantom v7.1 camera is chosen for this experimental campaign because of its availability and advanced high-speed capabilities. Although the 8-bit dynamic resolution and the small sensor size are the major disadvantages, the ease of utilization and the high sensitivity of its sensor to light are the advantages to employ such a camera in the study of liquid fragmentation in hypersonic cross flow conditions. The camera strictly measures the light intensity integrated on every pixel throughout the exposure time. Like all cameras, the usage of this camera should be considered with care as it reduces a three dimensional phenomenon into a 2 dimensional view.

### 3.3.2 Schlieren Photography

The Schlieren technique is an optical technique used to visualize optical inhomogeneities in transparent material not visible to the human eye, such as deviation in density of the medium for the case of a hypersonic wind tunnel testing. The inhomogeneities due to density change are localized differences in optical path length that cause the parallel light rays to deviate. This light deviation is converted to shadow in a schlieren system [129].

Classical Schlieren technique has been used to study the characteristic shock pattern of the flow topology. A schematic of the Schlieren set-up can be seen in

**Figure 3.8:** Phantom v7.1 high speed camera

Fig. 3.9. An enhanced light source (1000 W halogen lamp) [150] of Lunartron Electronics Ltd. is used as a continuous light source. The reflection of the light from a parabolic mirror produces a parallel light beam which is diverted into the test section through a flat mirror. This light beam crosses the flow in the test section and is reflected again through another flat mirror and a parabolic mirror, forcing the light to focus on the knife edge, which cuts the light according to the classical Schlieren technique. Finally, the light is projected by a last mirror to the high speed camera, which acquires Schlieren images with a shutter speed as low as 50$\mu$s. A typical Schlieren image is shown in Fig. 3.10, where the oblique shock wave downstream of the balloon is clearly visible. Looking at this Schlieren image carefully, one can also notice several shock - shock and shock - boundary layer interactions. Downstream of the balloon, expansion waves are visible as well in the wake of the balloon, indicating an increase of velocity in this region. Thanks to high speed Schlieren photography, it is also possible to observe the rapid fluctuations of the shock wave system.

The schlieren technique that is already installed to the H-3 facility is utilized during this experimental campaign because of its availability and easiness to align it. The only change on the existing schlieren setup is changing the light source with a more powerful one to be able to achieve shorter exposure times using the high speed camera.

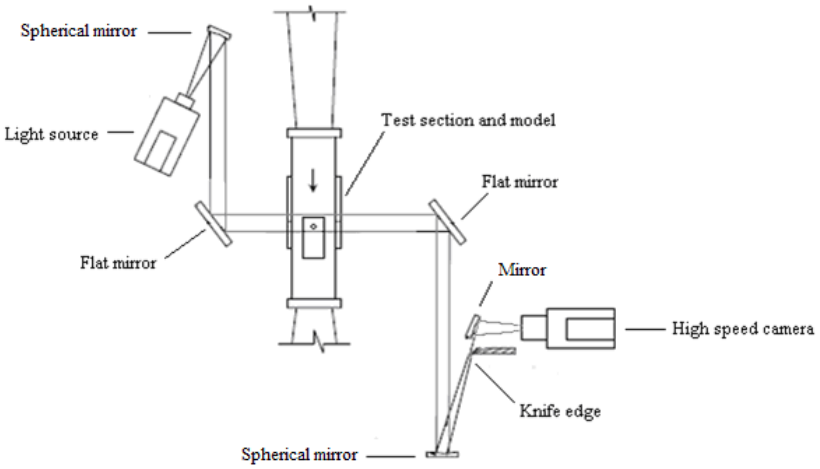


**Figure 3.9:** Schlieren photography set-up, schematic view

### 3.3.3 Back-Light Photography

To obtain back-light photographs [3], a halogen light source of 1600W power is employed on the opposite side of the test section, with respect to the position of the high speed camera. The back-light illumination creates a very sharp shadow of the boundaries of the water droplets, resulting in clear and detailed information about the break-up mechanism. As the light source is pointing directly at the camera, a very sharp image can be obtained, thanks to an exposure time as low as $2\mu$s. The recording frequency of the high speed camera is varied between 10000fps and 14000fps for balloon tests, whereas 60000fps rate is achieved for continuous liquid injection experiments. Four consecutive back-light illuminated photos are shown in Fig. 3.11, where the bursting of a balloon and fragmentation of water can be seen clearly [10, 94].

This set-up has been used to obtain a close-up view of the jet and to study the break up, fragmentation, atomization, velocity of the particles and the behavior of the flowfield topology. A schematic view of the back-light illumination test set-up can be seen in Fig. 3.12

### 3.3.4 Front-Light Photography

Front-light illuminated photography has been used to illuminate the test section and the light reflected from the liquid has been recorded by the high speed camera. This set-up is used to obtain a wide and general view of the flow field and study the jet from a macroscopic way. A schematic of the front-light illumination test set-up can be seen in Figure 3.13. The front light setup permits to observe a general behavior of the balloon fragmentation, but is not good for post-processing and obtaining

[3] also known as the *shadow technique*

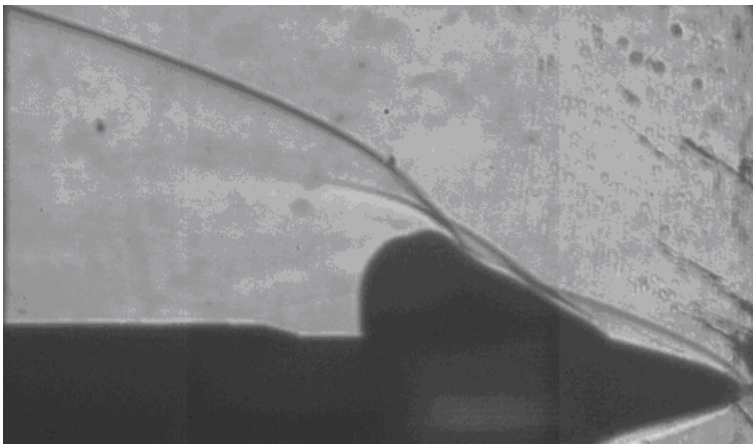

**Figure 3.10:** Schlieren Image of a water ballon exposed to Mach 6 flow (from right to left), with sharp leading edge support

scientific information, due to the lack of adequate contrast and high resolution in the images [94].

Similar to front-light illuminated photography, top view movies have also been

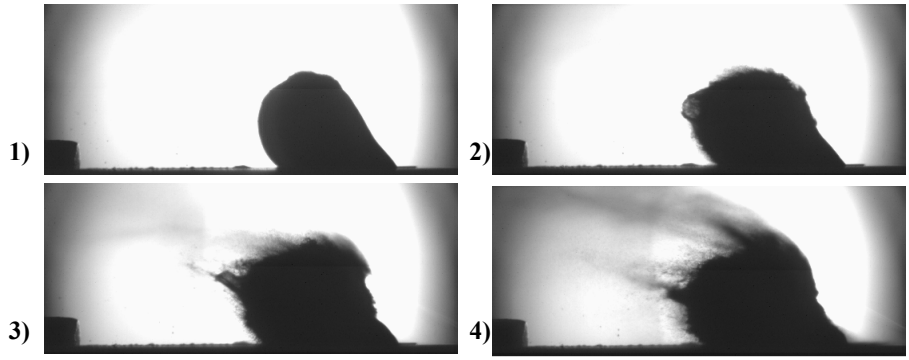


**Figure 3.11:** Four consecutive back-light images of a water balloon subject to Mach 6 flow, from right to left

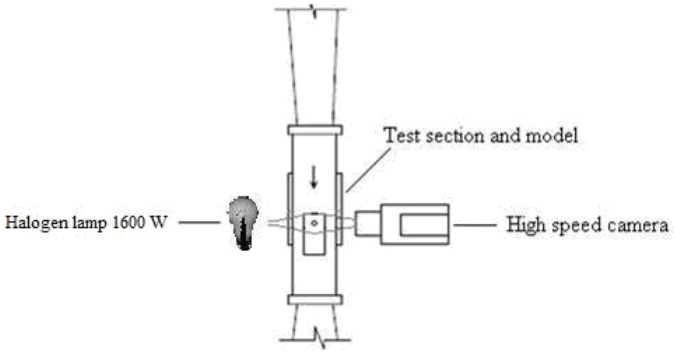


**Figure 3.12:** Back-light illumination test set-up, schematic view

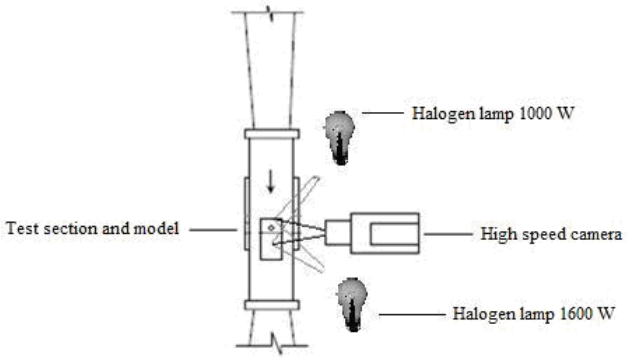


**Figure 3.13:** Front-light illumination test set-up, schematic view

recorded to study the spreading of the jet in the lateral extension and to investigate flow field moving in spanwise direction. A schematic of the top view test set-up can be seen in Fig. 3.14, where two light sources are on each side of the wind tunnel and the high speed camera is located above the test section, looking downwards towards the flat plate from above [15].

### 3.3.5 Oil Flow Visualization

Oil flow visualization is a flow visualization technique where the motion of a special oil painted on the wind tunnel model is recorded by a camera during the test. The oil is moved by the aerodynamic shear force, thus indicating the critical topological features such as separation, reattachment, vortex dominated flows, etc.

The usage of oil flow visualization technique is very empirical and requires a lot of know-how and practice. This technique is particularly adapted to the case of *long duration* facilities such as H-3 where the test conditions can be maintained during several seconds. Indeed, the oil is displaced on the model due to skin-friction and flows with the flow. At the end of the test, the remaining thickness of the oil is proportional to the skin-friction distribution and some skin friction lines are visible allowing flow structure interpretations. The intrusiveness of this technique is open to discussion and with respect to this issue, the adaptation of the technique to impulse or *short duration* facilities such as VKI Longshot piston-driven hypersonic wind tunnel (test duration around 30 msec) is really difficult and did not produce good results [150].

The visualization oil consists of a mixture of a titanium-oxide powder with oil whose viscosity is adapted to the problem. Better results have shown to be obtained with a titanium-oxide powder as thin as possible [126]. The prepared oil is painted on the model following an orientation perpendicular to the expected streamlines in such a way that the oil structures created during painting do not interfere with the flow pattern interpretation after test. This is mainly important in the low skin-friction regions where oil does not move.

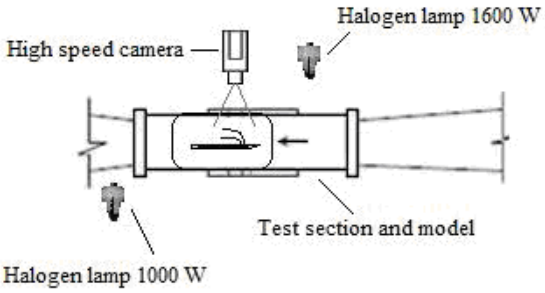


**Figure 3.14:** Top-view test set-up, schematic view

The oil paint consists of a mixture of a titanium-oxide powder and commercial corn oil, whose viscosity (72cp) is the most suitable for the test case. Thinner and more pure titanium-oxide powder yields better results. Following several trials, the best result is obtained with a mix of 3/4 of corn oil and 1/4 of titanium oxide in mass for a test at a total pressure of 20 bars. Olive oil has been found more suitable for the high Reynolds tests, probably due to the higher viscosity of the olive oil (84cp) compared to the viscosity of the corn oil (72cp) [126]. Only qualitative investigations have been performed using the oil visualization technique, although [13] proposes a correlation allowing to evaluate the surface shear stress distribution using discrete oil dots of uniform size, which is not feasible for the experimental campaign of this work due to low precision. The accuracy of this method largely depends on the uniformity of the size of the oil dots, which is not the case for a test case where the injected water deteriorates the oil paint.

### 3.3.6 LASER CROSS-SECTION VISUALIZATION

The laser cross-section visualization technique is used to visualize the liquid flowfield at several planes parallel to the flat plate. For this purpose, the high speed camera is installed at the top of the wind tunnel, recording the signature of the liquid flow at a certain plane parallel to the flat plate. The plane recorded by the high speed camera is illuminated by a laser sheet. The experimental set-up is presented in Fig 3.15, where the Mach 6 flow is towards the reader.

A *Quantel Twins Ultra 180* MiniYAG laser at 100mJ energy level (at 532nm wavelength) is used at 15Hz pulse frequency. Cylindrical and spherical lenses are utilized to convert the 6.35mm diameter laser beam into a laser sheet. The laser sheet is placed at 5, 10 and 15mm above the flat plate by a traversing mechanism. The thickness of the laser sheet is 1±0.2mm, and the duration of one pulse is 11±1

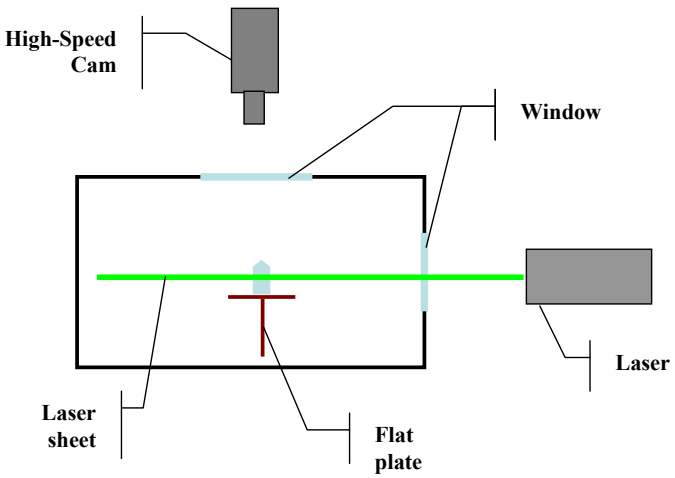


**Figure 3.15:** Laser cross-section visualization set-up, schematic view

nano-seconds. The high speed camera is placed above the wind tunnel to detect the signature of the liquid jet illuminated by the laser sheet. A Micro-Nikkor (Nikon) 105mm objective is used at an aperture opening of f1:11 [12].

### 3.3.7 Phase Doppler Interferometry

The Phase Doppler Interferometry (PDI) is a non-intrusive laser diagnostic technique [14] utilized for simultaneous measurement of size and velocity of individual spherical particles in poly-dispersed flow environments. The measurement principle is based on elastic light scattering. The light scattering interferometry utilizes the wavelength of light as a measurement scale and, as such, the performance is not easily degraded, in terms of received power, as it is for a system using light scattering intensity information for the estimation of the particle size [5].

The optical system consists of a laser emitting at a wavelength of 660 nm. A receiver equipped with three photodetectors is used to collect the light scattered by the particles and a Fourier transform based signal processor is used for the raw data processing. In the basic PDI system, the laser beam is divided into two beams of equal intensity by means of a beam splitter. A convergent lens is used to make these two beams crossing each other, thus creating a fringe pattern at the point of intersection. The volume defined by the intersection of the two beams corresponds to the measurement volume. A Bragg cell is used to shift the frequency of one beam in order to resolve the direction ambiguity that would occur for drops passing in a reverse direction. The phase shift produced by the different light refraction on the surface of the same droplet allows determining its size. In addition, the Doppler difference frequency allows computing the velocity of the droplet.

The PDI system used is capable of measuring a drop size ranging from 0.5 to 2000 $\mu$m and velocities up to 300 m/s downwind (-100 m/s for upwind particles), depending on the setup. During the experimental campaign, different configurations of the PDI instrumentation have been tested in order to catch both the horizontal velocity vector and the diameter of the atomized water particles [4]. Within this experimental campaign, the spray is considered to be generated through the water injection over the flat plate. The correct PDI setup to characterize this type of spray is illustrated in Fig 3.16. With this setup, one is able to detect the droplet diameter and the horizontal component of its velocity, paying attention to have a backward scattering angle (collection angle) between 30 and 40 degrees. Unfortunately this configuration cannot be realized in the VKI H-3 facility, due to the limitations on optical access to the test section.

The most difficult part of the configuration procedure is the impossibility to make a sensitivity analysis on the instrument's parameters. Many of the parameters play an important role on the setup of the PDI instrumentation. Since the VKI H-3 facility can run only for a few seconds, there is not enough time to play with all the parameters during a test to see how these parameters affect the measurements.

[4] called *spray* for simplicity from this point on

Among the high number of selectable configurations, there are the interchangeable lenses of both the receiver and transmitter, the collection angle, the photodetector gain, the analog filter and the sampling rate.

To get through the reduced optical accessibility of the VKI H-3 facility, different optical arrangements of the PDI instrumentation have been worked on. An optimum configuration is favored, disregarding the velocity of the particles but acquiring the correct particle size. In the PDI setup illustrated in Fig. 3.17, the transmitter is placed on one side of the facility with the laser beam pointing at the detection zone. The receiver is placed on the opposite side of the facility looking straight forward to the window (to avoid reflections) and focusing at the probe volume. With this configuration the probe volume is as small as possible, so the amount of noise created by spurious particles is reduced. The most important PDI setup parameters are

- The collection angle between the laser and the receiver: 24deg
- Focal length of the transmitter and the receiver: 1000mm

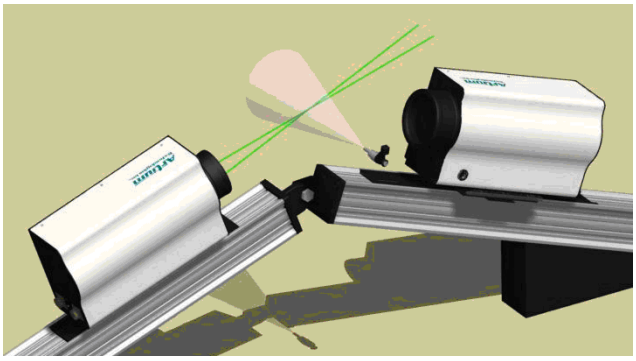

**Figure 3.16:** The optimum PDI configuration

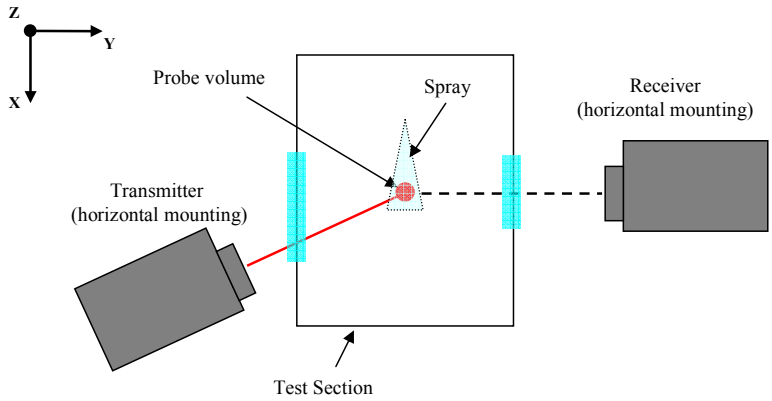


**Figure 3.17:** PDI setup (top view) at H-3 wind tunnel. The air flow is from the top to the bottom

- Wavelength of the laser: 660nm
- Beam waist: 336.1$\mu$m
- Fringe spacing: 11 $\mu$m
- Beam diameter: 2.5mm
- Receiver gain: 720V

One drawback of this system is that the velocity vector detected by the system is in y direction (see Fig. 3.17), which is not the interesting component for the tested configurations. However, as the main objective is to obtain data on droplet size, it is decided to continue with this setup despite its lack of velocity data [12, 94, 18].

# 4

# Liquid Injection Into Mach 6 Cross Flow

The present chapter is devoted to the experimental campaign for examining liquid injection into a crossing Mach 6 air flow. Experiments are conducted on a sharp leading edge flat plate with flush mounted injectors, as explained in Section 3.2.1. Water jets are introduced through different nozzle shapes at relevant jet-to-air momentum flux ratios. Sufficient temporal resolution to capture small scale effects is obtained by high-speed recording, while directional illumination allowed variation in field of view, as explained in Chapter 3 and Section 4.1. Shock pattern and flow topology visualized by Schlieren-technique is explained in Section 4.2. In Section 4.3, correlations are proposed on relating water jet penetration height and lateral extension with the injection ratio and orifice diameter for circular injector jets. Penetration height and lateral extension are compared for different injector shapes at relevant jet-to-air dynamic pressure ratios showing that penetration height decreases and lateral extension increases with the aspect ratio of the injectors. Section 4.4 presents a similar discussion on the lateral extension of the liquid jets. Probability density function analysis presented in Section 4.5 shows the distance necessary for the mixing of the jet with the cross-flow. Mean velocity profiles related with the liquid jet are also extracted by means of an ensemble correlation PIV algorithm. Finally, frequency analyses of the jet breakup and fluctuating shock pattern are performed using a Fast Fourier algorithm. The characteristic Strouhal numbers for the liquid jet breakup and for the separation shock fluctuation are presented in Section 4.7.

| Test no | $P_0$ (bar) | $T_0$ (K) | $\rho_\infty$ (kg/m$^3$) | $U_\infty$ (m/s) | $\rho_j$ (kg/m$^3$) | $U_j$ (m/s) | q (-) | Test Technique |
|---|---|---|---|---|---|---|---|---|
| 1 | 20.23 | 505.6 | 0.0724 | 944.39 | 997.93 | 11.38 | 2.0 | Schlieren |
| 2 | 20.15 | 508.2 | 0.0718 | 946.82 | 997.83 | 16.06 | 4.0 | Schlieren |
| 3 | 20.22 | 510.6 | 0.0717 | 949.05 | 997.78 | 25.43 | 10.0 | Schlieren |
| 4 | 20.16 | 502.9 | 0.0725 | 941.87 | 998.06 | 21.40 | 7.1 | Front-lighted |
| 5 | 20.25 | 503.4 | 0.0728 | 942.34 | 998.14 | 25.58 | 10.1 | Front-lighted |
| 6 | 20.15 | 501.6 | 0.0727 | 940.65 | 997.98 | 16.06 | 4.0 | Front-lighted |
| 7 | 20.07 | 513.2 | 0.0708 | 951.46 | 997.93 | 25.46 | 10.1 | Back-lighted |
| 8 | 20.12 | 509.6 | 0.0714 | 948.12 | 997.96 | 21.23 | 7.0 | Back-lighted |
| 9 | 20.73 | 511.7 | 0.0733 | 950.07 | 997.96 | 8.14 | 1.0 | Back-lighted |
| 10 | 20.12 | 508.5 | 0.0716 | 947.10 | 997.96 | 25.37 | 10.0 | Top view |
| 11 | 20.68 | 513.2 | 0.0729 | 951.46 | 997.91 | 21.52 | 7.0 | Top view |
| 12 | 20.35 | 506.3 | 0.0727 | 945.05 | 997.86 | 11.41 | 2.0 | Top view |

**Table 4.1:** Liquid jet and free stream conditions of the main liquid injection tests

## 4.1 EXPERIMENTAL PROCEDURE

Different experimental conditions have been studied corresponding to variations in dynamic pressure ratio, injector shape and wind tunnel stagnation pressure. Some characteristic examples of the 72 tests performed and the different experimental techniques are summarized in Table 4.1 [16]. Each injector presented in Section 3.2.1 is tested for relevant values of dynamic pressure ratio q, ranging between 1 and 10.

All experiments are carried out in the H-3 hypersonic wind tunnel of the von Karman Institute for fluid dynamics (see Section 3.1). Water is injected through a flat plate test model of 230 x 80 x 15 mm. The injectors are fitted beneath the flat plate while the orifice is flush mounted to the flat surface downstream of the sharp leading edge (see Section 3.2.1). An experiment always starts with the flat plate model in retracted position. After the test section is vacuumed, the fast acting valve is opened allowing the pressurized and heated dry gas to flow through the converging diverging nozzle into the vacuumed test section. Once Mach 6 flow is established the flat plate model is injected into the test section. Following a last check to ensure that the wind tunnel is not blocked, the water valve is opened and liquid jet is injected into crossing Mach 6 flow. At this moment, one researcher triggers the high speed camera, while another researcher monitors the mass flow rate of water through the rotameter. Typical test duration is 5 seconds, although the duration of a high-speed movie can be much shorter depending on the acquisition rate. Table 4.2 summarizes typical high-speed camera settings for different kinds of tests that are performed. A Nikon lens with 50mm focal length (aperture set at f1.4) is used for most of the cases. For close-up view images of back-lighted tests, a Nikon lens with 105mm focal length is used at an aperture opening of f2.4 [15].

| Test type | Exposure time ($\mu$s) | Resolution (pixel x pixel) | Frame rate (fps) |
|---|---|---|---|
| Schlieren | 80 | 600 x 300 | 10000 |
| Front-lighted | 30 | 512 x 184 | 21000 |
| Back-lighted | 2 | 200 x 100 | 60000 |
| Top-view | 70 | 200 x 300 | 15000 |

**Table 4.2:** Typical high speed camera settings

## 4.2 Shock Wave System

The shock system of the flowfield and the shock - shock interactions as well as the interactions between the liquid flow field and shock system can be seen on schlieren images. A sample image from a schlieren movie for a q=10 circular injector jet case, recorded at a sampling rate of 8810 Hz is shown in Fig. 4.1. The typical field of view for this setup (704 x 360 pixels$^2$) corresponded to 168 x 86 mm$^2$ in object space. Bow shock and leading edge shock are readily distinguishable which allows deduction of the leading edge shock angle. Based on weak disturbance theory, the Mach angle $\sigma$ is defined by $\sin(\sigma) = \mathrm{M}^{-1}$. The Mach number being between 5.9 and 6.1, should yield a theoretical wave angle between 9.44° and 9.74°. Image analysis returns an angle of approximately 9.89°. The latter verifies the assumption of a weak wave created by the leading edge of the flat plate. The discrepancy between the expected and the measured wave angles is believed to be due to effect of the shear layer of the flow on the schlieren imaging technique. The separation shock is also recognizable where the boundary layer detaches due to adverse pressure gradient within the boundary layer and upstream of the injection point. The boundary layer and its lift-off due to separation can be clearly seen by its intense white color.

In this example frame of a schlieren movie for a q=10 jet, the characteristic shock pattern can be clearly seen. The leading edge oblique shock is evident. The bow shock in front of the jet can be easily noticed as well, although close to the injection point it is difficult to differentiate it from the jet itself, due to the small distance between the jet surface and the shock. The separation shock is recognizable where the boundary layer detaches. The boundary layer and its separation can clearly be seen by its intense white color.

To understand the flow topology, schlieren images are compared with other images. Front-light images are used to obtain a wide view of the flow field, by front-illuminating the view with two halogen lamps of 1600 and 1000 Watts. Recorded images are used to extract penetration height data and to perform mixing analysis based on probability density functions (PDF), as explained in sections 4.3 and 4.5. A sample front-light illuminated image in case of a circular injector with injection ratio q = 10, recorded at a sampling rate of 26143 Hz, is presented in Fig. 4.2.

The typical field of view for this setup is 512 x 144 pixels$^2$, corresponding to 213 x 60 mm$^2$. Due to low contrast, front-light images are not very useful for post-processing. However, back-light illumination technique provides sharp images with sufficient contrast. Together with schlieren images, they provide a lot of information on the shock system and the general flow topology. One problem with the back-light illuminated images is that the camera sees the powerful light sources directly, which creates very bright, saturated regions on the images. To minimize the degrading influences of spatial variations in intensity during the image analysis of back-lighted photographs, a background image is subtracted beforehand. The background image is based on the ensemble averaged reference images of the illumination, i.e. images without liquid injection. Figure 4.3 shows a typical result of this background subtraction procedure. The first image on the top left corner of Fig. 4.3 is a typical image taken from a back-light illuminated movie, which has a non-uniform background. The idea is to subtract a reference image with the background only from this image, to get rid of the non-uniformity. As this procedure would result in negative intensity values, it is preferred to work with the inverted gray-scale images. The top right image of Fig. 4.3 is the inverted test image, whereas the bottom left image is the inverted image of the average of five background images taken when the test model is not injected into the test section. The difference of these two im-

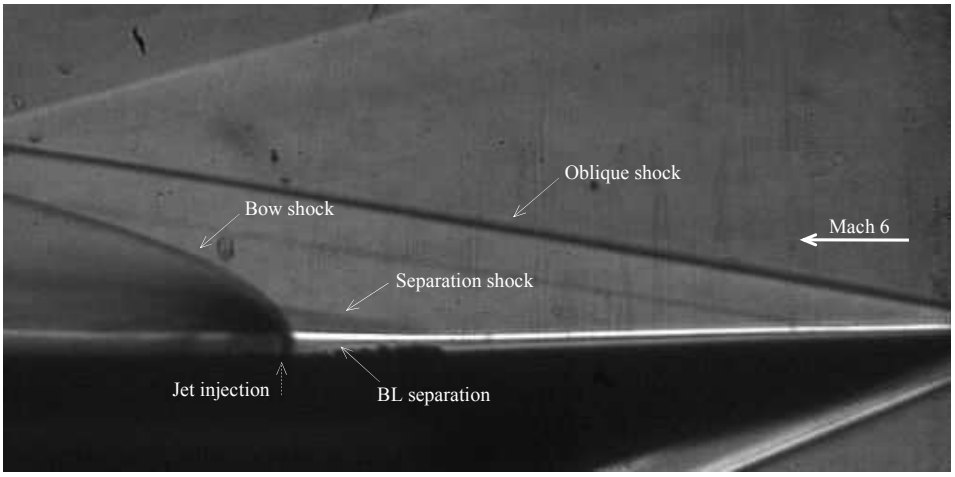


**Figure 4.1:** Typical schlieren image for a q=10 circular injector jet

**Figure 4.2:** Typical front-light illuminated image for a q=10 circular injector jet; Mach 6 flow from right to left

ages gives the image shown in bottom left corner of Fig. 4.3, where the background is now completely uniform. The saturated regions in the back-lighted images are problematic for image processing, as they do not present all the details. However, due to the nature of the back-light illumination technique, the presence of any water droplets (as long as they are bigger than a pixel size) would create a shadow, hence decreasing the negative effects of saturation. The typical pixel size for back-light illumination photography is $0.09 \pm 0.01$ mm.

Figure 4.4 shows four consecutive frames from a back-light illuminated movie with inverted gray-scales. This sample represents liquid injection through the circular injector, with q = 10, at a recording rate of 63492 Hz, resulting in a time difference of $15.75 \mu second$ between each frame. In the succession of images, the primary breakup and clump detachment on the windward region of the jet are visualized. In the literature, this process is explained as a result of the growing instabilities on the surface of the jet [45]. For the hypersonic conditions of this study, the clump detachment is more violent than in supersonic or subsonic injections. This attracts the attention on the influence of shock – shock interaction on the stability of the liquid column, yielding to a more abrupt breakup of the jet.

The relation between the clump detachment and the separation shock – bow shock interaction is identified more clearly in the high-speed schlieren recordings.

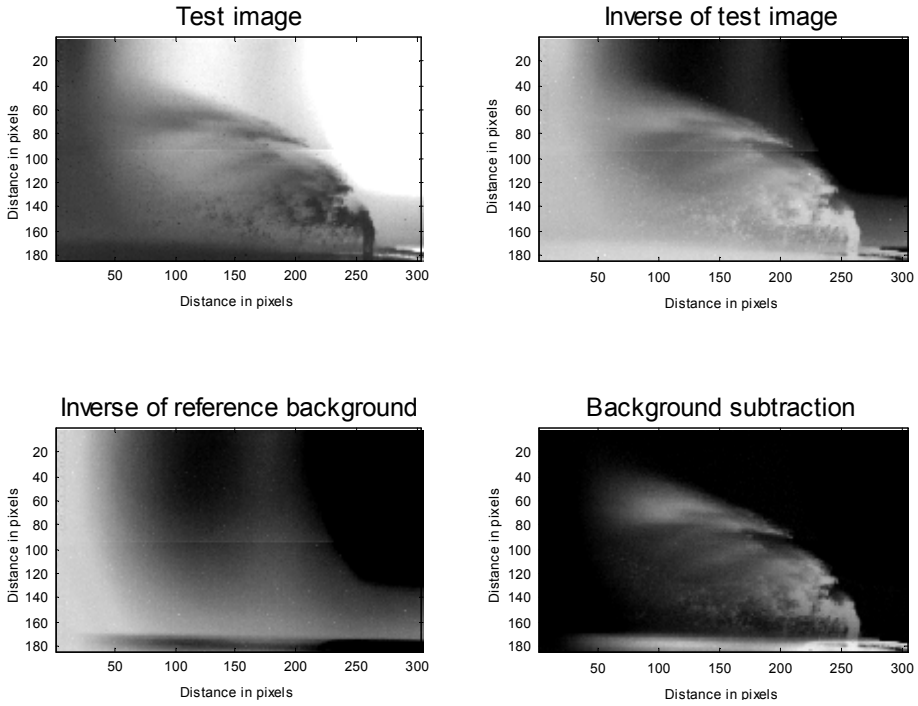


**Figure 4.3:** Background subtraction procedure for front-light illuminated images; Mach 6 flow from right to left, 1 pixel = 0.1mm

To better visualize this relation, a superposition between a schlieren image (Fig. 4.1) and the close-up view of a jet breakup image, for a q = 10 circular jet, is shown in Fig. 4.5. The image shows that the impingement point of the separation shock on the bow shock coincides with the clump detachment region on the windward region of the jet [16].

The discussion on the flow topology has been on single typical images up to now. However, valuable information can be obtained from high speed movies, by examining the fluctuation of the shock patterns, and the break-up of liquid jet. To be able to quantify these observations, mean and standard deviation of consecutive images are calculated using image processing tools of Matlab [89, 15].

An example of the mean and standard deviation schlieren images for a q=10 jet is shown in Fig. 4.6. The mean image indicates the average locations of the leading edge shock and bow shock. Contrary to this, the standard deviation image gives

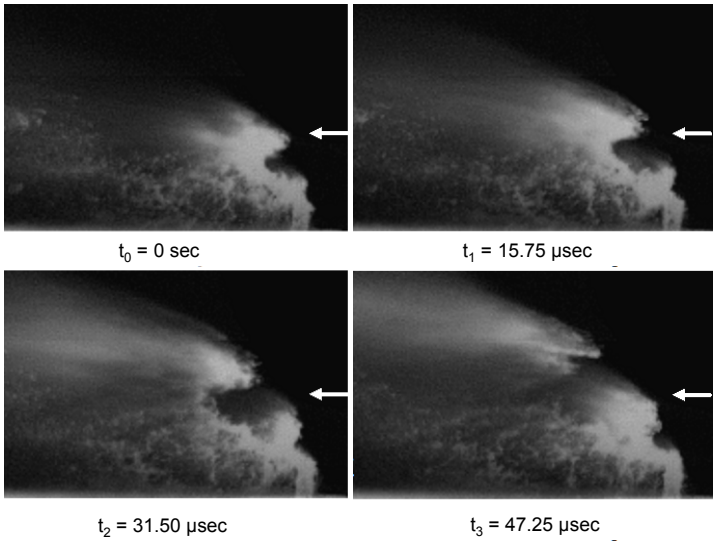


**Figure 4.4:** Succession of back-light images with inverted gray-scales; Mach 6 flow from right to left

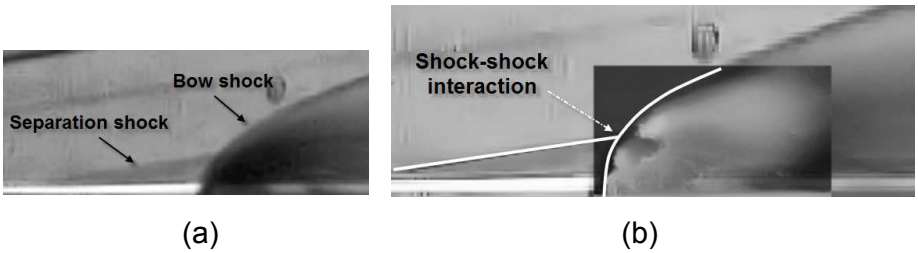


**Figure 4.5:** a) Schlieren image for q = 10 jet; b) superposition of schlieren image and close-up view of jet breakup; Mach 6 flow from left to right

information on the fluctuation envelope of the shock waves. Lighter color indicates higher standard deviation, which means there are a lot of fluctuations in those regions. Dark color corresponds to low standard deviation, meaning there is no or very little dynamics going on. Low standard deviation values are seen close to the injection point, where a relatively well defined jet body exists. As expected, high standard deviation values are clearly observed in the outer part of the jet where big clump detachment is produced. Also in the bow shock and in the separation shock, high standard deviation values are observed. This is due to the unsteady shock system, known as the whipping phenomenon. Even though the jet is relatively stable, the big clump detachment in the outer surface changes the bow shock shape changing the information propagated upstream affecting the separation shock. This phenomenon is observed as a vibration or whipping of the shock system. The fluctuation of the separation and shock waves can also be observed by simply watching the high speed movies, particularly for low dynamic pressure ratio injections. The standard deviation of all images of a movie helps characterizing the whipping phenomenon. Furthermore, it is possible to apply a *canny* algorithm to the standard deviation image to detect the boundaries [15, 89]. Such an image is shown in Fig. 4.7. The bow shock and the separation shock are easily recognizable. It is interesting to see the separation shock penetrating into the liquid column, playing an important role in the primary break-up of the jet.

High injection rate jets ($q \geq 6$) are characterized by a relatively well defined jet body with a substantial movement of the outer region of the jet where the jet disintegrates due to big clumps detachment process, while low injection rate jets ($q \leq 1$) show a continuous vibration and whipping motion of the entire jet. Jets with intermediate values of $1 < q < 6$ show a combined behavior of both characteristics. The standard deviation image of a q=10 injection rate jet is compared with a q=2 injection rate jet in Fig. 4.8. The q=10 jet has a low standard deviation value at the injection point (1), where the jet body is stable, and the high standard deviation values are seen in the vicinity of the bow shock, the outer part of the jet where the jet disintegrates due to big clumps detachment process and in the vicinity of

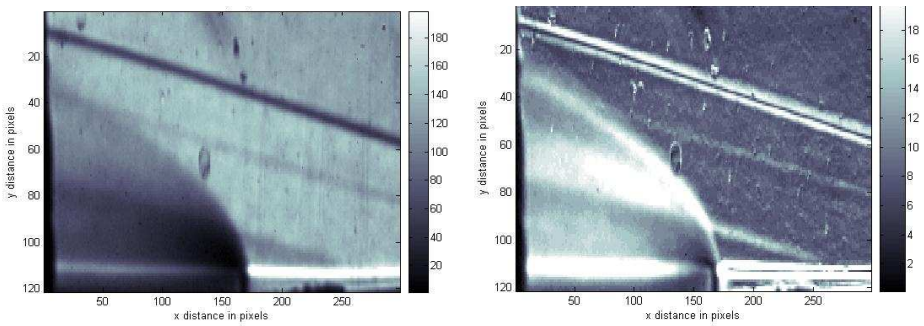


**Figure 4.6:** Mean (left) and standard deviation (right) of schlieren images for q=10 jet; Mach 6 flow from right to left, 1 pixel = 0.24 mm

the separation shock. As explained, there is a fluctuating shock system, in which the bow shock changes its shape continuously due to the disintegration of the outer part of the jet, changing the separation shock position upstream. This is noticed in the high standard deviation values. On the contrary, the q=2 jet has a high standard deviation value at the injection point (2), showing that the jet is vibrating and whipping and does not form a stable jet body that forms a stable obstacle in the free stream. As a stable and more energetic jet is formed at high injection rate cases, the bow shock penetrates more in the free stream (3) than for lower injection rates (4), where a stable jet is not formed; the jet vibrates and disintegrates continuously.

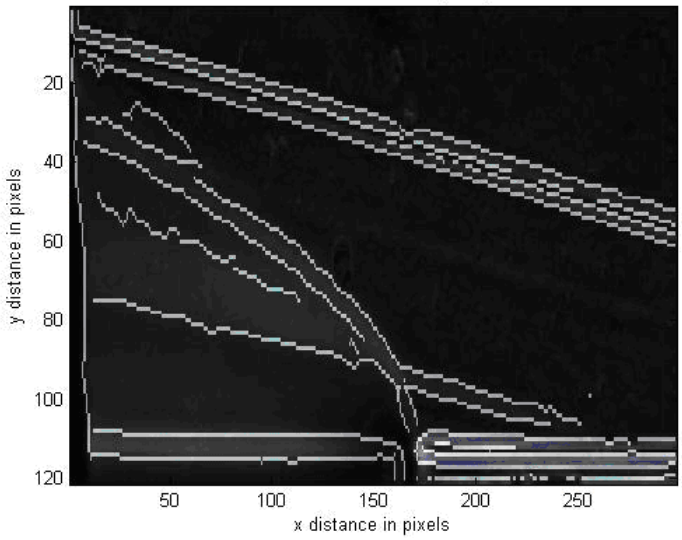


**Figure 4.7:** Detected boundaries in schlieren STD image for q=10 jet; Mach 6 flow from right to left, 1 pixel = 0.24 mm

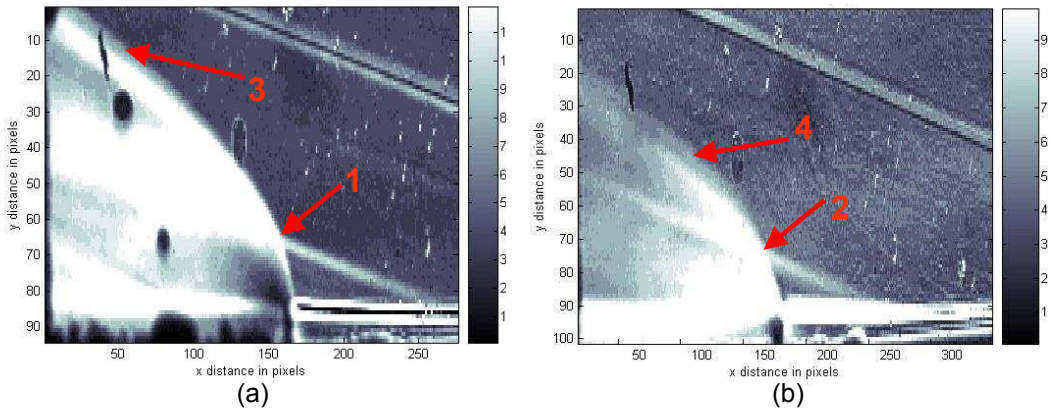


**Figure 4.8:** Standard deviation of schlieren images for q=10 (left) and q=2 (right) jets; Mach 6 flow from right to left, 1 pixel = 0.24 mm

## 4.3 Penetration Height

Measurement of variations in penetration height of liquid jets is obtained from front-light illuminated images (Fig. 4.2). The penetration height of the injected liquid is the utmost height that it can reach, despite the aerodynamic force applied by the hypersonic cross flow. This information can easily be obtained by finding out the border of liquid in front-light or back-light illuminated images. This is done thanks to contour detection algorithms [89, 16]. To facilitate contour detection of the jet, images are binarized. The standard deviation over 1000 binary images is used to determine the penetration height. Pixel intensities exceeding a pre-imposed intensity gradient threshold were set to unity and zero otherwise. Applying the edge detection technique to the mean or standard deviation images results in a clearly defined upper border of the liquid jet. This upper border is used in the detection of the penetration height at any distance from the liquid injection point. It is observed that the application of this technique to either mean or standard deviation images yields similar results. In the literature, the most popular technique is the edge detection on the average of images [83]. Nevertheless, working on the standard deviation images is preferred as these images provide better contrast. An example of the result is shown in Fig. 4.9, where the cross flow is from right to left and one pixel = 0.42mm. The error in estimating the penetration height by this technique is 2%, resulting from the error in reading the location of the uppermost boundary. However, one should keep in mind that this is only one of the error sources. The other error sources are the non-uniformity of the image background, the representativeness of the standard deviation for maximum penetration, the dependence on the threshold for edge detection technique, and finally the relative positions of the camera, light source and the water droplets. Although it has not been possible to carry out a detailed investigation to determine the resultant absolute error due to these error sources, different techniques are compared with each other to acquire a certain confidence level on the measurements.

The boundaries of the circular jet directly exposed to the free stream for different injection ratios are presented in Fig. 4.10. Correlations fitted to experimental profiles for circular jet injections into supersonic Mach = 1.94 cross flow based on shadowgraph [83] and Phase Doppler Particle Anemometry (PDPA) measurements [85] are plotted simultaneously, for comparison. These correlations, which are among the most recent ones in this kind of flow topology under compressible cross flow are chosen because the experimental conditions are identical to this study except for the cross flow Mach number and because of the lack of experimental data at hypersonic conditions. The correlations were obtained based on the least squares method, a method which was also used in the work of Gruber [46] and Leong [79] who have proposed similar expressions for penetration height. The expressions for the penetration height $h(x)$ as function of the spatial distance from the center of the orifice $x$ and orifice diameter $d_j$ measured with the shadowgraph and PDPA imaging

techniques are, respectively

$$\frac{h}{d_j} = 4.73 \times q^{0.3} \times \left(\frac{x}{d_j}\right)^{0.3} \tag{4.1}$$

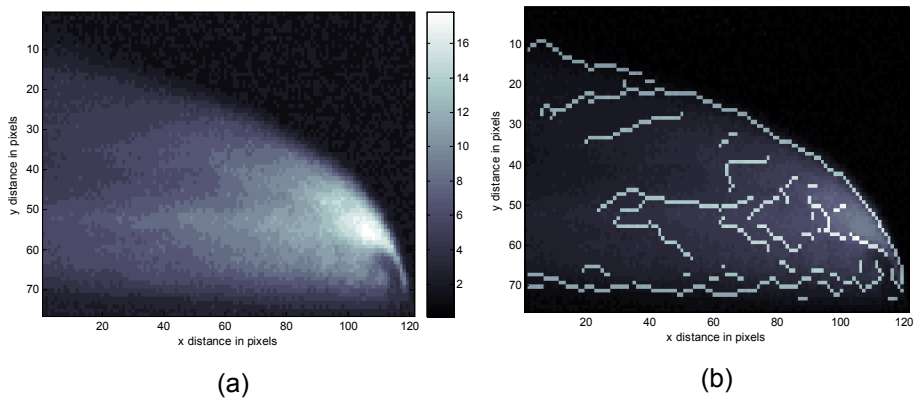


**Figure 4.9:** a) Standard deviation and b) detected boundaries for q = 10 jet, front-light illumination image; Mach 6 flow from right to left, 1 pixel = 0.42 mm

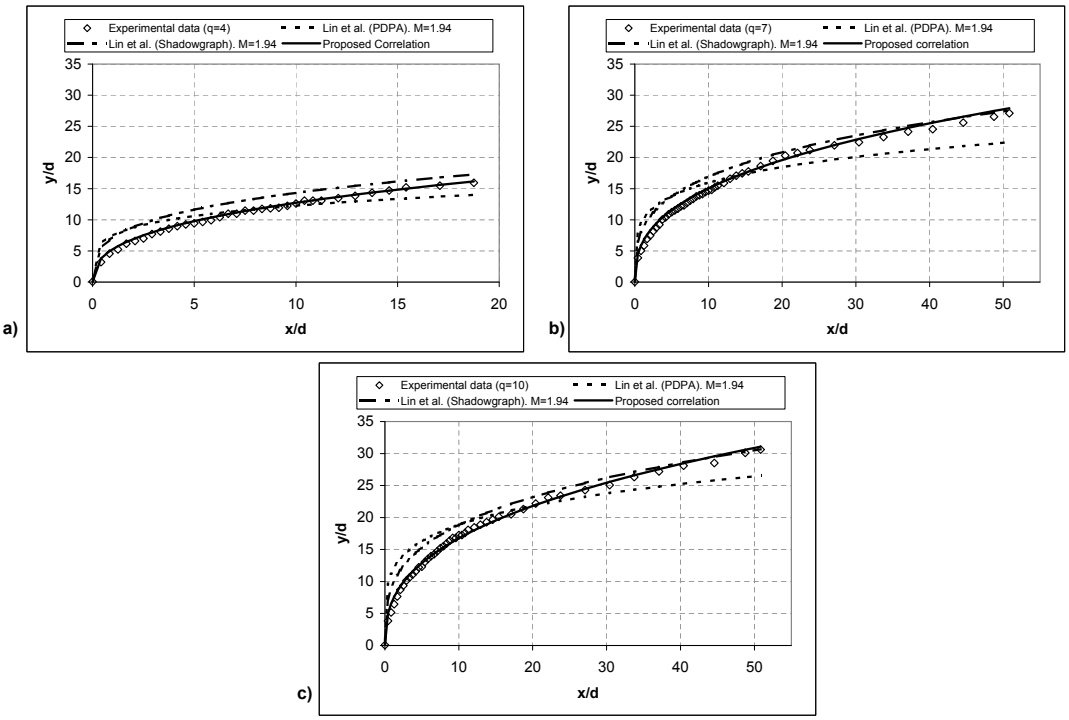


**Figure 4.10:** Penetration height versus downstream distance: a) q = 4, b) q = 7 and c) q = 10 jets

$$\frac{h}{d_j} = 3.94 \times q^{0.47} \times \left(\frac{x}{d_j}\right)^{0.21} \tag{4.2}$$

A comparison of the two techniques is presented in [85], claiming that PDPA is a more suitable technique as it describes spray penetration without ignoring significant amount of liquid volume. The shadowgraph technique is criticised to be insensitive to detect low-density large droplets, which are typically distributed at the upper portion of the spray plume. Although the correlations proposed in Eqns. 4.1 and 4.2 do not fit exactly with the experimental data at Mach 6 condition, the tendencies are similar. For this reason, and also because the mentioned correlations are derived for compressible flows, a modification of Eqs. 4.1 and 4.2 is suggested in Eq. 4.3, which fits the Mach 6 experimental observations better (Fig. 4.10). Equation 4.3 is for the 1mm diameter circular injector case. Although the utilized correlations all depend on the momentum flux ratio q, hence also on the freestream velocity, one may expect that this kind of correlation is representative of Mach number. However, the dicrepancy between Eqn. 4.3 and the other equations (4.1 and 4.2) for Mach 2 condition shows that the effect of Mach number is not well represented by the utilization of momentum flux ratio only.

$$\frac{h}{d_j} = 3.5 \times q^{0.3} \times \left(\frac{x}{d_j}\right)^{0.38} \tag{4.3}$$

The relative error between the correlations from literature (Eqns 4.1 and 4.2)

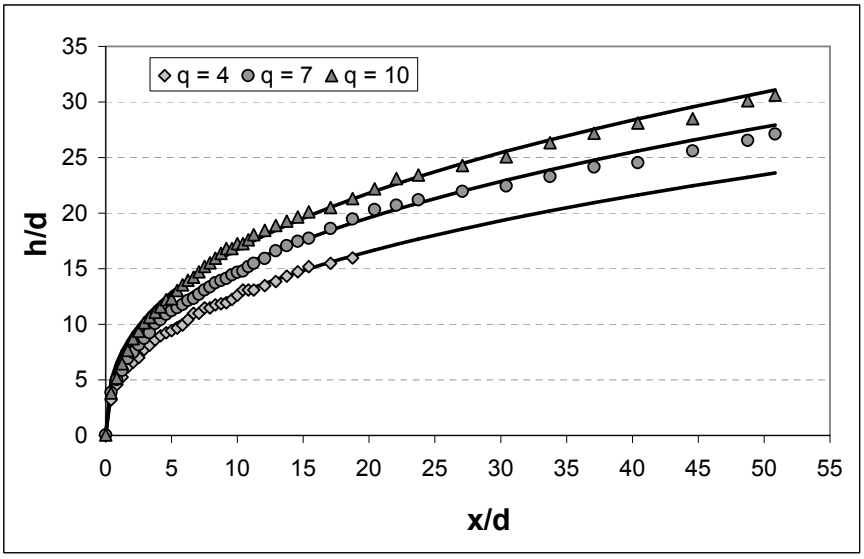


**Figure 4.11:** Penetration height comparison for q = 4, q = 7 and q = 10 jets

and the proposed one (Eqn. 4.3) varies in a range of 25-30% (especially in the region close to the injector, which might be critical for scramjet applications), justifying a new experimental fit for hypersonic cross flow condition. The profile for the M = 6 experimental points presents a less inclined slope for the jet trajectory, indicating the higher pressure distribution exerted by the hypersonic cross flow on the jet surface compared to supersonic cross flows.

Figure 4.11 presents a comparison of the measured penetration height values for liquid jets from the circular injector having momentum flux ratios of 4, 7 and 10. The penetration heights that are predicted by the proposed correlation (Eqn. 4.3) are also shown with solid lines for each case. The effect of the increasing momentum flux ratio on the penetration height can easily be noticed on this plot. Comparing the experimental data with the predicted curve, one can notice that they are in very good agreement close to the injection point but the discrepancy increases at downstream locations. The difference between the measured and predicted penetration height can be as high as 4% at downstream locations for which $x/d > 40$.

The evolution of the penetration height as a function of the injector aspect ratio at a downstream distance of $x/d_j = 5$ for different injector shapes is shown in Fig. 4.12. Jets emerging from the streamwise rectangular injector (Aspect Ratio = 1/3) penetrates slightly higher than the circular injector (AR = 1), whereas the liquid penetrates to lower height in the case of spanwise rectangular injector (AR = 3). The reason for this change in penetration height is that for the streamwise injector (AR = 1/3), the frontal (windward) area that sees the hypersonic cross flow is the smallest. The injected liquid is subjected to less momentum exchange with the free stream and thus exhibits a deeper penetration into the free stream. It can be concluded that the lift-off and the penetration height decreases as the aspect ratio increases as depicted in Fig. 4.12a. This change in penetration height is more pronounced for lower injection rates, as can be seen in Fig. 4.12a, for a q = 1 jet. These conclusions agree well with those presented by Haven and Kurosaka [51]. Although the results are

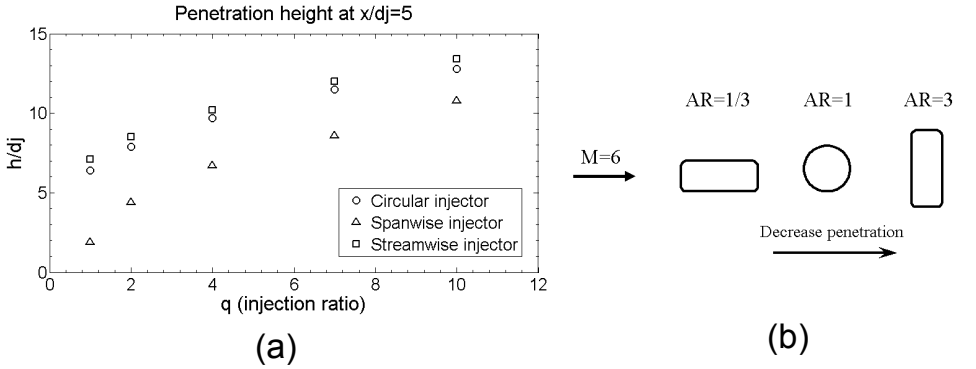


**Figure 4.12:** a) Penetration height for different injectors and b) effect of injector shape on penetration height

presented at a constant distance $x/d_j = 5$ as an example, similar results are obtained at different $x/d_j$ locations as well. As a result, spanwise rectangular injectors are more suitable for film cooling applications where the cooling fluid should be attached to the surface for low injection rates. A circular or streamwise rectangle injector on the other hand is more appropriate for fuel injection, where big penetration height and better mixing with crossflow are required [16].

## 4.4 Lateral Extension

The lateral extension of liquid injected into Mach 6 cross flow, or the width of the wetted area by the liquid, is determined by the top view images taken by the high speed camera. A similar threshold-based image binarization technique is applied as in section 4.3, followed by edge detection. The determination of the standard deviation is achieved by using 1000 images. An example of the calculated standard deviation and the detected boundaries are shown in Fig. 4.13, where one pixel corresponds to 0.33mm.

Just like for the penetration height, based on the least squares methods, an experimental fit is proposed for the lateral extension of circular jets emerging from

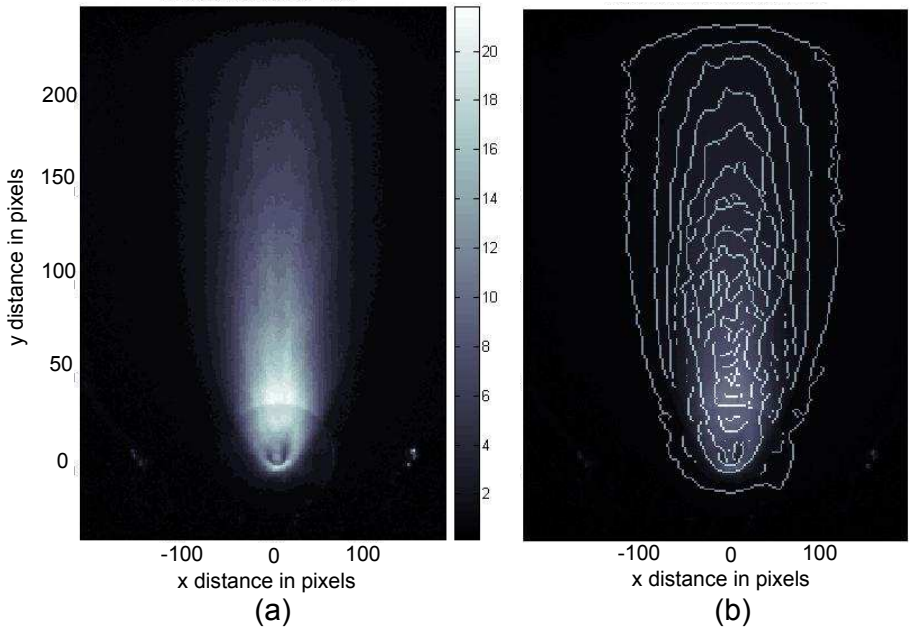


**Figure 4.13:** a) Standard deviation and b) detected boundaries for top-view images of q=10 jet; Mach 6 flow from bottom to top, 1 pixel = 0.33 mm

the circular injector, in Eq. 4.4.

$$\frac{w}{d_j} = 2.1 \times q^{0.38} \times \left(\frac{x}{d_j}\right)^{0.47} \tag{4.4}$$

Based on top view images, lateral extensions $w/d_j$ of the liquid jet are compared at x = 30 mm as an example, for the three injector shapes and various injection ratios (Fig. 4.14). The spanwise injector yields the widest lateral extension while the streamwise injector yields the lowest. For the spanwise injector (AR = 3), the increase in frontal (windward) surface of the liquid jet means more liquid can directly exchange momentum with the freestream flow, resulting in a quicker bending of the jet to have a lower penetration height. A conclusion that can be derived from this analysis is that the lateral extension of the jet increases as the aspect ratio increases (Fig. 4.14b). In agreement with the studies of Kolpin [73] and Joshi [61], the lateral extension of the jet depends less on the injection ratio than on the cross-sectional dimension of the injector and all injector profiles show an almost linear relation between lateral extension and injection rate (Fig. 4.14a).

Considering the top-view images, it should be said that these images lack sufficient light to be reflected by the liquid droplets and thus their quality is inferior compared to that of back-light illumination, front-light illumination and schlieren imaging techniques. In all these three techniques, the light source is aligned with the high-speed camera, resulting in a superior contrast. In the top-view imaging technique, the light source and the high-speed camera are located such that they are perpendicular to each other, resulting in an inferior contrast. Because of this reason, the outcomes of the top-view imaging technique and the predictions proposed by Eqn. 4.4 are compared with other techniques and are criticized in Section 5.2.

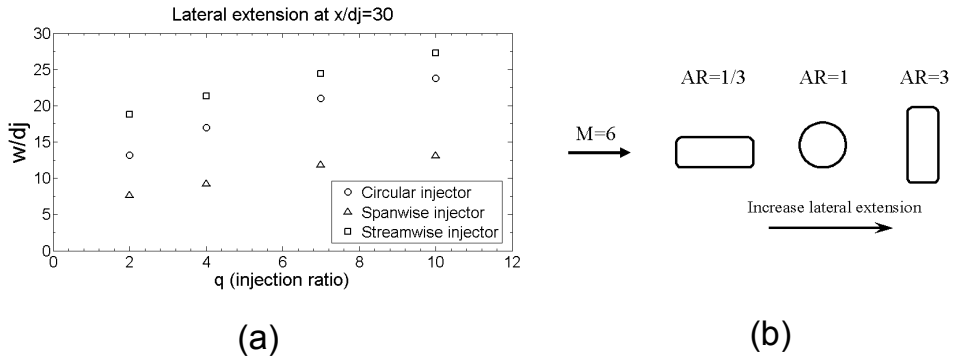


**Figure 4.14:** a) Lateral extension for different injectors and b) effect of injector shape on jet lateral extension

## 4.5 Mixing Analysis by Probability Density Function

The investigation of mixing between liquid jet and free air stream is based on front-light illuminated recordings. In view of a liquid's higher efficiency in light scattering compared to air, low pixel intensities would correspond to pure air with high intensity regions identifying pure water. Mixing fractions could be inferred from the intensity scales. Messersmith [100] introduced the concept of Probability Density Function (PDF) based on image intensities in the identification of transport characteristics of mixing layers. Messersmith measured the probability of occurrence of all mixture fractions at various locations within the mixing layer demonstrating the validity of this tool in the study of water - air mixed multi phase flows [100].

Based on 1000 consecutive images, the intensity probability distribution functions (PDF) for pixel intensities are retrieved. The PDFs show the probability of

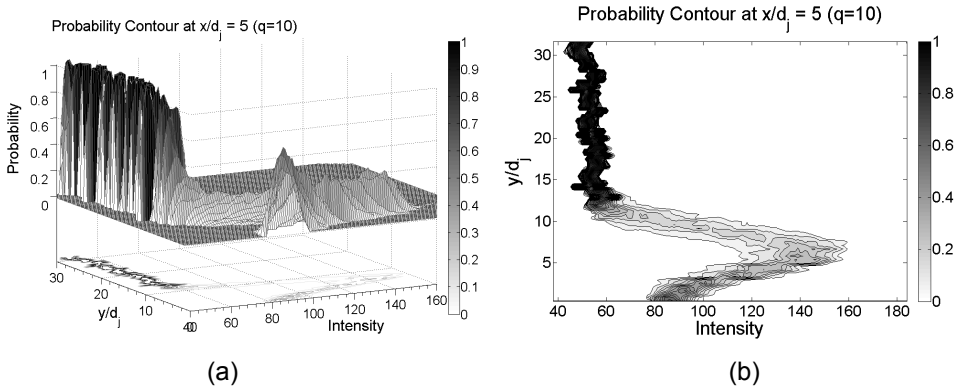


**Figure 4.15:** a) Probability contour at $x/d_j = 5$ and b) projection view

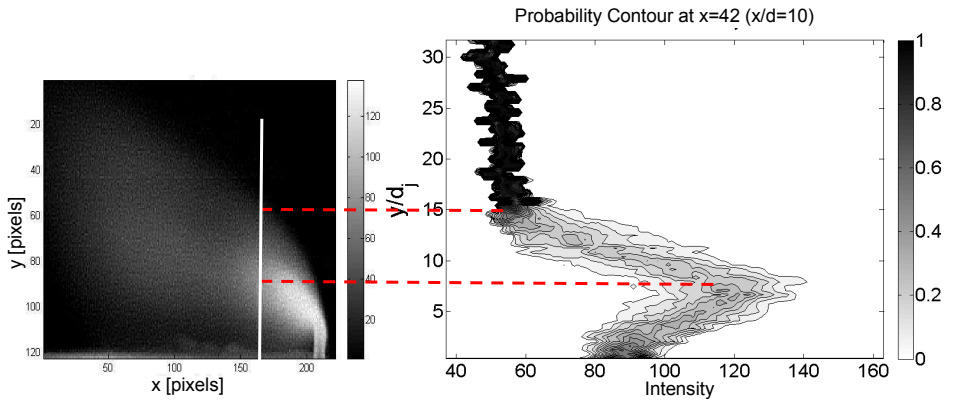


**Figure 4.16:** Penetration height and core height estimation from PDF; 1 pixel = 0.24 mm

occurrence of a specific signal intensity at a flow field location. The probability density function at any location is determined by calculating the probability of a specific intensity on that location of the image. This calculation is performed by considering the statistics of 1000 images. Thus, the estimation based on the PDF technique corresponds to a determination based on the average pixel level. Having a black background, in case of a liquid jet injection into a cross flow of air, signal intensities of zero would correspond to pure air and maximum signal intensities would correspond to pure water. Intermediate values would correspond to a specific mixture ratio of air and water. Fig. 4.15 depicts the PDF together with a top view projection for a downstream location of $x/d_j = 5$ [16]. At $y/d_j$ values exceeding 13, i.e. above the jet boundary, the small width of the probability contour indicates the high probability of finding a low intensity signal (Fig. 4.15b). This corresponds to the small variation in background intensity which in itself attains low values. With decreasing $y/d_j$ the liquid jet region is introduced with an accompanying increase in intensity due to light-scattering of liquid droplets. The sharp transition from low to high intensity facilitates determination of the jet's penetration height. As $y/d_j$

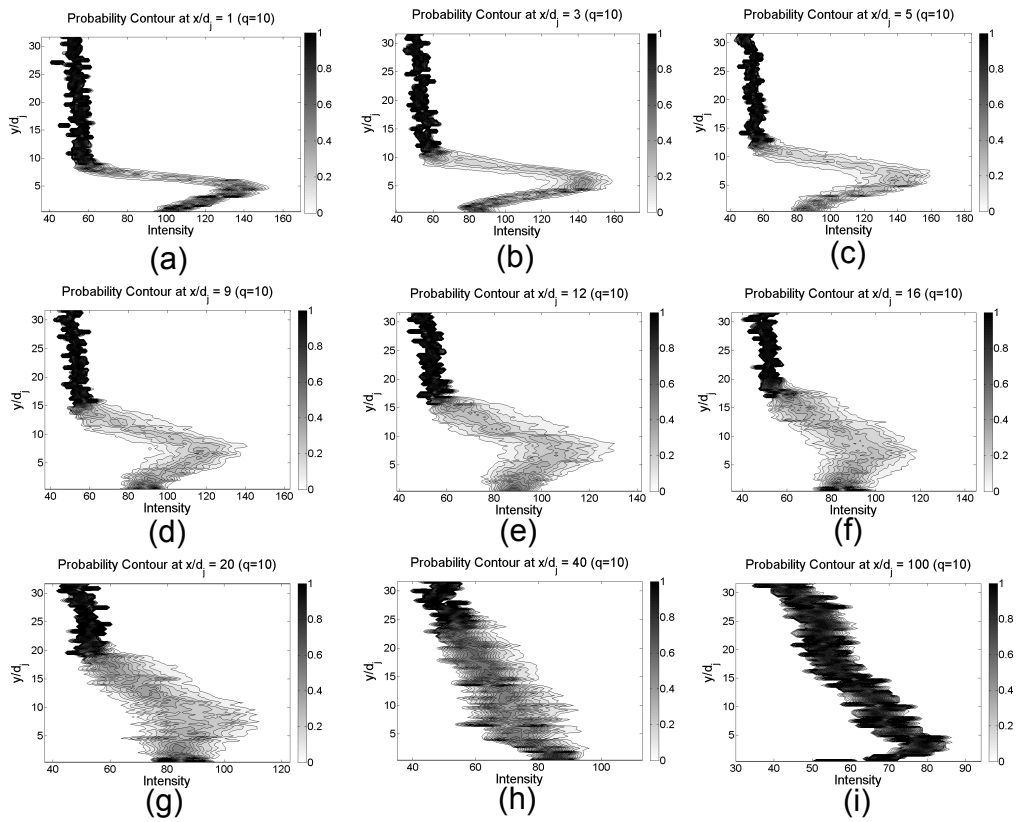


**Figure 4.17:** Probability contours for successive downstream locations: $x/d_j = 1$ (a), 3 (b), 5 (c), 9 (d), 12 (e), 16 (f), 20 (g), 40 (h) and 100 (i)

decreases further, a maximum intensity is reached, which can be identified as the height where there is the maximum population of water, which is called *the core height*. This procedure is also explained in Fig. 4.16 [15]. The two critical points on the pdf image (right) are shown by dotted lines, which are the height of the liquid core and the penetration height. These points can also be recognized on the mean image (left) at the same downstream location, which is selected to be 10 mm for this case. For this test case, 1 pixel is 0.24 mm.

Probability contours at successive downstream locations for a q = 10 jet case are presented in Fig. 4.17. For short downstream distances ($1 \leq x/d_j \leq 5$), the small width of the probability contours indicates inefficient mixing of the flow as a result of liquid phase passing in large clumps. With increasing downstream distance ($9 \leq x/d_j \leq 12$) the width of the contours increases. Intensity values have larger temporal fluctuations, indicating the presence of smaller clumps. These fluctuations increase further downstream ($12 \leq x/d_j \leq 20$) showing that the formed clumps decompose into smaller droplets due to the action of aerodynamic forces of the cross flow. At $x/d_j = 40$, full mixing between air and liquid (meaning the disappearance of the liquid core) can be inferred from the smoothened transition from low to high intensity and a simultaneous enlarging of contour width. Far downstream, at $x/d_j = 100$, the intensity values decrease considerably and the probability of finding a low intensity signal is very high (practically 100%), showing that water droplets are hardly captured by the camera. This fact could mean that the atomization process is complete and that no more droplet breakup happens. Lin [85] showed that completion of the liquid atomization process is reached after $x/d_j = 100$. Anyhow, this technique does not allow to estimate accurately whether the atomization of the water particles has been completed or not. Additional measurements to detect the droplet diameters should be performed. Although not documented, similar distances are witnessed before the occurrence of complete mixing for q = 4 and 7 circular jets.

The penetration height of the liquid jet can also be measured by PDF plots, as explained in Fig. 4.16. The penetration height values obtained for a q=10 jet from a circular injector are compared with the values obtained by edge detection algorithm as explained in Section 4.3. The penetration eight estimated by the proposed correlation (Eq. 4.3) is also presented as the black solid line. Looking at the comparison shown in Fig. 4.18, it can be observed that the two techniques agree very well, with a maximum deviation around 3%, which is the same amount of discrepancy between the penetration height correlation (Eq. 4.3) and experimental data. It should be noted that the edge detection method has an estimated uncertainty of 4% and the PDF technique has an uncertainty of 6% for dowsntream distances bigger than $x/d_j > 30$.

## 4.6 VELOCITY FIELD

The mean velocity field of the liquid jet particles is estimated by analyzing the recorded images by means of a VKI software based on the conventional Particle Image Velocimetry (PIV) technique [142, 16]. For the current kind of application, small scale structures are no longer of interest. Instead, displacements of the larger and more energetic structures require attention. To retrieve robust velocity information from the succession of images, the methodology is therefore based on the ensemble correlation approach [99].

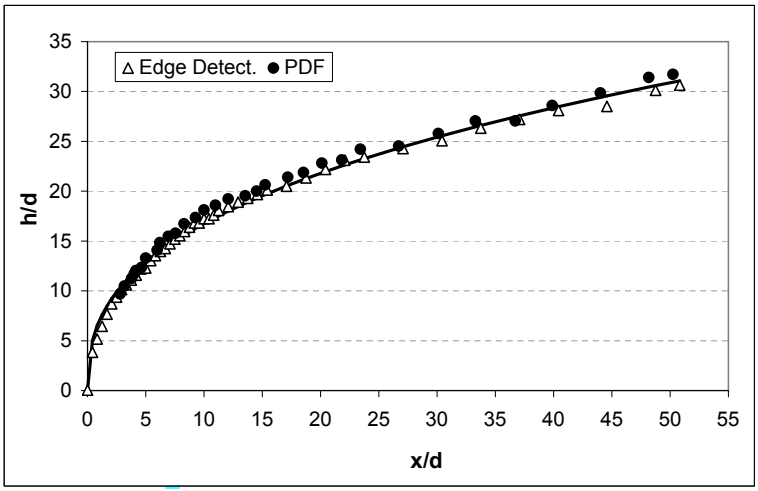


**Figure 4.18:** Penetration height of a q=10 jet by edge detection algorithm and PDF technique

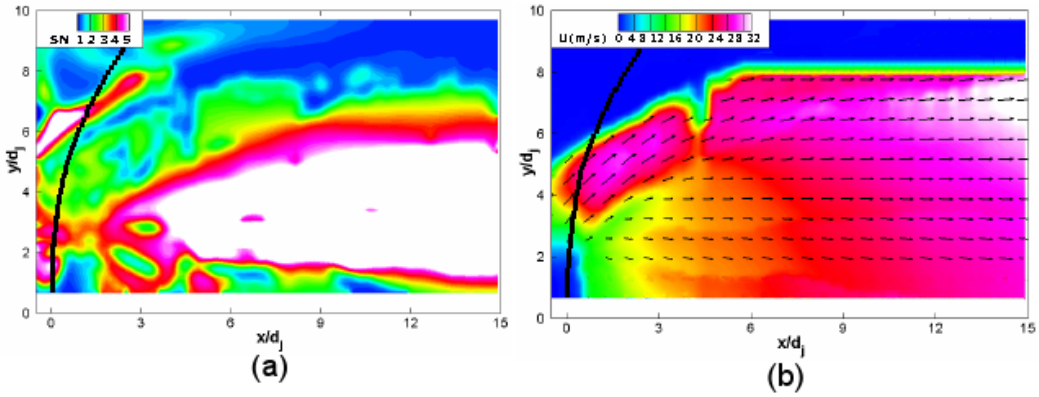


**Figure 4.19:** PIV measurement for streamwise injector at q = 7; Mach 6 flow from left to right a) Signal to noise ratio b) ensemble average velocity vectors superimposed onto average contours of horizontal velocity component.

As the detached clumps constitute detectable features within the recorded images, their motion can be traced by means of a cross-correlation operator between two successive images. Images are subdivided into so-called interrogation windows which are correlated. The resulting correlation map typically contains a dominant peak indicating the window-averaged displacement. This procedure is common within the PIV applications. However, PIV images typically consist of individual particle images whereas the intensity distributions in this case are continuous. In order to enhance the peak detectability within the correlation map, ensemble correlation is applied. The latter consists of averaging the individual correlation functions prior to analysis of the correlation map. To alleviate the degrading influence of spatial gradients in the reigning velocity field, images are iteratively deformed, such that the image features are better followed. Because the retrieved displacement vector represents a spatially filtered version of the underlying velocity field, smaller interrogation windows allow a reduced modulation effect. To obtain sufficient spatial resolution, iterative window deformation and refinement are incorporated [123]. Final window sizes of 17 x 17 pixels (1.37 x 1.37 $mm^2$) are applied in the analysis with an overlap factor of around 80% yielding a vector spacing of 3 pixels (0.24 mm). In total, 500 image couples are considered. Results presented hereafter refer to the case of a streamwise rectangular injector (AR = 1/3), with a jet/air dynamic pressure ratio of 7. The use of backlight illumination extended the measurement volume perpendicular to the image plane. As such, objects moving perpendicular to the field of view are captured as well, degrading the image quality due to blurring and decreasing the level of accuracy in the image analysis. As the ensemble-PIV technique is used for a dimensional analysis to predict the order of magnitude of the droplets velocity, no error estimation is performed. Nevertheless, it can be noted that the error in the estimation of in-plane velocity would be within $\pm 5\%$, due to an out-of-plane velocity component of 10%. However, for this type of injector, most of the displacement has been shown to be concentrated in the bulk flow direction (Figs. 4.12 and 4.14), reducing such inaccuracies. This is also advocated by the sufficiently high signal-to-noise ratios (SN $>$ 4) in the leeward part of the jet, where the speed of the water droplets is lower (Fig. 4.19a). This ratio is a measure of the correlation quality [69] indicating a limited number of erroneous displacements when exceeding a level of 1.5. In regions with strong temporal variation in image quality, i.e. at the windward region of the jet where detachment and bursting of clumps take place, a degradation in SN is noticeable but the levels remain acceptable (SN $>$ 3).

The velocity vector field, superimposed onto contours of the horizontal velocity is depicted in Fig. 4.19b, for the regions where the signal to noise ratio is greater than or equal to 2. High values of the velocity in the windward region of the jet show the rapid acceleration of the jet due to the aerodynamic forces of the cross flow. In the leeward region the velocity of the disintegrated small droplets is smaller whilst they accelerate progressively. The image analysis predicts a vertical velocity of around 20 m/s at the jet injection point thus matching the exit velocity of the liquid jet measured by the rotameter. At a downstream distance of 16 injector diameters, the

disintegrated small droplets in the leeward region reach a velocity of 40 m/s (Fig. 4.19b). The high velocity of the detached clumps in the windward region is not well captured as can be inferred from the lower signal to noise ratio value. Downstream of the strong bow shock, an air velocity of the cross flow in the order of 160 m/s can be expected from the normal shock relations. The measured particle velocities in the leeward region of the jet are lower, meaning that larger downstream distances are required for the water particles in this region to accelerate up to the free stream velocity. Figures 4.20 and 4.21 present velocity components in x and y directions, respectively.

Although it was possible to apply the ensemble-PIV analysis technique to the back-lighted images and it has been possible to extract information on the velocity

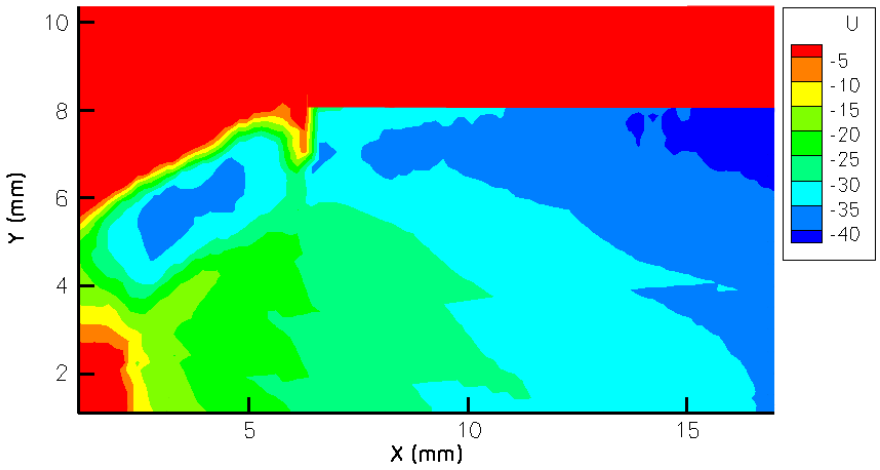


**Figure 4.20:** Velocity contours in x-direction, after ensemble-PIV analysis

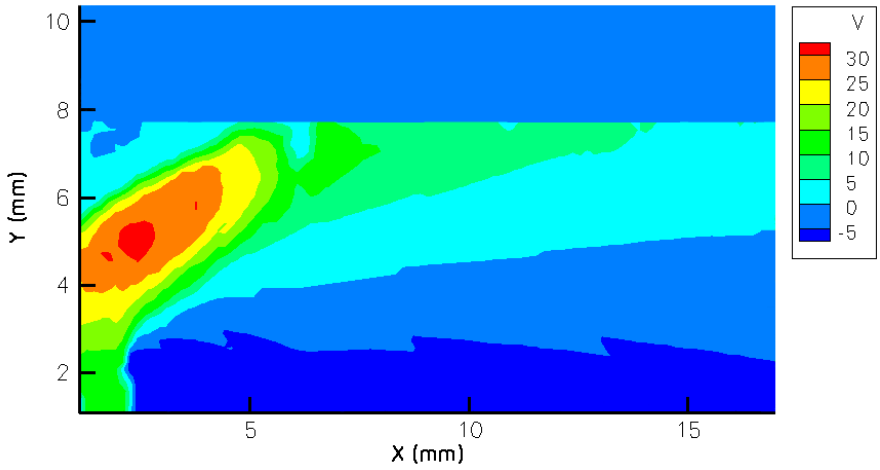


**Figure 4.21:** Velocity contours in y-direction, after ensemble-PIV analysis

of the liquid phase, the technique also demonstrates several drawbacks. Based on the analysis performed in Section 4.3, the expected penetration height of the liquid is indicated on the plots of Fig. 4.19 by the black solid line. The PIV analysis is not able to capture the true penetration of the liquid jet, as the results indicate a low signal to noise ratio close to the liquid – air stream border. An unexpected kink is observed at 4 injector diameters downstream location and 6 injector diameters above the flat plate. This kink is believed to be due to the poor performance of the ensemble-PIV algorithm in this region which suffers from an increased velocity gradient by the interaction of separation and bow shocks. The fact that the signal to noise ratio contour plot shows a similar kink exactly at this region is taken as an evidence to this statement. Because of all these reasons mentioned, the PIV analysis should be applied on back-light (or front-light) images with great caution, keeping in mind that the technique did not yield reliable results for this application. It may be recommended to use the technique on images obtained using a laser sheet, and at a higher frame rate.

## 4.7 Frequency Analysis

A frequency analysis of the clump detachment during the jet breakup and of the fluctuating shock pattern has been carried out by means of Fast Fourier Transforms on the times series of recorded pixel intensities. Power spectral densities are calculated by the method of Welch [153].

### 4.7.1 Jet Breakup and Clump Detachment

Growing axial waves lead to the primary breakup of the jet through clump detachment along the windward region of the jet and this tear of clumps is influenced by the bow shock – separation shock interaction [45]. The liquid fragmentation is expected to happen with a certain frequency, deserving a frequency analysis of the phenomena. In Fig. 4.22a, an instantaneous image of a back-lighted q = 10 circular injector jet case is shown. Frequency spectra of pixel intensities corresponding to different regions of the jet breakup are expected to indicate the existence of characteristic frequencies. Power spectral densities are plotted for representative pixels of three distinct regions in the frequency map in Fig. 4.22b-d. Pixel intensities in the windward part of the jet (1) are observed to possess a dominant frequency of 4.5 kHz which is related with the clump detachment. A Strouhal number can be defined based on the jet diameter and the jet exit velocity $St = \frac{f \times d_j}{U_j}$. With this definition of the velocity scale, a Strouhal number of $St = 0.18$ is obtained for the clump detachment and breakup of the liquid jet. The leeward region (2) is not in direct contact with the high speed cross flow and the clump fracture noticed in the windward part is absent. Instead, the jet disintegrates in small particles at a lower frequency of 1.5 kHz. In the free stream (3), no dominant frequency is apparent except for a 50 Hz peak attributed to electrical noise.

The pressure data of the injected water is also measured using a pressure trans-

ducer in order to check the fluctuation frequency of the injected water. The Fast Fourier transformation technique is used to obtain the frequency spectrum of the pressure data. A frequency peak content is noticed at 1300 Hz. As no water pump is utilized, it is not probable that such a high frequency in the water line is because of the fluctuations in the water tap. This frequency is thus believed to be due to the mechanical vibrations of the copper water pipe which is in contact with the complete H-3 wind tunnel facility. This frequency content might influence the pressure fluctuations of the water but it is difficult to make a definite statement about this hypothesis.

Concluding, clump detachment within the windward region is responsible for the primary breakup of the jet and occurs with a specific frequency of 4.5 kHz and $St = 0.18$. Almost identical frequencies are found for lower injection rates of the circular jet, such as q = 4 and 7. Similar Strouhal numbers are seen also in literature [105], although these previous investigations were not held for liquid injections into hypersonic cross flow.

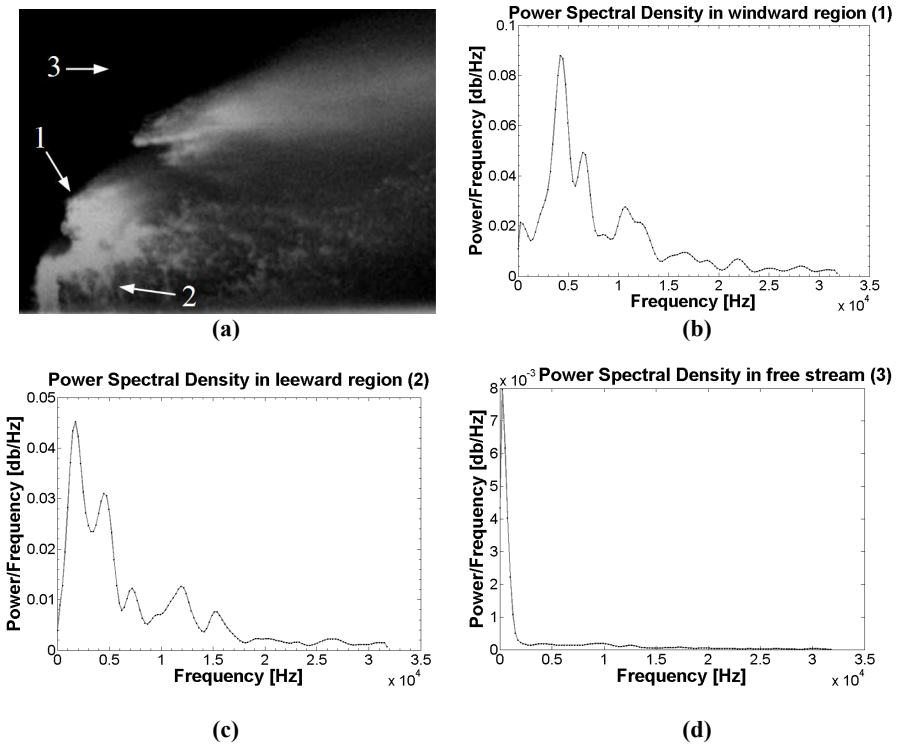


**Figure 4.22:** a) Instantaneous image of liquid jet breakup. Power spectral densities for pixels in b) windward region (1), c) leeward region (2) and d) free stream (3) of q = 10 circular jet

### 4.7.2 Fluctuating Shock Pattern

The whipping phenomenon is related with an interaction between the bow shock, separation shock and the impulse of the liquid jet and, as a consequence, a continuous vibration of the shock system. No detailed information is found in literature regarding the whipping phenomenon at similar conditions. Therefore, it needs to be investigated further. Figure 4.23 visualizes the standard deviation of the intensity signal for 1000 schlieren images. High amplitudes in RMS are observed to occur in the flow domain occupied by the fluctuating bow shock and separation shock. In the region spanned by the separation shock (1), a dominant frequency in pixel intensity appears around 300Hz. A Strouhal number can be defined as $St = \frac{f \times d}{(U_\infty - U_j)}$, based on the length of the separation shock (from the separation point to the impingement point of the separation shock on the bow shock) and the difference in velocity between the cross flow velocity and the jet exit velocity. Cortelezzi and Karagozian [30] explained in their study of the counter rotating vortex pair formation that either the jet velocity or the crossflow velocity may not be an appropriate velocity scale

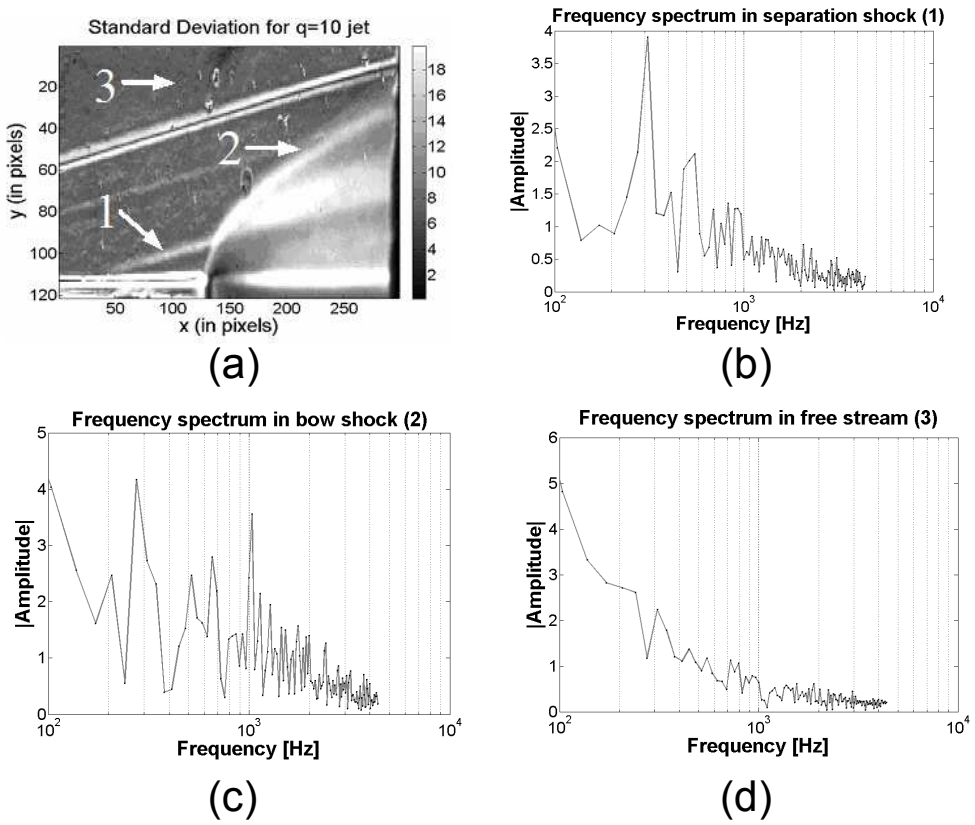


**Figure 4.23:** a) Standard deviation of 1000 images. Frequency spectrums for pixels in b) separation shock (1), c) bow shock (2) and d) free stream (3) of q = 10 circular jet

since the dynamics of the roll-up of the shear layer are dependent on both velocities. Based on this velocity scale, a Strouhal number of $St = 0.011$ is obtained for the separation shock oscillation. Frequencies in the same order of magnitude of 300 – 400 Hz for the separation shock fluctuation are found for different injection ratios as well, such as q = 2 – 10. In the bow shock region (2), in addition to the peak at 300 Hz, higher frequency peaks are present at 1 kHz and above [1]. These peaks indicate that the bow shock oscillation may be related with the high frequency clump detachment on the windward region of the jet.

[1] the peak at 100 Hz is a harmonic of the electrical noise peak at 50 Hz

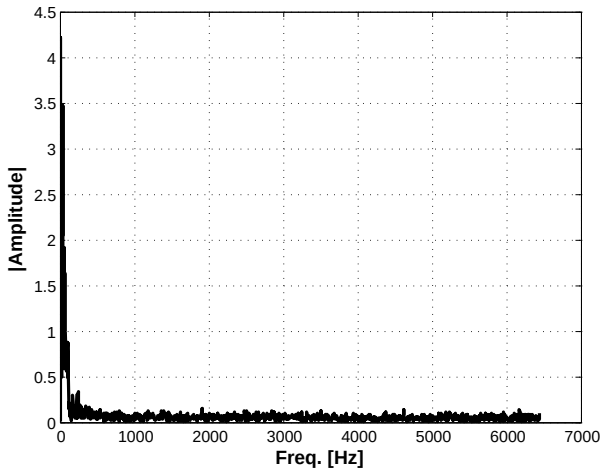


**Figure 4.24:** Frequency spectrum of the leading edge shock wave, for q=10 case

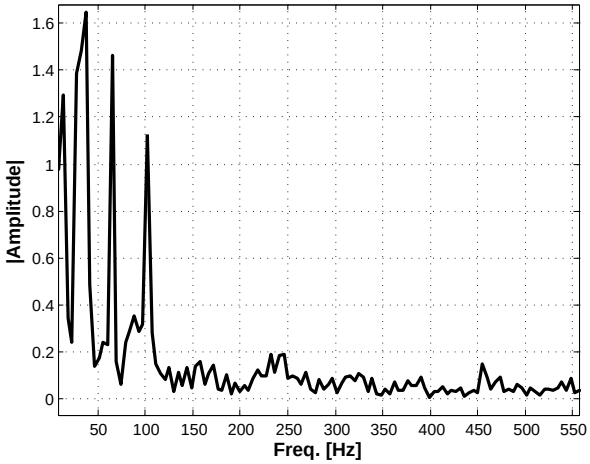


**Figure 4.25:** Frequency spectrum of the leading edge shock wave, for q=2 case (zoomed at lower frequencies)

In the free stream (3), no dominant frequency is observed apart from the electrical noise. Based on the fact that the schlieren images do not bear any information on the free stream (where there is no density gradient), the frequency analysis is repeated on the leading edge shock wave. Figure 4.24 shows that the frequency spectrum on the leading edge shock wave does not comprise any frequency peak higher than 100Hz, which is the same as presented in Fig. 4.23 (d). The same conclusion can also be obtained for the q = 2 case, for which a zoomed frequency spectrum is shown in Fig. 4.25.

The dominant frequencies are difficult to visualize for all pixels. Every pixel of the images contains multiple frequency peaks, some of them being the harmonics

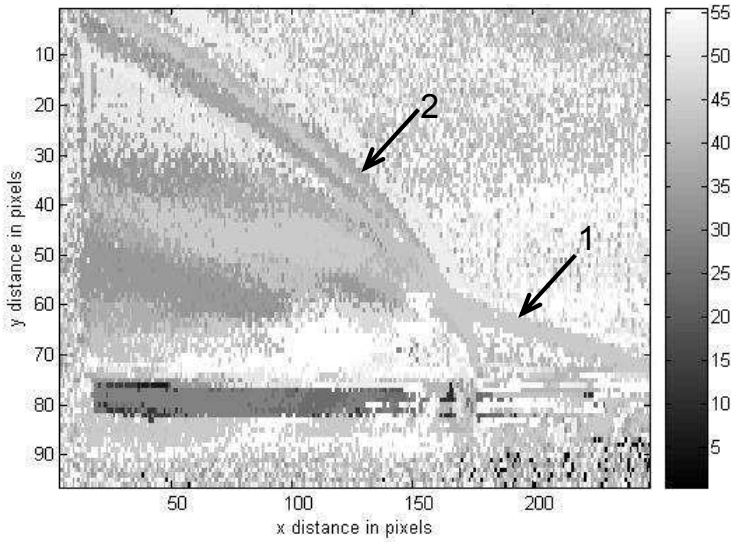


**Figure 4.26:** Frequency map for q=10 jet, with circular injector; schlieren image, Mach 6 flow from right to left, 1 pixel = 0.24 mm

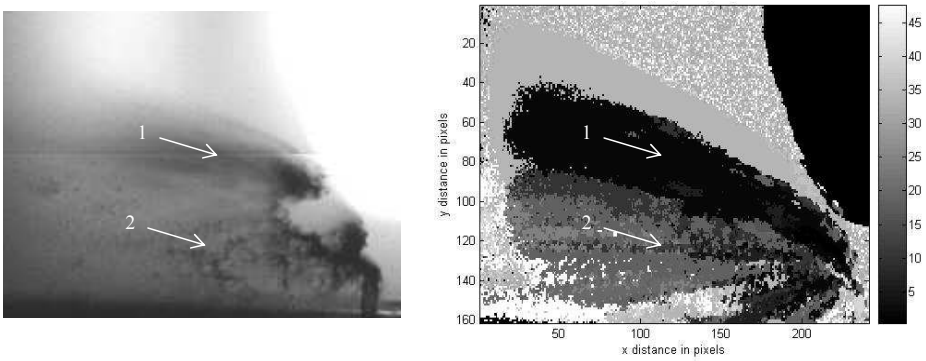


**Figure 4.27:** Frequency map for q=10 jet, with circular injector; back-light image, Mach 6 flow from right to left, 1 pixel = 0.08 mm

of a certain frequency peak, resulting in too much information which is difficult to visualize and to comprehend. To be able to visualize the frequency field of the whole domain in a simple way, a frequency map is created in which pixels with same decimal numbers have similar frequency peak values. For every pixel, three of the most dominant frequency peaks within their spectrums are taken. After this, the frequency range between the highest and lowest frequencies encountered in the flow are divided into six bins, whose width is one sixth of the complete frequency range. A value of 1 is given to the bin if any of three frequency peaks is within that bin; otherwise a value of 0 is given to that bin. At the end, a binary number is obtained, such that each digit of this binary number indicates if there is a frequency component within that bit or not. This binary number is then converted to corresponding decimal number and is assigned to the stated pixel [89, 15]. The highest digit of the resultant binary number is formed by the highest frequency present in the flow and the lowest frequency yields the smallest digit. Thus, for six bins covering the whole frequency domain, the formed decimal number can go up to 63. However, if the highest frequency decreases by only a single bin, the converted decimal number would decrease to 31. Thus, the map in effect will be highly effected by the highest frequency content available at each location, even if this frequency peak is only the third strongest at that location ant other processes are dominating the flow. Although this limits the usability of this technique, the results are worth presenting as they indicate regions with similar frequency content.

The image view of these decimal values can give us information about regions within the flow field with similar frequency peak content. Although a frequency map supplies no qualitative information on the frequency content, this method is used to catch fluctuating phenomena within the flow field, and to see if there is any influence among the different aspects of the flow field. A frequency map for a q=10 jet from a circular injector is shown in Fig. 4.26. Similar frequency content in the vicinity of separation shock (1) and the bow shock (2) can be observed. Following the line of separation shock in the downstream direction, it is observed that the liquid phase which is being disintegrated downstream of the bow shock has also similar frequency content with regions (1) and (2). This observation can be related with the whipping phenomenon. Based on all these observations, the most logical explanation about how different aspects of the flow field influence each other, creating the so-called whipping phenomenon, is as follows:

i. The injected liquid triggers creation of the bow shock.

ii. The varying angle of the bow shock results in an increased shear stress, forcing the liquid jet to deflect in the cross flow direction

iii. A separated flow region upstream of the injection point, thus a separation shock wave is created due to the existence of the bow shock and adverse pressure gradient inside the boundary layer.

iv. The separation shock wave interacts with the bow shock (shock - shock inter-

action) and penetrates into the liquid phase, causing the liquid to disintegrate at a high rate.

v. The liquid phase disintegrated by the separation shock penetrates less into the air stream, causing the bow shock to change and to be more inclined.

vi. The bow shock being more inclined towards the air stream causes the separation shock to move closer to the injection point and thus become more steep.

vii. The steeper separation shock interacts with the liquid phase at a higher position, causing a delayed disintegration. Thus, the liquid can penetrate higher, which causes the bow shock to be steeper.

viii. The configuration at item number (iii) is reached. A continuous and regular fluctuation of the shock system occurs with a loop between item (iii) and item (vii).

Special attention should be focused on item (iv) where the separation shock interacts with the bow shock. The point where this shock – shock interaction occurs is called a *triple point*. The phenomenon of the triple point, in which three shock waves intersect, is a very common one and occurs when a $\lambda$-foot is created by the interaction of a normal shock wave with the separation shock emerging from the boundary layer [138]. This is illustrated in Fig. 4.28. The existence of a triple point creates a shear layer with strong gradients. This shear layer is believed to play an important role in the fragmentation of the liquid, as the aerodynamic shear force is more evident in this region.

Another interesting observation is that the frequency map yields very similar results to a standard deviation image, that can be seen in Fig. 4.6. High standard deviation values mean that the intensity values fluctuate a lot. The frequency map shows that this fluctuation has a characteristic frequency content. Similarly, a frequency map is created for the back-lighted images of a q=10 test with a circular

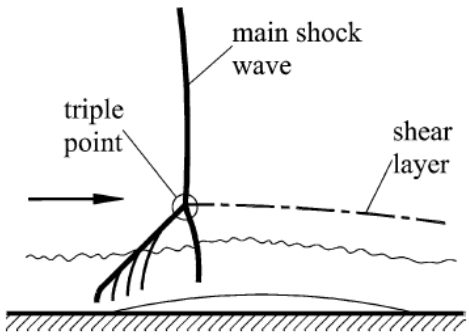


**Figure 4.28:** Triple point of a shock-shock interaction, after [138]

| Frequency (Hz) | Region (1) | Region (2) |
|---|---|---|
| 1000 | | |
| 2000 | | ✓ |
| 3000 | | ✓ |
| 4000 | | ✓ |
| 4500 | ✓ | |
| 5000 | ✓ | |

**Table 4.3:** Frequency content for the liquid jet, q=10

injector. As explained in Section 4.3, for high q jets, there is a sudden disintegration of the outer part of the jet as clumps detach. An estimation of the frequency of this sudden disintegration region can be made by frequency analysis and by investigating the frequency map. A background subtracted back-light image for a q=10 jet, together with the calculated frequency map for 3 peaks is shown in Fig. 4.27. The frequency map image is generated using 2000 images and 3 frequency peaks. Region (1) indicates the region where the separation shock meets the liquid phase and sudden disintegrations take place. Region (2) is the region where the liquid particles move rather slowly under the effect of the separated flow region. The frequency content corresponding to these two regions is shown in Table 4.3. Comparing regions 1 and 2 of Fig. 4.27, the frequency seems to be considerably higher in the upper region of the jet (region 1) than in the main jet body (region 2). This seems to be in good agreement with the observation that sudden disintegrations occur in the upper region, where both the velocity of the jet and the aerodynamic shear force are higher. The sudden disintegration of the upper region of the jet is a very high frequency phenomenon, which takes place at a frequency of 4500 Hz. This frequency value is also validated by looking at the high speed camera images sampled at 60 KHz; the sudden disintegration occurs every 10-15 frames, which seems to be in the order of magnitude of the estimated frequency. The frequency map method seems to distinguish well the regions of the flow field where the intensity signal changes with different frequency. Although the frequencies presented in Table 4.3 seem to be coherent among each other, they are not in agreement with the frequencies obtained from schlieren images, shown in Fig. 4.23. Fig. 4.26 shows that the separation shock, the bow shock and the core of the liquid phase share common frequency peaks. However, this frequency peak does not match with the value presented in Table 4.3. This is an indication that the frequency mapping technique is not entirely illustrative for the frequency analysis of the complete flowfield, and hence should be handled carefully. On the other hand, one should also keep in mind that the sampling rate of the schlieren images (around 10 kHz) and that of the back-light illumination images (around 60 kHz) are quite different, making the comparison of the two phenomena difficult.

# 5 Flow Visualization

The present chapter is devoted to the explanation of the tests performed to understand the flow topology of liquid injection into Mach 6 cross flow. The work presented in the previous chapter has been focusing always on the same plane, which is perpendicular to the wind tunnel model and parallel to the air stream. The outcomes of these work have shown that the flow field is very complex, with mixing, shock – shock interaction, recirculation zones, fragmentation, atomization, etc... An additional attempt has been made to acquire more details on the flow topology of liquid injection into hypersonic cross flow, by investigating the flow topology on planes that are parallel to the flat plate model. Oil flow visualization and laser cross section visualization tests are performed for this purpose, as explained in Section 5.1. The results of the experiments are discussed in Section 5.2. The chapter is concluded by comparing the results with those of gas injection into Mach 6 cross flow (Section 5.3.1) [126, 127] and also those of 3-D rigid obstacles in Mach 6 flow (Section 5.3.2) [143], performed by independent researchers [127, 143] at the same facility and under similar conditions.

## 5.1 Experimental Procedure

High-speed Schlieren photography, laser cross section visualization, oil visualization and acenaphtene sublimation techniques have been used during the investigations. All these techniques are basically dedicated to the study of the flow topology. Sublimation technique enables to highlight the regions of high surface heat flux while oil visualization shows skin friction contours. All tests, including gas injection and 3-D obstacles are performed at the VKI H-3 facility (see Section 3.1) using the flat plate model with flush liquid injectors mentioned in Section 3.2.1.

Visualization of the flow shock pattern is performed by means of the Schlieren imaging technique (see Section 3.3.2), and the high speed camera with a shutter time as low as 50$\mu$s. Oil flow visualization of liquid injection tests are recorded at a speed of 600fps. The usage of oil flow visualization technique is very empirical and requires a lot of know-how and practice. This technique is particularly adapted to the case of "long duration" facilities such as H-3 where the test conditions can be maintained during several seconds. Indeed, the oil is displaced on the model due to skin-friction and flows with the flow. At the end of the test, the remaining thickness of the oil is proportional to the skin-friction distribution and some skin friction lines are visible allowing flow structure interpretations. The visualization oil consists of a mixture of a titanium-oxide powder with oil whose viscosity is adapted to the problem. The prepared oil is painted on the model following an orientation perpendicular to the expected streamlines in such a way that the oil structures created during painting do not interfere with the flow pattern interpretation after test. This is mainly important in the low skin-friction regions where oil does not move. The oil used for H-3 testing was viscous enough to allow a vertical mounting of the flat plate in the facility. A high resolution picture of the displaced oil pattern is taken after the test, while a high-speed video recording is taken during the test [126].

The sublimation technique is very empirical and requires practical experience. The basic principle of the method is to apply a uniform thickness of a special sublimation paint on the model surface and expose it to the hypersonic flow. The paint starts sublimating proportionally to the local convective heat transfer rate, putting in evidence high and low heat-flux regions. Practically, the sublimation test procedure consists of first covering the model with a blue dye for increasing visualization contrast and then brush-painting with a mixture of acenaphtene dissolved into ether. Care is taken to impose a sublimation paint thickness as uniform as possible. The results are strongly dependent of the testing time that has to be adapted to the test conditions. Just like oil visualization tests, sublimation experiments are recorded using the high-speed camera, only for 3-D obstacle experiments [143].

The images of different cross-sections parallel to the flat plate model at several heights are obtained using a laser sheet illumination. A *Quantel Twins Ultra 180* MiniYAG laser at 100mJ energy level (at 532nm wavelength) is used at 15Hz pulse frequency. Cylindrical and spherical lenses are utilized to convert the 6.35mm diameter laser beam into a laser sheet. The laser sheet is placed at 5, 10 and 15mm above the flat plate by a traversing mechanism. The thickness of the laser sheet is 1mm, and the duration of one pulse is 11 nano-seconds. The high speed camera is placed above the wind tunnel to detect the signature of the liquid jet illuminated by the laser sheet. A Micro-Nikkor (Nikon) 105mm objective is used at an aperture opening of f1:11.

## 5.2 Flow Topology

Oil flow visualization technique is applied to investigate the flow topology of liquid injection into Mach 6 cross flow, in comparison to other visualization techniques such as the Schlieren photography technique (see Section 4.2) [16]. The effect of dynamic pressure ratio, $q = (\rho_j V_j^2)/(\rho_\infty V_\infty^2)$, and the effect of liquid injector shape are studied. In addition to the three injectors shown in Fig. 3.4, a circular injector with 2mm diameter is also used. Typical oil flow visualization pictures of water injected through different injectors are shown in Fig. 5.1, with the main topology presented in the schematic drawing of Fig. 5.2.

Although the quality of the oil is deteriorated significantly by the presence of water, it is still possible to detect the main lines describing the flow topology. Upstream of the injection point, the flow separates just like in the case of gas injection (explained in Section 5.3.1). The separation line, bow shock and the horseshoe vortex are similar for liquid and gas injection cases. The crossflow boundary layer also

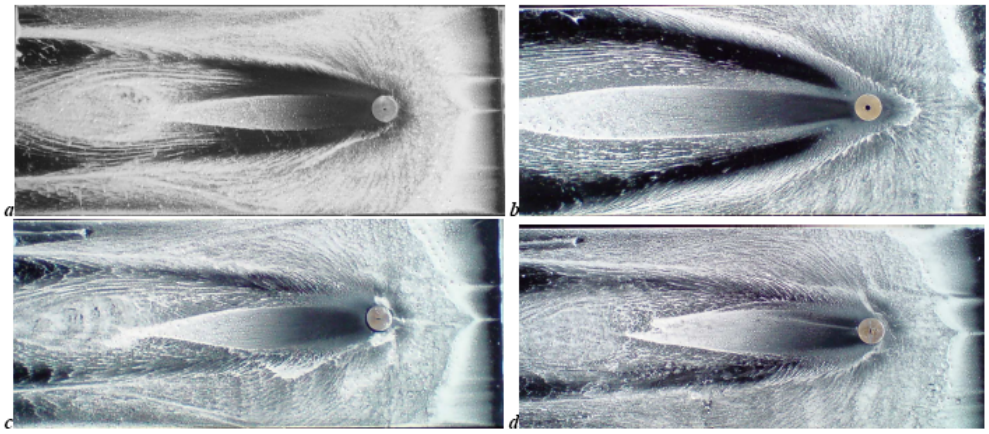


**Figure 5.1:** Oil flow visualization pictures for different injectors (q=2.5): a) 1mm circular b) 2mm circular c) Streamwise rectangular d) Spanwise rectangular; Mach 6 flow from right to left

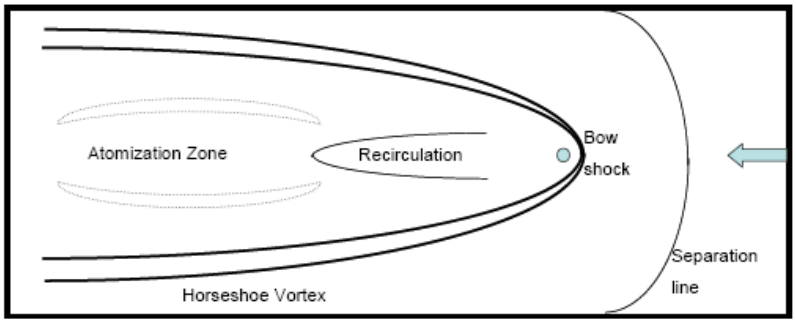


**Figure 5.2:** Main flow topology of liquid injection

separates downstream of the jet because it can not negotiate the adverse pressure gradient which is imposed on it by the flow around the jet. Fric and Roshko [40] used smoke from different sources to mark the vortices and to track the fluid (gas) within the vortex cores. They found that the wake vorticity comes from the boundary layer on the wall from which the jet issues and not from the jet fluid. They also found that the vorticity of the cross flow boundary layer is incorporated into the wake vortices, which extend from the wall to the bending jet. Downstream of the injection point, the separated flow region is much bigger (twice or more both in width and in length) in the case of liquid injection compared to gas injection. Above this recirculation zone, fragmentation of the injected liquid takes place by the existence of high aerodynamic shear forces. At the downstream end of the flat plate, a complex region is observed, where atomization of the injected liquid occurs. This is a complex three dimensional flow field. Looking at the oil flow pictures (Fig. 5.1), it is also possible to see the signatures of secondary vortices around this atomization and recirculation zone. Comparing the effect of injector shape, the 1mm diameter circular and streamwise rectangular injectors have very similar flow topologies [12, 112].

Schlieren pictures indicate that liquid injected from a spanwise rectangular injector has a lower penetration height than circular or streamwise injectors (see Section 4.2) [16]. Because of the increased amount of mass flow rate needed to have the same dynamic pressure ratio, the flow topology created by the 2mm diameter circular injector is different than the others. All dimensions, including distance of the separation line, the width and length of the recirculation zone downstream of the injection point, and the width of the wetted area are significantly higher for the 2mm circular injector tests. This is because of the bigger obstacle created in the flow by the higher mass flow rate of the 2mm circular injector, which has a surface area that is four times bigger than the other injectors.

The distance of the separation line from the injection point can be seen in Fig.

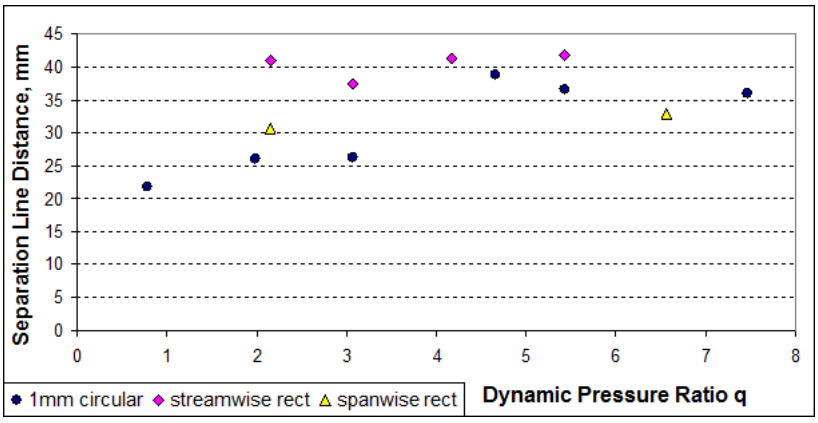


**Figure 5.3:** Separation line distance to liquid injection point; Oil flow visualization technique

5.3, for different injectors and for varying dynamic pressure ratio. As a general trend, the length of the separated flow region increases with increasing dynamic pressure ratio. Figure 5.4 presents two plots showing the lateral extension of the liquid jet, or in other words, the width of the region influenced by the liquid at 30mm and 60mm downstream of the injection point. Again, the general trend is that the width increases for increasing dynamic pressure ratio. Because of the deterioration of the oil paint by the presence of liquid, there is a high uncertainty (around 15%) associated with the values presented in Fig. 5.3 and Fig. 5.4. Thus, it is not feasible to compare the topologies of different injectors, although the general trend and the overall dimensions can be identified.

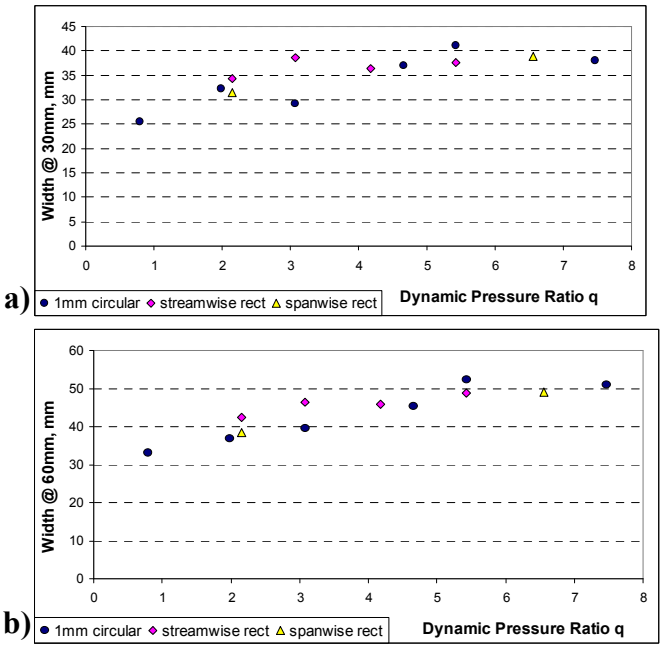


**Figure 5.4:** Lateral extension of injected liquid: 30mm (a) and 60mm (b) downstream of injector; Oil flow visualization technique

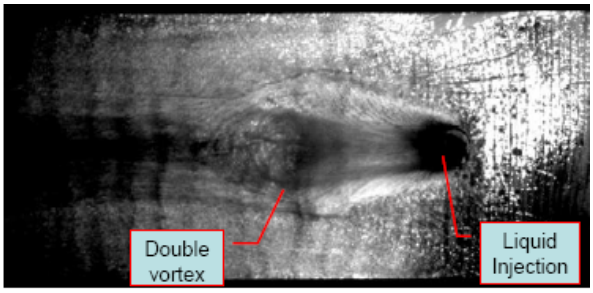


**Figure 5.5:** Double vortex moving downstream of liquid injection point; Oil flow visualization technique, Mach 6 flow from right to left

Another important observation is the existence and motion of a vortex pair (double vortex) during the beginning phase of the tests with low dynamic pressure ratio ($q \leq 3$). For all the tests of the experimental campaign, the flat plate is injected into the well-established Mach 6 freestream with the water valve open. The liquid jet is deflected by the aerodynamic force as soon as the model is injected. Exactly at this moment, the formation of a vortex pair close to the injection point and its motion in the downstream direction can be observed. The velocity of the double vortex structure decreases as it gets further away from the injection point. Figure 5.5 shows an image of the vortex pair observed during a test performed with the streamwise rectangular injector.

Oil flow visualization gives an idea of the flow topology on the wall of the flat plate model. However, knowing that the two phase flow field of liquid injection into hypersonic cross flow is indeed a complex three dimensional flow field, images of different cross sections are photographed using laser sheet cross section visualization technique. Tests are performed using 1mm diameter circular and spanwise rectangular injectors. A laser sheet is focused on planes parallel to the flat plate at heights of 5, 10 and 15 mm. Although high-speed camera recordings 1 mm above the surface are also performed for the 1mm diameter circular injector, these images are not very reliable due to strong reflection from the surface of the flat plate model. Top-view images are obtained by high-speed camera. The intensity recorded by the camera is proportional to the population of water particles passing through the plane of the laser sheet and reflecting light. The structure of a vortex pair presented in Fig. 5.5 can also be seen clearly on some of the laser sheet images obtained using the spanwise rectangular injector. Figure 5.6 presents two images where two separate

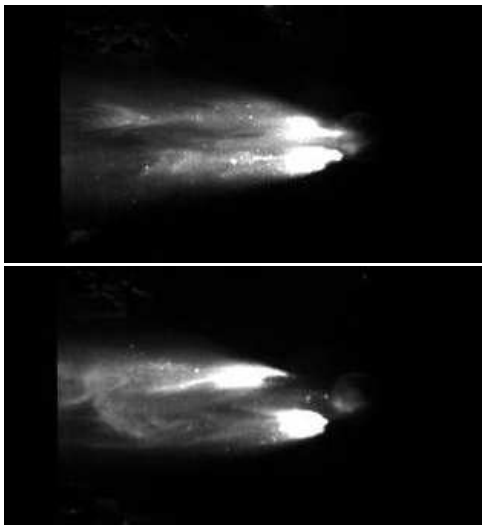

**Figure 5.6:** Double vortex structures photographed by laser sheet imaging, z=10mm, q=2.18

water chunks moving together are photographed at a height of 10mm above the flat plate for a dynamic pressure ratio of 2.18, indicating the presence of a liquid vortex pair.

A jet exhausting into a cross flow generates a complex flowfield with several distinguishable features. When the jet flux exits the injector, it is deflected by the freestream to follow a curved path downstream while its cross section changes. For the case of a circular injector, one can consider the pressure distribution due to potential flow around a rigid circular obstacle to be $C_p = 1 - 4sin^2\theta$, where $\theta$ is the angular component of the cylindrical coordinate. There are stagnation points ($C_p = 1$) upstream ($\theta = 0°$) and downstream ($\theta = 180°$), and minimum pressures ($C_p = -3$) at the lateral edges ($\theta = 90°$ and $\theta = 270°$). As a consequence, the flow spreads laterally into an oval shape. At the same time the cross flow shears the jet fluid along the lateral edges downstream to form a kidney shaped cross-section. At increasing distances along the jet path, this shearing force folds the downstream face over itself to form a vortex pair, which dominates the flow as shown in Fig. 5.7 [91]. The double vortex shown in Fig. 5.5 and in Fig. 5.6 corresponds to the counter rotating vortex pair shown in Fig. 5.7. Associated with the counter rotating vortex pair is the flow induced into the wake region of the jet from the freestream. This entrainment has been the subject of many investigations. When the locus of maximum vorticity is projected to the symmetry plane, the resultant line is called the vortex path. There is also a locus of maximum velocities in the symmetry plane which is called the jet centerline path. Also shown on Fig. 5.7 are the secondary vortices: the horseshoe vortex (2) and the wake vortex street (3) [91]. The atomization zone shown in Fig. 5.2 corresponds to the wake vortex region of

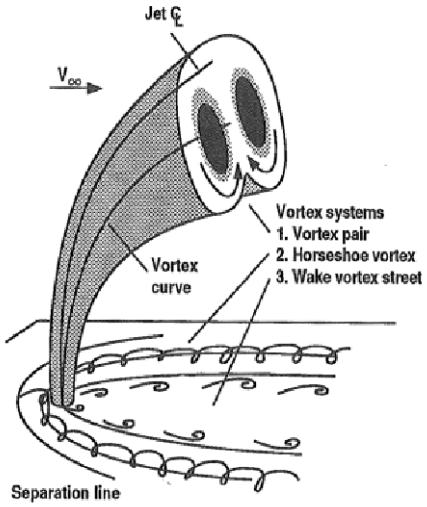


**Figure 5.7:** Sketch of the three vortex systems associated with the jet in a cross flow

Fig. 5.7.

Coming back to laser cross-section visualization, at least fifty images are used from each test to calculate the mean and standard deviation of the images obtained by laser sheet illumination. These images are used to estimate the lateral extension of liquid jet (width of wetted area) 10mm and 60mm downstream of the injection point. The uncertainty of these measurements are $\pm 4$ pixels or $\pm 1.2mm$, much less than the uncertainty associated with the oil flow visualization technique. Figure 5.8 presents the lateral extension 10mm downstream of both 1mm diameter circular (top) and spanwise rectangular (bottom) injectors, for q=2 and q=6 dynamic pressure ratios. The lateral extension of the liquid jet has a decreasing trend with decreasing dynamic pressure ratio and also with increasing height. The effect of the dynamic pressure ratio is due to the lower mass flow rate of the liquid injected into the flow. As

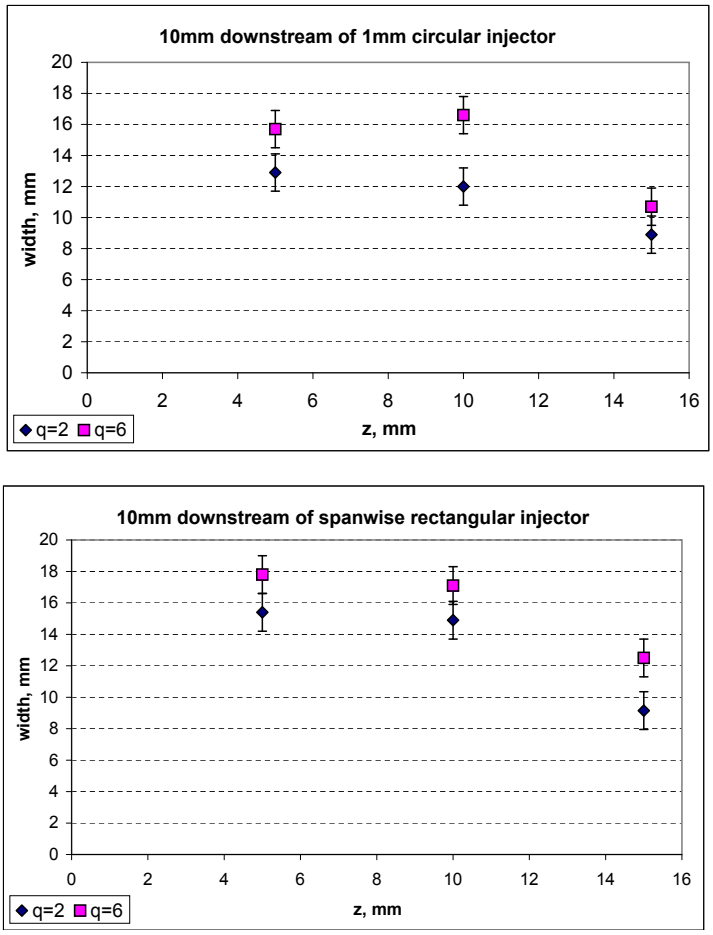


**Figure 5.8:** Lateral extension of liquid jet 10mm downstream of 1mm circular (top) and spanwise rectangular (bottom) injectors; laser sheet visualization technique

the measurement plane is moved higher above the flat plate, less water penetrates to that height, resulting in a lower width. Although it can still be observed that increasing the dynamic pressure ratio causes the width of the wetted area to increase at 60mm downstream of the injection point, the same conclusion can not be obtained for the measurement plane height of 10mm. Figure 5.9 shows that the width of the wetted region increases at higher measurement planes. This can be explained considering the amount of liquid that penetrates to higher locations. According to Schlieren and back-lighted illumination measurements of [16, 15], the penetration height of a q=6 water jet from a circular injector at 60mm downstream location is twice that of the height at 10mm downstream location. The location of the liquid core (where the liquid phase population is maximum) goes upwards as well, with the increasing downstream distance (see also the discussion associated to Fig. 4.17 in Section 4.5). With more liquid carried upwards at a long enough downstream

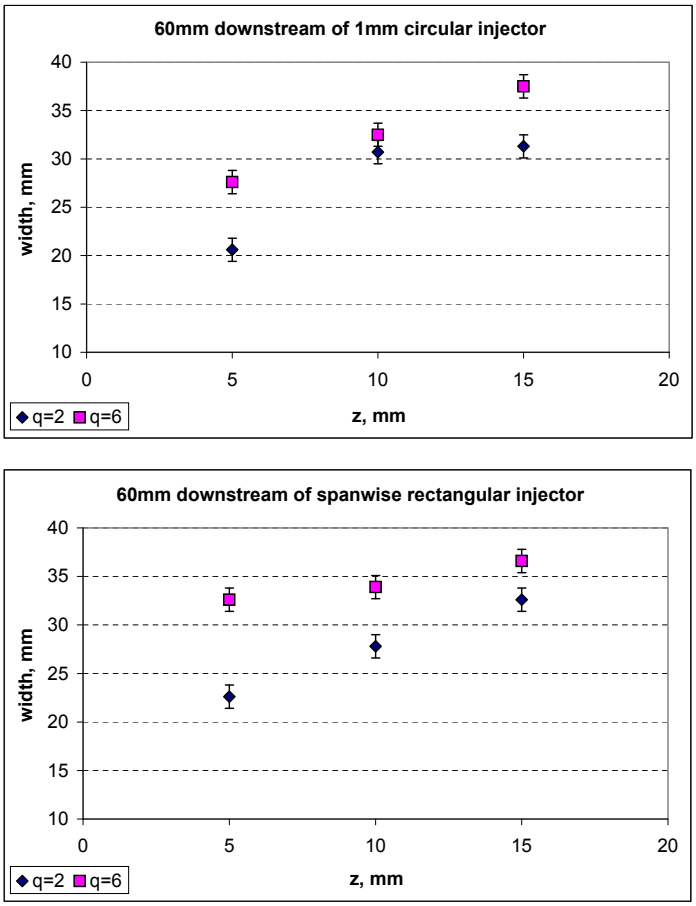


**Figure 5.9:** Lateral extension of liquid jet 60mm downstream of 1mm circular (top) and spanwise rectangular (bottom) injectors; laser sheet visualization technique

distance (such as 60d), the lateral extension of the injected liquid also increases as the measurement plane is moved upwards. The last conclusion that can be obtained from the data presented in Fig. 5.8 and 5.9 is that the width of the wetted region created by the spanwise rectangular injector is higher than that of the circular or streamwise rectangular injector, especially at locations close to the injection point. This conclusion is in agreement with the findings of Section 4.4 and [16, 15].

The data presented in Figures 5.8 and 5.9 can also be compared with the predictions of the proposed correlation following the top-view image analysis in Section 4.4. Equation 4.4 predicts a lateral extension of 8 and 12 mm, 10 mm downstram of the circular injector and for q = 2 and 6, respectively. Figure 5.8 (top plot) shows a decreasing trend of lateral extension at 10 mm downstream location, with the increasing height and this trend approaches to 8 mm and 11 mm, for q=2 and 6, respectively. The phenomenon is inverted for 60mm downstream location, where the lateral extension increases with increasing height from the wall, as shown in Fig. 5.9 (top plot). On the other hand, Eqn. 4.4 predicts a lateral extension of 19 mm and 28 mm, 60 mm downstram of the circular injector and for q = 2 and 6, respectively. These values correspond to the minimum points on the plot of Fig. 5.9 for the circular injector, where q = 2 plot starts from 19 mm lateral extension at z = 5mm and q = 6 plot starts from 28 mm lateral extension at z = 5mm. Although the values predicted by Eqn. 4.4 agree somehow with the laser cross-section visualization measurements, they always correspond to the minimum lateral extension no matter if the trend is increasing (at 60mm downstream location) or decreasing (at 10mm downstream location), according to Fig. 5.8 and Fig. 5.9. This indicates that the top-view measurements mentioned in Section 4.4 focus only on the core of the liquid phase and they lack sufficient light to be reflected from liquid droplets. Hence, the lateral extension correlation proposed in Eqn. 4.4 should be considered only for the core of the liquid phase, and not for the complete *wetted area*.

## 5.3 Similar Studies Performed in the H-3 Wind Tunnel by Independent Researchers

### 5.3.1 Comparison with Gas Injection

The complexity of the hypersonic flow regime is increased further when secondary flows are introduced by other means. For example, ablative materials used on thermal protection systems (TPS) of space vehicles experience release of pyrolysis gases, which might alter the flowfield and even the flight characteristics of the vehicles [147, 152]. Gas injection into hypersonic crossing flow can also be done on purpose, for example to promote turbulence to avoid choking of scramjet inlets due to complex shock-shock interactions [126, 22, 19]. Because of these reasons, air injection into a Mach 6 cross flow is studied by [126, 127] in the H-3 wind tunnel facility of the von Karman Institute. The main results are discussed here for a comparison of the flow topology between gas and liquid injection into hypersonic cross flow, exactly under the same conditions of the same wind tunnel.

Air is injected through a 1mm diameter circular injector (see Section 3.4) into Mach 6 cross flow. Five different experiments are carried out at different injected air total pressure to freestream static pressure ratios ($P_R$). Pressure transducers are employed to measure the two pressures. The freestream total pressure is always kept at 20bar ($\pm$1bar) and total temperature at 500K ($\pm$20K), which corresponds to a freestream unit Reynolds number of $16.8 \times 10^6 m^{-1}$. The typical features [44, 48] that can be observed on a Schlieren photo are shown in the schematic view of Fig. 5.10. Upstream of the injection point, the flow is separated due to adverse pressure gradient within the subsonic boundary layer. An oblique shock wave, emerging from the separation point, interacts with the bow shock just upstream of the injection point. Downstream of the injection point, it is possible to notice the Mach disk.

The post treatment of the oil flow visualization technique consists of measurements taken from the digital pictures recorded after each test. A schematic of the behavior of the supersonic jet within hypersonic flow is sketched in Fig. 5.11. Table 5.1 presents the test matrix and the main results of the five tests with gas injections at different pressure ratios, $P_R$, ranging between 35 to 170. The oil flow pictures have been compared to theory, previous works and recorded Schlieren images. The location of the first line left of the plate corresponds to the location of the separation shock upstream of the jet. The position of the separation shock moves further upstream, as the jet injection pressure ratio increases. This is believed to be due to the increased penetration of the jet into the hypersonic cross flow with increased pressure ratio, and also due to the amount of blockage induced. The clean dark region starting upstream of the jet injection indicates the location of the horseshoe vortex. Similarly, the starting point of the horseshoe vortex region upstream of the jet moves further upstream, as the jet injection pressure ratio is increased. However, the displacement rates are different. The width of the wake has also been measured at different locations downstream of the injection point. It can be noticed that the width of the jet increases as the pressure ratio is increased, referring to the amount

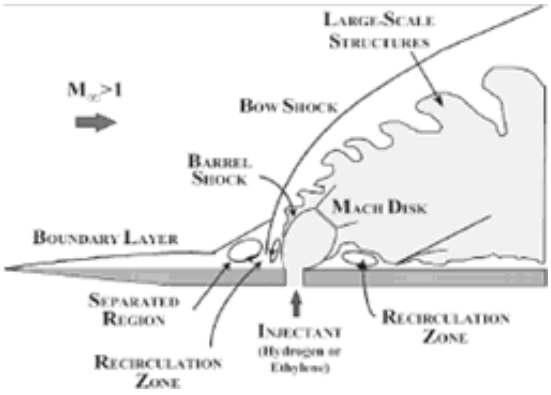


**Figure 5.10:** Shock and vortex system of gas injection into compressible cross flow; side view

of blockage induced by a bigger jet into the flow. As the pressure ratio increases, the penetration of the jet increases, and the expansion of the under-expanded jet gets also bigger, resulting in a bigger sized oblique shock.

The geometrical parameters presented in Fig. 5.11 are listed in Table 5.1: $a$ is the distance between the injection point and the separation line, $b$ and $c$ are the distance between the injection point starting and ending locations of the horseshoe vortex, respectively. Length of the separated flow region (recirculation region) downstream of the injection point is represented by $d$. Columns $e$, $f$ and $g$ represent the width of the three vortex lines 60mm downstream of the injection point. The streamwise thickness $(b-c)$ of the horseshoe vortex and the spanwise thicknesses $(f-e)$ of the horseshoe vortex are also shown in Table 5.1. Typical error of the measurements presented in Table 5.1 is 4%. The secondary vortices are formed along the horseshoe vortex, starting further downstream than the horseshoe vortex itself. The location of the secondary vortices can be presented by the thickness $(g-f)$, 60mm downstream of the injection point. Both of the separation regions, downstream and upstream of the injection point, become bigger as the pressure ratio is increased. The length of the separated flow region upstream of the injection point is almost tripled ($a$ in Table 5.1 and in Fig. 5.11), whereas the one downstream is increased only 50% ($d$ in Table 5.1 and Fig. 5.11). The starting point of the horseshoe vortex ($b$ in Table 5.1 and Fig. 5.11) is pushed further upstream and the thickness of it ($b-c$ in Table 5.1 and Fig. 5.11) is also increased by the increasing pressure ratio. However, the changes in the starting location and the width of the horseshoe vortex are only significant up to a pressure ratio of 100 (Case C), and do not change significantly for pressure

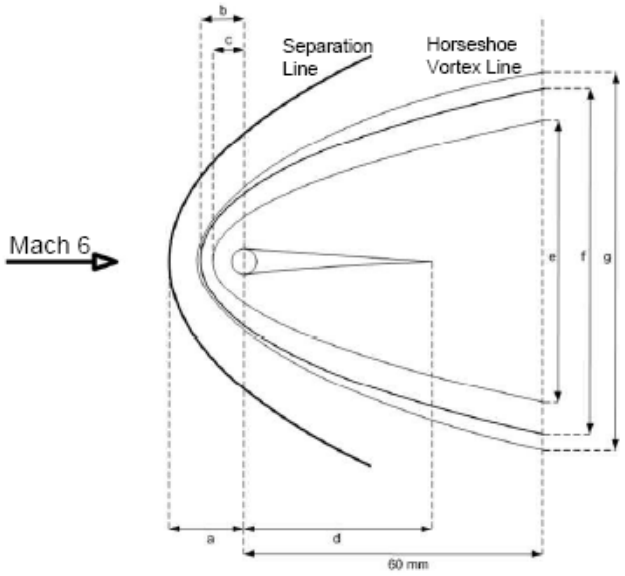


**Figure 5.11:** Main flow topology of gas injection into hypersonic cross flow; top view

| Case | Pr. Ratio | a | b | c | d | e | f | g | b-c | f-e |
|---|---|---|---|---|---|---|---|---|---|---|
| A | 169.0 | 12.20 | 7.90 | 4.60 | 43.55 | 33.70 | 45.75 | 52.65 | 3.30 | 6.90 |
| B | 135.9 | 10.80 | 7.90 | 4.50 | 44.40 | 30.95 | 42.90 | 50.65 | 3.40 | 7.75 |
| C | 102.4 | 11.35 | 7.13 | 4.40 | 37.60 | 28.60 | 39.45 | 46.50 | 2.73 | 7.05 |
| D | 67.0 | 9.75 | 6.05 | 4.30 | 35.10 | 24.75 | 34.75 | 41.30 | 1.75 | 6.90 |
| E | 34.2 | 4.70 | 4.00 | 2.50 | 30.00 | 20.50 | 28.50 | 35.40 | 1.50 | 6.90 |

**Table 5.1:** Test matrix for gas injection into Mach 6 cross flow; all dimensions in mm.

ratios higher than 130. The thickness of the horseshoe vortex downstream of the injection point ($f - e$ in Table 5.1 and Fig. 5.11) is independent of the pressure ratio.

### 5.3.2 Comparison with 3-D Obstacles

The relatively thick boundary layer of a hypersonic flow regime plays a central role in the micro-aerodynamics and thus a precise characterization of its state is very important for the design of a space vehicle. One of the main characteristics of the boundary layer is whether it is laminar or turbulent; with the main concern being the precise prediction of the aerodynamic drag. With the modern development of hypersonic vehicles, the efforts dedicated to the study of transition prediction have been intensified. Indeed, the convection heat-flux to the surface is a major issue for the design of a hypersonic vehicle and its thermal protection system (TPS). In this view, boundary-layer transition can have a dramatic effect, increasing surface heat-load by a factor of more than three. The lack of reliable methods for accurate transition predictions obliges vehicle designers to use a conservative approach and thus to oversize the thermal protection system. An unexpected early transition can be caused by surface roughness or damaged tiles of TPS, resulting in disastrous accidents such as the Columbia space shuttle crash. Furthermore, turbulent transition has also an important impact on vehicle aerodynamic performances, affecting vehicle drag, inducing aerodynamic stability degradation, lateral trim loads increase and potentially large vehicle impact dispersions [88, 116, 117, 122]. Because of all these considerations, it is of utmost importance to understand the flow topology around a 3-D rigid boundary (such as an isolated or distributed roughness element) within a hypersonic crossflow. Because of these reasons, the effects of 3-D rigid obstacles[1] in Mach 6 cross flow is studied by [143] in the H-3 wind tunnel facility of the von Karman Institute. The main results are discussed here for a comparison of the flow topology between liquid injection and 3-D obstacles within Mach 6 cross flow, exactly under the same conditions of the same wind tunnel.

The two main 3D roughness geometries considered, the cylinder and the ramp,

[1] also called "roughness elements"

are described in Fig. 5.12 with their geometrical parameters and reference points. The cylinder has a diameter $a$ of 4mm and a height $k$ of 1mm; whereas the ramp geometry has a height $k$ of 0.8mm and a frontal width $a$ of 0.8mm.

The ramp roughness element, shown in Fig. 5.12, is tested at the H-3 wind tunnel facility, using both sublimation and oil flow visualization techniques. The sublimation and the oil flow visualization pictures are shown in Fig. 5.13 and Fig. 5.14, whereas a close up view of the oil flow visualization close to the ramp element is presented in Fig. 5.15. In both Fig. 5.13 and Fig. 5.14, it is possible to detect the starting point of the secondary vortices, next to the main vortex pair [143].

Figure 5.15 yields the details on vortex formation which is specific to ramp geometry. Just downstream of the roughness element, one can notice a Y pattern taking place at the convergence point between the two structures emanating from the roughness sides. The comparison of oil flow visualization with sublimation and quantitative infrared thermography pictures [143] shows that a weak thermal footprint region takes place just downstream of the Y pattern. From this observation, a local detachment region can be suspected. It is important to mention that an excellent repeatability of this oil pattern has been obtained. The plot in Fig. 5.15 (bottom) presents a schematic of the observed oil pattern. Looking at the down-

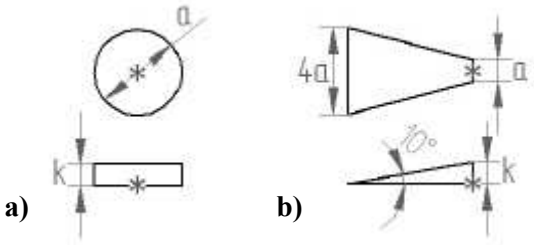


**Figure 5.12:** 3-D Roughness Elements: a) Cylinder b) Ramp

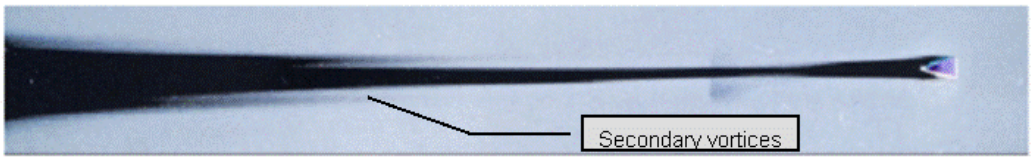


**Figure 5.13:** Sublimation picture of flow past 3D ramp

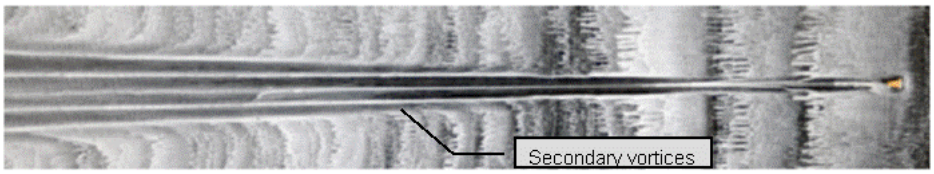


**Figure 5.14:** Oil visualization picture of flow past 3D ramp

stream direction, the expected rotational direction of the vortices just downstream of the ramp is presented on the left side as expected due to the compression of the flow passing the ramp and the resulting pressure gradient. The thick line shows the previously described Y structure but other V structures are observed downstream of the Y pattern. The orientation of the V patterns, sharp on the upstream side, shows that the visualization oil particles diverge from the wake axis, leading to the presentation on the right side of the rotational direction. This oil pattern interpretation shows a mismatch between the rotational direction of the vortices upstream and downstream of the Y structures. This mismatch is further analyzed through CFD results [2] [151], where the vortex pair generated just downstream of the 3-D ramp separates from the surface and lifts off, creating another vortex pair attached to the surface but rotating in the opposite direction, as shown in Fig. 5.16. This point, where the first vortex pair lifts off and creates a counter-rotating vortex pair

[2] by the Navier-Stokes solver LORE of L. Walpot

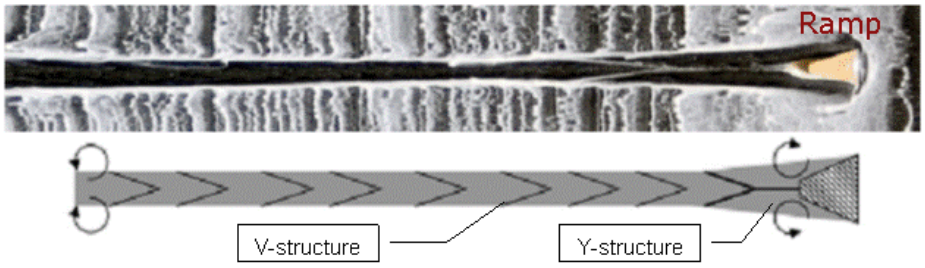


**Figure 5.15:** Schematic of oil visualization topology (down) compared with the oil flow visualization photograph (up); Mach 6 flow past 3D ramp (after [143])

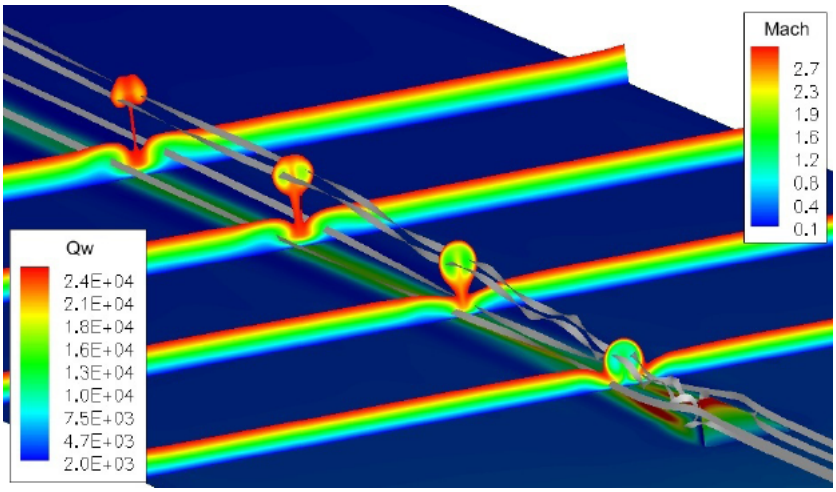


**Figure 5.16:** CFD Visualization of the flow structure downstream of a ramp roughness element (after [143])

corresponds to the end of Y-structure and beginning of V-structure shown on Fig. 5.15. In Fig. 5.16, one can clearly observe four vortices shown by the ribbons and their evolution. The boundary-layer in term of normalized total enthalpy is also plotted in the background. Variation of the skin friction coefficient from the same CFD calculation is shown in Fig. 5.17, in comparison with oil flow visualization lines, which are formed by the skin friction shear force [143, 151].

Another 3-D obstacle geometry that is studied is a cylinder with a diameter of 4mm and a height of 1mm (see Fig. 5.12). This geometry, which is significantly bigger than the ramp geometry, is preferred for comparison with liquid injection. Figure 5.18 presents the oil flow visualization (lower right corner) and sublimation photographs (bigger picture) of the Mach 6 flow past the cylinder obstacle. The oil flow picture stresses the skin friction contours, whereas the sublimation picture stresses heat flux contours. The colored lines on the sublimation picture, labeled as K between 30% and 110%, represent the heat flux measured experimentally using

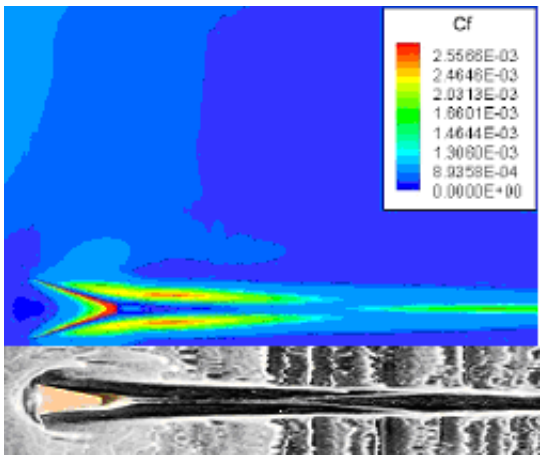


**Figure 5.17:** Comparison of CFD skin-friction distribution with oil flow visualization; Mach 6 flow past 3D ramp (after [143])

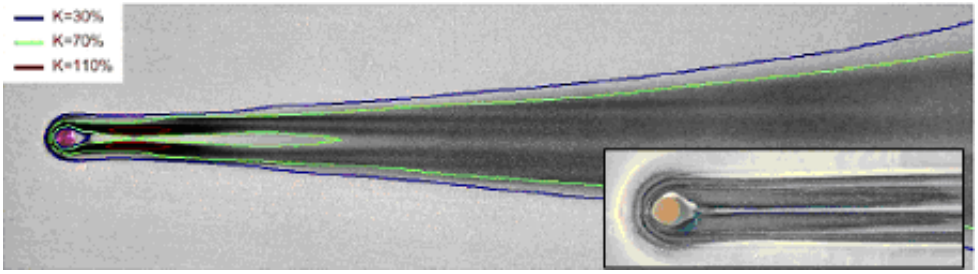


**Figure 5.18:** Oil flow visualization (lower right corner) and sublimation test picture compared to laminar (30%), transitional (70%), turbulent (110%) heat flux contours; for Mach 6 flow past a cylindrical obstacle (after [143])

infrared thermography as a function of the theoretical turbulent heat flux level [143]. In other words, regions having K below 30% represent laminar flow, regions having K below 70% represent laminar-transitional flow, and regions having K above 70% represent transitional-turbulent flow. The extreme level of 110% is chosen to indicate regions that are fully turbulent, chosen to be higher than 100% on purpose in case of a possible mismatch between the experimental and theoretical turbulent heat flux levels.

The definition of K is shown in Eq. 5.1. The numerator is the difference between the experimentally measured heat flux and the theoretical laminar heat flux. The denominator is the difference between the theoretical turbulent heat flux and the theoretical laminar heat flux. The 110% heat flux level is only observed in the close vicinity of the cylindrical element and up to five diameters downstream of it, on the sublimation picture of Fig. 5.18. The symmetric distribution of 110% heat flux contours suggests the presence of a vortex pair. In between and also downstream of 110% heat flux levels, one can observe a widening region covered by 70% (transitional) heat flux contour, which is a recirculation region. This recirculation region is also observed in the case of liquid injection (see Fig. 5.1 and Fig. 5.2), although the dimensions are not identical. Further downstream of the recirculation region, one can notice the widening of the wake region, which is again similar to the case of liquid injection, and also the starting of secondary vortices, which is similar to the case of gas injection (see Fig. 5.11, Fig. 5.13 and Fig. 5.14).

$$K(\%) = 100\frac{Q_{Exp} - Q_{ThLam}}{Q_{ThTurb} - Q_{ThLam}} \tag{5.1}$$

The vortex lift-off phenomenon mentioned for the ramp geometry (see Fig. 5.16) is also noticed for the cylindrical roughness element. The flow structure can be observed on Fig. 5.19 where flow streamlines and boundary-layer normalized total enthalpy profiles are plotted in planes perpendicular to the flow direction at different stations located at $\Delta x$ distance downstream of the roughness element location. The creation of many structures around the cylinder is confirmed as well as the vanishing of some of them downstream. Note that the lifting velocity of the detaching vortices is comparable to the ramp case, Fig. 5.16, keeping in mind that the ramp geometry is smaller than the cylinder, which has a wider wake.

## 5.4 Discussion

The double vortex observed during the flow topology tests of liquid injection into Mach 6 cross flow (see Fig. 5.5 and Fig. 5.6) is a phenomenon that is observed in various *Jets In Cross Flow* studies. Although no open literature is witnessed mentioning such a phenomenon for the case of liquid injected into hypersonic cross flow, the existence of a *counter-rotating vortex pair* is well documented in literature. Considering a (gas) jet exhausting into a cross flow, it generates a complex flowfield

with several distinguishable features. When the jet exits the injector, it is deflected by the freestream to follow a curved path downstream while its cross-section changes. For the case of a circular jet, the jet flow spreads laterally into an oval shape, thanks to the existence of the aerodynamic shear force created by the cross flow. At the same time, the cross flow shears the jet fluid along the lateral edges downstream to form a kidney shaped cross-section. At increasing distances along the path this shearing folds the downstream face over itself to form a vortex pair which dominates the flow as already shown in Fig. 5.7 [91].

Some of the earliest studies of this flow field [34] identified the formation of a counter-rotating vortex pair (CVP) flow structure, which was observed to dominate the cross-section of the jet, particularly in the far field (e.g. beyond 5–10 diameters downstream of injection). These time-averaged vortical structures are suggested to be associated with enhanced overall mixing efficiency for the transverse jet as compared with the free jet or mixing layer [30]. A schematic diagram of the global or mean flow features of the single jet in crossflow was provided in Fig 1.1 in Chapter 1. While the global features of the transverse jet can be understood and predicted in terms of the dynamics of the CVP, the generation and evolution of these vortical structures is a topic that is discussed by many investigators. Broadwell and Breidenthal [23] suggest that the CVP arises from the impulse associated with the jet and thus is a global feature of the far field, in which the CVP is convected downstream

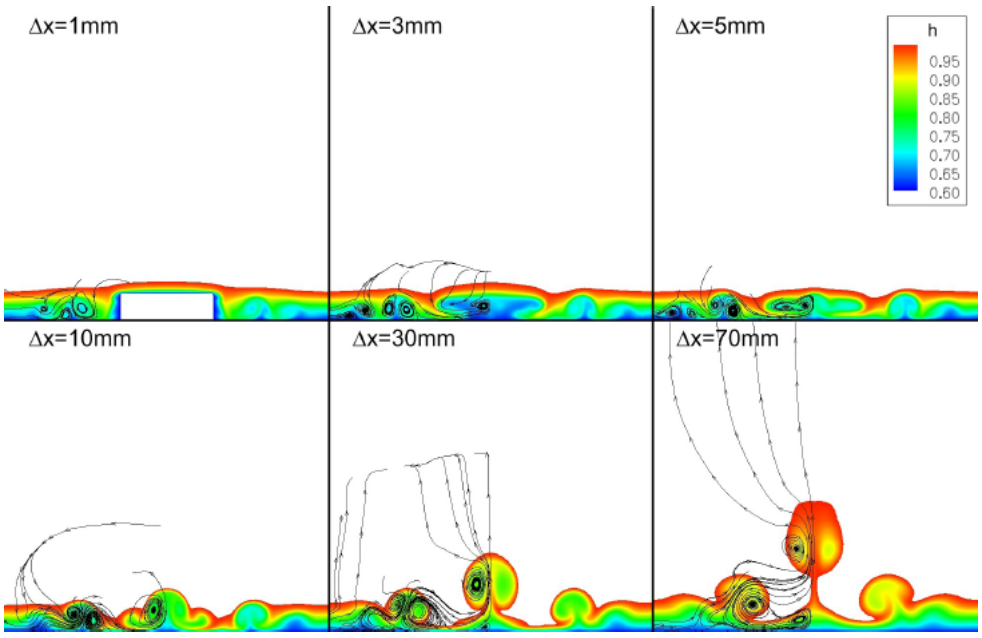


**Figure 5.19:** CFD simulation for cylindrical roughness in Mach 6 flow: Flow streamlines and normalized total enthalpy in planes perpendicular to flow direction at $\Delta x$ distances downstream of roughness location (after [143])

by the crossflow. Karagozian [64] was able to use vorticity associated with the jet impulse as well as that generated by deflection of the cross flow about the jet in the near field to predict average vortex pair strength, jet trajectories, and reaction lengths. The recent experiments of Kelso et al. [70] in both water and air suggest that periodic vortex ring roll-up from the nozzle occurs for the jet in cross flow, yet superposed on this process is a re-orientation of this shear layer vorticity imposed by the cross flow, which leads to a folding of the cylindrical vortex sheet. The superposition of these two mechanisms results in the interpretation of the evolution of the jet shear layer vortex rings as shown in Fig. 5.20(a), where there is a tilting of the upstream portion of the ring oriented with the mean curvature of the jet, and a tilting and folding of the downstream portion of the ring aligned with the direction of the jet. The re-orientation of the shear layer that is seen to lead to this tilting is shown schematically in Fig. 5.20(b). It is this tilting and folding which is thought to contribute to the circulation of the CVP. The experiments of Kelso [70] suggest, for example, that *the shear layer of the jet folds and rolls up very near to the pipe exit, leading to or contributing to the formation of the CVP*. It should be noted as well that two recent experimental investigations [132, 76] suggest that, instantaneously, the CVP can be either symmetric or asymmetric in shape under specific circumstances, and that end views of the jet in the far field can reveal axisymmetric as well as sinusoidal motion of the CVP [30].

The counter-rotating vortex pair is responsible from the formation of other vortical structures. The lift-off of vortices described for a flow past 3-D rigid obstacles is a phenomenon also observed for jet injection in cross flows. A study concerned with a circular jet of fluid injected normal to a very deep, broad stream and the

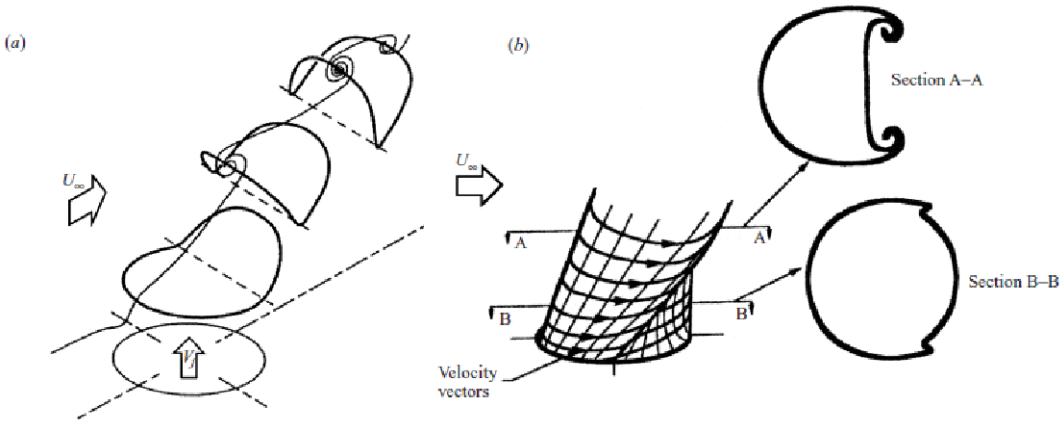


**Figure 5.20:** The interpretation for shear layer evolution in the transverse jet: (a) isometric view of the jet shear layer vortex rings, showing how they tilt and fold as they convect downstream, and (b) schematic diagram of the reorientation of the shear layer vorticity, leading to the folding of the cylindrical vortex sheet [70]

subsequent jet deflection and shape change of the separation boundary between the jet and the freestream fluid was performed by Chang [28]. Figure 5.21 presents the deformation of the boundary of such a jet, computed by Chang. Selected cross-sections were scaled to the distance traveled using the jet velocity and are shown on Fig. 5.21 for a distance of seven diameters ($\xi/D$). The roll-up of the jet efflux

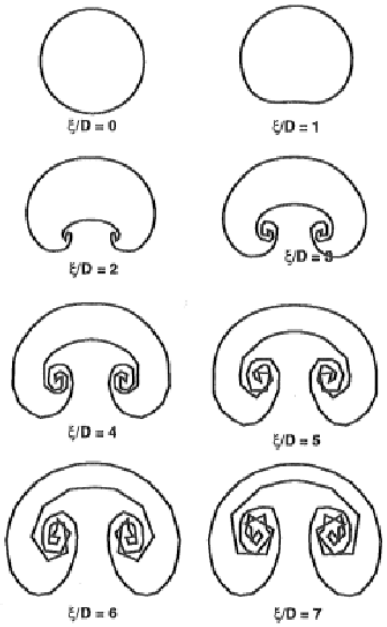


**Figure 5.21:** Selected cross-sections for the roll-up of a jet in cross flow into a vortex pair obtained from a Chang potential flow calculation [28]

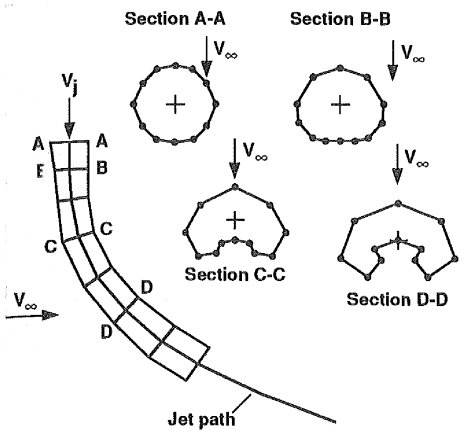


**Figure 5.22:** Representation of a jet wake with a changing cross-section (after [28])

into a vortex pair which is deflected downstream by the freestream flow is the primary contribution of the calculation of Chang. An empirically determined jet path was used to locate the jet efflux cross sections at varying (time marched) distances downstream as shown qualitatively on Fig. 5.22. These two Figures explain the formation of the counter-rotating vortex pair and the lift-off of wall-bounded vortices, creating secondary vortices not only for flows past rigid obstacles but also for liquid jet injection cases. Finally, one can conclude that the counter rotating vortex pair, the separated flow region (including the separation shock) and the horseshoe vortex are the most important common vortical structures appearing in all liquid, gas and 3-D obstacles exposed to hypersonic cross flow.

# 6

# Atomization Measurements

The present chapter is devoted to the presentation of the Phase Doppler Interferometry (PDI) measurements performed to determine the distribution, mean and Sauter Mean Diameter ($D_{32}$) of droplet dimensions. The atomization of a water liquid jet in Mach 6 air cross flow is investigated in this Chapter. Experiments are conducted in the VKI H3 Mach 6 hypersonic wind tunnel. A flat plate, with a flush mounted 1mm diameter circular injector, is used to inject water into the crossing hypersonic air stream. The experimental procedure is explained in Section 6.1. The distributions of the liquid droplet sizes are measured at different locations along the median plane on the jet using Phase Doppler Interferometry technique. The droplet size measurements are analyzed and treated to characterize the atomization process of the liquid jet. The calculated mean and Sauter diameters are compared with the existing correlations in the literature, as presented in Section 6.2.

## 6.1 Experimental Procedure

All experiments have been performed in the H3 Hypersonic Wind Tunnel of the von Karman Institute. The wind tunnel model to be tested is kept retracted before the test to avoid blockage of the wind tunnel and also to avoid excessive heating of the model during start-up. The test chamber is vacuumed prior to the test using a supersonic ejector. The model is injected into the flow field with a model injection arm, once the Mach 6 flow is fully established in the test chamber. Within this campaign, all experiments are performed at a stagnation pressure of 20bar ($\pm 0.3 bar$) and a stagnation temperature of 500K ($\pm 20K$), resulting in a unit freestream Reynolds number of $17 \times 10^6 m^{-1}$. Experiments have been carried out over a 230mm x 80mm flat plate with sharp leading edge. The Flat Plate is provided

with a 1mm diameter circular water injector for water injection. The main water supply is connected directly to a rotameter (L63/2400-16862 model) that is used to control and monitor the mass flow rate of injected water. With a manual valve it is possible to adjust the mass flow rate, therefore the velocity and the dynamic pressure of the water jet. Along its path, the pipe connecting the rotameter with the injector of the flat plate is covered with a solenoid resistor in order to heat the water. The heating of the water is necessary to prevent the formation of ice inside the test section due to the very low static temperature in the H3 wind tunnel (about 70 K). Detailed explanation of the test environment is presented in Chapter 3, with an emphasis on the Phase Doppler Interferometry setup in Section 3.3.7 [95].

Figure 6.1 shows a typical histogram of droplet diameters with the probability density function of the droplet size for a single test. To better investigate the particular distribution, a Log-Normal curve (bold line in Fig. 6.1) is fitted to the data set. A log-normal distribution is the probability distribution of a random variable whose logarithm is normally distributed. Although there is no theoretical model that can predict the parameters of the expected log-normal drop size distribution, the log-Normal fit is used for describing the droplet size distribution in sprays based on probability considerations [78]. The probability density function (PDF) for a log-normal distribution is given as:

$$PDF(n) = \frac{1}{dS\sqrt{2\pi}} exp\left(-\frac{(\ln d - \mu)^2}{2S^2}\right) \tag{6.1}$$

where n is the number of droplets having the diameter $d$. $S$ and $\mu$ are constants.

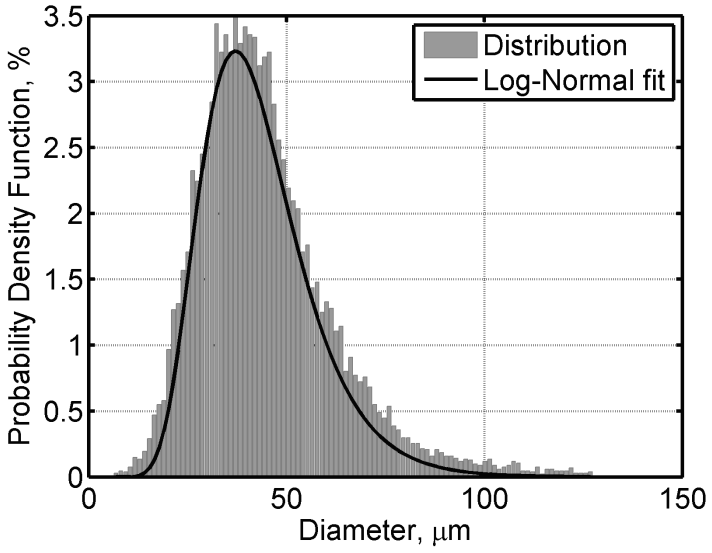


**Figure 6.1:** Log-Normal distribution of droplet diameter

Using $S$ and $\mu$, one can define the mean ($D_{10}$) and the standard deviation ($\sigma$) of the distribution using Eqn. 6.2 and Eqn. 6.3, respectively. Once the distribution of droplet diameters are known, the Sauter mean diameter can also be calculated statistically.

$$D_{10} = exp\left(\mu + \frac{S^2}{2}\right) \tag{6.2}$$

$$\sigma = \sqrt{exp(S^2 + 2\mu)exp(S^2 - 1)} \tag{6.3}$$

Figure 6.2 shows the evolution of the Sauter mean diameter (D32, see Eqn. 2.7) and the mean diameter (D10, see Eqn. 2.6) of the spray's droplets over the number of validated data points. It can easily be observed how the detected droplet

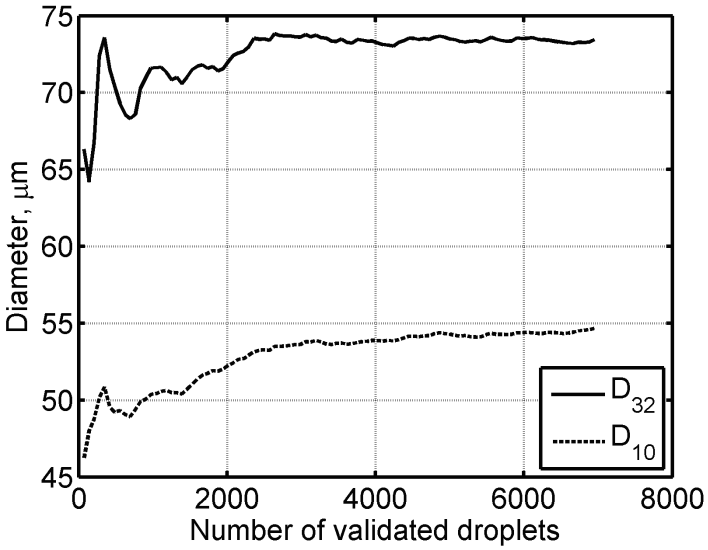


**Figure 6.2:** Convergence of Sauter mean diameter and mean diameter as a function of the number of validated droplet size measurements

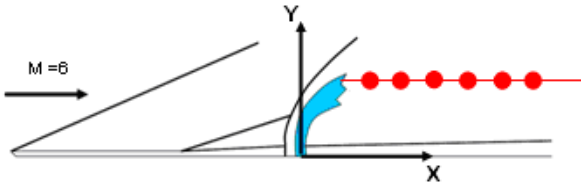


**Figure 6.3:** Probe volume position along x direction

size is oscillating at the beginning of the acquisition period, converging to a stable value after 3000 validated data points, for both mean and Sauter diameters. The test conditions are extremely difficult, as the test time is very short (maximum 10 seconds) due to the availability of compressed air, and the validation rate of the PDI system is usually less than 10% because of the non-sphericity of the droplets. Despite these facts, 3000 number of samples is accepted as the minimum number of points necessary per test condition to have a statistically meaningful result.

A first series of tests have been performed at y = 8mm above the flat plate. This first test campaign involves moving the probe volume position along the x direction between x = 14 mm and x = 35 mm downstream of the injector, as shown in Fig. 6.3, while the dynamic pressure ratio is kept constant at q = 4. A second test campaign has been made at a fixed probe volume position and for different levels of the dynamic pressure ratio q. A third test campaign has been made at x=35 mm and at varying heights from the flat plate, for different momentum flux ratios.

## 6.2 EXPERIMENTAL RESULTS

### 6.2.1 EFFECT OF DOWNSTREAM DIRECTION

The variation of the mean ($D_{10}$) and the Sauter Mean Diameter ($D_{32}$) of the droplets with respect to the distance from the injection point for a q=4 jet is presented in Fig. 6.4 and Fig. 6.5, respectively. All measurements are performed at 8mm above the wall, which corresponds to 40% of the overall penetration height at a downstream distance of $x/d_j = 35$. The definitions of the mean ($D_{10}$) and the Sauter Mean Diameter ($D_{32}$) were presented in Section 2.3, in equations 2.6 and 2.7.

Figures 6.4 and 6.5 show respectively how the Sauter mean diameter ($D_{32}$) and the mean diameter ($D_{10}$) decrease with increasing distance from the injection point,

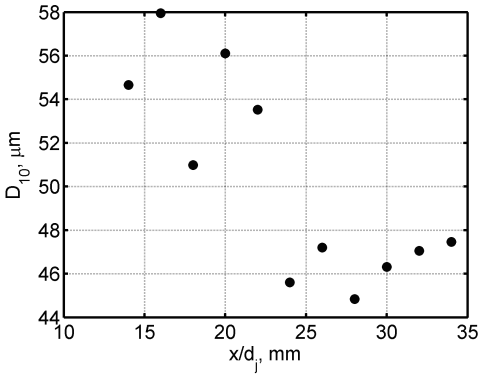


**Figure 6.4:** Mean diameter versus x-distance from the injector (y = 8mm, q = 4)

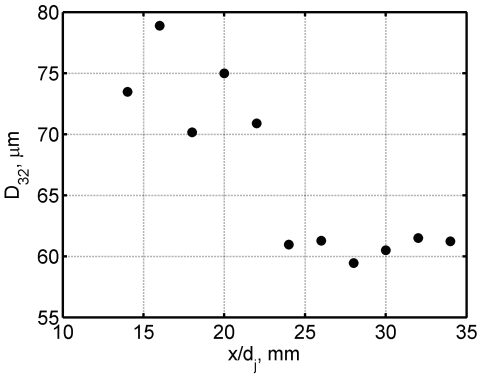


**Figure 6.5:** Sauter Mean Diameter versus x-distance from the injector (y = 8mm, q = 4)

for a constant momentum flux ratio of q = 4. Observing Fig. 6.5, the trend of the experimental data suggests a strong initial decrease of the $D_{32}$ with increasing x-distance from the injector until $x/d_j = 23$. Further downstream of this point, a constant value of $D_{32}$ is observed. This means that for the examined q = 4 liquid injection case, the final atomization diameter is reached at $x/d_j = 25$. The hypothesis is supported observing the experimental data concerning the mean diameter $D_{10}$ (Fig. 6.4), where a similar decreasing trend with that of Sauter mean diameter (Fig. 6.5) can be noticed [95, 94, 18].

The standard deviation of the experimental data can be calculated using the definition of statistical uncertainty, or by making use of Eq. 6.3. The plot of the standard deviation obtained as a function of the $x/d_j$ distance from the injector is shown in Fig. 6.6. The standard deviation represented in non-dimensional units on the y-axis of Fig. 6.6, is divided by each mean diameter value of the corresponding data set considered, thus corresponding to the percentage of the mean diameter. In other words, the standard deviation corresponds to the width of the distribution, for which an example is given in Fig. 6.1. A high standard deviation corresponds to a larger variety of droplet diameters, whereas a low standard deviation corresponds to mono-dispersed population of droplet diameters. As the ligaments are fragmented and as the droplets are atomized, a final droplet diameter is reached, which has a minimum standard deviation. The trend of Fig. 6.6 supports this hypothesis. The standard deviation of the droplet diameter distribution decreases with increasing downstream distance from the injection point. While looking at these plots, one should always keep in mind the high level of experimental uncertainty due to the high variety of droplet diameters that can be found in such an environment.

For $x/d_j = 35$ and at a height of 8mm above the flat plate, the variation of the

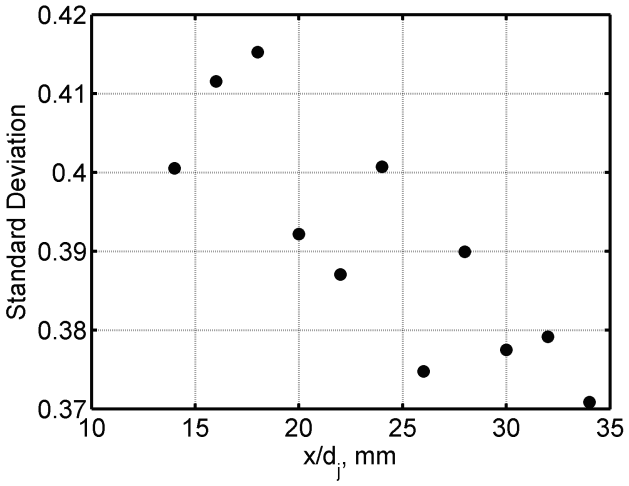


**Figure 6.6:** Standard deviation versus x-distance from the injector (y = 8mm, q = 4)

Sauter mean diameter and the mean diameter for different momentum flux ratio liquid injection cases are presented in Fig. 6.7 and Fig. 6.8, respectively. It is observed that both $D_{10}$ and $D_{32}$ are increasing with increasing momentum flux ratio, up to q=6. For the cases where the momentum flux ratio is greater than 6, the mean and Sauter mean diameters tend to stay constant.

### 6.2.2 EFFECT OF DISTANCE FROM THE WALL

A second experimental campaign [111] is carried out to check the trend of Sauter Mean Diameter with distance from the wall. All measurements are performed using the 1mm circular injector and at 35mm downstream of the injector. During this experimental campaign, the distance to the wall is changed between 5 and 13mm,

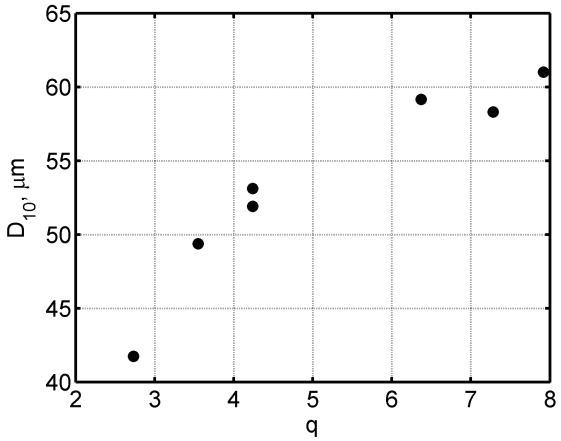


**Figure 6.7:** Mean diameter versus dynamic pressure ratio (x = 35mm, y = 8mm)

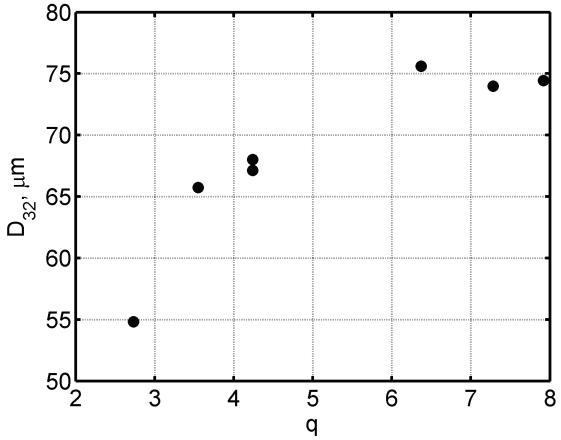


**Figure 6.8:** Sauter mean diameter versus dynamic pressure ratio (x = 35mm, y = 8mm)

| $q$ (-) | $y/d_j$ (-) | $y/\delta$ (%) | Counts | $D_{10}$ ($\mu m$) | $D_{32}$ ($\mu m$) | $\sigma$ ($\mu m$) |
|---|---|---|---|---|---|---|
| 3 | 5 | 27 | 13301 | 54 | 67 | 19 |
| 3 | 7 | 37 | 5459 | 48 | 58 | 12 |
| 3 | 9 | 48 | 1891 | 48 | 58 | 7 |
| 4 | 5 | 24 | 10193 | 67 | 83 | 14 |
| 4 | 7 | 34 | 4308 | 59 | 73 | 10 |
| 4 | 9 | 44 | 6275 | 57 | 70 | 11 |
| 5 | 5 | 23 | 11128 | 68 | 82 | 15 |
| 5 | 7 | 32 | 8911 | 68 | 82 | 13 |
| 5 | 9 | 40 | 5130 | 64 | 78 | 10 |
| 5 | 11 | 50 | 4511 | 55 | 68 | 9 |
| 7 | 5 | 21 | 11314 | 67 | 81 | 17 |
| 7 | 7 | 29 | 13399 | 67 | 81 | 18 |
| 7 | 9 | 37 | 4423 | 65 | 80 | 10 |
| 7 | 11 | 45 | 6770 | 65 | 79 | 11 |
| 7 | 13 | 54 | 2185 | 62 | 77 | 9 |

**Table 6.1:** Mean and Sauter Mean Diameter Test Matrix and Results

to investigate the effect of height on mean ($D_{10}$) and Sauter mean diameter ($D_{32}$) distributions. The test matrix and the results are shown in Table 6.1. The first column is momentum flux ratio (q), the second column is distance from the wall (normalized by the injector diameter, which is 1mm), the third column is the relative location of the measurement point with respect to penetration height (in percentage), the fourth column is the number of data points collected, the fifth column is the mean diameter ($D_{10}$), the sixth column is the Sauter mean diameter ($D_{32}$) and the last column is the standard deviation of the droplet size distribution. Typical uncertainties are $\pm 0.2$ for momentum flux ratio and $\pm 0.3mm$ for distance from the wall.

The outcome of the second test campaign is shown in Fig. 6.9 for q=4 and in Fig. 6.10 for q=7, where mean and Sauter mean diameter are plotted against distance from the wall. Both of these Figures, as well as the data presented in Table 6.1 shows a decreasing trend of $D_{32}$ as y, the distance from the wall, is increased. This is in agreement with the hypothesis that measuring the droplet size at a constant height from the wall despite the variation in momentum flux ratio (hence variation in penetration height) is not a proper selection. They are also in agreement with the data in literature [108, 109], which states that $D_{32}$ should decrease as one moves further away from the wall.

Table 6.1 presents a lot of interesting and valuable information. The fourth column presents the number of validated particles measured by the PDI system. As explained before, an effort is made to have a minimum of 3000 measurements per

point to have a statistically meaningful data set (see Fig. 6.2 and the associated discussion). Although this fact puts question marks on the validity of the (q=7, y=13mm=54% of penetration) and (q=3, y=9mm=48% of penetration) data sets, these measurement points are also included in the analysis as they agree well with the general trend. It can be noted that the number of validated measurements decreases significantly as the distance from the wall increases. This can be explained by the fact that the PDI system works only with spherical droplets. Close to the wall, where the cross flow velocity is low thanks to the bow shock with a 90 degrees to the flowfield, one can expect to find a bigger population of spherical droplets, which makes the life easier for the PDI system. On the contrary, the cross flow velocity becomes higher as one moves away from the wall, which increases the aerodynamic shear stress, which results in non-spherical droplets. Actually, the reason of not presenting any data above 50% of the penetration height for any momentum flux ratio condition is because no statistically meaningful data were obtained above the mentioned point. It is worth repeating at this point, that the core of the liquid flow (where the biggest population of water droplets is found) lies between 40% and 50% of the penetration height [16], as it was also shown by the probability density function (PDF) analysis in Section 4.5. The last important observation that can be drawn from the experimental data presented in Table 6.1 is that, mean diameter ($D_{10}$), Sauter mean diameter ($D_{32}$) and standard deviation ($\sigma$) decrease with increasing height, for a given momentum flux ratio. The descend in standard deviation means that a higher percentage of the droplets have similar size. At higher locations (such as 50% of the penetration height), the aerodynamic shear force is the dominant force that influences all of the liquid phase, which results in a *mono-dispersed* droplet size distribution with a relatively lower standard deviation. On the contrary, the regions close to the wall experience a re-circulating flowfield, where there is no single dominant force. This, obviously, results in a wider variety of droplet dimensions, thus a relatively higher standard deviation.

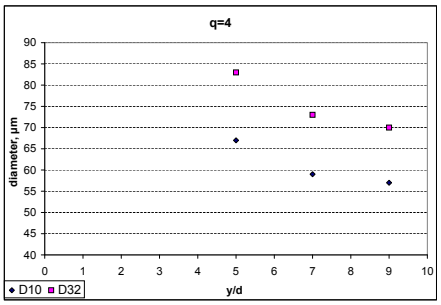


**Figure 6.9:** Mean and Sauter mean diameter versus distance from wall (x = 35mm, q = 4)

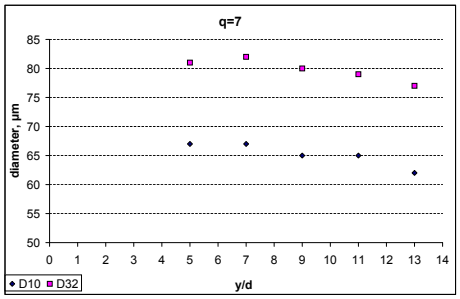


**Figure 6.10:** Mean and Sauter mean diameter versus distance from wall (x = 35mm, q = 7)

## 6.3 Discussion

The evolution of mean and Sauter mean diameters as a function of distance from the injection point is as expected. The diameter decreases asymptotically moving downstream of the injection point and eventually it reaches a constant value. This is an indication that the atomization process is completed at one point and downstream of this point, the mean or Sauter mean diameters do not change. This observation is also supported by the fact that the standard deviation of droplet diameter decreases with x, meaning that more droplets have diameters equal to or close to the measured mean diameter value. On the other hand, the behavior of mean and Sauter diameters as a function of momentum exchange ratio q is open to discussion. Several works on liquid atomization in compressible crossflows [80, 57, 50] suggest that the final Sauter mean diameter can be expressed as a function of Weber number and Reynolds number. The general form of this expression is shown in Eq. 2.8, where Re is the Reynolds number of the injected liquid based on the injector diameter and We is the Weber number. A more explicit form of the relation is shown in Eq. 6.4.

$$D_{32} = D_0 \left( \left( \frac{\rho_\infty d_j (U_\infty - U_j)^2}{\sigma_j} \right) \left( \frac{\rho_j d_j U_j}{\mu_j} \right) \right)^{-n} \tag{6.4}$$

where $D_0$ and n are constants. $D_0$ is taken as the injector diameter (1000$\mu$m in this case), and n is calculated to be 0.16 based on the experimental data, such that $D_{32}$ is in $\mu$m. These coefficients are in agreement with the data in the literature [80, 57, 50]. However, the proposed correlation between $D_{32}$ and the governing non-dimensional coefficients does not support the outcomes of Fig. 6.8, where the Sauter mean diameter is observed to be increasing with increased momentum flux ratio. Indeed, the momentum flux ratio can only be increased by increasing the liquid

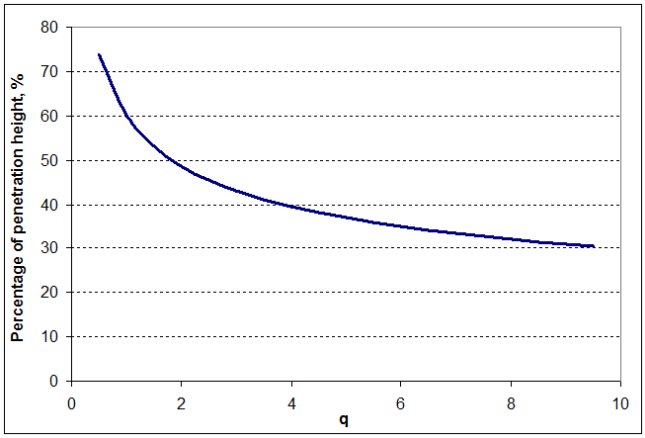


**Figure 6.11:** Relative penetration height $y/\delta$ for y = 8mm and x = 35mm

jet velocity; which would increase the $We.Re$ term in Eq. 2.8, as $U_\infty$ is always much bigger than $U_j$. The observation of $D_{32}$ decreasing with increasing momentum flux ratio is also documented by [108, 109]. This discrepancy in the measurements can be explained with the fact that all measurements are taken at a single location, at x = 35mm and y = 8mm, no matter what the momentum flux ratio is. However, it should be considered that both the starting location of the atomization zone, and also the penetration height of the liquid are proportional to the dynamic pressure ratio. The relation between dynamic pressure ratio and penetration height, $\delta$, is given in Eq. 4.3 [16]. The penetration height increases significantly with q, thus the relative location of the measurement point $y/\delta$ (for y = 8mm for all cases) changes also significantly, as presented in Fig. 6.11, for the range of q studied in this campaign [95]. Similarly, the relative location of the measurement point $y/\delta$ (for y = 8mm for all cases) is presented in Fig. 6.12, as a function of downstream distance.

As the momentum flux ratio q is increased during the test campaign, the measurements taken at $y = 8mm$ above the flat plate should be seen as measurements taken at lower heights. This can be explained as the reason for the unexpected increasing of $D_{32}$ with momentum flux ratio. Indeed, the Sauter mean diameter is expected to decrease as y is increased [108, 109]. For a correct measurement campaign, one should always take measurements at the same relative position, preferably in the plume region, where the diameter of droplets is expected to be minimum [109, 85]. The plume (or the core) of a liquid jet corresponds to the height where the liquid population is at a maximum [16], or it is the area where the liquid volume flux is greater than a certain value [85]. Typically, the plume is between 40% and 50% of the penetration height [16].

Despite the expected trend of $D_{32}$ decreasing with increasing height from the wall, there is not sufficient data to prove that the Sauter mean diamater is inversely proportional to the multiplication of Weber and Reynolds numbers, as suggested

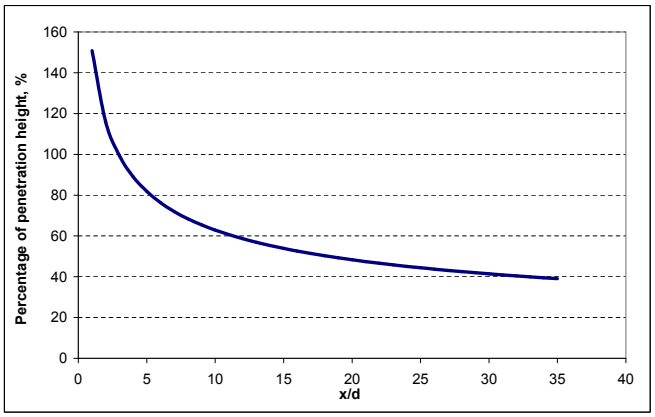


**Figure 6.12:** Relative penetration height $y/\delta$ for y = 8mm and q = 4

in Eq. 2.8. Figure 6.13 presents a different interpretation of the data presented in Table 6.1. The $D_{32}$ at certain percentages of the penetration height (namely at 50%, 37% and 27%) are interpolated within the existing data. The variation of $D_{32}$ as a function of q and at the prescribed relative distance from the wall are plotted in Fig. 6.13. This plot shows that the $D_{32}$ increases with increasing q even if one considers the same relative location for all measurements, which is in contradiction with the models existing in literature. The reliability of the data presented in Fig. 6.13 is open to discussion as the number of data points used in interpolation is extremely low to have a sound conclusion. Nevertheless, this also means that the presented assumptions for modeling of the $D_{32}$ distribution are not sufficient, even if they are necessary. The main assumption was that increasing momentum flux ratio q would only be possible by increasing liquid jet velocity, which would also increase the $We.Re$ term in Eq. 2.8 or Eq. 6.4. However, the complexity of the overall flow field is shown in the preceding Chapters, which indicated that the liquid phase can influence the gas flow field, whereas the contrary is also correct. This means that liquid injection into a hypersonic cross flow is a very complex flow field where there is a continuous interaction between the two phases, resulting in fragmentation, atomization, shock – shock interaction, shock – boundary layer interaction and a complicated vortex field. Increasing the liquid jet exit velocity (or the momentum flux ratio) also increases the penetration height, which influences the shape and thus the slope of the bow shock upstream of the liquid phase. The change in the slope of the bow shock results in a considerable change in the cross flow velocity, or $U_\infty$ in Eq. 6.4. Increasing the liquid jet velocity $U_j$ causes a decrease in the cross flow velocity $U_\infty$ at a certain percentage of the penetration height. This results in a decreasing $\Delta U = U_\infty - U_j$ with increasing q; explaining the increasing $D_{32}$ by increasing q, using Eq. 2.8 or Eq. 6.4.

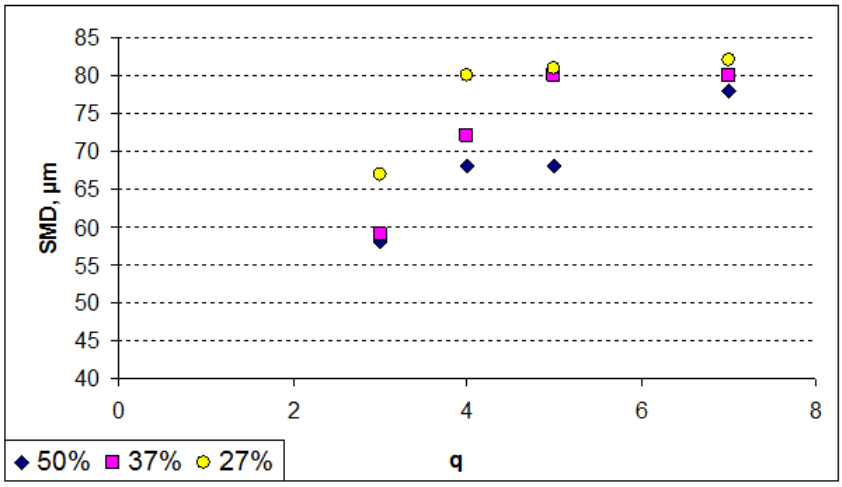


**Figure 6.13:** Variation of Sauter Mean Diameter against q, for certain relative height from the wall

The effect of changing the mass flow rate of liquid, or the momentum flux ratio, on the flow topology can be seen on the schlieren images presented in Fig. 4.8, where the schlieren images are presented for q = 10 and a q = 2 cases. It is already well known that the penetration height increases with the increasing momentum flux ratio, q. However, Fig. 4.8 shows that the shape and the local angle of the bow shock just upstream of the injection point changes as well. Figure 6.14 compares the angle of the bow shock wave as a function of distance from the wall for q = 2 and q = 10 cases. Although the freestream conditions are similar for both cases, the difference in the angles of different momentum flux ratio cases causes a considerable difference in the local conditions. The shock wave angle is 65 degrees for q = 2 at y = 8 diameters downstream location, whereas it is 74 degrees for q = 10 case. Calculating the post-shock conditions, it is observed that the Mach number reduces to 2.57 (local velocity is 1080 m/s) for q = 2, whereas the post-shock Mach number is 1.70 (local velocity is 715 m/s) for q = 10 case. The injection velocity of the liquid is 12 m/s for q = 2, whereas it is 25 m/s for q = 10 case. Based on all these velocity values for the extreme cases of q = 2 and q = 10, it is worth re-checking the dependence of $D_{32}$ on $We.Re$ term. Up to now, the $U_\infty$ term was always kept out of the analysis keeping in mind that the freestream velocity is always kept the same. However, one should rather be focusing on local conditions where the atomization is taking place. It is not appropriate to assume that the liquid droplet at 35 injector diameter downstream location is directly influenced by the freestream velocity, ignoring the effect of the shock-wave system. Thus it is recommended to replace the $U_\infty$ term with $U_g$ term, corresponding to the velocity of the gas (air) phase at the interrogated location. By similar reasoning, the density term $\rho_\infty$ should be replaced with $\rho_g$. A second criticism can be made for the Reynolds number term in Eqn. 6.4, which is based on liquid properties. This term considers the speed of the liquid (which is always assumed to be the injection speed) alone, and thus ignores the fact that the main mechanism causing atomization is the aerodynamic

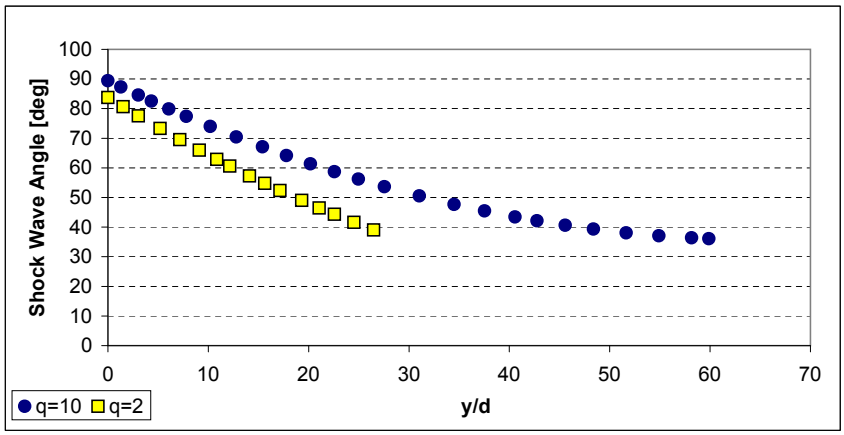


**Figure 6.14:** Variation of bow shock angle

shear force. As aerodynamic shear force is a function of the difference in velocity, one should consider the relative velocity, which is the difference in velocity between the gas and liquid phases. Thus, it is recommended to replace $U_j$ term with $U_g - U_j$ term in the definition of the Reynolds number. Plugging all these recommendations into Eqn. 6.4, the new proposal for the modeling of $D_{32}$ is expressed as

$$D_{32} = A.D_0 \left( \left( \frac{\rho_g d_j (U_g - U_j)^2}{\sigma_j} \right) \left( \frac{\rho_j d_j (U_g - U_j)}{\mu_j} \right) \right)^{-n} \tag{6.5}$$

where $D_0$ is the initial diameter (1 mm for this case), subscript $g$ corresponds to the local gas (air) conditions and subscript $j$ corresponds to liquid jet conditions. $A$ and $n$ are empirical constants. Replacing the terms with their corresponding values ($d_j = 10^{-3}m$, $\rho_j = 10^3 kg/m^3$, $\rho_g = 0.4 kg/m^3$, $\mu_j = 10^{-3} kg/(m.s)$ and $\sigma_j = 7.2 \times 10^{-2} N/m$) and proposing the empirical constants of $A = 2.2$ and $n = 0.16$ (by curve fitting to the experimental data); one obtains a distribution of $D_{32}$ ranging between $60\mu m$ and $75\mu m$ in the range of q = 2 and q = 10, which is in agreement with the measured values of $D_{32}$ in the same range, as presented in Fig. 6.8. This agreement supports the hypothesis that the local conditions should be considered for the cross flow and the Reynolds numbers should be based on the relative velocity between the gas and liquid jet phases.

A final criticism is on the validation rate of the PDI system. A typical validation rate at low speed (subsonic) conditions is higher than 70%, whereas the validation rate has been around 10% at hypersonic conditions studied in this thesis. This means that only 10% of the received signals are accepted to have a certain signal to noise ratio above the threshold. Although it would be possible to reduce this threshold to increase the validation rate, this is not done following the advice of the experts from Atrium (the company of the PDI system) as reducing the threshold would increase the noise level. The 90% of the signal are believed to be originating from non-spherical droplets. If this hypothesis is correct, the fact that there are non-spherical droplets is an indication that the atomization process is not complete yet. The size of the droplets in a completely atomized zone should be small enough not to allow the presence of non-spherical droplets or ligaments. However, to the best knowledge of the author, it is still not known at which diameter the droplets would become spherical at hypersonic cross flow conditions. All the previous findings, such as the variation of mean and Sauter mean diameters or the variation of standard deviation with downstream distance show that the distribution of measured droplets remain constant, indicating a balance between the aerodynamic shear force and the surface tension of the liquid. The measured droplet dimensions can also be well represented by the existing theoretical models based on local Weber and Reynolds number. Considering all these facts, the low validation rate of the PDI system should be taken as an indication that the accuracy of the measured droplet dimensions is open to discussion. Although the PDI technique does not seem to be well adapted

for hypersonic conditions, it is thought as a promising technique for the future considering the advances in optical technology.

# 7
# Fragmentation Tests

The work described in this chapter is a continuation of the investigations carried out in the previous Chapters, focusing not on the jet behavior, but on the break-up mechanism of the liquid exposed to hypersonic flow conditions. Figure 7.1 [94] presents the main features of liquid injected into compressible flow in a very simple way. There are two main processes that are experienced by the liquid: fragmentation and then atomization. The experimental study of liquid injection into hypersonic cross flow has created a quasi-steady flow field where many phenomena, including the atomization of liquid, could be investigated. However the initial break-up of the liquid jet before atomization could not be investigated because of the continuous injection of liquid into the flow field. This is seen as a missing point in the overall analysis. The main mechanisms yielding to the fragmentation of liquid into water chunks and to ligaments can not be observed well in the liquid injection experiments. To investigate the fragmentation physics, a new experimental procedure has been applied. The experiments involve the use of a balloon filled with water exposed to hypersonic cross flow at Mach 6. With this procedure it is possible to study the behavior of a single mass of water suddenly exposed to hypersonic flow under different boundary conditions. Compared to the continuous liquid jet injection tests, balloon tests provide a transient event. A high speed movie is recorded for each test and all the frames are post-processed by a set of algorithms developed for the mentioned purposes. This test case can also be seen as an experimental validation case for possible CFD applications where a sphere of liquid is suddenly exposed to hypersonic flow. The details of the experimental procedure are given in Section 7.1. The phenomenon of fragmentation and the effect of the shock wave system on fragmentation are discussed in Section 7.2. Finally, the motion of water chunks or droplets during fragmentation are analyzed in Section 7.3, where the techniques such

as *snake movement algorithm* or *time interpolation by discrete cosine transformation* are described.

## 7.1 EXPERIMENTAL PROCEDURE

Liquid fragmentation tests are simply performed by exposing a water-filled balloon to Mach 6 flow and taking measurements while the balloon bursts and the water is fragmented by the hypersonic cross flow. Two different supports are used as explained in Section 3.2.2, a sharp leading edge support and a blunt leading edge support. The first experiments are performed using the sharp leading edge support. Witnessing a complex interaction between the leading edge shock of the sharp support and the liquid phase, a second test campaign is carried out with the blunt support, which has a detached normal shock wave that has less interference with the liquid phase. Both supports are used in combination with the high speed camera to study the fragmentation physics of the water, under different boundary conditions. The procedure starts with a balloon filled with about 3 g of water, fixed on one of the two supports and mounted inside the test section of the wind tunnel. To assure the repeatability of the tests and the maintain a tight skin of the balloon, the balloon is twisted so that the rubber surface of the balloon is stretched. Although it has not been possible to measure how tight the balloon skin is, experience gained during testing has shown that the tightness of the skin is important for the success of the test. Especially during the first trials, some tests failed because either the balloon bursts before it reaches the centerline of the air stream, or it does not burst at all. Selected experiments are shown in Table 7.1, where the test number, type of the support used (sharp or blunt leading edge), test technique, image resolution, mass of water in the balloon, frame rate, exposure time and the focal length of the lens used are given.

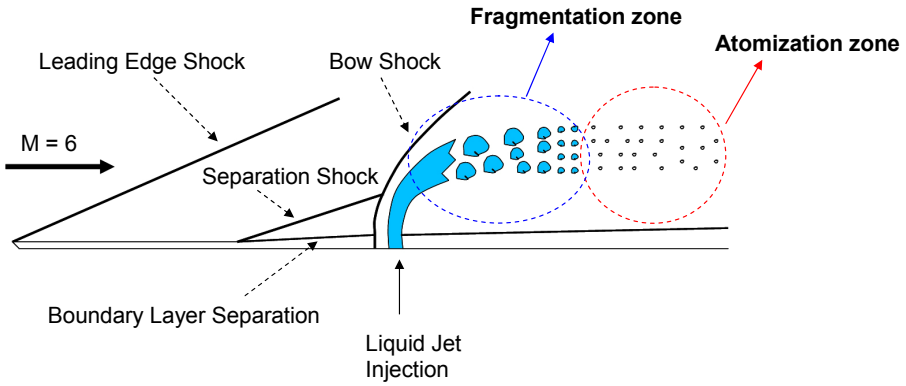


**Figure 7.1:** General flow topology of jet injection in compressible cross flow

| Test no | Support type | Test technique | Resolution (pixel x pixel) | Mass (gr) | Rate (fps) | Exposure ($\mu s$) | Lens |
|---|---|---|---|---|---|---|---|
| Sch4 | Sharp LE | Schlieren | 608 x 296 | 3.15 | 9009 | 70 | 200mm |
| Sch5 | Sharp LE | Schlieren | 608 x 296 | 3.25 | 9009 | 70 | 200mm |
| Schr1 | Blunt LE | Schlieren | 400 x 304 | 2.4 | 16000 | 25 | 200mm |
| Schr2 | Blunt LE | Schlieren | 400 x 304 | 2.6 | 16000 | 40 | 200mm |
| BL3 | Sharp LE | Back-light | 688 x 240 | 2.8 | 11019 | 2 | 50mm |
| BL6 | Sharp LE | Back-light | 608 x 304 | 2.9 | 10256 | 2 | 50mm |
| BL8 | Sharp LE | Back-light | 608 x 304 | 3.1 | 11695 | 2 | 50mm |
| BLR2 | Blunt LE | Back-light | 513 x 280 | 2.8 | 14035 | 2 | 50mm |
| BLR5 | Blunt LE | Back-light | 512 x 240 | 2.7 | 16000 | 2 | 105mm |
| FL5 | Sharp LE | Front-light | 608 x 240 | 2.7 | 14035 | 20 | 105mm |
| FL8 | Sharp LE | Front-light | 608 x 240 | 3.1 | 14035 | 15 | 105mm |

**Table 7.1:** Test matrix of selected balloon experiments

To obtain detailed information of the fragmentation behavior of the balloon test, different photographic techniques and high speed camera set-up have been used. Among these, the Schlieren technique and the back-light technique are the most important ones. The front-light technique is employed as well. All techniques are described in Section 3.3.

To obtain back-light illuminated movies, a halogen light source of 1600W power is employed on the opposite side of the test section, with respect to the position of the high speed camera. The back-light illumination creates a high contrast shadow of the boundaries of the bursting balloon and water droplets, resulting in clear and detailed information about the break-up mechanism. Since the light source is pointing directly at the camera, a very sharp image can be obtained, with an exposure time as low as $2\mu$s. The sampling rate is varied between 10000fps and 14000fps.

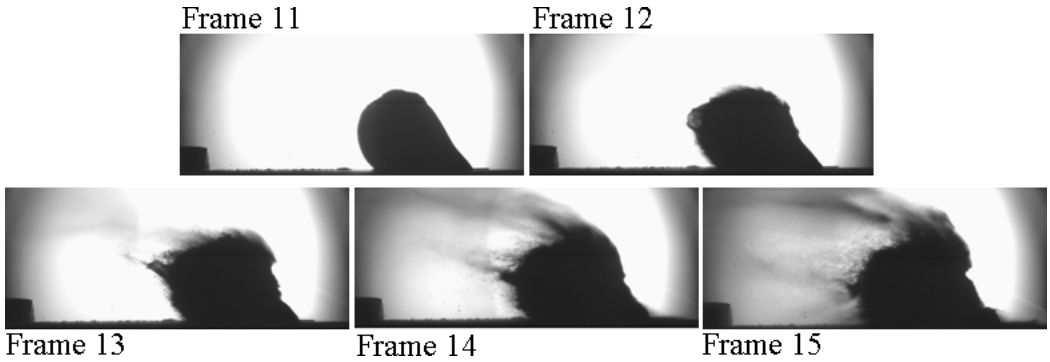


**Figure 7.2:** Five consecutive frames of a back-light illumination movie of a bursting balloon; Mach 6 flow from right to left

After the tests, the high speed camera images are post-processed using algorithms developed on a Matlab platform [89, 15, 94]. As the experiments with the bursting of a water balloon have a transient nature, it would not make sense to calculate the mean or standard deviation of the complete movie. The transient nature of the phenomenon does not require processing all the frames in a single file, but to divide them in small windows (5 or 10 frames each) and to compute the pixel intensity variations on such a window. As an example for the obtained results, 5 frames from a back-light illuminated movie (Fig. 7.2) are taken, where one can clearly see the bursting of the balloon. The first image on the upper left corner is taken while the balloon is bursting. The one on the upper right corner is the first image where the water droplets start leaving the original boundary of the balloon. From this small window of 5 frames, one can compute the standard deviation (Figure 7.3) and also the mean value of the images based on pixels' intensity.

## 7.2 FRAGMENTATION AND SHOCK WAVE SYSTEM

The bursting of the balloon filled with water and the fragmentation of the liquid sphere is recorded using the high speed camera both as Schlieren images and also as back-lighted (shadow) images. While consecutive back-lighted images are shown in Fig. 7.2, Fig. 7.4 shows consecutive Schlieren images at the moment of the bursting of the balloon. Looking at the running standard deviations of these consecutive images (Figure 7.3 for back-light illuminated images and Fig. 7.5 for Schlieren images) and comparing them gives an idea about the interaction between the shock wave system and liquid. Prior to the bursting of the balloon, the shock wave system is observed to be fluctuating for the case with the sharp leading edge support, whereas it is seen to be very stable for the blunt leading edge support tests. The

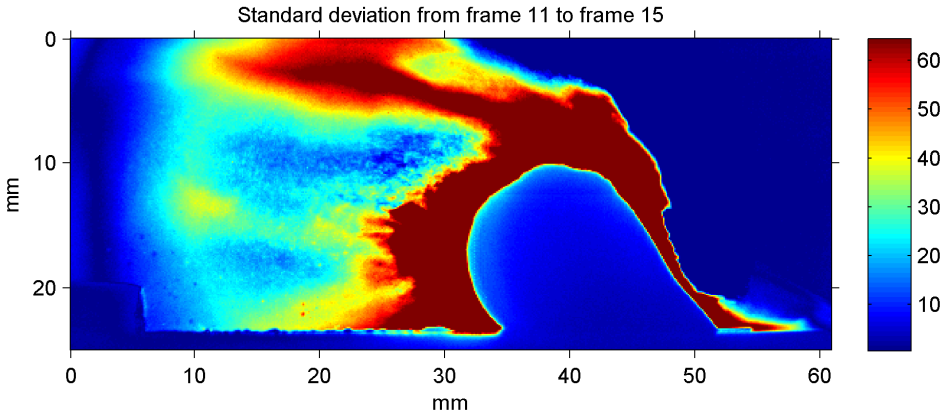


**Figure 7.3:** Running standard deviation of five frames; Mach 6 flow from right to left

shock wave system is composed of the leading edge shock of the support, the bow shock in front of the balloon and the separation shock. The point of interaction of these shock waves is associated with a locally increased heating rate [16], and this is where the balloon skin bursts.

Figure 7.5 shows the margin of the fluctuation of the shock system, owing to the standard deviation of 10 images before the balloon bursts. The two boundaries

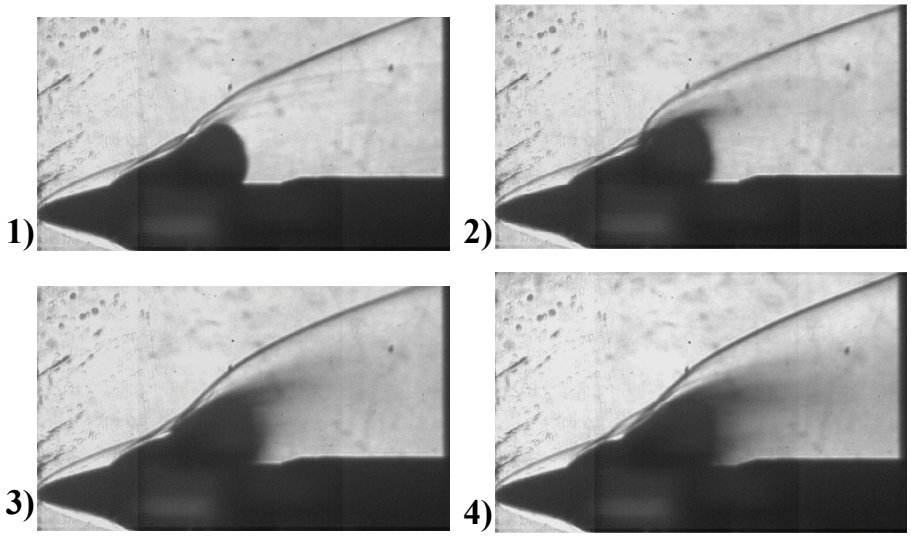


**Figure 7.4:** Four consecutive Schlieren images of the balloon bursting; Mach 6 flow from left to right

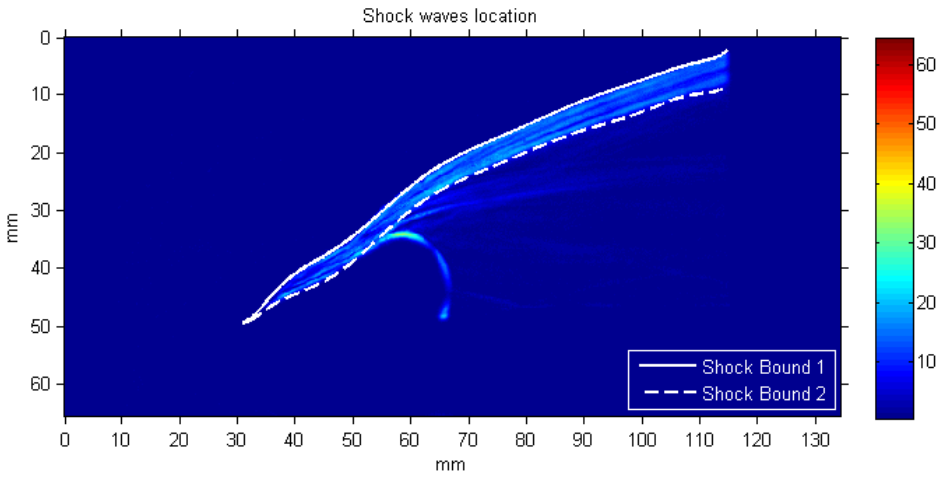


**Figure 7.5:** Standard deviation of ten Schlieren images, prior to the bursting of the balloon; Mach 6 flow from left to right

(dashed and solid lines) shown on Fig. 7.5 are the boundaries of the fluctuation envelope of the shock wave system prior to the bursting of the balloon. The shape of the shock wave is simulated using a polynomial curve fit. Knowing the location and the inclination of the shock wave, all fluid dynamic properties downstream of the shock wave can be calculated through the shock wave relations. Once the properties of the flowfield are known, the boundary conditions of the water balloon can be defined, including non-dimensional parameters such as Weber number. Considering the region where the fragmentation of liquid appears (the upper half part of the balloon), the Weber number downstream of the shock system is calculated to be $4.0 \pm 0.2 \times 10^4$. The same order of Weber number is calculated for the case of a blunt leading edge support, where the shock system is very stable, as shown in Fig. 7.6. According to Shraiber [130], a droplet exposed to Weber number at this order of magnitude is subject to a sheet stripping fragmentation (see also Section 2.3), also called shear breakup [56]. In this type of droplet fragmentation mode, the breaking mechanism is controlled by the shear stresses created by the aerodynamic forces; threads and shrouds starts to develop on the surface of the droplet, mainly in the upper part. Then, small droplets split off these threads. This process can be observed during the entire process of fragmentation, while the initial drop exists as a whole, with its overall dimension diminishing. Then, the main droplet breaks up into several fragments at a certain stage [10, 94].

The running standard deviation algorithm based on a five-frame window is also applied to the images obtained using front-light (see Fig. 7.7), as presented in Fig. 7.8. Several images are shown starting from the bursting of the balloon. The standard deviation images show the difference between the most dynamic zones (lighter color) and most stable zones (darker color). The images are confusing and the only hypothetical information that can be extracted is that it is a very complex and unsteady environment. Attention can be focused on the motion of the lighter color (dynamic) regions, which starts where the shock wave impinges the balloon (point of

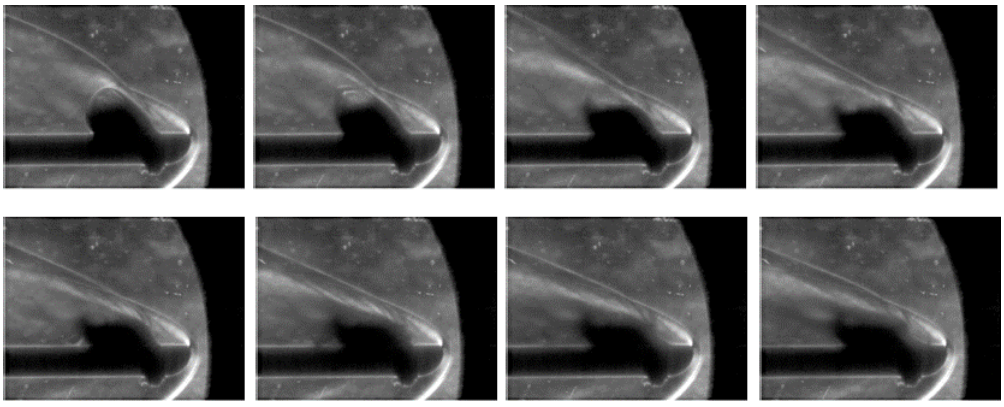

**Figure 7.6:** Eight consecutive schlieren images of the bursting balloon; Mach 6 flow from right to left, blunt leading edge support

bursting), moves downstream and towards the top, and finally draws a diagonal line from the bottom right (upstream) corner towards upper left (downstream) corner. Once most of the liquid is fragmented (7th and 8th images of Fig. 7.8), a very chaotic zone is observed on the downstream lower corner of the image, while the rest of the jet remains more stable, although it is unsteady. Another interesting observation

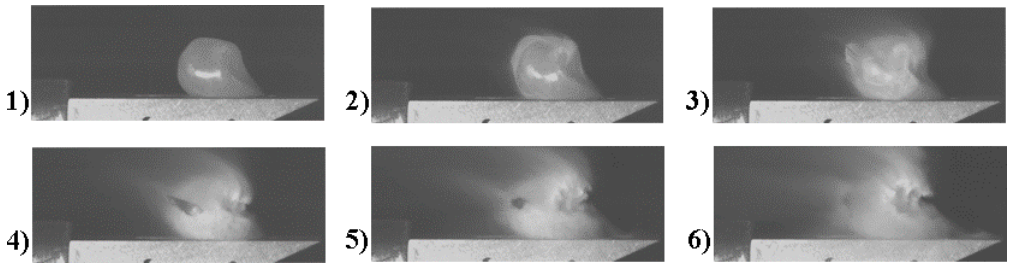


**Figure 7.7:** Six consecutive front-light illuminated images of the bursting water balloon; sharp leading edge support

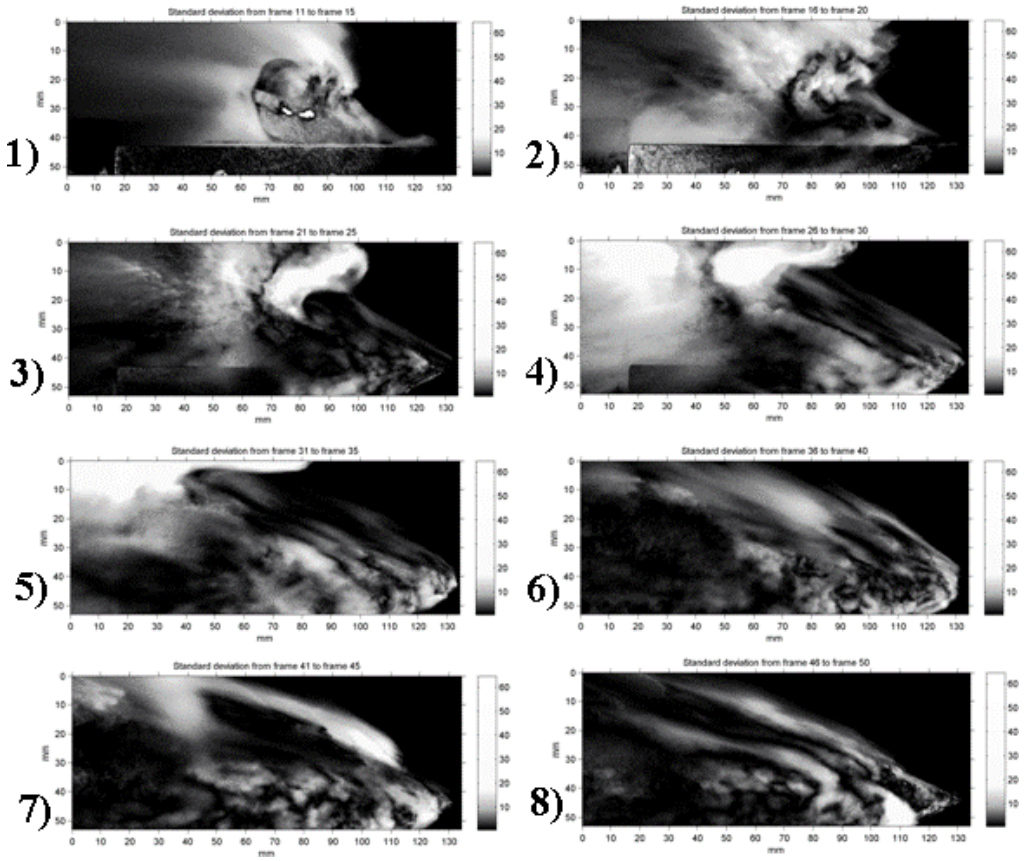


**Figure 7.8:** Running standard deviation of front-light illuminated images; water balloon with sharp leading edge support

that can be drawn from the images of Fig. 7.8 is that the shock wave separates the liquid region into two different zones. The region above the shock wave has a higher velocity, thus a lower pressure; whereas the lower region has a lower velocity hence a higher pressure. This pressure difference causes the water droplets in the lower zone to move to the upper zone, influencing the shape of the water column, thus also influencing both the shock wave and the pressure ratio. This fluctuation goes on, and in a global sense, it creates a recirculation zone. This recirculation can be seen more clearly on the second image of Figure 7.8. To be able to see the interaction between the shock wave and the liquid region, a comparison is performed between the schlieren images and back-lighted images. In Fig. 7.9, the standard deviation analysis applied to an entire back-lighted movie using a running window of 5 frames is presented. The dotted line shown on the images of Fig. 7.9 is the position of the leading edge shock wave when there is no balloon or liquid. These images help in validating the previous observation, about the nature of liquid diffusion and circulation following the bursting. The two major directions of the water are upper and downstream directions. Because of the fluctuating nature of the shock system, some liquid moves above the shock wave system [1]. Then the aerodynamic forces acting on the water trigger the breakup mechanism of the droplet, creating a cloud of small droplets. The cohesion force of these small droplets is very small compared to the energy of the discontinuity. The leading edge shock essentially penetrates into

[1] for sharp leading edge support case only

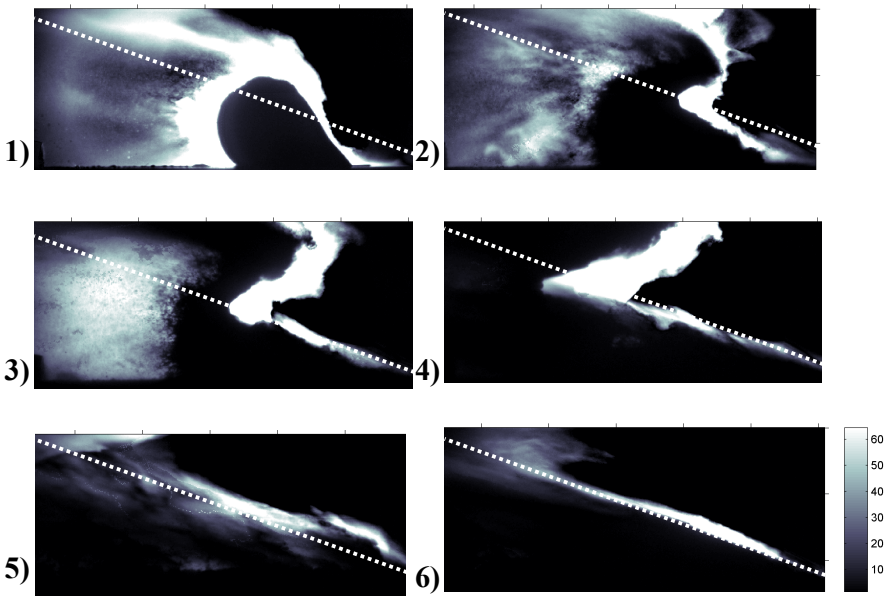


**Figure 7.9:** Running standard deviation of back-light illuminated images; water balloon with sharp leading edge support, Mach 6 flow from right to left

the water sphere, exposing them to two different regions with different velocity and corresponding Weber numbers. In this case the droplets above the shock wave are exposed to a higher velocity (and low pressure), which brings them away very fast compared to the droplets below the shock wave (low velocity, high pressure). At the end, the only remaining shock wave is the leading edge shock wave, with all liquid below it. The fragmentation of the liquid takes place close to the shock location, as the shear stress is the highest in the vicinity of the shock wave. This can be seen clearly looking at the high standard deviation areas close to the shock wave, on Fig. 7.9 [10, 94].

The same mechanism can be mentioned for the case of the blunt leading edge support. However, the shock system does not fluctuate in this case and there is no liquid observed above or upstream of the shock wave system. Figure 7.10 presents the outcomes of the running standard deviation algorithm applied to 100 frames of the movie, with a running window of 5 frames. The position of the bow shock, derived from the processing of the Schlieren images, is highlighted with a dotted white line. The bow shock created by the blunt leading edge support is very stable with respect to the oblique shock wave created by the sharp leading edge support. Indeed, this experimental procedure points out the significantly different behavior of the liquid following the bursting of the balloon. For the blunt leading edge support case, the stable strong bow shock located in front of the balloon changes radically

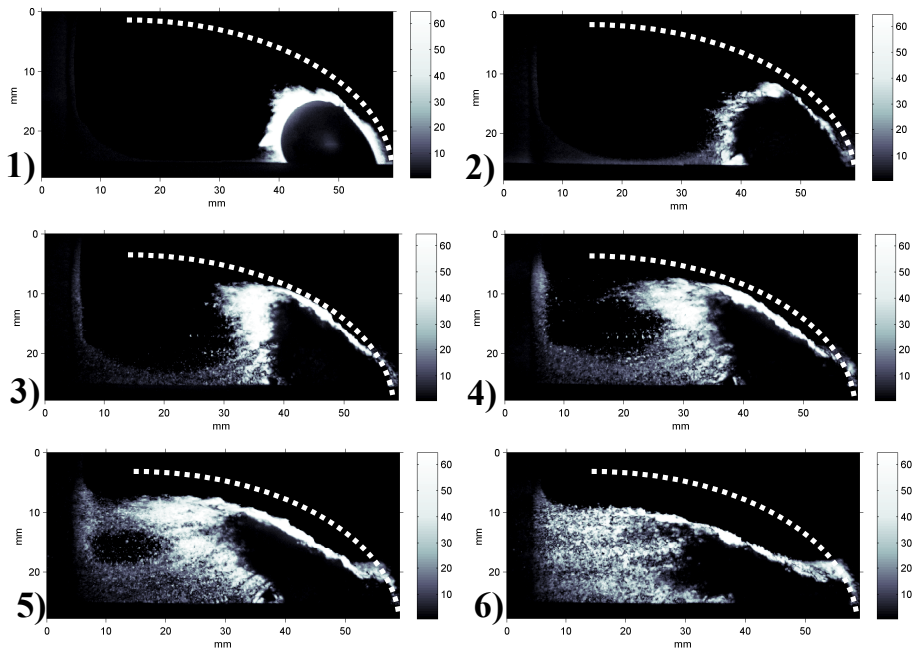


**Figure 7.10:** Running standard deviation of back-light illuminated images; water balloon with blunt leading edge support, Mach 6 flow from right to left

the fluid topology with respect to the oblique shock wave created with the sharp leading edge support. The first impression that one can have is that the water, contrary to what was happening with the sharp leading edge support, is not able to pass beyond the bow shock. The discontinuity created by a bow shock is more powerful than an oblique shock wave, because the rate of change in the angle of the shock wave is higher for a bow shock, which implies a higher shear force with respect to an oblique shock wave. Therefore, the expansion of water following the bursting is bounded on the right (or upstream) and on the top by the presence of the bow shock. The water in the upstream part of the balloon first tends to move in the upstream direction (see image 1 of Fig. 7.10), but then it is pushed back in the downstream and upper direction, aligned with the shape of the bow shock. This shock-wave-enforced motion of water phase creates a small recirculation before being taken away by the air stream. On the other hand, the water in the downstream part of the balloon simply follows the direction of the air stream [10, 94].

## 7.3 Motion of Liquid Boundary

Investigating the motion of the boundary of the balloon at the moment of bursting gives important information about the interaction between the air stream and the liquid phase. This investigation is performed using several post-processing techniques such as edge detection and snake algorithms, which are described in the following Section.

### 7.3.1 Post-processing tools

#### Edge Detection

An improved edge detection technique is utilized to observe the changes within the boundary of the water sphere. The main idea of this technique is to convert each acquired image, from a 256 levels (8 bit) gray image to a simple black and white image, using the "black and white" conversion function implemented in Matlab [89]. The use of this function is based on the employment of a threshold value, between 0 and 1, to determine the pixel intensity limit and discriminate the white pixels from the black pixels. Figure 7.11 shows an example application of this technique to a back-light illuminated image (see Frame 15 of Fig. 7.2, with threshold values between 0.2 and 0.6. From these sequences, the importance of the threshold value can be observed. A threshold value of 0.2 means that all the pixels that have an intensity (based on the color map) lower than the 20% of the maximum intensity value (256 for 8 bits) will be converted in black pixels, the remaining pixels will be white. The value of the threshold has to be chosen manually as a trade-off between the quality of the image and the quantity of information to be obtained. A good trade-off is always between 0.4 and 0.6. Although a threshold around 0.45 is used for most of the cases within this study, one should always keep in mind that the choice of the threshold value might change from experiment to experiment, depending on

the illumination and camera positions. Once the good threshold value is chosen and the black and white image is obtained, it is possible to get the contour of the liquid boundary.

### Snake Technique

Thanks to the edge detection technique, the border of liquid phase is known at every instant of the bursting and fragmentation process. Thus, it would be possible to follow how the border of the liquid region moves at every time step, using an appropriate technique. Common techniques for image segmentation, for example the edge based approach, can not split the image into its separate constituent objects because it does not use any kind of prior knowledge. Moreover, presence of noise and sampling artifacts deteriorate the performance and cause these techniques to either fail completely or require some kind of post-processing step to remove invalid object boundaries in the segmentation results. Instead, active contour models are used to develop an algorithm for following the boundary of liquid region. Active contour models, also known as "snakes" were introduced first by Kass et al. [67] as a solution to the task of finding salient contours like edges and lines in digitized images. The snake represents an object boundary or some other main image feature as a parametric curve that is allowed to deform from some arbitrary initial shape towards the desired final shape. The problem of finding this final contour is cast as an energy minimization problem with the intention that the final contour yields a local minimum of an associated energy functional E. The energy functional E of the contour is defined such that the energy of the contour attains a local minimum when the contour is spatially aligned with the shape or object boundary of interest in the image. The energy functional is thus based upon the spatial features of the images under inspection that one wants to detect. Essentially each snake can

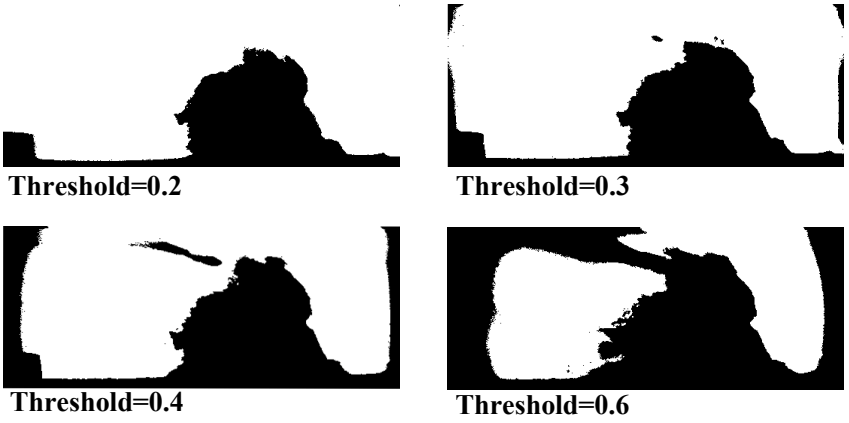


**Figure 7.11:** Effect of threshold on edge detection technique applied to a back-light illuminated image; Mach 6 flow from right to left

move under the influence of internal forces coming from the curve itself and external forces computed from the image data. The traditional snake model [67] had many severe problems which decreased their effectiveness, therefore in 1998, Xu [159, 160] proposed a new snake known as GVF snake. The basic model for the GVF snake was the same as the traditional snake. However they defined a new external force field known as gradient vector flow field, hence the name GVF.

The snake algorithms promises a segmentation technique that does not bias the final shape detection toward straight edges. They also perform the segmentation task without a known or predetermined shape and this property make them very useful in a variety of applications. Another motivation for the use of snakes is the ability of these models to fill in edges where weak image gradients are present. Thus snakes can also detect incomplete boundaries, something that was not possible with the previous approaches. To summarize, the main motivation for snake usage comes from its ability to capture non-rectilinear (curved) object boundaries and their robustness to weak and incomplete edges.

The basic mechanism of a snake consists of an initializing process with an arbitrary shaped contour close to the object boundary of the image to be detected. The algorithm proceeds and the snake starts deforming trying to minimize its energy functional at every step. In the process, it "shrinks-wraps" around the object boundary of the image and stops when it attains spatial local minima which is the point where the contour perfectly wraps around the object of interest. A program controlling a snake causes it to evolve so as to reduce its energy functional E. The contour of the snake is defined in the two-dimensional plane as $x(s)$ and the framework is defined as a sum of energy terms in the continuous spatial domain. The particular energy functional E is categorized as follows:

i. *Internal Energy:* is a function of the contour $x(s)$ itself and it specifies the tension and smoothness of the curve. It therefore depends on the internal properties of the snake, as elastic energy and bending energy.

ii. *External Energy (GVF):* is derived from the image under inspection using the gradient vector field.

$$E_{snake} = E_{elastic} + E_{bending} + E_{GVF} \tag{7.1}$$

The contour is treated as an elastic rubber band giving it an elastic potential energy. This energy consists of a first order derivative of the contour and it discourages stretching by introducing tension in the contour. Adjusting the weight $\alpha(s)$ allows to control the elastic energy along different parts of the contour. However for most applications $\alpha$ is assumed to be a constant throughout the curve. The elastic energy equation is expressed as:

$$E_{elastic} = \frac{1}{2} \int_s \alpha |x\prime|^2 ds \tag{7.2}$$

The relative elastic force at any point in the curve is oriented in the direction to the center of curvature, this causes the contour at these points to expand until the concavity is eliminated. The other action of elastic forces is to shrink the curve and is responsible for collapsing the contour to a single point in the absence of any opposing force. Figure 7.12 shows the action of elastic force on the curve. The initial snake was allowed to deform freely under the influence of elastic force alone. Notice how the concavities are eliminated and the entire curve shrinks. If the curve would be allowed to move freely for a few more iterations (and if the elastic force is the only force acting on the snake), it would eventually collapse to a point. The elastic forces also tend to evenly space the control points along the contour making it evenly sampled because a point at equal distance from its neighbors will experience minimum elastic force due to balancing of the opposite forces from its neighbors. For example, if three points are co-linear and equally spaced, then the force equals to 0.

The snake is also considered to behave like a thin metal strip in addition to being considered as an elastic band. This is one more physical property that is assigned to a snake. The contour should try to be a smooth curve or straight line and avoid sharp corners. Therefore the snake is considered to possess bending energy, which is given as the sum of squared curvatures of the snake, as in Eq. 7.3 where the bending factor $\beta(s)$ is considered constant along the snake.

$$E_{bending} = \frac{1}{2} \int_s \beta |x''|^2 ds \tag{7.3}$$

The second order derivative discourages bending. Sharp corners or points of high curvature are characterized as high frequencies and bending energy is more sensitive (very high) for contours having such sharp corners because the second order derivative will be very high for such contours. Setting $\beta(s)$ to 0 at a point means that we are relaxing our condition and allowing that point to develop a corner. Figure 7.13 helps to understand the action of bending force. The initial curve was allowed to deform under the influence of bending force alone, resulting in the final curve. Notice how all the corners are smoothed out, reducing the bending energy of

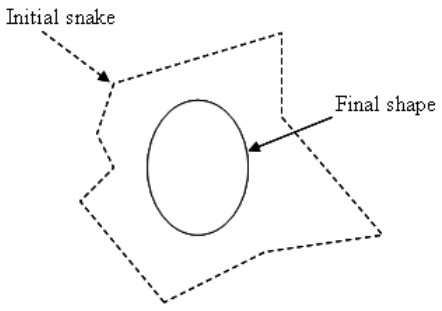


**Figure 7.12:** Snake's elastic force

the contour. This is exactly what bending force should be doing. If one continues this for more iterations, the bending force will eventually make the curve become a circle because a circle has the lowest bending energy.

The overall approach is to minimize the energy functional E as a starting point for designing a snake. The energy functional is the summation of internal energies and external energy. The external energy for this improved type of snake is characterized as a static external force field which is called the gradient vector field (GVF). To create a GVF, first an edge map has to be defined, based on the digitized image, such that it is larger near the image edges. We can use a few ways to define an edge map based on gray-level or binary edge map as follows:

$$f(x, y) = |\nabla I(x, y)| \tag{7.4}$$

where I(x,y) is the pixel intensity of the image. Three general properties of edge maps are important in the present context. First, the gradient of an edge map has vectors pointing towards the edges, which are normal to the edges at the edges. Second, these vectors generally have large magnitudes only in the immediate vicinity of the edges. Third, in homogeneous regions, where I(x,y) is nearly constant, the gradient of the edge map is nearly zero. Now considering all these properties, we can consider using the edge map as a simple external force in a snake algorithm. For the first property, a snake initialized close to an edge will converge to a stable configuration near that edge. This is a highly desirable property. Because of the second property, the range of action of the snake will be very small. Because of the third property, homogeneous regions will have no external forces whatsoever. These last two conditions are undesirable. The approach of the GVF is to extend the gradient map farther away from the edges and into homogeneous regions, using a computational diffusion process.

The GVF can be described as a generic vector field $\mathbf{v}(x, y) = [u(x, y), v(x, y)]$ minimized by a new energy functional (different from the one of the snake algorithm) as in Eq. 7.5, where u and v are vector field component in x and y direction both.

$$\epsilon = \iint \mu(u_x^2 + u_y^2 + v_x^2 + v_y^2) + |\nabla f|^2 |\mathbf{v} - \nabla f|^2 dxdy \tag{7.5}$$

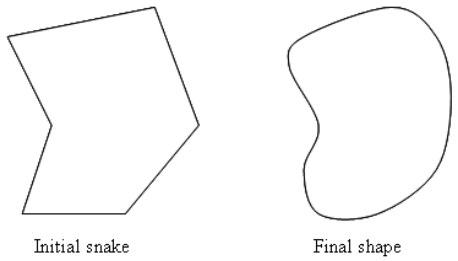


**Figure 7.13:** Snake's bending force

In particular looking at Eq. 7.5 one can see that when the gradient of the edge map f(x,y) is small, the energy is dominated by the sum of the squares of the partial derivatives of the vector field, yielding a slowly varying field. On the other hand, when the gradient of the edge map is large, the second term dominates the integrand, to minimize the energy functional $\mathbf{v} = \nabla(\mathbf{f})$. This produces the desired effect of keeping $\mathbf{v}$ nearly equal to the gradient of the edge map when it is large, but forcing the field to be slowly-varying in homogeneous regions. The parameter $\mu$ is a regularization parameter governing the trade-off between the first and the second term in the integrand; this should be set according to the amount of noise present in the image. Figure 7.14 shows how the GVF is pointing toward the edge of the image and is creating a vector field that expands farther away from the boundary. The first image of Fig. 7.14 shows a boundary alone, whereas the middle image shows the intensity of the vector field. The third image is a close-up view of the same vector field close to the boundary.

### Discrete Cosine Transform

The movement of contours detected at every image can be followed using the "snake" algorithm. However, the results are very sensitive to the time duration between two consecutive images. If there is an abrupt change in the contour shape, the algorithm is not very successful to follow the pattern perfectly, resulting in noisy patterns. A higher acquisition rate of the high-speed camera would result in more images within the investigated time, hence smoother motion vectors between two images, or between two vectors. To avoid this problem, one has to increase the image acquisition rate of the high speed camera. However, this is not possible as the acquision rate of the high speed camera is at its maximum given the conditions. Another solution would be the introduction of an artificial intermediate step, between the contours of two images. Because the acquisition rate of the camera is limited with the illumination and test conditions, it is decided to use interpolated time steps for the


**Figure 7.14:** Gravity Vector Field (GVF) creation

purpose of smoothing the displacement vevctors of the liquid boundary. For this, the "Discrete Cosine Transform" technique is used [94, 72, 1].

A discrete cosine transform (DCT) expresses a sequence of a finite number of data points in terms of a sum of cosine functions oscillating at different frequencies [19]. DCTs are important for numerous applications in science and engineering, from lossy compression of audio and images (where small high-frequency components can be discarded), to spectral methods for the numerical solution of partial differential equations. In particular, a DCT is a Fourier-related transform similar to the discrete Fourier transform (DFT), but using only real numbers. DCTs are equivalent to DFTs of roughly twice the length, operating on real data with even symmetry (since the Fourier transform of a real and even function is real and even), where in some variants the input and/or output data are shifted by half a sample. Like any Fourier-related transform, discrete cosine transforms (DCTs) express a function or a signal in terms of a sum of sinusoids with different frequencies and amplitudes. Like the discrete Fourier transform (DFT), a DCT operates on a function at a finite number of discrete data points. The obvious distinction between a DCT and a DFT is that the former uses only cosine functions, while the latter uses both cosine and sinus function (in the form of complex exponentials).

The Fourier-related transforms that operate on a function over a finite domain, such as the DFT or DCT or a Fourier series, can be thought of as implicitly defining an extension of that function outside the domain. That is, once a function $f(x)$ is written as a sum of sinusoids, one can evaluate that sum at any $x$, even for $x$ where the original $f(x)$ was not specified. The DFT, like the Fourier series, implies a periodic extension of the original function. A DCT, like a cosine transform, implies an even extension of the original function. The general formulation for one-dimensional discrete cosine transform for a signal $x(n)$ is the one expressed in Eq. 7.6, giving back a vector $y(k)$ that contains the frequency coefficients of the DCT.

$$y(k) = w(k) \sum_{n=1}^{N} cos \frac{\pi(2n-1)(k-1)}{2N}, \ k = 1, ..., N \tag{7.6}$$

Where $w(k)$ is a parameter function of the signal vector size

$$w(k) = \begin{cases} \frac{1}{\sqrt{N}}, & k = 1 \\ \sqrt{\frac{2}{N}}, & 2 \leq k \leq N \end{cases} \tag{7.7}$$

The general formulation for one-dimensional inverse discrete cosine transform (IDCT) is given in equation Eq. 7.8. Starting from the frequency coefficients vector $y(k)$, one can retrieve the original signal $x(n)$

$$x(n) = \sum_{k=1}^{N} w(k) y(k) cos \frac{\pi(2n-1)(k-1)}{2N}, \ k = 1, ..., N \tag{7.8}$$

Where the parameter w(k) is function of the size of the coefficients vector y(k).

$$w(k) = \begin{cases} \frac{1}{\sqrt{N}} & k = 1 \\ \sqrt{\frac{2}{N}} & 2 \leq k \leq N \end{cases} \tag{7.9}$$

In our case, the discrete cosine transform is used for interpolation of the contours of the exploding balloon, studying its evolution in time [1] and extending virtually the number of frames that can be acquired by the high speed camera. In particular, we are interested in extraction of the local balloon boundaries from discretely sampled data. To facilitate this task we interpolate between discrete contours in time as described below. Applying the snake algorithm to two different frames of the high speed camera, we end up with two different discrete curves, made of a set of points. In order to interpolate between them, we start by defining the parameters of each of the original contours, and then create a contour interpolated in time simply by taking the arithmetic average of the parameters. If we consider the two-dimensional point coordinates for each frame (see Fig. 7.15) as two separate vector x and y, we can treat them as a one-dimensional signal and use the discrete cosine transform, to find the contour between two frames.

Using the DCT as a new frequency domain shape parameterization has many advantages. It produces real coefficients, and has excellent energy compaction properties. Armed with these frequency coefficients as a new curve parameters, we can

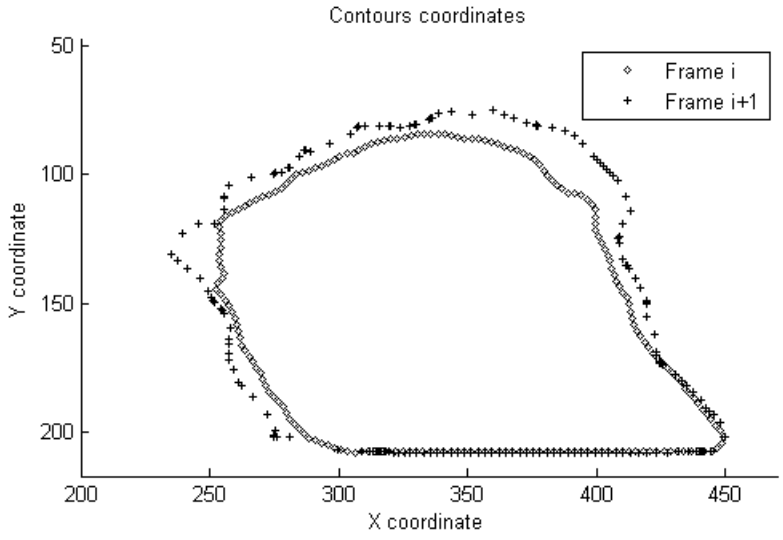


**Figure 7.15:** Coordinates of the contours from frames i and i+1

directly perform the actual interpolation, that simply corresponds to an interpolation in the time considering two frames taken in two different time instants, i and i+1. In Fig. 7.16, a zoom of the frequency coefficients plot for the x-coordinate of two different frames (i and i+1) can be seen. A linear interpolation can be made

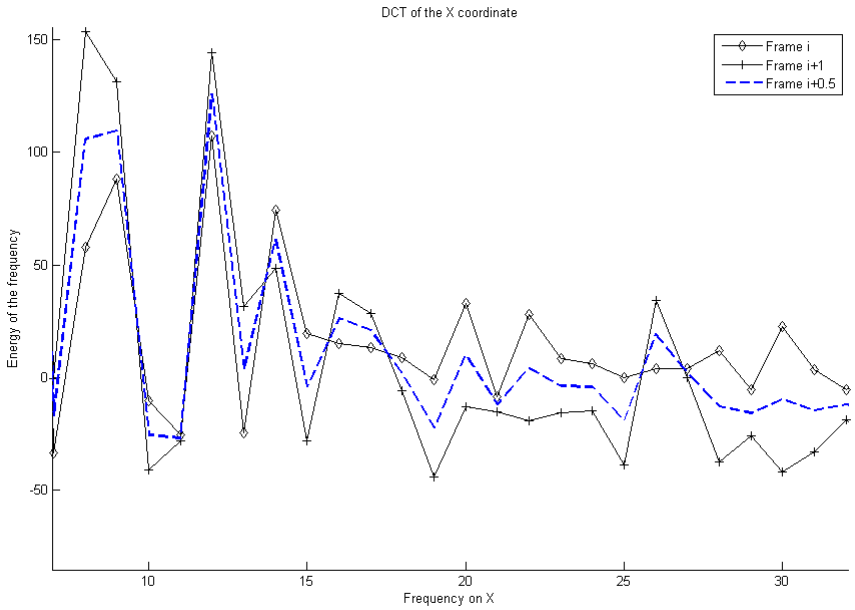


**Figure 7.16:** Frequency coefficients of x-coordinate of frames i, i+1 and the interpolated frame i+0.5

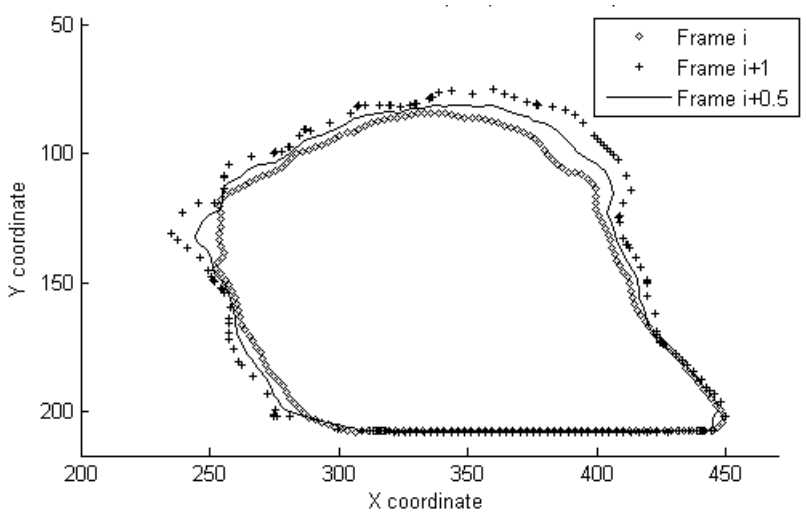


**Figure 7.17:** Contour of the interpolated frame i+0.5

between the frequency coefficients both on x and y coordinates. The interpolated values for x-coordinate are plotted in Fig. 7.16 again, where the new coefficients are created halfway between frame i and frame i+1. The new series is called *i+0.5*. Finally the inverse discrete cosine transform (IDCT) is used to transform the interpolated components back into the spatial domain, creating a new balloon boundary between the two frames i and i+1. The contour of the interpolated frame can be seen in Fig. 7.17.

The so called time interpolation through discrete cosine transform is very powerful, and allows the user to create a virtually infinite number of interpolated frames. Obviously the interpolated frames are only a representation of the real evolution of the balloon boundaries. No real information is created, going beyond the sample rate of the high speed camera. The most probable intermediate contour is created using this technique, in the absence of higher frame rate high-speed camera images.

### 7.3.2 Liquid Boundary Segments

The back-lighted images obtained by the high speed camera are converted into purely black and white images using an improved edge detection technique. These images show the boundary of the liquid region at every instant following the bursting of the balloon (see Fig. 7.2). Combined with the snake algorithm, the liquid boundary at every frame can be analyzed to see how the boundary of the liquid is moving. Time interpolation between two consecutive images is applied whenever necessary. The results can be seen in Fig. 7.18, which shows the bursting of a balloon at Frame 10. Time duration between each frame is $71\text{x}10^{-6}$ seconds. The moment the balloon bursts is taken as the first frame. The first plot in Fig. 7.18 presents the motion of the liquid boundary calculated by comparing the contour of the intact balloon with the contour of the first image after bursting. If the first frame is the frame where the balloon bursts, the first plot considers frames 1 and 2, the second plot considers frames 2 and 3, etc...

The combination of the three algorithms (edge detection, time interpolation by DCT and snake) allows accurate identification of the boundary of the balloon and/or liquid phase and the determination of quantitative information about the location of the liquid boundary over different frames. The movement of the curve identifying the boundary between two different frames is represented by a set of vectors. The direction and the magnitude of each vector suggest the most probable direction and the magnitude of the displacement for each discrete point of the curve. However, as the liquid is fragmented, the motion vectors become more and more complex and the analysis of the overall motion is difficult by looking at the plots of Fig. 7.18. For this reason, the balloon boundary is divided into different small segments, to follow their individual motions. The outcome of this algorithm is presented in Fig. 7.19, where eight different segments (each indicated with a letter) with each of their motion vectors for eight frames starting from the yet-intact balloon frame are presented. Knowing the sampling time of the frame acquisition, it is also possible to compute

the velocity of the segments. The detailed information on all eight segments are exposed in Fig 7.20 for segments (a) to (d) and Fig. 7.21 for segments (e) to (h).

Looking at the overall motion of the segments of Fig. 7.20 and Fig. 7.21, one can identify four significant regions of the balloon boundary, for the case of the sharp leading edge support:

i. The first region (segments a and b) is the one that faces the flow, where the

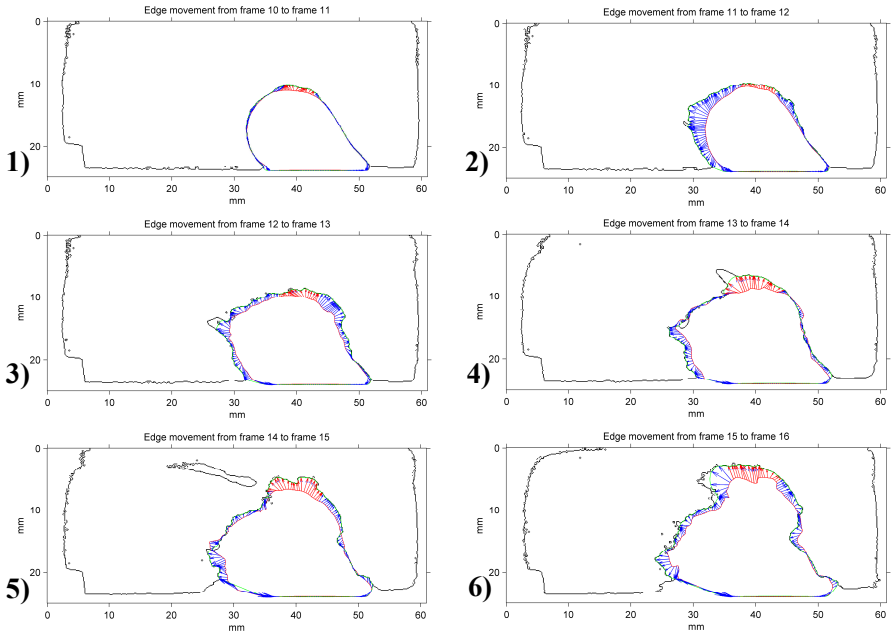


**Figure 7.18:** Motion vectors of liquid boundary; sharp leading edge support, Mach 6 flow from right to left

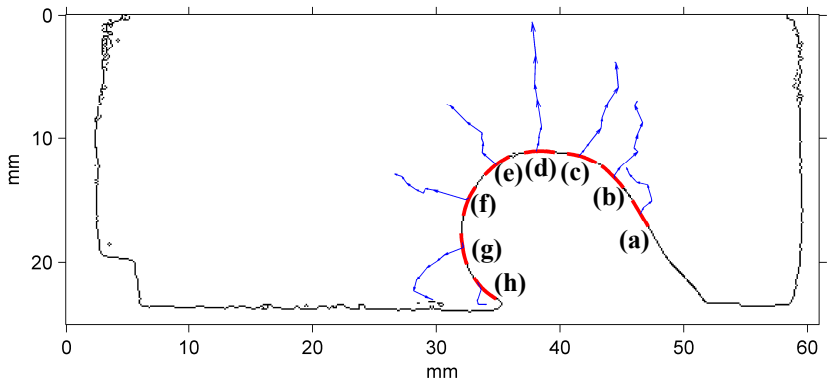


**Figure 7.19:** Motion vectors of liquid boundary segments; sharp leading edge support, Mach 6 flow from right to left

shock wave impacts. The motion of the segment (a), shown in Fig. 7.20, illustrates clearly the behavior of that part of the balloon boundary. At the beginning of the explosion, the water moves against the freestream direction, due to the pressure difference between the lower pressure freestream and the higher pressure inside the balloon. Then, when the energy of the water is dissipated, the kinetic energy of the free stream overcomes the energy of the water and the liquid is pushed downstream. The segment (b) has similar behavior although its motion lags segment (a). In the overall, both segments tend to go upwards. This is both because of the high pressure inside the balloon (which pushes the liquid phase away from the center of the balloon) and also because of the pressure difference created by the shape of the shock system.The shock system has a more inclined shape at the top, resulting in higher velocity and lower pressure.

ii. The second region (segments c and d) is the upper part of the balloon. For both of the segments, the strong tendency of the water to expand upward can be observed. Again the pressure difference between the water contained into the balloon and the air stream is the driving force of the initial motion. The segment (c) has a similar direction of motion as segments (a) and (b).

iii. The third region (segments e and f) is the downstream (left) part of the bal-

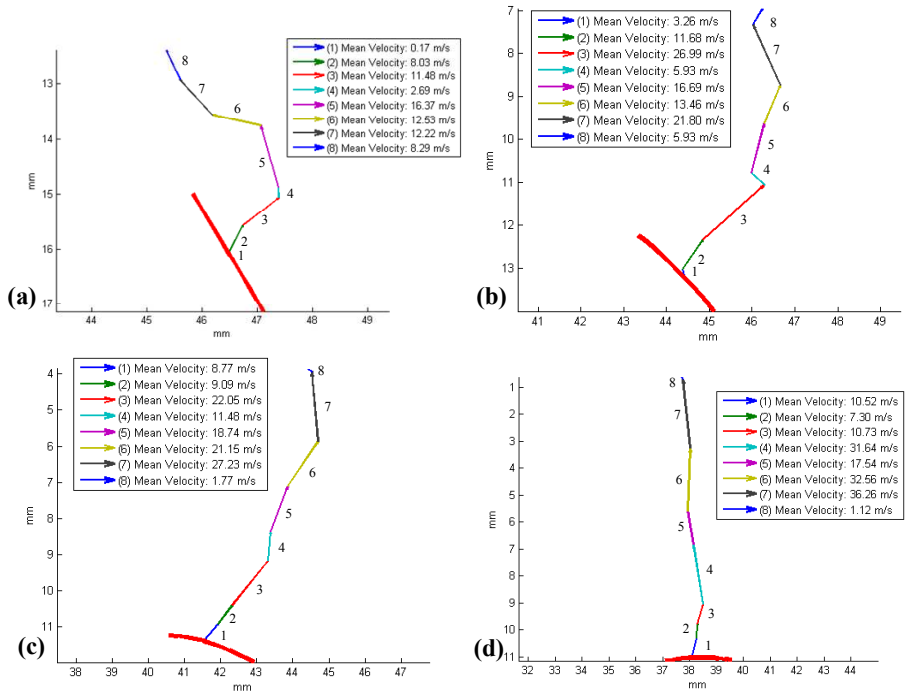


**Figure 7.20:** Motion vectors of liquid boundary segments (a), (b), (c) and (d); sharp leading edge support

loon boundary. The motion of these segments is driven both by the pressure difference between liquid and air regions, and also by the shear force of the freestream. The liquid, under the influence of the aerodynamic shear force, fragments into smaller chunks before it is atomized in smaller droplets. This kind of fragmentation mechanism is called sheet stripping (see also Sections 2.3 and 7.2).

iv. The fourth and the last region (segments g and h) is the one near the bottom of the balloon. In this region, which remains in the wake of the balloon, the water clearly experiences a recirculation as can be seen from the direction of the motion vectors.

A similar analysis is performed on the motion of liquid boundary segments for the case of the blunt leading edge support. Figure 7.22 presents the general view of the motion of six selected segments, while Fig. 7.23 shows the vectors of each segment in detail. The velocity values are not shown on these plots. although the size of each vector is proportional to its velocity. The main difference is that the shock system is very stable, and the liquid never passes above or upstream of the shock wave. It is also worth noting that 21 motion vectors could be included for blunt leading edge support, whereas only eight vectors were included for the sharp leading edge support case. The reason is that water chunks remaining inside the

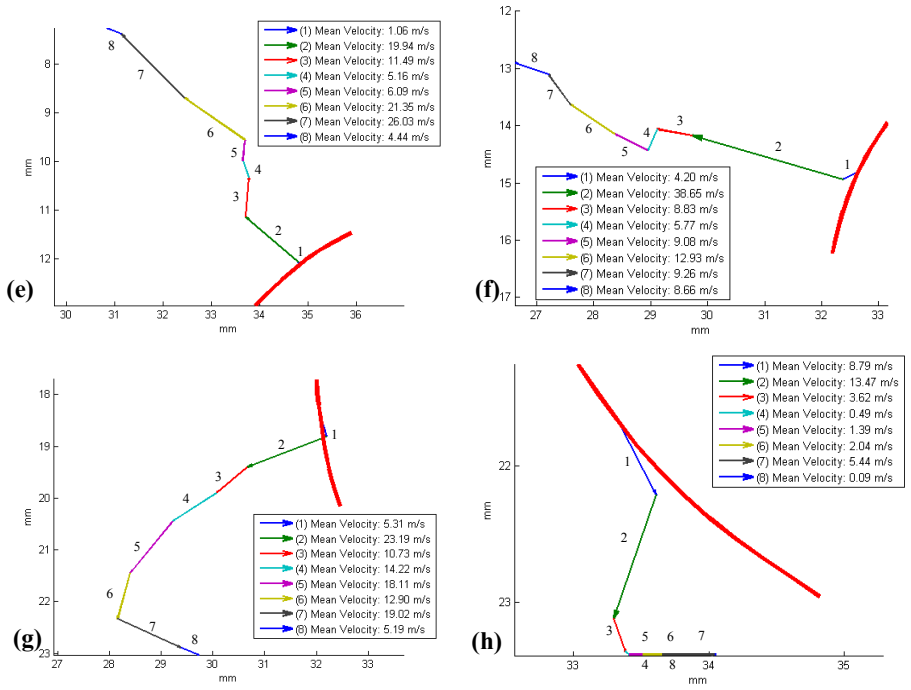


**Figure 7.21:** Motion vectors of liquid boundary segments (e), (f), (g) and (h); sharp leading edge support

stable shock system of the blunt support face a lower velocity, thus their motions are slower and they spend more time within the frame of the image, compared to the sharp leading edge support case. The fragmentation occurs in the close vicinity of the shock wave system, hence it takes a longer time compared to the sharp leading edge support.

Looking at the overall motion of the segments of Fig. 7.23, one can identify three significant regions of the balloon boundary, for the case of the blunt leading edge support:

i. The first region (segments a and b) is the frontal zone of the balloon. Following bursting of the balloon, the water expands in the orthogonal direction (upstream) with respect to the balloon boundary, due to the pressure gradient between the higher pressure within the water balloon and the lower pressure of air stream. Then, the direction of the water boundary changes completely, experiencing reversing. The water is carried away in the downstream direction by the air stream.

ii. The second region (segments c and d) is identified as the upper part of the balloon. Like the first region, the initial motion of this segment is directed in the orthogonal direction with respect to the boundary, moving in upstream and upper direction. However, this motion is affected by the air stream forcing it first to go lower and then in the downstream direction. In the overall, the initial trend of the water front to move in the upper and upstream direction is forced to change in downwards and downstream direction, resulting in a circular path and then continuing with the air stream.

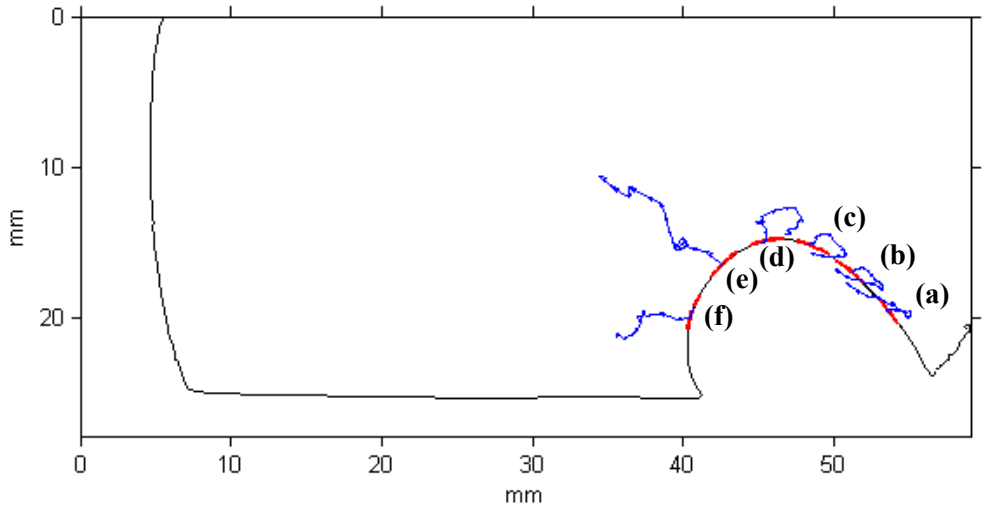


**Figure 7.22:** Motion vectors of liquid boundary segments; blunt leading edge support, Mach 6 flow from right to left

iii. The third region (segments e and f) includes the back part of the balloon. The behaviour of this region is less complex compared to that of the others, as both forces driving the liquid phase (balloon pressure and aerodynamic force) are in the same direction. In general, the boundary of this region just moves in the downstream direction. Segment (e) has a tendency to go upwards, whereas segment (f) has a tendency to go downwards, indicating the presence of a recirculation region.

The motion of the segments of the water balloon shown in Fig. 7.19 and Fig. 7.22 resemble the motion of a compressible flow past a sphere [162], where a recirculation region is observed downstream of the sphere.

## 7.4 DISCUSSION

The studies presented in the previous chapters with the continuous injection of liquid into the hypersonic cross flow were not suitable to study the fragmentation

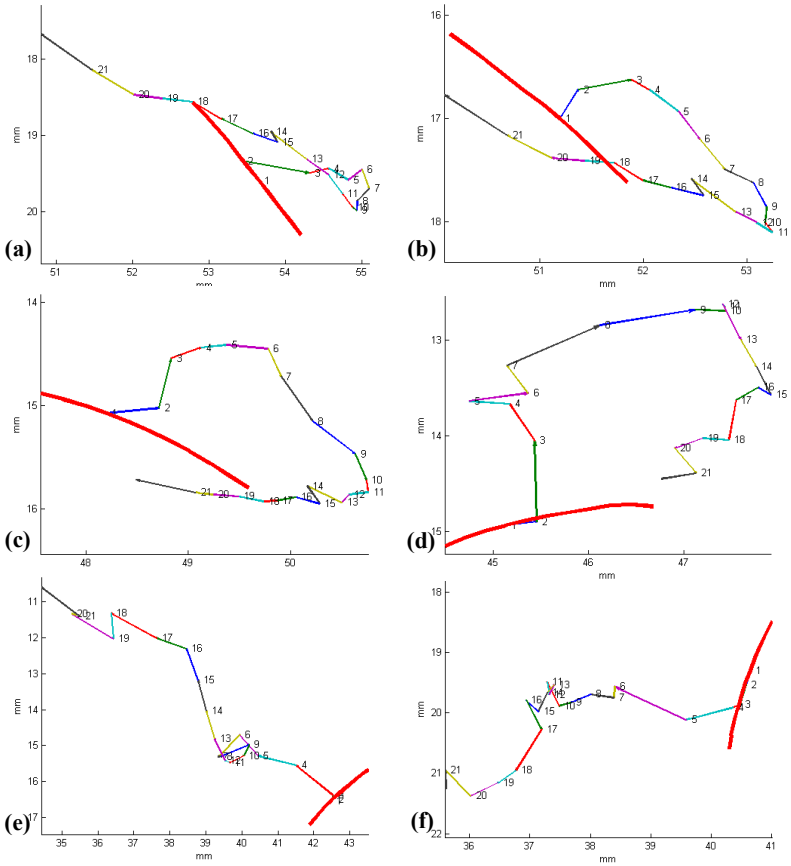


**Figure 7.23:** Motion vectors of liquid boundary segments; blunt leading edge support

mechanism in detail, as they possessed a quasi steady state. The ideal case to study the fragmentation of liquid exposed to high-speed flow would be exposing an intact drop of liquid suddenly to cross flow, such as creating a drop in a shock tube with a perfect timing as it was done by [59] at Mach 2 conditions. Unfortunately, the H-3 wind tunnel (because of its starting procedure) did not allow such an experimental condition. This is why it was preferred to use balloons filled with water and exposed to Mach 6 flow. Fortunately, the high-speed bursting of the balloon skin (in $2\mu$ second) allowed to study a transient case where one can investigate the fragmentation of a volume of water exposed to Mach 6 flow. In this way, it was possible to get more information on the fragmentation of liquid under the same conditions with that of liquid injection.

By making use of the schlieren and back-light illumination images taken during the bursting of the balloon and the fragmentation of the water exposed to Mach 6 flow, it was possible to calculate the corresponding Weber number and observe that the fragmentation happens in the *sheet stripping* mode, where the main mechanism is the aerodynamic shear force. On the other hand, the aerodynamic shear force is maintained by the complex flow field, which is governed by the external geometry constraints. The two different geometries studied, the sharp leading edge and the blunt leading edge supports, yielded different shock wave systems. The shock wave generated by the sharp leading edge has a chaotic interaction with the balloon, causing an unstable flow field. On the other hand, the shock wave generated by the blunt leading edge support is very stable, not interfering with the balloon. The fragmentation of the liquid takes almost twice the time in the case of the blunt leading edge support, compared to the sharp leading edge support. This simple analysis has shown that the external geometry constraints are important and they can play an important role on the liquid fragmentation as they shape the shock wave system and thus the aerodynamic shear force.

The main criticism on this technique is the utilization of a balloon, which was the only means to make this experiment possible. Especially for the sharp leading edge case, the chaotic interaction between the flow field (shock wave) and the balloon makes it difficult to carry out a scientific analysis on the repeatability and the uncertainty of the tests. The time and the exact location of the bursting of the balloon are difficult to predict. It took many unsuccessful attempts to finally be able to repeat "similar" experiments having "similar" initial conditions and behaviors. The blunt leading edge support case was much easier to handle, as it does not involve an unstable shock wave system. The high-speed images taken during the bursting of the balloon showed that this is a very fast phenomenon, and the balloon skin perfectly follows the original boundary of the balloon. However, later analysis showed that this circumferential motion of the balloon skin does not pose an effective shear force on the boundary of the liquid phase. On the contrary, the presence of a balloon creates a force in the normal direction to the surface of the water sphere, because of the inner pressure of the balloon being much higher than the static pressure of the flow field. The fact that the water phase is accelerated by the balloon pressure

creates an additional initial condition which is not compatible with the desired test conditions. Finally, the complex two-phase flow field does not allow the researchers to perform detailed measurements in the wake of the balloon, to calculate the local Weber number. All analysis in this Chapter is based on a global Weber number calculated using the freestream conditions.

# 8 Conclusion

The present chapter summarizes the work performed to study the fragmentation and atomization of liquid exposed to Mach 6 cross flow. The main conclusions of the work performed to understand the flow topology of liquid injected into hypersonic cross flow, the fragmentation mechanism, the transient behaviour of liquid and air flow fields and the droplet size distribution of atomized liquid are all described in this section, with relevant discussions. The summary of the complete work is given in Section 8.1, which is followed by the main conclusions in Section 8.2. Finally, lessons learned will be mentioned in Section 8.3, with a touch of recommendations for the future.

## 8.1 Summary

An experimental investigation has been carried out to study the fragmentation of liquid injected into Mach 6 cross flow, by means of optical techniques. All experiments are carried out at the H-3 Mach 6 wind tunnel facility of the von Karman Institute for Fluid Dynamics, at a total pressure of 20bar and a total temperature of 500K. Two different experimental set-ups are utilized to reach the goals of the campaign. The first set-up involves injection of liquid through an injector flush mounted to a flat plate. The second set-up involves exposure of a water-filled balloon to Mach 6 flow. The main results are obtained by image processing of photographic measurement techniques including Schlieren photography. The liquid injection into Mach 6 cross flow case is further investigated by flowfield visualization and phase doppler interferometry to detect the droplet dimension.

High-speed imaging is obtained thanks to a Phantom v7.1 high-speed camera, which is utilized during Schlieren photography, front-light illuminated photography,

back-light illuminated photography and top-view photography sessions. The same camera is also utilized during oil-flow visualization tests and laser sheet illuminations of cross-sections. Typical data processing techniques include averaging, standard deviation, edge detection and frequency mapping. Phase Doppler Interferometry technique is used to detect the droplet dimensions. Detailed information on the experimental set-up and all measurement techniques are provided in Chapter 3.

## 8.2 Main Conclusions

Liquid jet injection into Mach 6 hypersonic flow is investigated experimentally by a high-speed camera and by employing different image processing techniques. Water is injected at different momentum flux ratios through different injector shapes having different aspect ratios. Correlations for the penetration height and lateral extension are proposed relating the injection momentum ratio and orifice diameter. Comparison of penetration heights for different injectors at certain downstream locations revealed that penetration height decreases as the injector's aspect ratio increases. In the same way, the lateral extension of the jet increases proportionally with the increasing aspect ratio of the injector. Injectors with higher aspect ratios are therefore more suitable for film cooling applications, e.g. for the cooling of combustion chambers in scramjets or for active thermal protection systems of space vehicles. On the other hand, streamwise rectangular and circular injectors with low aspect ratios are more suitable for fuel injection in scramjet applications. The results on penetration height for different injector geometries are in agreement with Mach 3 investigations of [61], indicating that the fundamental mechanism is similar for Mach 3 and Mach 6 cross flow cases. Mixing of the jet with the surrounding hypersonic cross flow, as investigated by the probability density function technique, is shown to be complete at a distance of $x/d_j = 40$, independent of the momentum flux ratio. The fracture of clumps for a circular q=10 jet appears at a frequency of 4.5 kHz and St=0.18 based on the jet diameter and velocity. Similar values are obtained for lower injection rates and other injectors. This liquid fracture can be influenced by the bow shock-separation shock interaction. The separation shock fluctuates at a frequency of 300-400Hz and St=0.011 (based on the cross flow and jet velocities difference and the separation shock length) independent of the injection ratio. Higher frequencies are found for the bow shock fluctuation (1kHz and more). This indicates a probable coupling between these two phenomena of liquid clumps' detachment and shock system fluctuation. A mechanism that is coupled between the liquid column, bow shock and separation shock is proposed, which serves the purpose of explaining the whipping phenomenon [16]. On the other hand, the discrepancy between the frequency peaks detected for the schlieren and back-light illumination images is believed to be due to the difference in the acquisition rate of the high-speed camera in these two techniques.

Flow topology that is generated by the injection of liquid into crossing hypersonic flow is investigated and compared to the flow topology generated by the injection of gas and by the existence of 3D roughness elements in hypersonic crossflow, to better

visualize the vortical flow patterns and to understand the main mechanisms driving the flow topology. Oil flow visualization, Schlieren photography, sublimation and laser sheet imaging techniques are employed for this purpose. The results of the experimental techniques are validated against each other. The flow topologies of the three obstacles (gas, liquid, 3D) are observed to have many similarities, like the existence of a separation region and a bow shock upstream of the injection or roughness point, although the typical distances and dimensions of these flow topologies may vary depending on the nature of the obstacle and non-dimensional numbers associated to the obstacles. Downstream of the injection or roughness point involves more complicated flow topologies. The downstream of the injection or roughness point is always dominated by vortices and recirculation regions. Occurrences of secondary vortices are typical with gas, liquid injections and 3D roughness elements, which are believed to be the triggering mechanism for laminar to turbulent transition. In the case of liquid injection, the flow field is very complicated due to the three-dimensional behavior of the liquid phase, being fragmented, atomized and finally mixed with air. The occurrence and initial displacement of the liquid double vortex are observed in some of the high speed movies, as well as by the laser sheet imaging technique. Among the 3D roughness elements studied, the cylindrical element possesses very similar flow topology compared to liquid or gas injections. On the other hand, the 3D ramp element has a unique flow topology, where one can observe the lifting off of the initial vortex pair, while generating a counter-rotating vortex pair attached to the surface [12].

During the second experimental campaign, the transient fragmentation of a water sphere is investigated, by an experimental campaign where a balloon filled with water is injected into a hypersonic flow at Mach 6 and a high speed camera, in combination with different techniques, is used to acquire information on the unsteady phenomena affecting the water. The investigation consists of the determination of the break-up mechanism that happens to a droplet suddenly exposed to a hypersonic cross flow. Various data processing algorithms, such as the *snake* or the time interpolation, are then applied to process the images and acquire useful information. The investigation on Schlieren images yields results about the shock wave profile and location. It has been possible to extract information regarding the location, angle and fluctuation of the shock waves, and thus to make an estimation of the fluid properties, such as Weber number, downstream and upstream of the discontinuities. The most important information, in terms of both quality and quantity, is obtained by the analysis of the back-light illumination movies. Using developed post-processing tools, information on the direction and the velocity of the liquid boundary has been collected. The most important discovery is that the fragmentation process of water is a shock wave dominated process, also including the involvement of high shear stress due to aerodynamic forces. In the case of an oblique shock wave, the penetration and the fragmentation behavior of water is dominated by the shock wave, and furthermore it is affected by the presence of a high shear stress that starts detaching clumps and fragmenting the water from the top. In the case of a bow shock (which

is the case for a blunt leading edge support), the bursting process is protected by a stable shock wave, where the fragmentation process is similar, but seems to be delayed in time due to lower shear stress [10].

Finally, the Phase Doppler Interferometry technique has been applied to the liquid injection set-up to determine the distribution of droplet size. Overall, the technique is observed to be very challenging for such a high velocity stream, because of the high frequency phenomena occurring, relatively short test duration (seconds compared to minutes), limited optical access and finally because of the majority of non-spherical liquid droplets under the influence of a high aerodynamic shear stress. Nevertheless, the measurements agree with the previous observations such that the mixing and hence the atomization of the liquid phase is completed at a distance of $x/d_j = 35$ downstream of the injection point. The measurements of mean ($D_{10}$) and Sauter mean diameters ($D_{32}$) are compared with the models existing in literature and it has been concluded that the Sauter mean diameter is inversely proportional with the Weber number multiplied by the Reynolds number. This has been proven only by taking measurements both in the streamwise ($x$) direction and in the vertical ($y$) direction, as the momentum flux ratio influences the penetration height and thus the relative location of the measurement point with respect to the trajectory of the liquid phase [95]. There exists a need of more experimental evidence to support the validity of this theorem for hypersonic cross flow cases.

As an overall evaluation, it can be said that the findings of previous researches on the same problem for high supersonic cross flow cases (where cross flow Mach number is equal to or greater than 2) can also be applied to Mach 6 case, with caution. The mechanisms yielding to fragmentation and the flow topology are similar. The main difference for the Mach 6 cross flow case is that the flow topology is much more dominated by the shock wave system, as the shear flow and the pressure differences created by the shock wave system are the leading factors shaping the flow topology and thus the fragmentation mechanism. Although the high speed of the flow field makes it difficult to visualize the flow patterns and vortex systems (that are believed to be very important if one desires to understand the complete flow topology), the advances in technology makes it possible to visualize such phenomena at an adequately high speed.

## 8.3 Lessons Learned and Recommendations for Future Work

The work presented in this thesis, to the best knowledge of the researchers, is the first time where an experimental investigation on liquid fragmentation in hypersonic cross flow conditions is published in open literature. The previous works were either for lower cross flow velocity conditions, or were not published due to their confidentiality. Hence, this work is seen as an initial step taken to enlighten a not-so-well-known field of hypersonic aerodynamics concerning multi-phase flow. There are many possible enhancements to carry out the research further and obtain

more detailed and accurate results. This Section presents a self-criticism on the instrumentation and techniques applied, while providing suggestions for researchers aiming at studying the topic in the future.

### 8.3.1 Facility and Experimental Set-Up

The H-3 facility of the von Karman Institute that is used for the whole test campaign is a blow down type Mach 6 wind tunnel. The facility is observed to be adequate for the purpose of the test campaign. The biggest advantage of this facility is the test duration, that can go up to 15 seconds depending on the test Reynolds number and availability of compressed air. This duration is very long, compared to mili-second duration of shock tubes that are usually employed for similar tests. The only disadvantage of a blow-down type facility is that it consumes a lot of compressed air. Depending on the duration of the test, the H-3 facility consumes between 5 and 10 bars of the $40m^3$ compressed air from the 40bar reservoir. This limits the number of tests to 10 tests per day, under ideal conditions.

The facility has a dedicated Schlieren system and windows on both sides and at the top with high quality glasses, which proved to be very useful during the whole test campaign. The only optical access problem came from the diffuser of the facility, prohibiting the researchers to align the laser and the receiver elements of the PDI system with an angle larger than 30degrees.

The utilization of the high-speed camera and optical measurement techniques such as schlieren photography are all methods that convert three dimensional phenomena into two dimensional visualizations. The sensor of the high-speed camera always measures the integrated intensity of the light along the complete light path. Similarly, the schlieren technique measures the deviation of light due to the existence of density gradients not only in the region of interest, but on the complete path of the light rays. This path also includes, for example, the shear layer which is emerging from the walls of the converging-diverging nozzle of the wind tunnel facility. All these factors make the comprehension of images more difficult. The researcher should always be aware of the three dimensionality of the flow field and keep in mind the possible effects on two dimensional photographs. One good way of better comprehending the complex three-dimensional flow field is to make visualizations from different angles and on different planes. The oil flow visualization techniques are utilized in this study for this reason. The computational fluid dynamics tools would also be very useful in seeing the three-dimensional field. However, the numerical solution of a multi-phase flow field problem with fragmentation and atomization is a very challenging problem, that is not easy at all to develop and apply successfully.

The set-up used to inject water into the freestream (see Section 3.2.1) is basically a rotameter to control the mass flow rate of water and a valve to open or close the water supply. This set-up is connected to tap water. To avoid freezing in the low pressure test section for long duration tests, the water is heated to 30C by a flexible resistance wrapped around the water-tube. Although this simple and

practical set-up has proved to be robust and useful throughout the whole test campaign, there are a few possibilities to enhance the quality of the tests. Avoiding tap water and using de-mineralised water would certainly decrease the uncertainty on liquid properties such as density or viscosity, and it would also avoid the problem of blocking the liquid injectors through depositing of calcium and other minerals. The fluctuation of the mass flow rate of injected water during the test is one of the most important uncertainty sources. This could be avoided by using water from a pressurized container and utilising a flow meter instead of the rotameter. An electric valve to open or close the water supply (instead of the manual valve used in this study) would reduce the number of people necessary to perform a test.

An attempt is made to compare the flow topology of liquid injection into hypersonic cross flow with the flow topologies of gas injection and rigid 3D obstacles in hypersonic cross flow. Owing to the success of this comparison, which allows the researchers to detect more details in the flow topology, it is recommended to continue such comparisons further. The existing measurements of [143] are used in this study to see the flow topology of wedge and short cylinder obstacles. The same kind of flow visualization tests can be performed using a deflected and long cylindrical element, that imitates the penetration height trajectory of liquid injection.

### 8.3.2 Non-dimensional numbers and Parameters

The experimental campaign presented in this test has been limited to water injection through a 1mm diameter circular (or equal area rectangular) injector at 90 degrees into a Mach 6 cross flow with a total pressure of 20 bars and a total temperature of 500K. Due to the complexity of the investigated problems, and also to check the repeatability, several measurement techniques are applied almost always on the same test conditions, requiring hundreds of tests per measurement technique. The only important parameters that are varied considerably are the mass flow rate of injected liquid and the geometry (thus the aspect ratio) of the injectors. Although the variation of the mass flow rate of liquid has allowed a big range of momentum flux ratio of q (between 2 and 10), the other critical non-dimensional numbers such as Weber, Reynolds or Ohnesorge (see Section 2.2) are varied very little or not at all.

A list of parameters that can be varied in the future studies are listed below.

- Liquid: Water provides a very comfortable work environment for such an experimental test campaign as it is available easily, non-toxic, non-flammable and as it requires minimum cleaning after the test. However, once the measurement techniques and data processing algorithms are developed for water, it would be advisable to test different liquids such as glycerine, hexanol, ethanol, prophanol, etc [136]... Different liquids having different properties (viscosity, surface tension, density) would yield a wide range of Weber and Ohnesorge numbers to investigate. On the other hand, the researchers comparing different liquids should pay attention to the fact that different chemical reactions might

occur (including flashing) depending on the liquid and test conditions. The availability, storage, toxicity, flammability, potential damage to the facility and optical elements and cleaning of the liquid after the test are all important issues that need to be considered prior to the test campaign.

- Freestream conditions: During the experimental campaign presented in this thesis, the flow properties are kept constant at Mach 6, 20bar total pressure and 500K total temperature, resulting in a freestream unit Reynolds number of $18 \times 10^6 m^{-1}$. All these parameters could be varied to study the effect of the freestream conditions on penetration height, flow topology, fragmentation mechanism and Sauter mean diameter of the injected liquid. Although total pressure and total temperature are the control parameters that can be varied easily depending on the facility, the freestream Reynolds number should be considered as the main flow parameter, together with Mach number. The effect of Mach number (thus compressibility) of the freestream can be examined only in a facility with adaptable nozzle walls or in a facility where the nozzle can be changed easily. Facilities operating at Mach numbers higher than 8 will require a lot of compressed air, increasing the test cost and decreasing the test duration. One should also keep in mind that Mach numbers higher than 10 are only possible during flights at high altitudes, where the freestream air properties (and thus the Reynolds number) vary significantly. For space vehicles flying at higher altitudes, flights can even take place in the rarefied regime of the atmosphere. In such cases, the Knudsen number should also be taken into account in addition to Mach and Reynolds numbers.

- Injector geometry: Three different liquid injectors are utilized to study the effect of aspect ratio on penetration height and lateral extension of liquid jets injected into Mach 6 cross flow. The exit area of all injectors are kept the same to be able to have the same mass flow rate at similar momentum flux ratio tests. This study has shown that the injector geometry has a very important effect on flow topology as it can change the windward area of the liquid jet which is in direct contact with the cross flow. Correlations predicting penetration height and lateral extension are proposed for the 1mm diameter circular injector. The fact that these correlations are not valid for the rectangular injectors, despite them having the same cross sectional area, indicates that the aspect ratio and the geometry play important roles on the trajectory of the injected liquid. More experimental data is needed to find out a relation between different injector geometries. The injector geometries tested during this campaign are basic generic shapes selected for a general purpose study. Depending on the application, a three dimensional injector geometry can also be designed and tested to see its effect on the vortex system of the flow field. This design can also include a variation in the injection angle of liquid into the cross flow, an important parameter [86] that has not been examined within this study. Varying the exit area of the injector would help the researchers to vary the Ohnesorge number. However, one should pay attention to the mass flow

rate of liquid when the exit diameter is changed. To give an example, one needs four times more mass flow rate to have the same momentum flux ratio with a 2mm diameter circular injector, compared to that of a 1mm diameter circular injector. Such a difference in mass flow rate changes the flow topology completely even though the momentum flux ratio remains the same [12].

### 8.3.3 PHOTOGRAPHIC ELEMENTS

The high-speed photography technique has been an extremely useful tool during the experimental campaign presented in this thesis, providing the majority of the results and conclusions. The most important elements used are the high-speed camera including the lens, the Schlieren system including the mirrors and optics and finally the optical access to the facility.

The optical elements need to be of high quality and clean all the time. Although the windows can (and have to be) cleaned frequently using proper cleaning agents, the same can not be said for mirrors of the Schlieren system. These mirrors are coated with a special layer to enhance reflection and any attempt to clean them may result in permanent scratches. The best way of keeping them clean is covering them properly whenever they are not used, avoiding them to get dirty. If they are needed to be cleaned, professional cleaning agents that do not involve chemical ingredients and clean dry compressed air should be utilized.

The Phantom v7.1 high-speed camera utilised during the whole experimental campaign has been found to be adequate for the purpose. The camera has a resolution of 800 x 600 pixels, a memory of 1GB and a minimum exposure time of $2\mu sec$. Although it is possible to find a better camera thanks to the recent advancements in high-speed photography, the cost of such a high-speed camera remains high. The frame rate and memory of the Phantom v7.1 were acceptable. Typical frame rates during the test campaign changed between 10000 and 60000 frames per second. Although higher frame rates would be appreciated for some cases, the limitation on frame rate was not because of the camera, but other reasons such as available light or triggering of the camera. Triggering has been an important issue for the transient water-balloon tests that are completed in less than a second. An automatic triggering mechanism that would sense the bursting of the balloon (for example by the shadow of the liquid moving in the downstream direction right after bursting of the balloon) is highly recommended to increase the frame rate while shooting transient phenomena. The main shortcoming of the Phantom v7.1 high-speed camera is believed to be the low resolution of the sensor. The full resolution of 800 x 600 pixels has to be reduced further for frame rates higher than 5000 frames per second, down to less than 256 x 256 pixels for 60000 images per second. Many features can not be captured at this low resolution, such as the wavelength of Rayleigh-Taylor waves as in the work of [59], for stability analysis.

While working with a high-speed camera with the intention of acquiring high frame rate movies, the most important element is the available light. The choice of

light source and how the light is projected are therefore very critical. During this experimental campaign, halogen lamps of 1000 to 1600 Watts are used. Although more powerful light sources are always preferable, it should be kept in mind that most of the bulbs consume their power by radiating an enormous amount of heat, decreasing the intensity of illumination. This is especially critical for the Schlieren technique, where a point light source is needed. For front-light illumination and back-light illumination photography, another very important aspect is the uniformity of the illumination. Several (more is better) light sources should be used from different directions to ensure a uniform illumination. Semi-transparent papers can be used to diffuse the light for back-illumination set-up. Care should be taken on the distance between the light source and semi-transparent paper, as a trade-off is necessary on the amount of illumination (closer) and uniformity (further away). No matter how powerful the light source is and no matter how good the lens is, the minimum exposure time of a single frame is determined by the high-speed camera, which is $2\mu sec$ for Phantom v7.1 camera. As the exposure time affects the sharpness of the image, it is normal that one would like to shoot images at even lower exposure times, in the order of nanoseconds. This is only possible by using high-frequency spark generators, instead of continuous light sources. However, spark generators that can work at such high frequencies (in the order of 100kHz) and such low exposure times (in the order of nanosecond) have their own problems. They can not keep the same power level, they can not run for long enough durations, they are difficult to synchronize and they are expensive.

The objective attached to the camera is also very important, as it can block most of the available light. Different objectives should be used for different techniques. A wide-angle objective is more suitable for front-light illumination photography, whereas a tele-objective is preferred for back-light illumination movies. Instead of using one objective with zooming capability, several fixed focal length objectives should be preferred, as they have superior optical quality and they have larger aperture openings. All objectives are recommended to be used at their maximum aperture setting, as this minimizes both the amount of light blocked and the depth of field. With a small depth of field, once can focus on the cross-section of interest, neglecting the layers out of interest.

### 8.3.4 Experimental Techniques

Photographic techniques are the main measurement techniques utilized during the experimental campaigns and they have proven to be extremely useful with the proper image processing tools. As the capabilities of high-speed photography techniques are improved in terms of optical access, uniformity of illumination, exposure time and frame rate as discussed in Section 8.3.3, the accuracy of the results would also be improved. The technology is continuously advancing, allowing researchers to purchase better high-speed cameras, optical windows, lights, lenses and mirrors

for cheaper prices. At the data processing part, Matlab [1] is a very powerful tool for image processing. There are open source alternatives to Matlab platform, such as SciLab [2], Octave [3] and FreeMat [4], although none of these software platforms are compared with Matlab within the scope of this work.

The Phase Doppler Interferometry (PDI) technique is applied to determine the mean and Sauter mean diameter distribution of the liquid injected into Mach 6 cross flow. PDI is a very well established technique for this purpose. However, one should keep in mind that this is an advanced and complicated technique with many parameters such as refraction angle, gain for the receiver, data acquisition frequency, mixing frequency, filter frequency, thresholds for receivers, etc... The proper alignment of the laser and receiver is the most critical element for obtaining accurate results. The utilization of this technique is more straightforward for continuous and low speed spray applications. Unfortunately, the same observation is not valid for the experiments carried out in this study because of the short duration of the experiments and the complexity of the flowfield. High aerodynamic shear force causes the liquid phase to fragment in ligaments and then in non-spherical droplets, decreasing the detection capability of the PDI system. The short duration tests make it difficult to optimize the parameters. The low optical access of the wind tunnel prevents the researcher to have a set-up where the positions of the receiver and the laser have the optimum angles. Finally, the vibration of the complete facility during a test causes vibration of the PDI elements, resulting in misalignment. All these difficulties, combined with the necessity of obtaining a minimum number of validated data to have a statistically meaningful data set, make it very difficult to work with PDI at a Mach 6 wind tunnel. Nevertheless, this study has shown that it is possible to take droplet size measurements. The experimental data collected in this study indicates that the atomization mechanism is more complex for hypersonic cross flow cases, compared to lower velocity conditions. More experimental data are needed to study the effect of spatial location and injector geometry on final SMD value.

There are other measurement techniques that are suitable for studying liquid fragmentation under compressible cross flow conditions, as suggested by [77]. The spectroscopic techniques such as Raman scattering, is beneficial for studying mixing properties. "Planar Laser Induced Fluorescence" (PLIF) and "Planar Laser Induced Fluorescence and Phosphorescence"(PLIFP) techniques are other non-intrusive spectroscopic techniques to study the flowfield in detail. The researchers are encouraged to apply these techniques on liquid fragmentation studies under the effect of hypersonic cross flows.

Finally, the evaluation of the repeatability of the experiments performed in this study has been an issue that deserves discussion. The complex nature of the flow field combined with the unsteady phenomena resulting from shock – shock and shock

[1] http://www.mathworks.com/
[2] http://www.scilab.org/
[3] http://www.gnu.org/software/octave/
[4] http://freemat.sourceforge.net/

– boundary layer interactions has made it difficult to carry out a scientific repeatability analysis for the chaotic experimental conditions. For the liquid injection tests, the repeatability is tried to be ensured by averaging thousands of images from different measurement techniques. This has been possible by the quasi-steady state of the liquid injection tests. The agreements in mean and standard deviation analysis, as well as the agreements among different techniques (such as edge detection and probability density function techniques for penetration height determination) have yielded a certain level of confidence. The issue of repeatability for the atomization measurements using phase doppler interferometry technique is checked by merging the droplet size distributions obtained from several tests performed at the same test conditions. It is observed that the droplet size distribution obtained after merging the results of several tests results in an expected distribution that can be represented by a log-normal fit. The statistical quantities (such as mean or Sauter mean diameter) from individual tests performed at similar conditions agreed with each other, within an envelope of $\pm 3\%$. Ensuring the repeatability has been the major issue for the balloon tests, which are extremely chaotic especially for the sharp leading edge support cases. At the beginning of the test campaign, many trials have been made to be able to obtain a repeatable pattern of the bursting of the water balloon and the fragmentation of the water inside. Due to the difficulty to measure and compare the repeatability of the experimental results, it is decided to control rather the boundary conditions of the experiments. This was ensured by controlling the mass and the diameter of the water balloon before every test. The mass or diameter of the balloon were not allowed to vary more than $\pm 10\%$. During the experimental work performed for this campaign, the major effort has been trying different measurement techniques for the purpose of checking the validity of applying such techniques under hypersonic flow condition and, whenever possible and feasible, collecting experimental data at hypersonic conditions. Focusing on the application of many techniques, the repeatability of the tests has been regarded as of secondary importance. However, it is believed that better repeatability can be obtained in the future by performing more measurements and controlling the boundary conditions of the tests more carefully.

# Bibliography


[1] R. Abu-Gharbieh, G. Hamarneh, T. Gustavsson, and C. Kaminski, *Flame front tracking by laser induced fluorescence spectroscopy and advanced image analysis*, Optics Express, 8 (2001), pp. 278–287.

[2] D. Adler and A. Baron, *Prediction of a three-dimensional circular turbulent jet in crossflow*, AIAA Journal, 17 (1979), pp. 168–174.

[3] M. Albertson, Y. Dai, R. Jensen, and H. Rouse, *Diffusion of submerged jets*, Trans. ASCE, 115 (1950), pp. 639–664.

[4] H. Albrecht, *Laser Doppler and Phase Doppler Measurement Techniques*, Springer, 2003.

[5] H.-E. Albrecht, M. Borys, N. Damaschke, and C. Tropea, *Laser Doppler and Phase Doppler Measurement Techniques*, Springer, 2003. ISBN 3540678387.

[6] J. Anderson, *Hypersonic and High Temperature Gas Dynamics*, AIAA, 2000.

[7] Anon., *Symposium on Analysis of a Jet in a Subsonic Crosswind*, in NASA SP-218, Sept. 1969.

[8] K. Aoyagi and P. K. Snyder, *Experimental Investigation of a Jet Inclined to a Subsonic Crossflow*, AIAA, No 81-2610 (1981).

[9] C. O. Asma, D. Masutti, J. Beloki Perurena, and O. Chazot, *Liquid Fragmentation in High Speed Flows*, vol. 2009-04 of VKI Lecture Series, von Karman Institute for Fluid Dynamics, March 2009, ch. Fragmentation of Liquid in Hypersonic Cross Flow. ISBN 978-2-930389-92-3.

[10] C. O. Asma, D. Masutti, and O. Chazot, *Experimental investigation of liquid fragmentation in hypersonic crossflow*, in 27th AIAA Applied Aerodynamics Conference, June 2009. AIAA 2009-3506.

[11] C. O. Asma and P. Rambaud (Editors), *Liquid Fragmentation in High Speed Flows*, vol. 2009-04 of VKI Lecture Series, von Karman Institute for Fluid Dynamics, Rhode Saint Genèse, Belgium, March 2009. ISBN 978-2-930389-92-3.

[12] C. O. ASMA, S. TIRTEY, AND F. SCHLOEGEL, *Flow topology of gas, liquid and 3d obstacles in hypersonic flow*, in 27th AIAA Applied Aerodynamics Conference, June 2009. AIAA 2009-3944.

[13] E. ATRAGHJI, *More Than Meets the Eye: The Oil Dot Technique.*, Flow Visualization II, (1982), pp. 619–628.

[14] W. D. BACHALO, *Spray Diagnostics for the Twenty-First Century*, Atomization and Sprays, 10 (2000), pp. 439–474.

[15] J. BELOKI PERURENA, *Experimental investigation of a liquid jet injection into a crossing hypersonic crossflow*, Project Report 2007-04, von Karman Institute for Fluid Dynamics, Rhode Saint Genèse, Belgium, June 2007.

[16] J. BELOKI PERURENA, C. O. ASMA, R. THEUNISSEN, AND O. CHAZOT, *Experimental investigation of liquid jet injection into mach 6 hypersonic crossflow*, Experiments in Fluids, DOI 10.1007/s00348-008-0566-5 (2008). Published electronically.

[17] A. BEN-YAKAR AND R. HANSON, *Cavity flameholders for ignition and flame stabilization in scramjets: review and experimental study*, AIAA paper, 3122 (1998).

[18] S. BERNHARDT, *Measurement of droplet size of liquid injected into a hypersonic cross-flow*, Stagiaire Report 2008-23, von Karman Institute for Fluid Dynamics, Rhode Saint Genèse, Belgium, August 2008.

[19] S. BERRY, R. NOWAK, AND T. HORVATH, *Boundary Layer Control for Hypersonic Airbreathing Vehicles*, AIAA Paper, 2246 (2004), p. 2004.

[20] J. BLANCHARD, Y. BRUNET, AND A. MERLEN, *Influence of a counter rotating vortex pair on the stability of a jet in a cross flow: an experimental study by flow visualizations*, Experiments in Fluids, 26 (1999), pp. 63–74.

[21] H. BOERRIGTER, *Calibration of the H3 wind tunnel using pitot probes*, Internal Note IN 94, von Karman Institute for Fluid Dynamics, Rhode Saint Genèse, Belgium, November 1993.

[22] R. BOYCE, S. GERARD, AND A. PAULL, *The HyShot scramjet flight experiment–flight data and CFD calculations compared*, 12th AIAA International Space Planes and Hypersonic Systems and Technologies, (2003), pp. 2003–7029.

[23] J. BROADWELL AND R. BREIDENTHAL, *Structure and mixing of a transverse jet in incompressible flow*, Journal of Fluid Mechanics Digital Archive, 148 (2006), pp. 405–412.

[24] T. BRZUSTOWSKI, *In Turbulent Combustion*, Progress in Astronautics and Aeronautics, 58 (1977), pp. 407–430.

[25] E. CALLAGHAN AND R. RUGGERI, *A General Correlation of Temperature Profiles Downstream of a Heated-AirJet Directed Perpendicularly to an Air Stream*, Storming Media, 1951.

[26] E. E. CALLAGHAN AND R. S. RUGGERI, *Investigation of the Penetration of an Air Jet Directed Perpendicularly to an Air Stream*, Tech. Report TN 1615, NACA, June 1948.

[27] I. CATTON, D. HILL, AND R. MCRAE, *Study of Liquid Jet Penetration in a Hypersonic Stream*, AIAA Journal, 6 (1968), pp. 2084–2089.

[28] H. C. CHANG, *Aufrollung Eines Zylindrischen Strahles Durch Querwind*, PhD thesis, Univ. of Goettingen, Germany, 1942. English translation USAF-ARL 73-0131, Sept. 1973.

[29] S. CHIU, K. ROTH, R. MARGASON, AND J. TSO, *A numerical investigation of a subsonic jet in a crossflow*, In AGARD, Computational and Experimental Assessment of Jets in Cross Flow 14 p (SEE, (1993).

[30] L. CORTELEZZI AND A. KARAGOZIAN, *On the formation of the counter-rotating vortex pair in transverse jets*, Journal of Fluid Mechanics, 446 (2001), pp. 347–373.

[31] E. CURRAN, *Scramjet Engines: The First Forty Years*, Journal of Propulsion and Power, 17 (2001), pp. 1138–1148.

[32] N. DAMASCHKE, G. GOUESBET, G. GREHAN, AND C. TROPEA, *Optical techniques for the characterization of non-spherical and non-homogeneous particles*, Measurement Science and Technology, 9 (1998), pp. 137–140.

[33] J. DELERY, *Shock/Shock and Shock-Wave/Boundary-Layer Interactions in Hypersonic Flows*, Tech. Report 761, AGARD, 1989. Part 9.

[34] R. FEARN AND R. WESTON, *Vorticity associated with a jet in a cross flow*, AIAA Journal, 12 (1974), pp. 1666–1671.

[35] R. FEARN AND R. WESTON, *Induced pressure distribution of a jet in a cross-flow*, NASA, TN D-7916, (1975).

[36] R. FEARN AND R. WESTON, *Velocity field of a round jet in a cross flow for various jet injection angles and velocity ratios*, Tech. Report TP-1506, NASA, 1979.

[37] R. L. FEARN, H. DODDINGTON, AND R. WESTPHAL, *LDV Studies of a Jet in Crossflow*, Tech. Report No 80238-60, NADC, 1981.

[38] R. L. FEARN AND R. P. WESTON, *Induced velocity field of a jet in a crossflow*, Tech. Report TP-1087, NASA, May 1978.

[39] T. Fric and A. Roshko, *Vortical structure in the wake of a transverse jet*, Journal of Fluid Mechanics, 279 (1994), pp. 1–47.

[40] T. F. Fric and A. Roshko, *Structure in the Near Field of the Transverse Jet*, in Proceedings of Seventh Symposium on Turbulent Shear Flows, Aug 1989, pp. 6.4.1 – 6.4.6. Vol 1 (A90–35176).

[41] S. Frolov, V. Aksenov, and I. Shamshin, *Shock wave and detonation propagation through U-bend tubes*, Proceedings of the Combustion Institute, 31 (2007), pp. 2421–2428.

[42] B. Gelfand, S. Frolov, and M. Nettleton, *Gaseous detonations: a selective review*, Progress in energy and combustion science, 17 (1991), pp. 327–371.

[43] G. Gentry, R. Margason, L. R. Center, N. Aeronautics, S. Administration, and U. States, *Jet-induced Lift Losses on VTOL Configurations Hovering in and Out of Ground Effect*, National Aeronautics and Space Administration, 1966.

[44] M. Gruber, A. Nejad, T. Chen, and J. Dutton, *Mixing and Penetration Studies of Sonic Jets in a Mach 2 Freestream*, Journal of Propulsion and Power, 11 (1995), pp. 315–323.

[45] M. R. Gruber, A. S. Nejab, T. H. Chen, and J. C. Dutton, *Bow shock/jet interaction in compressible transverse injection flowfields*, AIAA journal, 34 (1996), pp. 2191–2193.

[46] M. R. Gruber, A. S. Nejad, T. H. Chen, and J. C. Dutton, *Transverse Injection from Circular and Elliptic Nozzles into a Supersonic Crossflow*, Journal of Propulsion and Power, 16 (2000), pp. 449–457.

[47] T. Grunberg, *The measurement of disturbance levels in the VKI H3 Mach 6 hypersonic tunnel,*, Stagiaire Report 2008-20, von Karman Institute for Fluid Dynamics, Rhode Saint Genèse, Belgium, July 2008.

[48] A. Gülhan, G. Schütte, and B. Stahl, *Experimental Study on Aerothermal Heating Caused by Jet-Hypersonic Crossflow Interaction*, Journal of Spacecraft and Rockets, 45 (2008), pp. 891–899.

[49] L. Harms, *Experimental Investigation of the Flow Field of a Hot Turbulent Jet With Lateral Flow*, Part II. NASA TT F-15706, (1974).

[50] D. Harvey, *Drop size distribution resulting from liquid jet injection across a supersonic stream*, AIAA Journal, 11 (1973), pp. 826–830.

[51] B. Haven and M. Kurosaka, *Kidney and anti-kidney vortices in crossflow jets*, Journal of Fluid Mechanics, 352 (1997), pp. 27–64.

[52] J. Hermanson and M. Winter, *Mie scattering imaging of a transverse, sonic jet in supersonic flow*, AIAA journal, 31 (1993).

[53] J. Hilbing and S. Heister, *Droplet size control in liquid jet breakup*, Physics of Fluids, 8 (1996), p. 1574.

[54] J. Hilbing, S. Heister, and C. Spangler, *A Boundary-Element Method for Atomization of a Finite Liquid Jet*, Atomization And Sprays, 5 (1995), pp. 621–638.

[55] W. Hinson, P. Gooderum, and D. Bushnell, *Experimental Investigation of Multiple-jet Liquid Injection Into Hypersonic Flow*, Langley Research Center, National Aeronautics and Space Administration, Clearinghouse for Federal Scientific and technical Information, Springfield, VA 22151, 1970.

[56] L. Hsiang and G. Faeth, *Near-limit drop deformation and secondary breakup*, International Journal of Multiphase Flow, 18 (1992), pp. 635–652.

[57] R. Ingebo, H. Foster, and N. G. R. Center, *Drop-size distribution for crosscurrent breakup of liquid jets in airstreams*, National Advisory Committee for Aeronautics, 1957.

[58] Y. Ivanov, *Shape of the centerline of an axisymmetric fan type jet in a cross flow*, Izv. VUZ Aviotsionnaya Teknika, 4 (1963).

[59] D. Joseph, J. Belanger, and G. Beavers, *Breakup of a liquid drop suddenly exposed to a high-speed airstream*, International Journal of Multiphase Flow, 25 (1999), pp. 1263–1303.

[60] D. D. Joseph, G. S. Beavers, and T. Funada, *Rayleigh–Taylor instability of viscoelastic drops at high Weber numbers*, Journal of Fluid Mechanics, 453 (2002), pp. 109–132.

[61] B. P. Joshi and J. A. Schetz, *Effect of injector shape on penetration and spread of liquid jets*, AIAA Journal, 13 (1975), pp. 1137–1138.

[62] A. Karagozian, *Background on and Applications of Jets in Crossflow*, Manipulation and Control of Jets in Crossflow, (2003).

[63] A. Karagozian, K. Wang, A. Le, and O. Smith, *Transverse gas jet injection behind a rearward-facing step*, Journal of Propulsion and Power, 12 (1996), pp. 1129–1136.

[64] A. R. Karagozian, *An analytical model for the vorticity associated with a transverse jet*, AIAA Journal, 24 (1986), pp. 429–436.

[65] A. R. Karagozian, K. S. C. Wang, and O. I. Smith, *Manipulation and Control of Jets in Crossflow*, Centre International des Sciences Mecaniques, Springer, 2003, ch. Jets Injected Normally into Compressible Crossflow. ISBN 3-211-00753-9.

[66] D. KARWAT, *Phase doppler particle anemometry analyses of liquid jets injected in hypersonic crossflow*, Stagiaire Report 2008-08, von Karman Institute for Fluid Dynamics, Rhode Saint Genèse, Belgium, 2008.

[67] M. KASS, A. WITKIN, AND D. TERZOPOULOS, *Snakes: Active contour models*, International Journal of Computer Vision, 1 (1988), pp. 321–331.

[68] M. S. KAVSAOGLU, I. S. AKMANDOR, C. CIRAY, AND K. FUJII, *Navier-Stokes Simulation of Two and Three Dimensional Jets in Crossflow*, AIAA, (1991).

[69] R. KEANE AND R. ADRIAN, *Theory of cross-correlation analysis of PIV images*, Applied Scientific Research, 49 (1992), pp. 191–215.

[70] R. KELSO, T. LIM, AND A. PERRY, *An experimental study of round jets in cross-flow*, Journal of Fluid Mechanics Digital Archive, 306 (2006), pp. 111–144.

[71] A. M. KEUTHE, *Investigation of the Turbulent Mixing Regions Formed by Jets*, J. Applied Mech., (1935), pp. A87–A95.

[72] S. KHAYAM, *The Discrete Cosine Transform (DCT): Theory and Application*, Department of electrical & computing engineering, Michigan State University, (2003).

[73] M. KOLPIN, K. HORN, AND R. REICHENBACH, *Study of Penetration of a Liquid Injectant into a Supersonic Flow*, AIAA Journal, 6 (1968), pp. 853–858.

[74] A. KROTHAPALLI, L. LOURENCO, AND J. BUCHLIN, *Separated flow upstream of a jet in a crossflow*, AIAA journal, 28 (1990), pp. 414–420.

[75] D. KÜCHEMANN AND J. WEBER, *Aerodynamics of Propulsion*, McGraw-Hill, 1953.

[76] D. KUZO, *An experimental study of the turbulent transverse jet*, PhD thesis, California Institute of Technology, 1995.

[77] G. LAMANNA, I. STOTZ, AND B. WEIGAND, *Liquid Fragmentation in High Speed Flows*, vol. 2009-04 of VKI Lecture Series, von Karman Institute for Fluid Dynamics, March 2009, ch. A Review of Experimental Techniques To Study Liquid Fragmentation.

[78] A. LEFEBVRE, *Atomization and sprays*, CRC Press, 1989.

[79] M. LEONG, V. MCDONELL, AND G. SAMUELSEN, *Effect of Ambient Pressure on an Airblast Spray Injected into a Crossflow*, Journal Of Propulsion And Power, 17 (2001), pp. 1076–1084.

[80] D. LESS AND S. JA, *Transient behavior of liquid jets injected normal to a high velocity gas stream*, AIAA, 24 (1986), pp. 1979–1986.

[81] H. LI, N. AERONAUTICS, AND C. SPACE ADMINISTRATION. AMES RESEARCH CENTER, MOFFETT FIELD, *Breakup of a liquid jet in supersonic crossflow*, AIAA journal, 30 (1992), pp. 1919–1921.

[82] H. LIEPMANN AND J. LAUFER, *Investigations of Free Turbulent Mixing*, NACA TN 1257, (1947).

[83] K. LIN, P. KENNEDY, AND T. JACKSON, *Penetration heights of liquid jets in high-speed crossflows*, in AIAA Aerospace Sciences Meeting & Exhibit, 40 th, Reno, NV, 2002.

[84] K. LIN, P. KENNEDY, AND T. JACKSON, *Structures of Aerated Liquid Jets in High Speed Crossflows*, AIAA Paper, 3178 (2002), p. 2002.

[85] K. LIN, P. KENNEDY, AND T. JACKSON, *Structures of Water Jets in a Mach 1.94 Supersonic Crossflow*, AIAA Paper, 971 (2004).

[86] K. LIN, K. PJ, AND J. TA, *Spray penetration heights of angled-injected aerated-liquid jets in supersonic crossflows*, in 38th AIAA Aerospace Sciences Meeting and Exhibit, Jan 2000. AIAA 2000-0194.

[87] T. LIN, L. SPROUL, M. OLMOS, AND N. THYSON, *Flight-Dynamics Instability Induced by Heat-Shield Ablation Lag Phenomenon*, Journal Of Spacecrafts And Rockets, 40 (2003), pp. 615–621.

[88] T. C. LIN, *The Influence of Laminar Boundary Layer Transition on Entry Vehicle Design and Its Performances*, in 45th AIAA Aerospace Sciences Meeting and Exhibit, 2007. AIAA 2007-309.

[89] A. MARANGOZ, *Investigation of liquid jet injection into a hypersonic cross flow*, Project Report 2006-21, von Karman Institute for Fluid Dynamics, Rhode Saint Genèse, Belgium, June 2006.

[90] R. MARGASON, *The Path of a Jet Directed at Large Angles to a Subsonic Free Stream.*, master's thesis, Virginia Polytechnic Institute, 1968.

[91] R. MARGASON, *Fifty years of jet in cross flow research*, in Computational and Experimental Assessment of Jets in Crossflow, AGARD, ed., Nov. 1993. CP-534.

[92] R. MARGASON, S. KJELGAARD, W. SELLERS III, C. MORRIS JR, K. WALKEY, AND E. SHIELDS, *Subsonic panel methods- A comparison of several production codes*, in AIAA 23 rd Aerospace Sciences Meeting, 1985.

[93] R. MARGASON AND J. LAMAR, *Vortex-lattice FORTRAN Program for Estimating Subsonic Aerodynamic Characteristics of Complex Planforms*, Langley Research Center, National Aeronautics and Space Administration, USA, 1971.

[94] D. MASUTTI, *Experimental investigation of liquid fragmentation in hypersonic crossflow*, Project Report 2008-14, von Karman Institute for Fluid Dynamics, Rhode Saint Genèse, Belgium, June 2008.

[95] D. MASUTTI, S. BERNHARDT, C. O. ASMA, AND R. VETRANO, *Experimental characterization of liquid jet atomization in mach 6 crossflow*, in 39th AIAA Fluid Dynamics Conference, June 2009. AIAA 2009-4220.

[96] G. MATEER AND H. LARSON, *Unusual Boundary-Layer Transition Results on Cones in Hypersonic Flow*, AIAA Journal, 7 (1969), pp. 660–664.

[97] R. T. MCLOSKEY, J. M. KING, L. CORTELEZZI, AND A. R. KARAGOZIAN, *The actively controlled jet in crossflow*, Journal of Fluid Mechanics, 452 (2002), pp. 325–335.

[98] H. MCMAHON AND D. MOSHER, *Experimental Investigation of Pressures Induced on a Flat Plate by a Jet Issuing into a Subsonic Crosswind*, Analysis of a Jet in a Subsonic Crosswind, NASA SP-218, (1969), pp. 49–62.

[99] C. MEINHART, S. WERELEY, AND J. SANTIAGO, *A PIV Algorithm for Estimating Time-Averaged Velocity Fields*, Transactions - American Society Of Mechanical Engineers Journal Of Fluids Engineering, 122 (2000), pp. 285–289.

[100] N. MESSERSMITH AND J. DUTTON, *Characteristic features of large structures in compressible mixing layers*, AIAA Journal, 34 (1996), pp. 1814–1821.

[101] N. MESSERSMITH AND J. DUTTON, *Mie scattering measurements of probability density functions in compressible mixing layers*, Experiments in Fluids, 21 (1996), pp. 291–301. Springer Publication.

[102] R. MINECK, R. MARGASON, AND L. R. CENTER, *Pressure Distribution on a Vectored-thrust V/STOL Fighter in the Transition-speed Range*, National Aeronautics and Space Administration, 1974.

[103] C. L. MOORE AND J. A. SCHETZ, *Effects of Non-Uniform Velocity Profiles on Dual Jets in a Crossflow*, AIAA, (1985).

[104] D. MOSHER, *An Experimental Investigation of a Turbulent Jet in a Cross Flow.*, PhD thesis, Georgia Institute of Technology, Atlanta, GA, Dec. 1970.

[105] Z. MOUSSA, J. TRISCHKA, AND S. ESKINAZI, *The near field in the mixing of a round jet with a cross-stream*, Journal of Fluid Mechanics Digital Archive, 80 (2006), pp. 49–80.

[106] S. Muraggapan, E. Gutmak, and C. Carter, *Control of penetration and mixing of an excited supersonic jet into a supersonic cross-stream*, in 43rd AIAA Aerospace Sciences Meeting and Exhibit, Reno, Nevada, USA, Jan 2005. AIAA 2005-612.

[107] A. Nejad and J. Schetz, *Effects of viscosity and surface tension on a jet plume in supersonic crossflow*, AIAA journal, 22 (1984), pp. 458–459.

[108] A. Nejad, J. Schetz, and A. Jakubowski, *Mean droplet diameter resulting from atomization of a transverse liquid jet in a supersonic airstream*, in AIAA International Meeting and Technical Display, Baltimore, May 1980. AIAA-80-0899.

[109] A. S. Nejad, J. Schetz, and A. Jakubowski, *Effects of Properties and Location in the Plume on Droplet Diameter for Injection in a Supersonic Stream*, AIAA Journal, 21 (1983).

[110] K. L. Orloff and P. K. Snyder, *Using a 3-dimensional laser anemometer to determine mean streamline patterns in a turbulent flow*, tech. report, N-87-11143, National Aeronautics and Space Administration, Moffett Field, CA (USA). Ames Research Center, 1984.

[111] A. D. Ozuncer, *Phase doppler interferometry measurements of liquid injected in mach 6 cross flow*, Stagiaire Report 2009-XX, von Karman Institute for Fluid Dynamics, Rhode Saint Genèse, Belgium, May 2009. To be published.

[112] D. Ozuncer, *Oil flow visualization of liquid injection into mach 6 crossflow*, Stagiaire Report 2008-43, von Karman Institute for Fluid Dynamics, Rhode Saint Genèse, Belgium, September 2008.

[113] L. Rayleigh, *On the instability of jets*, Proceedings of the London Mathematical Society, 10 (1878), pp. 4–13.

[114] L. Rayleigh, *On the resultant of a large number of vibrations of the same pitch and of arbitrary phase*, Phil. Mag., 10 (1880), pp. 73–78.

[115] R. Reichenbach and K. Horn, *) investigation of injectant properties on jet penetration in a supersonic stream*, AIAA, 9 (1971), pp. 469–672.

[116] E. Reshotko, *Boundary-Layer Stability and Transition*, Annual Reviews in Fluid Mechanics, 8 (1976), pp. 311–349.

[117] E. Reshotko and A. Tumin, *Role of Transient Growth in Roughness-Induced Transition*, AIAA Journal, 42 (2004), pp. 766–770.

[118] L. Rosenhead, *The Formation of Vortices from a Surface of Discontinuity*, in Proceedings of Royal Society of London, 1932, pp. Series A, Vol 134.

[119] K. ROTH, *Influence of the Thin-Layer Approximation on Jet in Crossflow Computations*, AIAA Paper, (1990), pp. 90–3056.

[120] R. RUGGERI, E. CALLAGHAN, D. BOWDEN, AND N. G. R. CENTER, *Penetration of Air Jets Issuing from Circular, Square, and Elliptical Orifices Directed Perpendicularly to an Air Stream*, National Advisory Committee for Aeronautics, 1950.

[121] K. SALLAM, C. AALBURG, AND G. FAETH, *Breakup of round nonturbulent liquid jets in gaseous crossflow*, AIAA journal, 42 (2004), pp. 2529–2540.

[122] W. SARIC, H. REED, AND E. WHITE, *Stability and Transition of Three-Dimensional Boundary Layers*, Annual Reviews in Fluid Mechanics, 35 (2003), pp. 413–440.

[123] F. SCARANO AND M. RIETHMULLER, *Iterative multigrid approach in PIV image processing with discrete window offset*, Experiments in Fluids, 26 (1999), pp. 513–523.

[124] J. SCHETZ, E. KUSH, AND P. JOSHI, *Wave phenomena in liquid jet breakup in a supersonic crossflow*, AIAA, 18 (1980), pp. 774–778.

[125] J. A. SCHETZ AND A. K. JAKUBOWSKI, *Experimental study of surface pressures induced on a flat plate and a body of revolution by various dual jet configurations*, CR 166422, NASA, Dec. 1982.

[126] F. SCHLOEGEL, *Active boundary layer for supersonic flow*, Project Report 2008-26, von Karman Institute for Fluid Dynamics, Rhode Saint Genèse, Belgium, June 2008.

[127] F. SCHLOEGEL, G. PANIAGUA, AND S. TIRTEY, *Active boundary layer trip for supersonic flows*, in Sixth European Symposium on Aerothermodynamics for Space Vehicles, Versailles, France, November 2008, European Space Agency.

[128] S. SCHNEIDER, *Effects of High-Speed Tunnel Noise on Laminar-Turbulent Transition*, Journal of Spacecraft and Rockets, 38 (2001), pp. 323–333.

[129] G. S. SETTLES, *Schlieren and shadowgraph techniques*, Springer, 2001. ISBN 3540661557.

[130] A. SHRAIBER, A. PODVYSOTSKY, AND V. DUBROVSKY, *Deformation and Breakup of Drops by Aerodynamic Forces*, Atomization And Sprays, 6 (1996), pp. 667–692.

[131] G. SIMEONIDES, *The VKI hypersonic wind tunnels and associated measurement techniques*, Technical Momerandum TM 46, von Karman Institute for Fluid Dynamics, Rhode Saint Genèse, Belgium, November 1990.

[132] S. H. Smith and M. G. Mungal, *Mixing, structure and scaling of the jet in crossflow*, Journal of Fluid Mechanics, 357 (1998), pp. 83–122.

[133] J. R. Smy and E. C. P. Ransom, *The Structure of Single Jets at Large Angles to a Cross-Flow*, Tech. Report HSA-KAD-R-GEN-2288, Hawker-Siddeley Aviation LTD, June 1976.

[134] P. Snyder and K. Orloff, *Three-dimensional laser Doppler anemometer measurements of a jet in a crossflow*, Unknown, (1984).

[135] P. Snyder and K. L. Orloff, *Three-dimensional laser Doppler anemometer measurements of a jet in a crossflow*, Unknown, (1984).

[136] J. Srulijes and F. Seiler, *Liquid Fragmentation in High Speed Flows*, vol. 2009-04 of VKI Lecture Series, von Karman Institute for Fluid Dynamics, March 2009, ch. Shock Tube Experiments at ISL on Liquid Fragmentation.

[137] P. Stainback and L. Kubendran, *The Measurement of Disturbance Levels in the Langley Research Center 20-inch Mach 6 Tunnel*, National Aeronautics and Space Administration, Langley Research Center; National Technical Information Service, distributor, 1994.

[138] R. Szwaba, P. Doerffer, K. Namieśnik, and O. Szulc, *Flow structure in the region of three shock wave interaction*, Aerospace Science and Technology, 8 (2004), pp. 499–508.

[139] G. Taylor, *Flow induced by jets*, J. Aero. Sci, 25 (1958), pp. 464–465.

[140] G. I. Taylor, *The instability of liquid surfaces when accelerated in a direction perpendicular to their planes*, Proceedings of the Royal Society of London. Series A, Mathematical and Physical Sciences, (1950), pp. 192–196.

[141] P. Taylor and D. J. Watkins, *An Investigation of Inclined Jets in a Crosswind*, Tech. Report CP-308, AGARD, Nov. 1981. Paper no 6.

[142] R. Theunissen, N. Buchmann, P. Corieri, R. M. L., and C. Darquenne, *Experimental investigation of aerosol deposition in alveolar lung airways*, in 13th International symposium on applications of laser techniques to fluid mechanics„ Lisbon, Portugal, 2006.

[143] S. C. Tirtey, *Characterization of a Transitional Hypersonic Boundary Layer in Wind Tunnel and Flight Conditions*, PhD thesis, Université Libré de Bruxelles, Brussels, Belgium, December 2008.

[144] W. Tollmien, *Calculation of Turbulent Expansion Process*, Math. Mech, 6 (1926), p. 468. Translated from original in German.

[145] T. T. TRAN, *Acetone Planar Laser-Induced Fluorescence and Phosphorescence for Mixing Studies of Multiphase Flows at High Pressure and Temperature*, PhD thesis, Georgia Institute of Technology, May 2008.

[146] T. T. TRAN, Y. KOCHAR, AND J. SEITZMAN, *Acetone photophysics at near critical to supercritical conditions*, in 46th AIAA Aerospace Sciences Meeting and Exhibit, Jan 2008. AIAA 2008-264.

[147] B. VANCRAYENEST AND D. FLETCHER, *Emission Spectroscopic Survey of Graphite Ablation in the VKI Plasmatron*, in 9 th AIAA/ASME Joint Thermophysics and Heat Transfer Conference, San Francisco, California, 2006, AIAA. AIAA 2006-2907.

[148] E. VILLERMAUX, *Fragmentation*, Annual Review of Fluid Mechanics, 39 (2007), pp. 419–446.

[149] R. VOGLER, *Surface Pressure Distributions Induced on a Flat Plate by a Cold Air Jet Issuing Perpendicularly from the Plate and Normal to a Low-speed Free-stream Flow*, National Aeronautics and Space Administration, 1963.

[150] A. WAGNER, *Investigation on roughness induced transition at the vki longshot facility*, Project Report 2008-29, von Karman Institute for Fluid Dynamics, Rhode Saint Genèse, Belgium, June 2008.

[151] L. WALPOT, *Development and Application of a Hypersonic Flow Solver*, PhD thesis, T.U. Delft, Delft, Netherlands, 2002.

[152] A. WATERFALL, *Effect of Ablation on the Dynamics of Spinning Re-Entry Vehicles*, Journal of Spacecraft and Rockets, 6 (1969), pp. 1038–1044.

[153] P. WELCH, *The use of fast Fourier transform for the estimation of power spectra: A method based on time averaging over short, modified periodograms*, Audio and Electroacoustics, IEEE Transactions on, 15 (1967), pp. 70–73.

[154] R. WESTON AND F. THAMES, *Properties of aspect-ratio-4.0 rectangular jets in a subsonic crossflow*, J Aircraft, 16 (1979), pp. 701–707.

[155] A. WIERZBA AND E. TAKAYAMA, *Experimental investigation of the aerodynamic breakup of liquid drops*, AIAA, 26 (1988), pp. 1329–1335.

[156] J. WILLIAMS AND M. N. WOOD, *Aerodynamic interference effects with jet lift schemes on V/STOL aircraft at forward speeds*, 1965., (1965), pp. 619–651.

[157] P. WOOLER, *Flow of a Circular Jet Into a Cross Flow*, Journal of Aircraft, 6 (1969), pp. 283–284.

[158] P. WOOLER, H. KAO, M. SCHWENDEMANN, H. WASSON, AND H. ZIEGLER, *V/STOL Aircraft Aerodynamic Prediction Methods Investigation*, tech. report, AFFDL-TR-72-26, Vols. l-lV, US Air Force, 1972.

[159] C. Xu and J. Prince, *Gradient Vector Flow: A New External Force for Snakes*, in IEEE Computer Society Conference On Computer Vision And Pattern Recognition, Institute Of Electrical Engineers INC (IEEE), 1997, pp. 66–71.

[160] C. Xu and J. Prince, *Snakes, shapes, and gradient vector flow*, Image Processing, IEEE Transactions on, 7 (1998), pp. 359–369.

[161] S. Yoon, S. Heister, J. Epperson, and P. Sojka, *Modeling multi-jet mode electrostatic atomization using boundary element methods*, Journal of Electrostatics, 50 (2001), pp. 91–108.

[162] C. J. Yugve and Sedin, *Laminar Supersonic Flow Calculations Around Spheres and Cylinders*, in 17th ICAS Conference, Sept. 1990. ICAS Paper 6.6.4.

[163] H. Ziegler and P. Wooler, *Multiple Jets Exhausting into a Crossflow*, Journal of Aircraft, 8 (1971), pp. 414–420.

[164] E. Zornoza-Garcia-Andrade and A. Blanco Mateo, *Penetration and atomization of a liquid jet injected in a crossing hypersonic stream*, Stagiaire Report 2007-15, von Karman Institute for Fluid Dynamics, Rhode Saint Genèse, Belgium, September 2007.